

# **ACOUSTIC TRANSDUCTION – MATERIALS AND DEVICES**

**Period 1 January 1999 to 31 December 1999**

**Annual Report**

**VOLUME II**

**OFFICE OF NAVAL RESEARCH  
Contract No: N00014-96-1-1173**

**APPROVED FOR PUBLIC RELEASE –  
DISTRIBUTION UNLIMITED**

**Reproduction in whole or in part is permitted for any  
purpose of the United States Government**

**Kenji Uchino**

**20000815 043**

**PENNSSTATE**



**THE MATERIALS RESEARCH LABORATORY  
UNIVERSITY PARK, PA**

# REPORT DOCUMENTATION PAGE

Form Approved  
OMB No. 0704-0188

Public reporting burden for this collection of information is estimated to average 1 hour per response, including the time for reviewing instructions, searching existing data sources, gathering and maintaining the data needed, and completing and reviewing the collection of information. Send comments regarding this burden estimate or any other aspect of this collection of information, including suggestions for reducing this burden, to Washington Headquarters Services, Directorate for Information Operations and Reports, 1215 Jefferson Davis Highway, Suite 1204, Arlington, VA 22202-4302, and to the Office of Management and Budget, Paperwork Reduction Project (0704-0188), Washington, DC 20503.

1. AGENCY USE ONLY (Leave blank)		2. REPORT DATE 06/12/2000	3. REPORT TYPE AND DATES COVERED ANNUAL REPORT 01/01/2000-12/31/2000	
4. TITLE AND SUBTITLE  ACOUSTIC TRANSDUCTION -- MATERIALS AND DEVICES			5. FUNDING NUMBERS  ONR CONTRACT NO. N00014-96-1-11173	
6. AUTHOR(S)  KENJI UCHINO				
7. PERFORMING ORGANIZATION NAME(S) AND ADDRESS(ES)  Materials Research Laboratory The Pennsylvania State University University Park, PA 16802			8. PERFORMING ORGANIZATION REPORT NUMBER	
9. SPONSORING / MONITORING AGENCY NAME(S) AND ADDRESS(ES) Office of Naval Research    Office of Naval Research ONR 321SS                      Regional Office Chicago Ballston Centre Tower One 536 S Clark Str., RM 208 800 N Quincy Street           Chicago IL 60605-1588 Arlington VA 22217-5660			10. SPONSORING / MONITORING AGENCY REPORT NUMBER	
11. SUPPLEMENTARY NOTES				
12a. DISTRIBUTION / AVAILABILITY STATEMENT			12b. DISTRIBUTION CODE	
13. ABSTRACT (Maximum 200 words)  SEE FOLLOWING PAGE				
14. SUBJECT TERMS			15. NUMBER OF PAGES	
			16. PRICE CODE	
17. SECURITY CLASSIFICATION OF REPORT  UNCLASSIFIED	18. SECURITY CLASSIFICATION OF THIS PAGE  UNCLASSIFIED	19. SECURITY CLASSIFICATION OF ABSTRACT  UNCLASSIFIED	20. LIMITATION OF ABSTRACT	

## GENERAL INSTRUCTIONS FOR COMPLETING SF 298

The Report Documentation Page (RDP) is used in announcing and cataloging reports. It is important that this information be consistent with the rest of the report, particularly the cover and title page. Instructions for filling in each block of the form follow. It is important to *stay within the lines* to meet optical scanning requirements.

Block 1. Agency Use Only (Leave blank).

Block 2. Report Date. Full publication date including day, month, and year, if available (e.g. 1 Jan 88). Must cite at least the year.

Block 3. Type of Report and Dates Covered. State whether report is interim, final, etc. If applicable, enter inclusive report dates (e.g. 10 Jun 87 - 30 Jun 88).

Block 4. Title and Subtitle. A title is taken from the part of the report that provides the most meaningful and complete information. When a report is prepared in more than one volume, repeat the primary title, add volume number, and include subtitle for the specific volume. On classified documents enter the title classification in parentheses.

Block 5. Funding Numbers. To include contract and grant numbers; may include program element number(s), project number(s), task number(s), and work unit number(s). Use the following labels:

C - Contract	PR - Project
G - Grant	TA - Task
PE - Program Element	WU - Work Unit Accession No.

Block 6. Author(s). Name(s) of person(s) responsible for writing the report, performing the research, or credited with the content of the report. If editor or compiler, this should follow the name(s).

Block 7. Performing Organization Name(s) and Address(es). Self-explanatory.

Block 8. Performing Organization Report Number. Enter the unique alphanumeric report number(s) assigned by the organization performing the report.

Block 9. Sponsoring/Monitoring Agency Name(s) and Address(es). Self-explanatory.

Block 10. Sponsoring/Monitoring Agency Report Number. (If known)

Block 11. Supplementary Notes. Enter information not included elsewhere such as: Prepared in cooperation with...; Trans. of...; To be published in... When a report is revised, include a statement whether the new report supersedes or supplements the older report.

Block 12a. Distribution/Availability Statement. Denotes public availability or limitations. Cite any availability to the public. Enter additional limitations or special markings in all capitals (e.g. NOFORN, REL, ITAR).

DOD - See DoDD 5230.24, "Distribution Statements on Technical Documents."

DOE - See authorities.

NASA - See Handbook NHB 2200.2.

NTIS - Leave blank.

Block 12b. Distribution Code.

DOD - Leave blank.

DOE - Enter DOE distribution categories from the Standard Distribution for Unclassified Scientific and Technical Reports.

NASA - Leave blank.

NTIS - Leave blank.

Block 13. Abstract. Include a brief (Maximum 200 words) factual summary of the most significant information contained in the report.

Block 14. Subject Terms. Keywords or phrases identifying major subjects in the report.

Block 15. Number of Pages. Enter the total number of pages.

Block 16. Price Code. Enter appropriate price code (NTIS only).

Blocks 17. - 19. Security Classifications. Self-explanatory. Enter U.S. Security Classification in accordance with U.S. Security Regulations (i.e., UNCLASSIFIED). If form contains classified information, stamp classification on the top and bottom of the page.

Block 20. Limitation of Abstract. This block must be completed to assign a limitation to the abstract. Enter either UL (unlimited) or SAR (same as report). An entry in this block is necessary if the abstract is to be limited. If blank, the abstract is assumed to be unlimited.

## ABSTRACT

This report describes the research performed over the period of 1 January 1999 to 31 December 1999 on a MURI under Office of Naval Research contract N00014-96-1-1173 on the topic "Acoustic Transduction: Materials and Devices" brings together work from the Materials Research Laboratory (MRL), the Applied Research Laboratory (ARL), and the Center for Acoustics and Vibrations (CAV) at The Pennsylvania State University. As has become customary over many years research on the program is described in detail in the 87 technical appendices to this report and only a brief narrative description connecting this research is given in the text.

Perhaps the most outstanding accomplishment of the year is a "spin on" from our earlier single crystal studies now involving Brookhaven National Laboratory and Professor Gonzalo's group in Madrid, Spain. Using exceptionally homogeneous polycrystal lead zirconate titanate samples prepared in MRL, precise synchrotron x-ray analysis has confirmed a new monoclinic phase at lower temperature in composition close to the important morphotropic phase boundary. This work demands a re-thinking of both intrinsic and extrinsic contributions to response in this most important practical transducer material family. Domain Engineering/Domain Averaging in lead zinc niobate:lead titanate (PZN:PT) in lead magnesium niobate:lead titanate (PMN:PT) and in barium titanate ( $\text{BaTiO}_3$ ) continues to offer single crystal systems with outstanding transducer and actuator properties and new insights into the field induced strain mechanisms in all perovskite type piezoelectrics. Excellent progress with the new high strain irradiated P(VDF:TrFE) relaxor ferroelectric copolymer system has helped catalyze a new DARPA initiative in this area and a re-awakening of interest in the whole area of electrostrictive polymer systems.

A primary objective of this MURI grouping was to help shorten the time constant for new materials and device concepts to be applied in practical Navy Systems. We believe this has now been realized in joint work on the composite cymbal type flextensional arrays for large area projectors, and in the progress made towards a micro-tonpitz array system.

Original work on new step and repeat piezoelectric high strain systems continues to make good progress now using commercial motion rectifiers to produce both linear and rotary systems with high torque capability. New composite designs are pushing toward 1 mm diameter motors in the size regimen where there are real difficulties for conventional electromagnetic designs.

A new area of activity this year is in piezoelectric transformers where a circular symmetry design in conjunction with controlled inhomogeneous poling is shown to offer capabilities which are of real interest for energy recovery actuator power systems. Basic studies have evolved a new environmental SEM technique for high resolution domain wall studies without changing problems. Work is continuing on reliable measurements of electrostrictive constants in simple solids confirming by both direct and converse methods and permitting the first generalization of trends in these fundamentally important coupling constants.



# **ACOUSTIC TRANSDUCTION – MATERIALS AND DEVICES**

**Period 1 January 1999 to 31 December 1999**

**Annual Report**

**VOLUME II**

**OFFICE OF NAVAL RESEARCH  
Contract No: N00014-96-1-1173**

**APPROVED FOR PUBLIC RELEASE –  
DISTRIBUTION UNLIMITED**

**Reproduction in whole or in part is permitted for any  
purpose of the United States Government**

**Kenji Uchino**

**PENNSTATE**



---

**THE MATERIALS RESEARCH LABORATORY  
UNIVERSITY PARK, PA**

## APPENDICES

### VOLUME I

#### GENERAL SUMMARY PAPERS

1. Cross, L.E., "Newnham Festschrift Introduction." Guest Editorial, Mat. Res. Innovations **2**, 251 (1999).
2. Newnham, R.E., "Ceramics into the Next Millennium," *British Ceramic Transactions* **98**(5), 251-255 (1999).
3. Uchino, K. and S. Takahashi, "New Trend in Multilayer Ceramic Actuators," Proc. Int'l Symp. Dielectric Ceramics, Amer. Ceram. Soc. '98; Ceramic Trans., Vol. 100, Dielectric Ceramic Materials, p.455 - 468 (1999).
4. Uchino, K., "Smart Composite Materials," Chap.5.19, Comprehensive Composite Materials, Elsevier Science, Oxford, UK (2000). [in press]
5. Kelly, A., R. Davidson, and K. Uchino "Smart Composite Materials Systems," Chap.5.20, Comprehensive Composite Materials, Elsevier Science, Oxford, UK (2000). [in press]
6. Fousek, J., L.E. Cross, and D.B. Litvin, "Possible Piezoelectric Composites Based on the Flexoelectric Effect." Materials Letters **39**, 287-291 (1999).

#### 2.0 MATERIALS STUDIES

##### 2.1 Polycrystal Perovskite Ceramics

7. Noheda, B., D.E. Cox, G. Shirane, J.A. Gonzalo, L.E. Cross, and S.-E. Park, "A Monoclinic Ferroelectric Phase in the  $\text{Pb}(\text{Zr}_{1-x}\text{Ti}_x)\text{O}_3$  Solid Solution." Applied Physics Letters **74**(14), 2059-2061 (1999).
8. Noheda, B., J.A. Gonzalo, R. Guo, S.-E. Park, L.E. Cross, D.E. Cox, and G. Shirane, "The monoclinic phase in PZT: new light on morphotropic phase boundaries," Proceedings of the Workshop on Fundamental Physical of Ferroelectrics, Aspen, CO (February 2000).
9. Noheda, B., J.A. Gonzalo, L.E. Cross, R. Guo, S.-E. Park, D.E. Cox, and G. Shirane, "Tetragonal-to-monoclinic phase transition in a ferroelectric perovskite: The structure of  $\text{PbZr}_{0.52}\text{Ti}_{0.48}\text{O}_3$ ," *Physical Review B* **61**(13), 8687 (April 2000).
10. Guo, R., L.E. Cross, S.-E. Park, B. Noheda, D.E. Cox, and G. Shirane, "Origin of the high piezoelectric response in  $\text{PbZr}_{1-x}\text{Ti}_x\text{O}_3$ ," *Physical Review Letters* **84**(23) (June 2000).
11. Zhang, Q.M., "Electromechanical Properties of Lead Zirconate Titanate Piezoceramics Under the Influence of Mechanical Stresses," IEEE Transactions on Ultrasonics, Ferroelectrics, and Frequency Control **46**(6) (November 1999).
12. Wang, H., W. Jiang, and W. Cao, "Characterization of Lead Zirconate Titanate Piezoceramic Using High Frequency Ultrasonic Spectroscopy," J. Appl. Phys. **85**, 8083-8091 (1999).
13. Zhao, J., V. Mueller, and Q.M. Zhang, "The Influence of External Stress on the Electromechanical Response of Electrostrictive 0.9PMN-0.1PT in the DC Field Biased State," J. Mater. Res. **14**, 948-956 (1999).

## 2.0 MATERIALS STUDIES

### 2.1 Polycrystal Perovskite Ceramics (continued)

14. Zhao, J., A.E. Glazounov, and Q.M. Zhang, "Change in Electromechanical Properties of 0.9PMN-0.1PT Relaxor Ferroelectric Induced by Uniaxial Compressive Stress Directed Perpendicular to the Electric Field," *Appl. Phys. Lett.* **74**, 436-438 (1999).
15. Albert, E.F., A.S. Bhalla, and T. Takenaka, "Large Hydrostatic Piezoelectric Constant and Temperature Dependence of the Piezoelectric Properties Bi(Ni<sub>1/2</sub>Ti<sub>1/2</sub>)O<sub>3</sub>:PbTiO<sub>3</sub> Ceramics," *Ferroelectrics Letters* **25**, 45-52 (1999).
16. Alberta, E.F. and A.S. Bhalla, "Investigation of the Lead Indium Niobate-Lead Magnesium Niobate Solid Solution," *Materials Letters* **40**, 114-117 (1999).
17. Alberta, E.F. and A.S. Bhalla, "Electrical Properties of the Morphotropic Phase Boundary in Pb(In<sub>1/2</sub>Ta<sub>1/2</sub>)O<sub>3</sub>-PbTiO<sub>3</sub> Ceramics," *Ferroelectrics Letters* **26**, 117-123 (1999).
18. Kim, J.S., S.J. Kim, H.G. Kim, D.C. Lee, and K. Uchino, "Piezoelectric and Dielectric Properties of Fe<sub>2</sub>O<sub>3</sub>-Doped 0.57Pb(Sc<sub>1/2</sub>Nb<sub>1/2</sub>)O<sub>3</sub>-0.43PbTiO<sub>3</sub> Ceramic Materials," *Jpn. J. Appl. Phys.* **38**(Part 1, No. 3A), 1433-1437 (1999).

## VOLUME II

19. Liu, S.F., I.R. Abothu, S. Komarneni, P. Poosanaas, D.S. Paik, Y. Ito, and K. Uchino, "PLZT Ceramics Prepared from Conventional and Microwave Hydrothermal Powders," *Ferroelectrics* **231**, 179-185 (1999).
20. Chen, Y. H., S. Hirose, D. Viehland, S. Takahashi, and K. Uchino, "Mn-Modified Pb(Mg<sub>1/3</sub>Nb<sub>2/3</sub>)O<sub>3</sub>-PbTiO<sub>3</sub> Ceramics: Improved Mechanical Quality Factors for High Power Transduction Applications," *Jpn. J. Appl. Phys.* (1999). [accepted].
21. Chen, Y.H., S. Hirose, D. Viehland, and K. Uchino, "Doping Effects in Pb(Mg<sub>1/3</sub>Nb<sub>2/3</sub>)O<sub>3</sub>-PbTiO<sub>3</sub> Ceramics for High Power Transduction Applications," *Mater. Res. Soc. Fall Mtg. '99*, LL.5.9, Boston (Nov. 29-Dec.3, 1999).
22. Du, X.H., Q.M. Wang, U. Belegundu, and K. Uchino, "Piezoelectric Property Enhancement in Polycrystalline Lead Zirconate Titanate by Changing Cutting Angle," *J. Ceram. Soc. Jpn.* **107**(2), 190-191 (1999).

### 2.2 Single Crystal Systems

23. Wada, S., S.E. Park, L.E. Cross, and T.R. Shrout, "Engineered Domain Configuration in Rhombohedral PZN-PT Single Crystals and their Ferroelectric Related Properties," *Ferroelectrics* **221**, 147-155 (1999).
24. Liu, S.-F., S.E. Park, T.R. Shrout, and L.E. Cross. "Electric Field Dependence of Piezoelectric Properties for Rhombohedral 0.955Pb(Zn<sub>1/3</sub>Nb<sub>2/3</sub>)O<sub>3</sub>-0.045PbTiO<sub>3</sub> Single Crystals," *Journal of Applied Physics* **85** (5), 2810-2814 (1999).
25. Erhart, J. and W. Cao, "Effective Material Properties in Twinned Ferroelectric Crystals," *J. Appl. Phys.* **86**, 1073- 1081 (1999).

## 2.0 MATERIALS STUDIES

### 2.2 *Single Crystal Systems (continued)*

26. Yin, J., B. Jiang, and W. Cao, "Elastic, Piezoelectric and Dielectric Properties of  $0.955\text{Pb}(\text{Zn}_{1/3}\text{Nb}_{2/3})\text{O}_3$ - $0.045\text{PbTiO}_3$  Single Crystal with Designed Multidomains," IEEE Transactions UFFC **47**, 285-291 (2000).
27. Wada, S., S.E. Park, L.E. Cross, and T.R. Shrout, "Defect-induced Domain Configuratrion in Relaxor PZN Single Crystal and Its Origin." Trans. of the Mat. Res. Soc. Of Japan **24**(1), 19-22 (1999).
28. Belegundu, U., X. Du, and K. Uchino, "Switching Current In  $\text{Pb}(\text{Zn}_{1/3}\text{Nb}_{2/3})\text{O}_3$ - $\text{PbTiO}_3$  Single Crystals, MRS Meeting, Boston (November 1999).
29. Park, S.-E., S. Wada, L.E. Cross, and T.R. Shrout, "Crystallographically Engineered  $\text{BaTiO}_3$  Single Crystals for High-Performance Piezoelectrics." Journal of Applied Physics **86**(5), 2746-2750 (1999).
30. Du, X.H., Q.M. Wang, U. Belegundu, A. Bhalla, and K. Uchino, "Crystal Orientation Dependence of Piezoelectric Properties of Single Crystal Barium Titanate," Mater. Lett. **40**, 109-113 (1999).
31. Lu, .Y., Z.-Y. Cheng, E. Park, S.F. Liu and Q.M. Zhang, "Linear Electro-optic Effect of  $0.88\text{Pb}(\text{Zn}_{1/3}\text{Nb}_{2/3})$ - $0.12\text{PbTiO}_3$  Single Crystal," Jpn. J. Appl. Phys. **39**, 141-145 (2000).

### 2.3 *High Strain Polymers*

32. Bharti, V., H.S. Xu, G. Shanthi, Q.M. Zhang, and K. Liang, "Polarization and Structural Properties of High Energy Electron Irradiated P(VDF-TrFE) Copolymer Films," J. Appl. Phys. **87**, 452-461 (2000).
33. Cheng, Z.-Y., T.-B. Xu, V. Bharti, S. Wang, and Q.M. Zhang, "Transverse Strain Response in the Electrostrictive P(VDF-TrFE) Copolymer," Appl. Phys. Lett. **74**, 1901-1903 (1999).
34. Cheng, Z.-Y., V. Bharti, T.B. Xu, S. Wang, Q.M. Zhang, T. Ramotowski, F. Tito, and R. Ting, "Transverse Strain Responses in Electrostrictive P(VDF-TrFE) Films and Development of a Dilatometer for the Measurement," J. Appl. Phys. **86**, 2208-2214 (1999).
35. Bharti, V., Z-Y Cheng, S. Gross, T.B. Xu, and Q.M. Zhang, "High Electrostrictive Strain under High Mechanical Stress in High Energy Electron Irradiated Poly(vinylidene fluoride-trifluoroethylene) Copolymer Films," Appl. Phys. Lett. **75**, 2653-2655 (1999).

## 3.0 TRANSDUCER STUDIES

### 3.1 *Composite Structures*

36. Geng, X. and Q.M. Zhang, "Resonance Modes and Losses in 1-3 Composites for Ultrasonic Transducer Applications," J. Appl. Phys. **85**, 1342-1350 (1999).
37. Tressler, J. and K. Uchino, "Piezoelectric Composite Sensors," Chap.5.25, Comprehensive Composite Materials, Elsevier Science, Oxford, UK (2000). [in press]
38. Tressler, J.F., S. Alkoy, A. Dogan, and R.E. Newnham, "Functional Composites for Sensors, Actuators and Transducers," Composites Part A: Applied Science & Manufacturing **30**, 477-482 (1999).

3.0 TRANSDUCER STUDIES

3.1 *Composite Structures (continued)*

39. Tressler, J.F. and R.E. Newnham, "Capped Ceramic Underwater Sound Projector: The "Cymbal" Transducer," J. of Acoustical Soc. America **105**(2), part 1, 591-600 (1999).

VOLUME III

40. Zhang, J., W.J. Hughes, P. Bouchilloux, R. Meyer Jr., K. Uchino, and R.E. Newnham, "A Class V Flextensional Transducer: The Cymbal," Ultrasonics **37**, 387-393 (1999).

41. Zhang, J., W.J. Hughes, R.J. Meyer Jr., K. Uchino, and R.E. Newnham, "Cymbal Array: A Broad Band Sound Projector," Ultrasonics **37**, 523-529 (2000).

3.0 TRANSDUCER STUDIES

3.1 *Composite Structures (continued)*

42. Zhang, J., W.J. Hughes, A.C. Hladky-Hennion and R.E. Newnham, "Concave Cymbal Transducers," Materials Research Innovations **2** (5), 252-255 (1999).

43. Alkoy, S., R.E. Newnham, A.C. Hladky, A. Dogan, and J.K. Cochran, Jr., "Piezoelectric Hollow Spheres for Microprobe Hydrophones," Ferroelectrics **226**, 11-25 (1999).

44. Carlson, W.B., R.E. Newnham and D.P. Williams, "Piezotensegritic Structures for Transducer Applications," Materials Research Innovations **3**, 175-178 (1999).

45. Newnham, R.E. and A. Amin, "Smart Systems: Microphones, Fish Farming, and Beyond," Chemtech **29**(12), 38-47 (1999).

3.2 *3-Dimensional Acoustic Intensity Probes*

46. Bastyr, K.J., G.C. Lauchle, and J.A. McConnell, "Development of a Velocity Gradient Underwater Acoustic Intensity Sensor," J. Acoust. Soc. Am. **106**, 3178-3188 (1999).

47. Lauchle, G.C. and W.A. Kargus, IV, "Scaling of Turbulent Wall Pressure Fluctuations Downstream of a Rearward Facing Step," J. Acoust. Soc. Am. **107**, L1-L6 (2000).

3.3 *Piezoelectric Transformers*

48. Koc, B., S. Alkoy, and K. Uchino, "A Circular Piezoelectric Transformer with Crescent Shape Input Electrodes," Proc. IEEE Ultrasonic Symp., Lake Tahoe, Nevada, Oct. 17-21 (1999).

49. Koc, B. and K. Uchino, "Disk Type Piezoelectric Transformer with Crescent Shape Input Electrodes," Proc. NATO- Advanced Research Workshop: Piezoelectric Materials, Advance in Science, Technology and Applications, Predeal, Romania (May 24-27, 1999).

#### 4.0 ACTUATOR STUDIES

##### 4.1 *Materials and Designs*

50. Uchino, K., "Recent Trend of Piezoelectric Actuator Developments," Proc. Int'l Symp. Micromechatronics and Human Science '99, p.3-9, Nagoya, Japan (Nov. 23-26, 1999).
51. Yao, K., W. Zhu, K. Uchino, Z. Zhang and L.C. Lim, "Design and Fabrication of a High Performance Multilayer Piezoelectric Actuator with Bending Deformation," **46** (4), 1020-1027 (1999).
52. Wang, Q.-M., X.-H. Du, B. Xu, and L.E. Cross, "Electromechanical Coupling and Output Efficiency of Piezoelectric Bending Actuators," IEEE Transactions on Ultrasonics, Ferroelectrics, and Frequency Control **46** (3), 638-646 (1999).
53. Wang, Q.-M. and L.E. Cross, "Analysis of High Temperature Reduction Processing of RAINBOW Actuator," Materials Chemistry and Physics **58**, 20-25 (1999).
54. Glazounov, A.E., Q.M. Zhang, and C. Kim, "Torsional Actuator Based on Mechanically Amplified Shear Piezoelectric Response," Sensors and Actuators A79, 22-30 (2000).
55. Yoo, J.-H., J.-I Hong, and W. Cao, "Piezoelectric Ceramic Bimorph Coupled to Thin Metal Plate as Cooling Fan for Electronic Devices," Sensors and Actuators **79**, 8-12 (1999).

##### 4.2 *Photostriction*

56. Poosanaas, P., K. Tonooka and K. Uchino, "Photostrictive Actuators," J. Mechatronics (1999) [in press].
57. Poosanaas, P. and K. Uchino, "Photostrictive Effect in Lanthanum-Modified Lead Zirconate Titanate Ceramics near the Morphotropic Phase Boundary," J. Mater. Chem. and Phys. **61**, 36-41 (1999).

### VOLUME IV

##### 4.3 *High Force Torsional Actuators*

58. Frank, J.E., G.H. Koopmann, W. Chen, and G.A. Lesieutre, "Design and Performance of a High Force Piezoelectric Inchworm Actuator," Proceedings of SPIE 6<sup>th</sup> Annual International Symposium on Smart Structures and Materials, 1999.
59. Koopmann, G.H., G.A. Lesieutre, J. Frank, and W. Chen, "Design and Performance of a Linear Piezoelectric Wedgeworm Actuator," Piezoelectric Materials: Advances in Science, Technology and Applications, 383-390 (2000).
60. Frank, J. E.M. Mockensturm, W. Chen, G.H. Koopmann, and G.A. Lesieutre, "Roller-Wedgeworm: A Piezoelectrically-Driven Rotary Motor," 10<sup>th</sup> International Conference on Adaptive Structures and Technologies, Paris (October 1999).

#### 4.4 Piezoelectric Mini Motors

61. Glazounov, A.E., S. Wang, Q.M. Zhang, and C. Kim, "High Efficiency Piezoelectric Motor Combining Continuous Rotation with Precise Control Over Angular Positioning," *Appl. Phys. Lett.* **75**, 862-864 (1999).
62. Uchino, K. and B. Koc, "Compact Piezoelectric Ultrasonic Motors," *Ferroelectrics* **230**, 73-86 (1999).
63. Kim, J.S., M.J. Park, and K. Uchino, "Composite Ultrasonic Motors Using a Piezoelectric Disk and an Elastic Body of "Windmill" Type," *Ferroelectrics* **232**, 185-190 (1999).
64. Koc, B., P. Bouchilloux, and K. Uchino, "Piezoelectric Micromotor Using A Metal-Ceramic Composite Structure," *IEEE Trans. Ultrasonic, Ferroelectrics, and Frequency Control* (1999).

#### 5.0 MODELING and CHARACTERIZATION

##### 5.1 Simulation

65. Cao, W., S. Tavener, and S. Xie, "Simulation of Boundary Condition Influence in a Second-Order Ferroelectric Phase Transition," *J. Appl. Phys.* **86**, 5739-5746 (1999).
66. Shen, M. and W. Cao, "Acoustic Band-Gap Engineering Using Finite Size Layered Structures of Multiple Periodicity," *Appl. Phys. Lett.* **75**, 3713-3715 (1999).
67. Uchino, K., and H. Aburatani, "Field Induced Acoustic Emission in Ferroelectric Ceramics," *Proc. 101st Annual Mtg. of Amer. Ceram. Soc., Symp. Dielectric Materials and Devices*, SE-56, Indianapolis, April 25 - 28 (1999). [accepted]
68. Uchino, K., J. Zheng, Y.H. Chen, X. Du, S. Hirose, and S. Takahashi, "Loss Mechanisms in Piezoelectrics—Extrinsic and Intrinsic Losses." *Mater. Res. Soc. Fall Mtg. '99, LL.1.6*, Boston, Nov. 29-Dec.3 (1999).
69. Uchino, K. and S. Hirose, "Loss Mechanisms in Piezoelectrics," submitted to *IEEE UFFC Transactions* (1999).

#### VOLUME V

70. Uchino, K., J. Zheng, Y.H. Chen, X. Du, and S. Hirose, "Loss Mechanisms in Piezoelectrics," *Mater. Res. Soc. Fall Mtg. '99*, Boston (Nov. 29-Dec.3, 1999).

##### 5.2 Thin and Thick Films

71. Abothu, I.R., Y. Ito, P. Poosanaas, S. Kalpat, S. Komarneni, and K. Uchino, "Sol-Gel Processing of Piezoelectric Thin Films," *Ferroelectrics* **232**, 191-195 (1999).
72. Kalpat, S., I.R. Abothu, A. Akiba, H. Goto, S. Trolier-McKinstry, and K. Uchino, "Dielectric and Piezoelectric Property Dependence on Highly Textured (100), (111) and Random Thin Films Grown by RF Sputtering," *Symp. LL Proc., Mater. Res. Soc. Fall Mtg. '99, LL.1.3*, Boston, Nov. 29-Dec.3 (1999).
73. Xu, F., F. Chu, and S. Trolier-McKinstry, "Longitudinal Piezoelectric Coefficient Measurement for Bulk Ceramics and Thin Films Using Pneumatic Pressure Rig," *J. Appl. Phys.* **86** (1) 588 -594 (1999).



## 5.0 MODELING and CHARACTERIZATION

### 5.2 *Thin and Thick Films (continued)*

74. Shepard, J. F., Jr., F. Chu, I. Kanno, and S. Trolier-McKinstry, "Characterization and Aging Response of the  $d_{31}$  Piezoelectric Coefficient of Lead Zirconate Titanate Thin Films," J. Appl. Phys. **85**(9), 6711-6716 (1999).
75. Xu, B., Y. Ye, L.E. Cross, J.J. Bernstein, and R. Miller, "Dielectric Hysteresis from Transverse Electric Fields in Lead Zirconate Titanate Thin Films." Applied Physics Letters **74** (23), 3549-3551 (1999).
76. Xu, B., R.G. Polcawich, S. Trolier-McKinstry, Y. Ye, L.E. Cross, J.J. Bernstein, and R. Miller, "Sensing Characteristics of In-Plane Polarized Lead Zirconate Titanate Thin Films," Applied Physics Letter **75** (26), 4180 (December 1999).
77. Xu, B., L.E. Cross, and D. Ravichandran, "Synthesis of Lead Zirconate Titanate Stannate Antiferroelectric Thick Films by Sol-Gel Processing." J. Am. Ceramic Soc. **82** (2), 306-312 (1999).
78. Xu, B., Y. Ye, Q.-M. Wang, and L.E. Cross, "Dependence of Electrical Properties on Film Thickness in Lanthanum-Doped Lead Zirconate Titanate Stannate Antiferroelectric Thin Films." Journal of Applied Physics **85** (7), 3753-3758 (1999).

### 5.3 *Domain Studies*

79. Belegundu, U., X.H. Du, A. Bhalla, and K. Uchino, "Effect of Electric Field on Domain Formation in Relaxor Based  $\text{Pb}(\text{Zn}_{1/3}\text{Nb}_{2/3})\text{O}_3\text{-PbTiO}_3$  Single Crystals," Ferroelectrics Letters **26** (5-6), 107-116 (1999).
80. Belegundu, U., X.H. Du, L.E. Cross and K. Uchino, "In Situ Observation of Domains in  $0.9\text{Pb}(\text{Zn}_{1/3}\text{Nb}_{2/3})\text{O}_3\text{-}0.1\text{PbTiO}_3$  Single Crystals," Ferroelectrics **221**, 67-71 (1999). (First Author Supervised by Candidate).
81. Hatch, D.M. and W. Cao, "Determination of Domain and Domain Wall Formation at Ferroic Transitions," Ferroelectrics **222**, 1-10 (1999).
82. Cao, W. and S.N. Zhu, "Observation of Ferroelectric Domains in  $\text{LiTaO}_3$ ," Ferroelectrics **226**, 27-35 (1999).
83. Zhu, S.N. and W. Cao, "Imaging of 180 Ferroelectric Domains in  $\text{LiTaO}_3$  by Scanning Electron Microscopy," Phys. Stat. Sol. (a) **173**, 495-502 (1999).
84. Mueller, V., H. Beige, and Q.M. Zhang, "Nonlinear Ferroelectric Domain Wall Response," Ferroelectrics **222**, 295-302 (1999).
85. Liu, R., R. Guo, A.S. Bhalla, L.E. Cross, M. Levy, and R.M. Osgood Jr., "Optical Observation of Dynamic Ferroelectric Phase Transition and Static Domain Structures in Crystal Ion Sliced (CIS)  $\text{LiNbO}_3$  Film." Materials Letters **39**, 264-267 (1999).

### 5.4 *Electrostriction*

86. Eury, S., R. Yimnirun, V. Sundar, P.J. Moses, S.J. Jang, and R.E. Newnham, "Converse Electrostriction in Polymers and Composites," Mat. Chem. and Phys. **61**, 18-23 (1999).
87. Yimnirun, R., S.M.-L. Eury, V. Sundar, P.J. Moses, S. Jang, and R.E. Newnham, "Electrostriction Measurement on Low Permittivity Dielectric Materials," Journal of European Ceramics Society **19**, 1269-1273 (1999).

# **MATERIALS STUDIES**

***(continued)***

# **APPENDIX 19**

## PLZT Ceramics Prepared from Conventional and Microwave Hydrothermal Powders

SHI-FANG LIU, ISAAC ROBIN ABOTHU\*,  
SRIDHAR KOMARNENI, PATCHARIN POOSANAAS,  
DONG-SOO PAIK, YUKIO ITO\* and KENJI UCHINO

*Materials Research laboratory, The Pennsylvania State university,  
University Park PA 16802 U.S.A*

*(Received December 8, 1998)*

Phase pure PLZT (3/52/48) powders were synthesized at a low temperature of 138°C by both conventional and microwave hydrothermal (MH) methods without using excess lead content. PLZT ceramics fabricated from the above powders resulted in 96% of theoretical density upon sintering. Properties such as crystallinity, morphology of the as prepared MH powders and densification and microstructure of the sintered pellets were studied. These properties of MH samples were compared with the properties of those prepared by conventional hydrothermal method (CH).

**Keywords:** Microwave and conventional hydrothermal; PLZT ceramics

### INTRODUCTION

Lanthanum doped lead zirconate titanate (PLZT) ceramics have emerged as the most promising family of materials<sup>[1]</sup> for electrooptic<sup>[2]</sup> and photostriction<sup>[3]</sup> applications. Many solid state reaction processes have been reported<sup>[4,5]</sup> and the studies suggest the importance of chemical homogeneity and powder sinterability for low processing temperatures in fabricating high quality ceramics. It is well recognized now that high quality sinterable powder is an essential prerequisite for multicomponent ceramics. Sol-gel process is a

---

\* Permanent address: Institute of Materials Research and Engineering (IMRE), National University of Singapore, Singapore -119260

versatile technique to prepare very fine powders because of distinct advantages such as low processing temperature, better control over stoichiometry and chemical homogeneity. We have reported PLZT ceramics with greater than 93% of theoretical density by sol-gel process<sup>[3]</sup>. Besides the above two methods for the fabrication of fine powders, hydrothermal method has gained its importance in the fabrication of highly dense electroceramics from very fine powders. In CH method the reactions are carried out in an aqueous environment in the presence of hydroxide ion<sup>[6]</sup>. The advantages of hydrothermal method are (i) low temperature process, (ii) environmentally friendly as the reactions are carried out under closed system conditions, (iii) teflon-lined bombs are used which is very important for highly caustic solutions when used and (iv) ultrafine powder synthesis. There are no reports on the synthesis of PLZT powders by hydrothermal method to the authors' knowledge.

A recent innovation of the hydrothermal process is the introduction of microwaves into the reaction vessels to produce fine ceramic powders rapidly<sup>[7]</sup>. The primary advantages of using microwaves in the hydrothermal system are (i) rapid kinetics leading to savings of time and energy (ii) rapid internal heating and (iii) synthesis of new materials. In view of the above advantages, an attempt is made here to prepare PLZT by MH method and evaluate this method for its phase formation, sinterability and microstructure in comparison to that prepared by CH method.

### **Experimental**

Aqueous solutions of lead nitrate  $[\text{Pb}(\text{NO}_3)_2]$ , lanthanum chloride  $[\text{LaCl}_3]$ , niobium chloride  $[\text{NbCl}_5]$ , oxyzirconium chloride  $[\text{ZrOCl}_2 \cdot 8\text{H}_2\text{O}]$  and titanium tetrachloride  $[\text{TiCl}_4]$  of reagent grade (Aldrich) were the starting chemicals to get the composition  $(\text{Pb}_{0.96}\text{La}_{0.03})(\text{Zr}_{0.51}\text{Ti}_{0.47}\text{Nb}_{0.01})\text{O}_3$ . Stoichiometric inorganic salts of (1M) lead nitrate, (0.5M) oxyzirconium chloride, (0.3M) lanthanum chloride and (0.01M) niobium chloride were dissolved in 20 ml of 0.5 M aqueous solution of  $\text{TiCl}_4$  followed by the addition of KOH (to make the solution 10M with respect to KOH) as a catalyst of the hydrothermal reaction

(Table 1). The mixture was stirred with teflon bar for 30 minutes in 125 ml capacity teflon vessel of Parr bomb (Parr Instrument Co., USA). The experimental set up for MH and CH were described in our earlier work <sup>[7]</sup>. It was assumed in this study that 49 psi was equivalent to 138°C. After the MH and CH treatments, the solid and solution phases were separated by centrifugation before characterization. For powder XRD studies, the solid fractions were dried below 100°C after they were washed with deionized water. Powder XRD patterns of the dried samples were recorded using X-ray diffractometer (Scintag model DMC 105), with  $\text{CuK}\alpha$  radiation in the range of 20-60° 2 $\theta$ . The powders were pressed into disks and sintered at 1150, 1250°C for 4hrs & 1270°C for 2hrs. Densities of the sintered bodies were measured by the Archimedes' method. Microstructural studies were done on samples thermally etched at 1200°C for 20 mins. A gold layer was then sputter coated on the samples. Microstructural investigation was performed with a scanning electron microscope (Model ISI-DS-130, Akashi Beam Tech. Corp., Japan).

### Results and discussion

The experimental data obtained in the synthesis of PLZT by MH and CH methods are shown in Table 1. From the data, it is clear that phase pure PLZT was obtained at the lowest temperature used i.e., 138°C by MH as well as CH methods. In the case of MH method, 2 hrs of treatment time was used to obtain the phase pure PLZT powders while 2.5 hrs was used in the case of CH method. XRD patterns for both MH and CH as prepared powders are depicted in Figure 1, SEM micrographs for the PLZT powders prepared by MH and CH methods are shown in Figure 2. It is obvious from the figure that both MH and CH methods yielded aggregated powders with particle diameter in the range of 1-4 $\mu\text{m}$ , the crystals were of cubic morphology. The pellets prepared from the powders obtained by both MH and CH processing conditions were sintered at 1150, 1250°C for 4hrs and 1270°C/2hrs. All the characterization studies were

done on the pellets with the highest density prepared from powders obtained by both MH and CH at 138°C and sintered at 1250°C for 4 hrs.

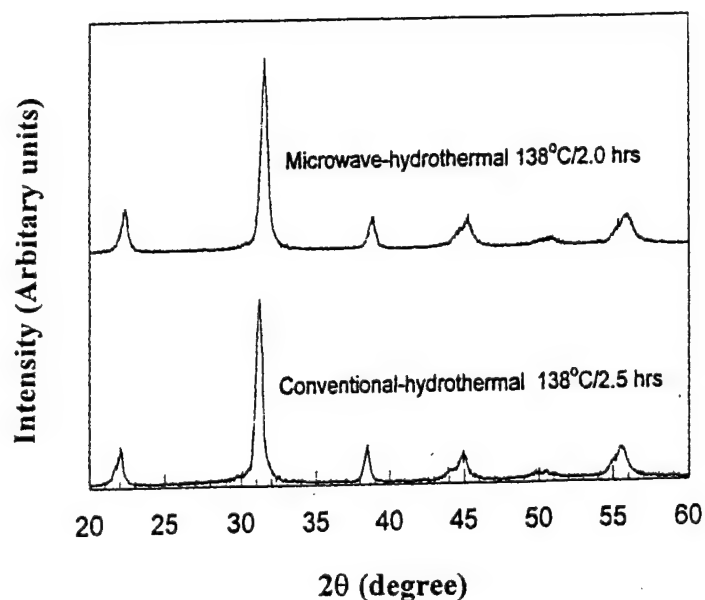


FIGURE 1. XRD patterns of PLZT powders

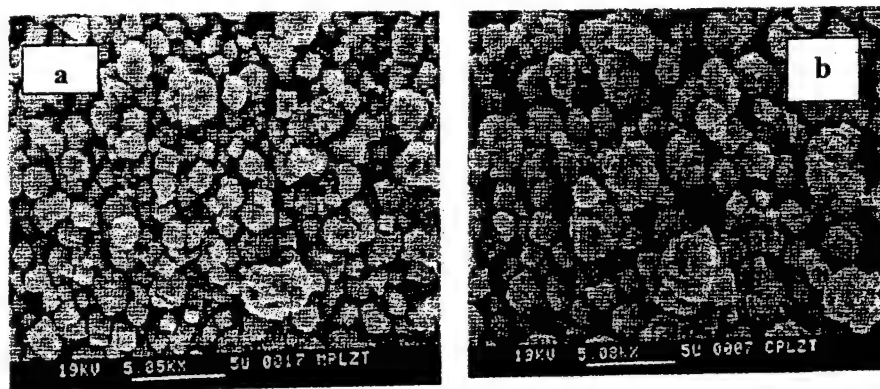


FIGURE 2. SEM micrographs of PLZT powders synthesized at 138°C by (a) microwave and (b) conventional hydrothermal methods

Figure 3 shows SEM microstructures of PLZT sintered pellets. From the figure it is clear that in MH method the average grain size is about 2.5  $\mu\text{m}$  whereas CH method yielded ceramics with average grain size around 2  $\mu\text{m}$  with high density (96%) ceramics in both the cases.



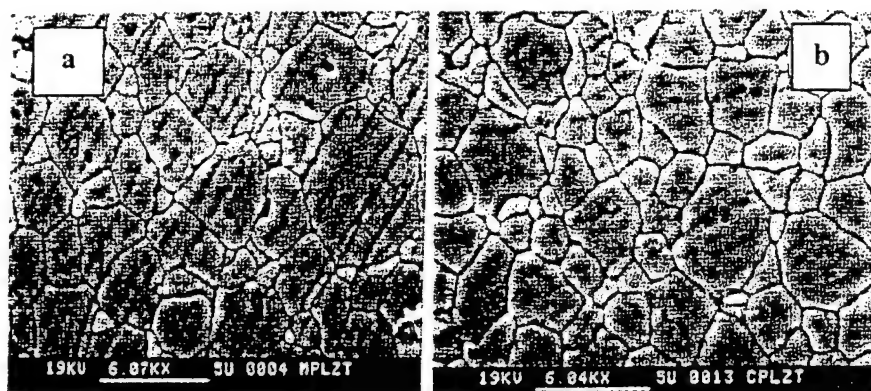


FIGURE 3. SEM micrographs of thermally etched PLZT pellets derived from (a) microwave and (b) conventional hydrothermal powders synthesized at 138°C and sintered at 1250°C for 4h.

### Conclusion

Phase pure PLZT powders were successfully prepared at a low temperature of 138°C by MH and CH methods. However, the former method may lead to energy savings because of rapid heating to temperature. No excess lead content was used during this process. The pellets sintered at 1250°C for 4 hrs showed 96% of theoretical densities and grain sizes of around 3 $\mu$ m. No lead vapors were apparently released during these processes as the reactions were done in closed system.



### References

- [1] G.H. Haertling and C.E. Land, *J. Am. Ceram. Soc.* **54**, 1 (1971).
- [2] J.R. Matdonado and A.H. Meitzler, *IEEE, Trans. Electronic Devices ED*, **17**, 148 (1970).
- [3] P. Poosanas, A. Dogan, A.V.P. Rao, S. Komarneni and K. Uchino, *J. of Electroceramics* **1**, 105 (1997).
- [4] S.S. Chandratreya, R. M. Fulrath, and J.A. Pask, *J. Am. Ceram. Soc.* **64**, 422 (1981).
- [5] B.V. Hiremath, A.I. Kingon, and J.V. Biggers, *J. Am. Ceram. Soc.* **66**, 790 (1983).
- [6] Q.H. Li, M.S. thesis, The Pennsylvania State University, U.S.A. (1993).
- [7] S. Komarneni, R. Roy and Q.H. Li, *Mater. Res. Bull.* **27**, 1393 (1992).

# **APPENDIX 20**

# **Mn-Modified $\text{Pb}(\text{Mg}_{1/3}\text{Nb}_{2/3})\text{O}_3$ - $\text{PbTiO}_3$ Ceramics: Improved Mechanical Quality Factors for High Power Transducer Applications**

Yun-Han Chen<sup>1</sup>, Seiji Hirose<sup>2</sup>, Dwight Viehland<sup>3</sup>, Sadayuki Takahashi<sup>4</sup>, and Kenji Uchino<sup>1</sup>

<sup>1</sup>International Center for Actuators and Transducers, Material Research Laboratory

The Pennsylvania State University, University Park, PA 16802

<sup>2</sup>Yamagata University, Yonezawa-shi, Yamagata 992, Japan

<sup>3</sup>Code 2132; Naval Undersea Warfare Center, Newport, RI 02835

<sup>4</sup>NEC Corporation, 4-1-1, Miyazaki, Kawasaki-shi 216, Japan

(Received June 14, 1999)

Piezoelectric ceramics are potential high-power electro-acoustic sources, and have been studied for many years. However, when these devices are driven under high level vibration, the electromechanical characteristics depart significantly from the conventional linear piezoelectric relationships due to the loss and nonlinear behavior in terms of elastic and dielectric properties. In this paper, we present results concerning the development of modified  $\text{Pb}(\text{Mg}_{1/3}\text{Nb}_{2/3})\text{O}_3$ - $\text{PbTiO}_3$  (PMN-PT) ceramics with improved mechanical quality factors for high-power application. We have focused efforts on base PMN-PT compositions close to the morphotropic phase boundary. Evidence will be presented which indicates that the improved mechanical quality factor results from the introduction of "hard"

characteristics into PMN-PT by the substituents. Investigations of the nonlinearity of the electromechanical properties on the vibrational amplitude were performed using a constant displacement method. The degradation of the mechanical quality factor with increasing drive amplitude also presents thermal stability problems for the usage of these materials in high power transducer applications.

**KEYWORDS:** PMN-PT, MPB, high-power piezoelectric, mechanical quality factor, nonlinearity

## 1. Introduction

Piezoelectric ceramics have been studied for many years, but only recently that interests have arisen to use them as high-power electro-acoustic projectors/sources such as ultrasonic motors and transformers. However, when these materials are electrically driven to high mechanical vibration levels near resonance, the electromechanical property characteristics depart significantly from the conventional linear piezoelectric relationships<sup>1-4)</sup>. The deviations are due to the presence of nonlinear contributions in both the real and imaginary components of the apparent dielectric, electromechanical, and elastic responses. Experimentally, with respect to standard piezoelectric resonance methods, several effects are known to occur under high vibration level excitations. These include: (i) a shift of the resonance frequency<sup>1),2)</sup>; (ii) a decrease of the mechanical quality factor  $Q_m$ <sup>4)</sup>; (iii) an appearance of a jump and/or a hysteresis in the admittance spectrum during a frequency sweep<sup>1),2)</sup>; and (iv) heat generation (due to the lower  $Q_m$ ) that not only degrades the electromechanical properties<sup>5)</sup>, but also may result in thermal stability problems for transducer engineers.

The current lack of a deterministic understanding of these nonlinearities presents a serious problem for their usage in high power applications. Available piezoelectric data on lead zirconate titanate (PZT) and lead magnesium niobate lead titanate (PMN-PT) ceramics have generally been obtained only under small fields. A few researchers have investigated the behavior of piezoelectric materials under high power driving conditions. Beige and Schmidt have shown the presence of strong non-linearities in the dielectric, piezoelectric, and elastic responses. These studies were performed using a resonance method and demonstrated the presence of strong asymmetries in resonance curves. Phenomological analysis demonstrated that the source of all three types of non-linearities was due to the acentric nature of the polarization. Also, Takahashi et al.<sup>4)</sup> have reported high-power measurements on piezoelectric materials by using constant vibration velocity method. In this method,



the vibration velocity of the specimen is held constant by varying the applied voltage as the frequency is swept through the natural resonance mode of the specimen. With this constant vibrational velocity method, asymmetries or hysteresis jumps in the admittance spectrum can be avoided. This method has been applied to materials such as lead zirconate titanate (PZT) modified with Nb and Fe, lead manganese antimonate-lead magnesium niobate-lead titanate (PMS-PMN-PT), and lead manganese antimonate-lead zirconate titanate (PMS-PZ-PT). In general, it has been found that with increasing vibration level, the mechanical quality factor,  $Q_m$ , is decreased dramatically. Tashiro et al.<sup>5)</sup> have also reported a temperature rise during high drive level conditions in PZT-based materials using this method.

Undoubtedly, domain wall motions/vibrations contribute significantly to the electromechanical and mechanical non-linearities. In addition, they will significantly impact the imaginary components of the responses. It is well known that the dielectric loss factor depends dramatically on the amplitude of AC electrical field. The large loss factors under moderate drives results in the conversion of a significant amount of the stored electrical energy into heat. Domain wall motion/vibrations will also contribute significantly to the apparent piezoelectric and mechanical loss factors<sup>6-7</sup>. In general, these loss factors have been shown to be directly related to the dielectric loss factor. Also, previous internal friction investigations of martensitic phases under AC mechanical excitation have revealed the presence of strong nonlinearities in the mechanical quality factor with increasing drive levels<sup>8-9</sup>. These nonlinearities result from a stress dependence of the unrelaxed moduli. With increasing AC drive, the unrelaxed moduli are driven towards the relaxed condition, resulting in ferroelastic domain boundary motion and a significant decrease in the mechanical quality factor. Clearly, in systems containing ferroelectric or ferroelastic (proper or improper) domain boundaries, phase angles are dominantly

controlled by the dynamics of domains. In ferroelectric systems, both the dielectric and mechanical quality factors will be dominated by the dynamics of ferroelectric domains.

In high-power applications, heat generation limits the application of many potential materials. "Soft" piezoelectric materials are known to have significantly higher performance coefficients, relative to hard materials<sup>9)</sup>. However, the enhanced performance of "soft" materials can not be taken advantage of during high power applications, due to thermal stability conditions in transducer design. Rather, the only materials which can be used in these applications are "hard" piezoelectrics. These materials have significantly degraded piezoelectric coefficients and electromechanical coupling coefficients, relative to "soft" one. The near linear nature of the polarization under drive in "hard" materials results in much reduced hysteretic losses on cycling of a field. The reduced losses of "hard" materials result from a domain wall pinning by defect dipoles. In general, it has been observed that higher valent substituents induced "soft" behavior, whereas lower valent ones induced "hard" behavior<sup>9)</sup>.

Ideally, for high power transducer applications, one wants the combination of high electromechanical performance of "soft" piezoelectrics, with the low hysteretic losses of "hard" ones. Another alternative is the electrostrictive relaxor ferroelectrics, which develops piezoelectric properties under DC bias<sup>10)</sup>. These materials have slim quadratic hysteresis loops, but as of yet, their application in high power transducers has also been limited in part by thermal stability considerations. One of the purposes of this work was to attempt to develop PMN-PT ceramics which had been modified by substituents which might induce some degree of "hard" characteristics. High-power, high-Q PMN-PT based ceramics would have important applications in actuators and transducers.

This paper focuses on the high-power piezoelectric characteristics of  $\text{Pb}(\text{Mg}_{1/3}\text{Nb}_{2/3})\text{O}_3\text{-PbTiO}_3$  (PMN-PT) based ceramics which have been modified with Fe or Mn. The perovskite lead magnesium niobate  $\text{Pb}(\text{Mg}_{1/3}\text{Nb}_{2/3})\text{O}_3$  (PMN) is a well-known relaxor with a diffuse phase transition<sup>12),13)</sup>. The

piezoelectric properties of PMN can be enhanced by the addition of PT<sup>14</sup>). The PMN-PT solid solution system exhibits a morphotropic phase boundary (MPB) between a pseudo-cubic and a tetragonal phase at about 30-35 mole % of PT<sup>15</sup>). The dielectric and piezoelectric constants for materials near the MPB are abnormally high as reported by many researchers, such as Lejeune<sup>16</sup>). Although the PMN-PT system has been actively studied for a small electric-field response, the characterization for high power applications has seldom been made.

## **2. Sample Preparation and Experimental Procedure**

PMN-PT powders were formed using the columbite precursor method developed by Swartz and Shrout<sup>17</sup>. In this method, the formation of a parasitic pyrochlore phase ( $\text{Pb}_3\text{Nb}_4\text{O}_{13}$ ) is eliminated. Specimens were prepared for compositions close to the morphotropic phase boundary (MPB) with a PT-content of 33 at.% (i.e., 0.67PMN-0.33PT). This composition will be referred to as PMN-PT through the remaining portions of this paper. Modified PMN-PT ceramics were prepared using Fe or Mn substituents. These particular substituents were chosen in PZT they are conventionally used for making the properties "harder".

In the first stage of powder preparation (columbite precursor step),  $\text{MgO}$  and  $\text{Nb}_2\text{O}_5$  powders were mixed in a stoichiometric ratio. After calcination at  $1200^\circ\text{C}$  for 4hrs, a precursor columbite phase,  $\text{MgNb}_2\text{O}_6$ , was formed. Single phase columbite formation was confirmed by X-ray diffraction. In the second stage, the columbite precursor was mixed in stoichiometric ratios with  $\text{PbO}$  and  $\text{TiO}_2$ . In order to insure proper mixing of a 30 vol.% slurry with de-ionized water, careful dispersion was performed by pH adjustments using ammonia, thus reducing both steric hindrance and electrostatic repulsion (pH adjustment by ammonia). The slurry was vibratory-milled, dried and then calcined at  $700^\circ\text{C}$  for 4 hours. The calcined powders were examined by x-ray diffraction to insure phase purity.

The powders were then fabricated into green bodies by cold isostatic pressing (CIP), in order to increase the green body densities and reduce the deformation due to the inhomogeneous pressure. Sintering was then performed in a Pb-rich atmosphere by placing a small amount of mixed powders of PbO and ZrO<sub>2</sub> in a closed crucible to reduce PbO volatility. Different sintering temperatures and times were tested, in order to best determine the sintering profiles for the different samples. After sintering, the samples were cut and polished to 40mm×5mm×1mm rectangular plates. Gold-sputtering was then used to deposit electrodes on both surfaces. Finally, the specimens were poled by being immersed in silicon oil at 100°C and with an applied field of ~2.5 kV/mm for 20 min.

Scanning electron microscopy (SEM) with energy dispersion x-ray spectroscopy (EDS) (Model HITACHI S-3500N made by Philips) was used to check the grain sizes and the composition homogeneity of the specimens. The dielectric properties were measured using a computer controlled HP 4284A LCR meter. Temperature dependent measurements were performed using a FLUKE 8840 multimeter in conjunction with a Delta Design environmental chamber in the temperature range between 25 and 250°C. Dielectric measurements were performed both before and after poling. The polarization and strain were then simultaneously measured as a function of an applied AC electrical field. The P-E behavior measured using a computer controlled modified Sawyer-Tower circuit. Low frequency, hysteresis data were obtained using a bipolar triangle waves at room temperature. The system measured the  $\epsilon$ -E behavior using an inductance (LVDT) method. The electromechanical properties were determined by measurement of impedance spectra under low level constant voltage drive using a HP4194, and by measurements of impedance spectra at different vibration velocities under constant-current driving conditions. In the constant current method, the voltage applied to the specimen is varied as the frequency is varied through that of the natural resonance in a manner which results in a constant vibration velocity. This method avoids asymmetric resonance curves, which are

known to be problems in impedance measurements under high drive power conditions<sup>1),2)</sup>. Figure 1 shows the block diagram of this constant current method. Further information concerning this method has previously been published<sup>4)</sup>.

### **3. Results and discussions**

#### **3.1 Crystallographic and microstructures**

X-ray diffraction patterns are shown in Figure 2(a) for specimens with 0, 1, 1.7, 2.5, and 3.2 at.% Mn. The pyrochlore/perovskite phase ratios by volume were much less than 0.1% for all these compositions. Clearly, the Mn-modified specimens used in this investigation were nearly phase pure. However, for a Mn content of 3.2 at.%, a small additional peak was observed close to the perovskite 200 peak, indicating small concentrations of a secondary phase either associated with pyrochlore formation or Mn-exsolution. The lattice constants were determined from this data. A plot of the lattice constant as a function of Mn-concentration is shown in Figure 2(b). From the data in this figure, it can be seen that the pseudo-cubic structure does not change significantly with varying Mn doping concentration, over the range investigated. Similarly, phase pure perovskite materials were found by X-ray diffraction for Fe-modified PMN-PT.

Grain sizes were determined for Fe- and Mn-modified specimens for various substituent concentrations by SEM, as shown in Figure 3(a). The grain size of the unmodified base PMN-PT composition was found to be about 5  $\mu\text{m}$ . Upon modification with Fe, the average grain size was found to decrease to about 3  $\mu\text{m}$  for  $x=1$  at.% and remained unchanged with further increase in Fe concentration. For the Mn-modified materials, the average grain size was found to be about 5  $\mu\text{m}$ , which is equal to that of the unmodified base composition. These data clearly demonstrate minor microstructural changes with compositional modification and with increasing substituent

concentrations. Consequently, changes in properties with increasing substituent concentrations can not be attributed to changes in microstructural characteristics associated with the polycrystalline nature of the material. Rather, such changes will need to be explained based on changes in structural-chemical-property relationships.

The possibility of secondary phase formation was further investigated using the EDS attachment to the SEM. Small quantities of secondary phases were observed near grain boundaries for the Mn-modified materials. EDS analysis revealed that the local composition of these regions were rich in Mn and Mg. This result indicates that Mn does have a limited solubility in the PMN-PT perovskite phase, tending to exsolve at concentrations in excess of about 3 at.%. Similarly, Fe substituents are known to have limited solubility in PZT, limiting their concentrations in the fabrication of "hard" piezoelectric ceramics. Thus, in our investigations, substituent concentrations in excess of 3.2 at.% were not investigated.

## **3.2 Weak field properties**

### **3.2.1 Fe-modified PMN-PT**

Figure 4 shows the mechanical quality factor ( $Q_m$ ) and  $d_{33}$  value for Fe-modified PMN-PT as a function of Fe-concentration. The mechanical quality factor was found to be approximately 75 and to be nearly independent of Fe-concentration over the compositional range investigated. These values are close to those found for conventional "soft" piezoelectrics, such as La-modified PZT (PLZT) or Nb-modified PZT<sup>(4),5,18)</sup>. In these cases, the relatively large mechanical losses are believed to be directly due to the large dielectric losses that are incurred under small electrical drives. In "soft" materials, large losses occur due to domain boundary vibrations or excitations that are readily stimulated under weak ac drive conditions.

The results in Figure 4 are contradictory to that observed for Fe-modified PZT<sup>4),5),9)</sup>. In both cases, Fe is substituted onto the B-cation sites. But, in PZT-based materials, Fe-modification results in the development of “hard” piezoelectric behavior and consequently an enhanced mechanical quality factor. Whereas in PMN-PT based materials, Fe-modification results in the preservation of “soft” piezoelectric behavior and no change in the mechanical quality factor. Obviously, something different is occurring. A possible explanation resides in the consideration of the multiple B-cation sites that are available for substituent occupancy in PMN-PT. In PZT based materials, Fe substitution on the B-site must result in the displacement of a +4 cation (Zr or Ti) for a +3 one (Fe). However, in PMN-PT based materials, Fe substitution on the B-site can result in either the displacement of a +2 (Mg), a +4 (Ti) or a +5 (Nb) cation. The B-site cation sublattice that the Fe (+3) preferentially occupies will have a significant impact upon the charge compensation mechanism, and consequently upon the nature of the defects that are introduced into the structure that subsequently interact with domains. The lack of changes in the mechanical quality factor of PMN-PT with increasing Fe-concentration indicates that the Fe-substituents may prefer to occupy the lower valent sites.

### 3.2.2 Mn-modified PMN-PT

To induce “hard” characteristics in PMN-PT, it will be necessary to modify the base composition with a lower valent substituent on a higher valent site, similar to that for PZT<sup>9)</sup>. In mixed B-site cation materials, identification of a lower valent substituent is not straight forward, as discussed above. In the course of this work, various other modified PMN-PT compositions were fabricated. Interesting results were found for Mn-modified PMN-PT. Data are shown in Figures 5(a)-(d) for these materials.



Figure 5(a) shows the mechanical quality factor as a function of Mn-concentration. The unmodified base composition had a  $Q_m$  of approximately 75, as reported above. Upon modification with one at.% Mn, the mechanical quality factor increased to about 400. Upon further increment of the Mn concentration,  $Q_m$  peaked at about 600 for  $x=2.2$  at.%. At higher concentrations, the value of  $Q_m$  decreased slightly. Clearly, the mechanical quality factor is increased significantly by Mn modification. The increment in the mechanical quality factor indicates that the PMN-PT properties may become increasingly “hard” with moderate Mn concentrations. “Hardening” of piezoelectric behavior is believed to occur due to a pinning of domains by dipolar defects at domain boundaries<sup>9</sup>. Thus, the domain boundaries can not dissipate mechanical/electrical energies under weak drives. Before dielectric or mechanical absorption can occur, the domain depinning must be stimulated.

Further evidence of the “hardening” of the PMN-PT electromechanical behavior can be seen in Figures 5(b)-(d). In Figure 5(b), the piezoelectric coefficient ( $d_{31}$ ) is shown as a function of Mn concentration. With increasing Mn concentration, the value of  $d_{31}$  can be seen to decrease dramatically. Upon increment of the Mn content between 0 and 1 at.%, the value of  $d_{31}$  decreased by approximately 50%. In Pb-based perovskites, the piezoelectric constant at room temperature is believed to be dominantly due to domain wall contributions<sup>19</sup>. In fact, in PZT, Landau-Devonshire analysis has revealed that the intrinsic (single crystal single domain) response can account for only about 20-25% of the experimentally observed values. The remaining portions of the piezoelectric response have been attributed to domain wall contributions. Consequently, modification of PMN-PT or PZT base compositions with impurities and/or defects which tend to pin domain boundaries will result in dramatic decreases in the piezoelectric response. In fact, “hard” PZT materials are well known to have significantly lower electromechanical performance coefficients for this particular reason. The data shown in Figure 5(b) is consistent with the conjecture that Mn modification results in a partial

“hardening” of the piezoelectric behavior of PMN-PT. Also, the elastic compliance ( $s_{11}^E$ ) is shown in Figure 5(c) as a function of Mn concentration. With increasing Mn concentration, the elastic compliance was found to decrease by about 40%, i.e., the elastic constant stiffened. Domain boundary motion is a dissipative phenomenon which results in a softening of the elastic constant, as is well known in ferroelastic and martensitic materials<sup>8,20</sup>. Thus, pinning of domain boundaries would result in a stiffening of the linear elastic constant. In general, as an unrelaxed elastic modulus (i.e., the mechanical quality factor) is decreased, more elastic energy can be stored within the specimen during a cycle of a field<sup>8</sup>). Consequently, the relaxed modulus (i.e., the elastic stiffness) is increased.

The electromechanical coupling coefficient as a function of Mn concentration is shown in Figure 5(d). The value of the coupling coefficient can be seen to vary some between 0 and 3.2 at.%, but the value remains in the vicinity of 0.30. The coupling factor does not decrease with increasing Mn concentration, as the value of  $d_{33}$  is decreased. This is because the elastic constant is stiffened, as the piezoelectric constant is decreased. Less displacement is occurring under electrical drive in the Mn-modified materials, however the displacement has greater force due to the enhanced elastic stiffness. Thus, the electromechanical coupling coefficient between stored electrical and mechanical energy forms is not significantly altered.

The dielectric responses of the Mn-modified PMN-PT specimens are shown in Figure 6. Figure 6(a) shows the  $10^2$  Hz room temperature dielectric constant and loss as a function of Mn concentration. The dielectric constant and dielectric loss factor were both decreased by about 50% with increasing Mn concentration between 0 and 3.2 at.%. The temperature dependent characteristics of the dielectric constant for these specimens are shown in Figure 6(b). The temperature of the dielectric constant maximum, which is the effective phase transition temperature, was nearly independent of the Mn concentration. However, the magnitude of the dielectric constant was significantly altered over a wide

temperature range. In the temperature range below about 150°C, the dielectric constant was continuously decreased with increasing Mn concentration, as illustrated in Figure 6(b). In the temperature range between about 150°C and  $T_{\max}$ , the dielectric constant was increased by Mn modification. However, at temperatures above  $T_{\max}$ , the dielectric constant was decreased by Mn modification. Furthermore, in this temperature range, the dielectric constant was strongly dependent upon small Mn concentrations (<1 at.%), but was nearly independent upon further increments in concentrations.

The changes in the Mn-dependence of the dielectric constant with temperature might be explained by considering the influence of pinning upon the domain dynamics. In the lower temperature range (25 to 150°C), domains may be pinned by defects induced by Mn modification. Increasing Mn concentration then results in enhanced pinning effects, and thus a reduction in the magnitude of the dielectric constant. However, with increasing temperature, thermal energy may be sufficient to cause a depinning of domains. Over a narrow temperature range near  $T_{\max}$ , the enhancement of the dielectric constant by Mn modification may occur due to the dynamics of domain depinning under thermal fluctuations. Stronger dielectric losses were also observed in this temperature range, as shown in Figure 6(c). Enhanced dielectric absorption with increasing Mn concentration can be understood on the basis of domain depinning effects.

The suppression of the dielectric constant near and above  $T_{\max}$  by Mn modification, which was nearly independent of concentration for  $x > 1$  at.%, may reflect the influence of defects/impurities on the residual nature of the diffuse phase transition in PMN-PT. Further evidence in support of this possibility can be seen in Figure 6(d), which shows the temperature dependent dielectric data taken at various frequencies (100, 1k, 10k, 100kHz) for undoped and Mn-modified specimens ( $x=2.5$  at.%). In the unmodified material, a slight frequency dependence was observed only over a narrow temperature

range about  $T_{\max}$ . However, upon Mn modification, much stronger frequency dispersion was induced. In PMN-PT materials, over a wide range of PT contents, a local polarization is known to persist until about  $320^{\circ}\text{C}$ <sup>21)</sup>. The data in Figure 6(d) indicate that Mn modification results in changes in the local polarization formation and the subsequent dynamics of the polarization fluctuations. However, Mn does not induce relaxor behavior in the lower temperature states. Rather, defect-domain interactions seemingly occur which result in domain pinning. Further evidences of domain pinning can be found in the strong field properties.

### 3.3 Strong field properties of Mn-modified PMN-PT

#### 3.3.1 Polarization and strain behavior

The P-E behaviors are shown in Figures 7(a)-(d) for  $x=0, 1, 2.5$ , and  $3.2$  at.% Mn, respectively. Correspondingly, the S-E behaviors are shown in Figures 7(e)-(h). With increasing Mn concentration, the saturation polarization and remanent polarizations are decreased, whereas the coercive field is increased. These results are consistent with the conjecture that Mn induces a degree of “hardness” into PMN-PT. In “hard” PZTs, domain pinning by dipolar defects internally biases the polarization. Poling, then, results in the development of a net dipolar field and an asymmetric hysteresis loop<sup>9),22)</sup>. However, in the quenched state, random dipolar fields are believed to reduce the switchable polarization, as can also be observed in Figure 7. Defect pinning enhances the squareness of the P-E curves, and at the same time also reduces the switchable polarization. Under low to moderate drive levels, reduced energy losses will be incurred under cycling of an AC electrical field. However, if a threshold field is exceeded and domain depinning occurs, the energy lost per cycle will increase dramatically.

“Hardening” of the P-E behavior with increasing Mn concentration also results in reduced electrically induced strains, as shown in Figures 7(e)-(h). In these figures, it can be seen that the

saturation strain decreases from ~0.3% to 0.2% with increasing Mn concentration between 0 and 3.2 at.%. In addition, the degree of hysteresis in the butterfly-like loops is also significantly increased, similarly the value of the piezoelectric coefficient was reduced (see Figure 7(a)-(d)). These results demonstrate that increasing “hardness” in PMN-PT ceramics results in decreased electromechanical performance. Higher mechanical quality factors and lower energy dissipations may be achieved under low to moderate drives with increasing Mn concentration, however electromechanical performance is also degraded. Similar trade-offs exist in modified PZT ceramics between “hard” and “soft” varieties.

### 3.3.2 Amplitude dependent electromechanical properties

For a longitudinal  $d_{31}$  mode with both ends of the sample are mechanically free, the relationship between vibration velocity  $v$  and the driving field  $E_{d0}$  can be written as given in following equation

$$-AtE_{d0} + Zv = 0 \quad (1)$$

and

$$v = \frac{AtE_{d0}}{Z} = \frac{4}{\pi} \sqrt{\frac{\epsilon_{33}^T}{\rho}} k_{31} QE_{d0} \quad (2)$$

where  $A$  is the force factor,  $t$  is the thickness,  $Z$  is the mechanical impedance at the end of the sample,  $\rho$  is the density,  $\epsilon_{33}^T$  is the relative permittivity at constant stress, and  $k_{31}$  is the coupling factor. From the resonance frequency and the maximum displacement  $\xi_m$  at the ends of the specimen, the vibration velocity ( $v$ ) can be estimated by the following equation .

$$v = \frac{1}{\sqrt{2}} \omega_r \xi_m \quad (3)$$

Figure 8 shows the room temperature impedance spectra for PMN-PT modified with 3.2 at.% Mn. Data are shown for various vibration velocities. This data was taken using the constant current/displacement method, which is illustrated in Figure 1.

The impedance spectra in Figure 8 clearly demonstrate significant changes with increasing vibration velocity. The vibration velocity is linearly proportional to the AC electrical drive field. With increasing vibration velocity, the minimum in the impedance is shifted in frequency. The frequency of minimum impedance represents a characteristic frequency at which the amplitude displacement is most susceptible to small electrical drives. At low vibration velocities, the resonance frequency did not shift much with increasing velocity in the range of 0.027 to 0.041 m/sec, although significant changes in impedance were observed. However, with increasing vibration velocity between 0.041 and 0.122 m/sec, significant changes in both the frequency and impedance were observed. At further increments in the drive velocity, significant changes in frequency were observed, although the magnitude of the impedance was not changed significantly. Also, changes in the curvatures of the impedance spectra can be seen with increasing vibration velocity.

These results clearly demonstrate the presence of nonlinearities in the complex elastic response, which are stimulated under electrical drive. The shift in the characteristic frequency indicates the presence of higher order elastic constants. The shifting to lower frequencies is due to a softening of the elastic stiffness under excitation. The changes in the impedance magnitude reflect changes in the drive amplitude required to achieve a constant displacement. The decrease in the changes in impedance at higher drive levels indicates the presence of a positive third order nonlinear damping. However, to be more accurate, it is necessary to calculate the dependence of the elastic constant and

mechanical quality factor on the vibration velocity. To achieve this, we used equation (4) to calculate the observed mechanical quality factor  $Q_m$  near the resonance frequency, where  $V_d$  is the driving voltage at a frequency  $f_1$  and  $f_2=f_r^2/f_1$ ,  $V_{do}$  is the driving voltage at the resonance frequency  $f_r$ , and  $k_p$  is then equal to  $(V_d-V_{do})/V_{do}$

$$Q_m = \frac{f_r}{f_2 - f_1} \sqrt{k_p (k_p + 2)} \quad (4).$$

Figure 9(b) shows the dependence of the resonance frequency on the vibration velocity. This data could also have been shown as a function of AC electrical drive, because the driving voltage is linearly proportional to the vibration velocity for low field and become nonlinear when the field becomes large, as shown in Figure 9(a). From the data in Figure 9(b), the corresponding data for the dependence of the elastic compliance was calculated, as shown in Figure 9(c). In both figures, data are shown for specimens with various Mn concentrations. In these figures, the elastic stiffness (and the resonance frequency) can be seen to increase with increasing Mn concentration. Similar results were shown earlier in section 3.2. The data also reveals that the elastic stiffness decreases with increasing vibration velocity for all specimens investigated. However, the degree of elastic nonlinearity was decreased significantly with increasing Mn concentration.

Figure 9(d) shows the dependence of the mechanical quality factor on the vibration velocity for specimens with various Mn concentrations. For the base composition, the value of  $Q_m$  was low and decreased from ~75 to 35 with increasing vibration velocity between 0.04 and 0.1 m/sec. In the vibration velocity range investigated, no threshold was found below which nonlinearity in  $Q_m$  did not occur. However, these trends were significantly altered by Mn modification. For Mn concentrations

greater than or equal to 1 at.%, the value of  $Q_m$  was dramatically increased and a pronounced threshold in the vibration velocity was observed below which nonlinearity in  $Q_m$  was not found. This threshold velocity was equal to  $\sim 0.1$  m/sec, and was not observed to be dependent upon the Mn concentration for  $1 < x < 3.2$  at.%. With increasing vibration velocity above that of the threshold, the value of  $Q_m$  decreased rapidly, beginning to approach that of the base composition for higher drive levels. Also, the value of  $Q_m$  was different for the various Mn modified compositions at a constant drive level, however the degree of change in  $Q_m$  with increasing drive level was relatively constant.

We believe that the nonlinearities in  $Q_m$  and in the elastic stiffness can be best explained by considering domain dynamics and domain pinning effects. As discussed in section 3.2, mechanical damping is incurred due to domain wall vibrations. Nonlinearity in  $Q_m$  occurs when the domain wall dynamics are driven by external excitation. Consequently, the relaxed modulus (i.e., the elastic stiffness) is decreased, as less elastic energy can be stored within the specimen during a cycle of a field. In the base composition, domain pinning effects may not exist. Consequently, no threshold vibration velocity is observed. However, in Mn modified materials, before domain dynamics can be excited, domain breakaway (depinning domains from defects) would have to be driven by the external field. Consequently, the mechanical quality factor would be high at low and moderate drive levels, but would decrease significantly as a critical field level is surpassed.

The data in Figure 9 provide important information concerning the role of Mn in PMN-PT ceramics. The nonlinear complex elastic data provide the strongest support presented in this paper concerning the presence of domain pinning effects. It also clearly underscores the limitations of these materials in applications requiring high-power density, high-Q materials. Our materials do have an improved combination of properties, i.e., a high  $Q_m$  and good electromechanical properties. However, the operational range over which these optimized properties can be realized is limited, as the "hard"



characteristics induced in the PMN-PT are degraded with increasing drive amplitude. The degradation of  $Q_m$  with increasing drive amplitude will also result in heat generation and thermal stability problems, which will also limit the materials usage as high-power sources.

### 3.3.3 Heat generation and thermal stability considerations

Heat generation is one of the big problems for materials under high-level drive conditions. The temperature rise,  $\Delta T$ , resulting from heat generation and dissipation effects can be expressed as follows;

$$\Delta T = \frac{\omega_r W}{k(T)A} \left(1 - e^{-\frac{t}{\tau}}\right), \quad (5)$$

where  $W$  is the loss energy of the sample per driving cycle,  $\omega_r$  the resonant angular frequency,  $A$  the surface of the sample,  $k(T)$  defined as the overall heat transfer coefficient, and the time constant  $\tau$  is expressed as

$$\tau = \frac{Mc}{k(T)A} \quad (6)$$

where  $M$  is the mass of the sample, and  $c$  is the specific heat.

As  $t \rightarrow \infty$ , the maximum temperature rise in the sample becomes

$$\Delta T = \frac{W\omega_r}{k(T)A} = \frac{W\omega_r}{Mc} \tau \quad (7)$$

The dissipated-vibration-energy per second,  $\omega_r W$  can then be calculated as follows,

$$\omega_r W = U \omega_r Q_m^{-1} = \frac{1}{2} M v^2 \omega_r Q_m^{-1} \quad (8)$$

$$U = \frac{1}{2} \kappa Y_0^E S_m^2 V \quad (9)$$

$$S_m = \frac{\pi \xi_m}{l} \quad (10)$$

$$Y_0^E = \frac{l^2}{\pi^2} \rho \omega_r^2 \quad (11)$$

where  $U$ ,  $v$ ,  $S_m$ ,  $l$ ,  $V$ ,  $\rho$ , and  $\kappa$  are the stored mechanical energy, the vibration velocity, the maximum strain, the vibrator length, the volume, the density and the shape factor, respectively. The shape factor depends on the vibrator shape and vibration mode.

Figure 10 shows the the saturation temperature rise induced by the mechanical damping as a function of the vibration velocity. The saturation temperature was determined by balancing the heat generated by the mechanical dissipation process and that heat radiated after a period of time while the sample was being driven under particular vibrational velocities. From equations (7) and (8), it can be seen that the temperature rise is proportional to the square of the vibrational velocity and inversely proportional to mechanical quality factor. Because the mechanical quality factor  $Q_m$  dropped significantly for vibrational velocities greater than 0.2 m/sec, the temperature rise increased rapidly, as shown in Figure 10. For a vibrational velocity of 0.2 m/sec, the temperature rise was equal to approximately 20°C for all Mn-modified specimens. This is large, but is a significant improvement over that for the base PMN-PT composition, which will induce similar temperature rises at significantly lower vibrational velocities.

In consideration that the dielectric loss factor increases with increasing temperature (see Figure 5(c)), the temperature rise induced by higher vibrational velocities shown in Figure 10 presents a serious problem for thermal stability conditions. For example, assuming a vibrational velocity of 0.2

m/sec, a temperature rise of 20°C is encumbered. This temperature rise results in an increase in the dielectric loss factor, and consequently the mechanical quality factor. In turn, this will increase the temperature rise, according to equation (8), resulting in yet higher loss factors and lower quality factors. In applications as high power transducers, this presents a serious heat flux/dissipation problem.

Our results are important in that they show significantly improved mechanical quality factors in PMN-PT ceramics which are induced by Mn modification. Under high excitation levels, the mechanical quality factor is seriously degraded. Mn modified PMN-PT ceramics have promise for improved performance under moderate drive conditions as high performance transducers and actuators. However, the mechanical quality factor and the nonlinearities induced by increasing vibrational velocity are still inferior to those found in commercially available "hard" PZT materials, but the modified PMN-PT compositions developed in this investigation have superior electromechanical properties.

#### 4. Summary

In this paper, investigations of the influence of Mn and Fe substituents on the electromechanical properties of PMN-PT were performed. These substituents have conventionally been used to make PZT electrically "harder". The purpose of the work was to develop high performance PMN-PT ceramics with significantly improved mechanical quality factors for higher-power transducer applications. Our results show that Fe substituents do not significantly affect the properties of PMN-PT, as commonly occurs in PZT. However, Mn substituents significantly improve the mechanical quality factor, although its piezoelectric constant is partially compromised in relation to the base composition. Investigations of the vibrational amplitude dependence of the mechanical factor revealed a serious decrease with increasing displacement magnitude. Mn-modified PMN-PT has

significant promise for high power applications. However, it will be necessary not to exceed a critical operational power level in order to reduce the total losses and subsequent heat generation.

#### **Acknowledgement**

This research is supported by USA Office of Naval Research through the grant no. N00014-96-1-1173.

## References

1. H. Beige and G. Schmidt, *Ferroelectrics* **41**, (1982) 39.
2. G. Sorge, H. Beige, and C. Scheiding, *Ferroelectrics* **41**, (1982) 51.
3. V. Mueller and Q.M. Zhang, *J. Appl. Phys.* **83**, (1998) 3754.
4. S. Takahashi, S. Hirose, and K. Uchino, *J. Am. Ceram. Soc.* **77**, (1994) 2429.
5. S. Tashiro, M. Ikehiro, and H. Igarashi, *Jpn. J. Appl. Phys.* **36**, (1997) 3004.
6. A. Nowick and B. Berry, *Anelastic relaxations in crystalline solids*, Academic Press, New York (1972).
7. D. Damjanovic, Ph.D. Dissertation, The Pennsylvania State University, University Park, PA (1987).
8. A. Aning, T. Suzuki, and M. Wuttig, "Nonlinear Anelasticity in Solids", *J. Phys. Chem. Solids* **45**, (1984) 481.
9. Tan Qi, Ph.D. Dissertation, University of Illinois, Urbana, IL (1998).
10. W. Pan, W. Gu, D. Taylor, and L.E. Cross, "Induced Piezoelectricity in lead magnesium niobate", *Jpn. J. Appl. Phys.* **28**, (1989) 653.
11. J.F. Li, X.H. Dai, A. Chow, and D. Viehland, *J. Mater. Res.* **10**, (1995) 926.
12. L.E. Cross, *Ferroelectrics* **76**, (1987) 241.
13. G. Schmidt, *Phase Transitions* **20**, (1990) 127.
14. N.C. Kim, PhD Dissertation, The Pennsylvania State University, University Park, PA (1992).
15. W. Huebner, S. Jany, T.R. Shrout, and N. Kim, *Ferroelectrics* **93**, (1989) 341.
16. M. Lejeune and J.P. Boilot, *Mater. Res. Bull.* **20**, (1985) 493.
17. S. Swartz and T. Shrout, *Mat. Res. Bull.* **17**, (1982) 1245.
18. D. Viehland, M. Wuttig, and L.E. Cross, *J. Appl. Phys.* **69**, (1991) 6595.

19. M.J. Haun, PhD Dissertation, The Pennsylvania State University, University Park, PA (1987).
20. M. Wuttig and C. Lin, *Acta Metall.* **31**, (1983) 1117.
21. G. Burns and F. Dacol, *Sol. State Commun.* **58**, (1980) 567.
22. A.P. Levanyuk and A.S. Sigov, Gordon and Breach Science Publishers, New York, New York (1988).

Figure 1: High-power measurement system with constant current driving

Figure 2: (a) Xray diffraction patterns and (b) Lattice constant  $a$  of  $0.67\text{Pb}(\text{Mg}_{1/3}\text{Nb}_{2/3})\text{O}_3\text{-}0.33\text{PbTiO}_3$  with  $x$  at.%Mn doping

Figure 3: (a) Grain size vs. doping concentration of  $0.67\text{Pb}(\text{Mg}_{1/3}\text{Nb}_{2/3})\text{O}_3\text{-}0.33\text{PbTiO}_3$  +  $x$  at.% Mn or Fe. (b) SEM picture of  $0.67\text{Pb}(\text{Mg}_{1/3}\text{Nb}_{2/3})\text{O}_3\text{-}0.33\text{PbTiO}_3$  + 3.2 at.% Mn

Figure 4: Mechanical quality factor  $Q_m$  and Piezoelectric constant  $d_{33}$  of  $0.67\text{Pb}(\text{Mg}_{1/3}\text{Nb}_{2/3})\text{O}_3\text{-}0.33\text{PbTiO}_3$  with  $x$  at.% Fe

Figure5: (a) Mechanical quality factor  $Q_m$  (b) Piezoelectric constant  $d_{31}$  (c) Elastic constant  $s_{11}^E$  (d) Coupling factor  $k_{31}$  of  $0.67\text{Pb}(\text{Mg}_{1/3}\text{Nb}_{2/3})\text{O}_3\text{-}0.33\text{PbTiO}_3$  with  $x$  at.% Mn

Figure 6: (a) Relative permittivity and dielectric loss of  $0.67\text{Pb}(\text{Mg}_{1/3}\text{Nb}_{2/3})\text{O}_3\text{-}0.33\text{PbTiO}_3$  +  $x$  at.% Mn doping at 100 HZ at room temperature. (b) Relative permittivity and (c) dielectric loss vs. temperature of  $0.67\text{PMN}\text{-}0.33\text{PT}$  with  $x$  at.% Mn doping at 100 Hz. (d) Relative permittivity of  $\text{PMN}\text{-}\text{PT}$  (67/33) with 2.5 at.% Mn doping (lower curves) and without doping (upper curves) after poling for frequencies of 100, 1k, 10k, 100kHz.

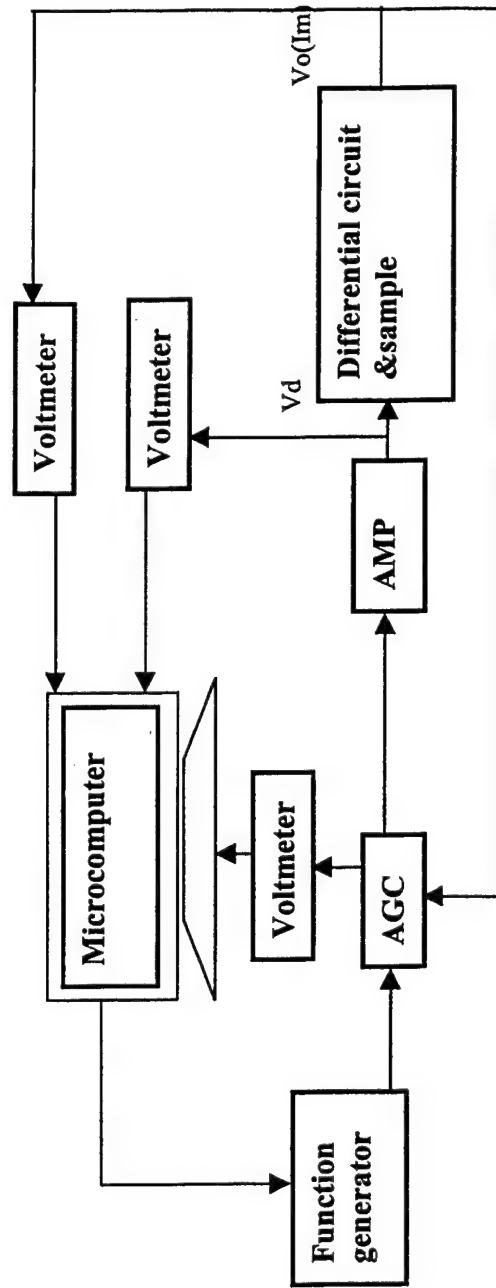
Figure 7: The P-E hysteresis loop of  $0.67\text{Pb}(\text{Mg}_{1/3}\text{Nb}_{2/3})\text{O}_3$ - $0.33\text{PbTiO}_3$  with (a) 0 at.%Mn (b) 1 at.%Mn (c) 2.5 at.%Mn (d) 3.2 at.%Mn and the strain vs. electrical field for (e) 0 at.%Mn (f) 1 at.%Mn (g) 2.5 at.%Mn (h) 3.2 at.%Mn

Figure 8: Impedance Spectrum of  $0.67\text{Pb}(\text{Mg}_{1/3}\text{Nb}_{2/3})\text{O}_3$ - $0.33\text{PbTiO}_3$  + 3.2 at.%Mn with different vibration velocity  $x$  m/sec at room temperature

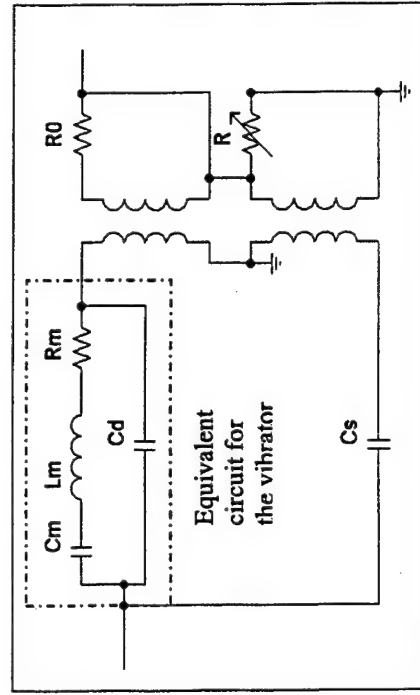
Figure 9: (a)Vibration velocity vs. driving voltage; (b)resonance frequency, (c) compliance elastic constant, and (d)mechanical quality factor  $Q_m$  vs. vibration velocity of  $0.67\text{Pb}(\text{Mg}_{1/3}\text{Nb}_{2/3})\text{O}_3$ - $0.33\text{PbTiO}_3$  +  $x$  at.% Mn .

Figure 10: Temperature rise vs. vibration velocity, and of  $0.67\text{Pb}(\text{Mg}_{1/3}\text{Nb}_{2/3})\text{O}_3$ - $0.33\text{PbTiO}_3$  +  $x$  at.% Mn .

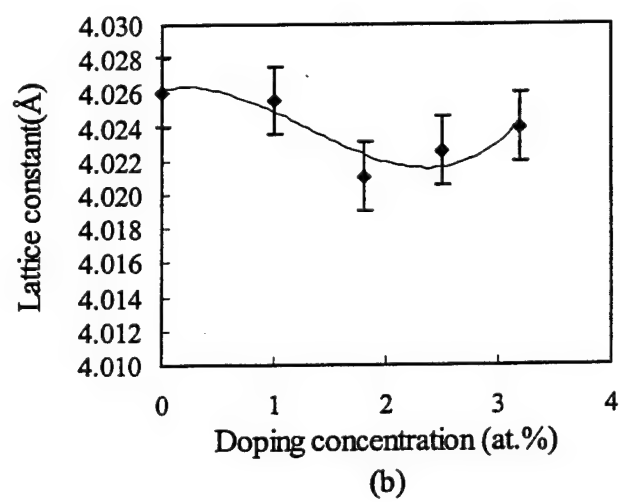
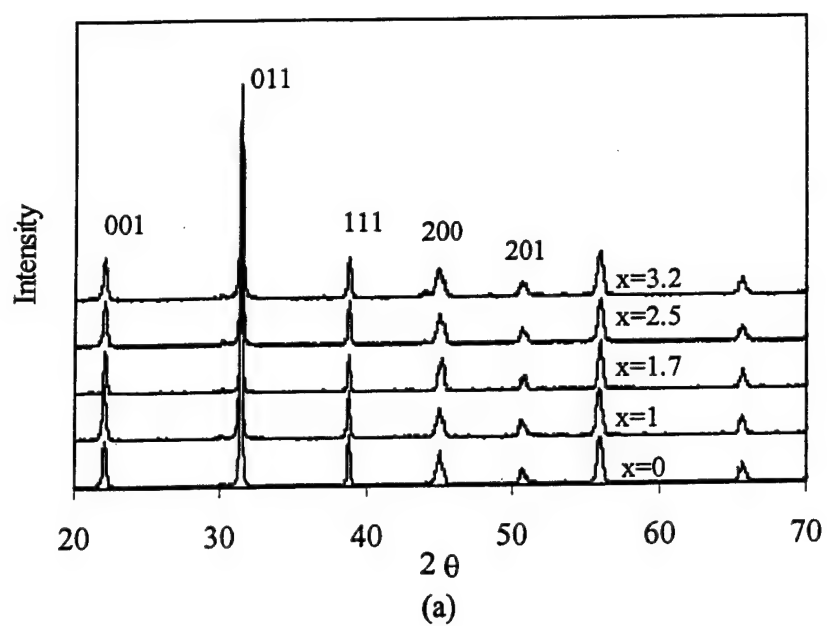


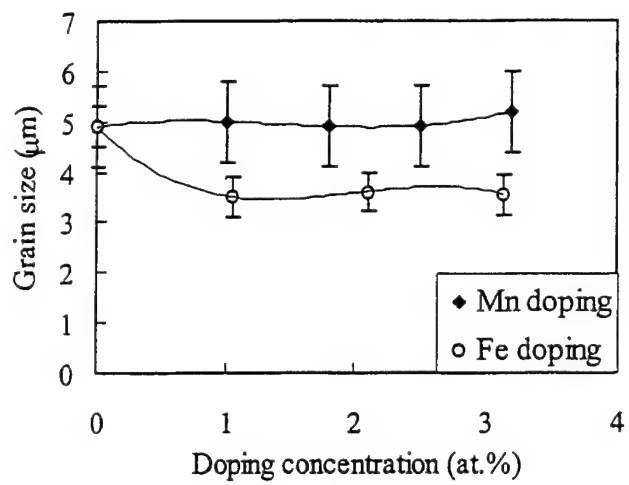


AGC: Auto gain Control  
AMP: Amplifier

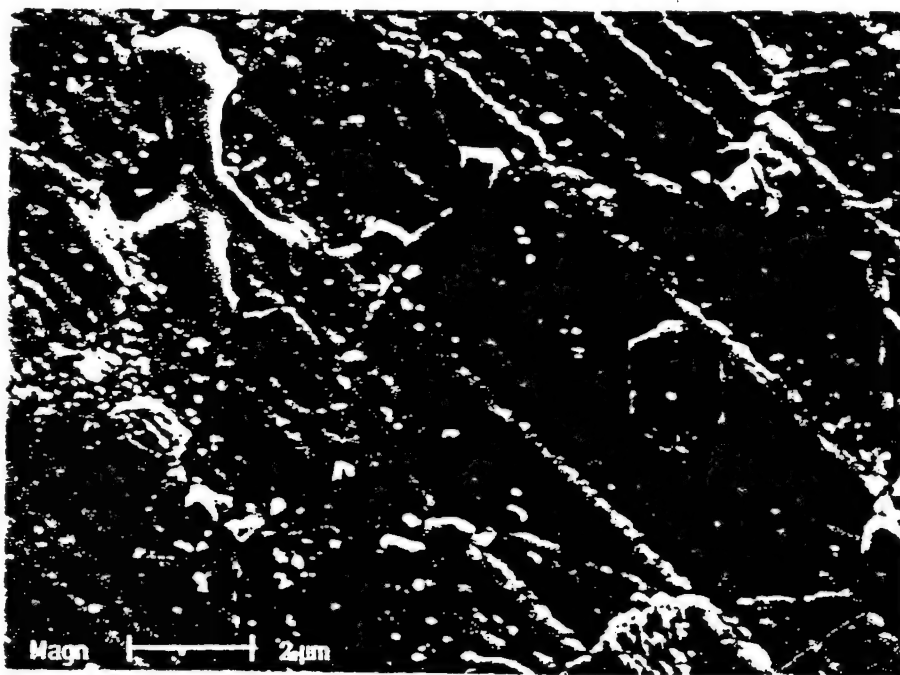


Differential  
circuit &  
sample

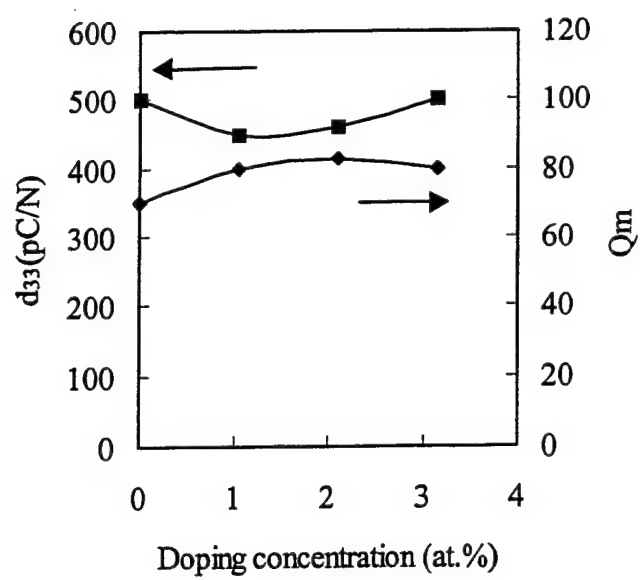


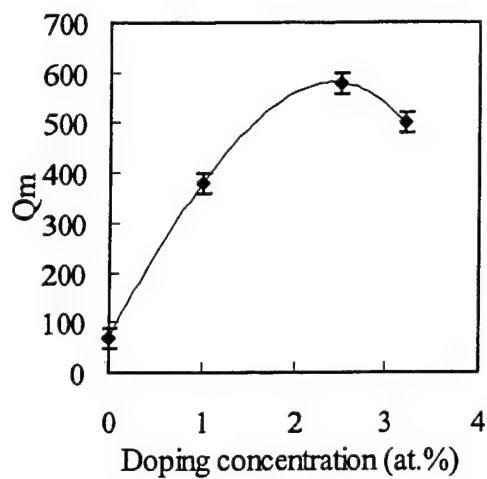


(a)

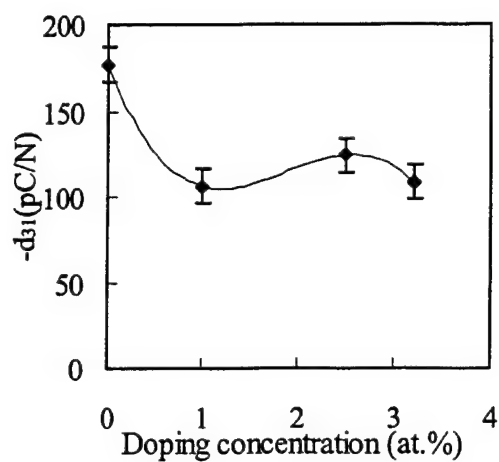


(b)

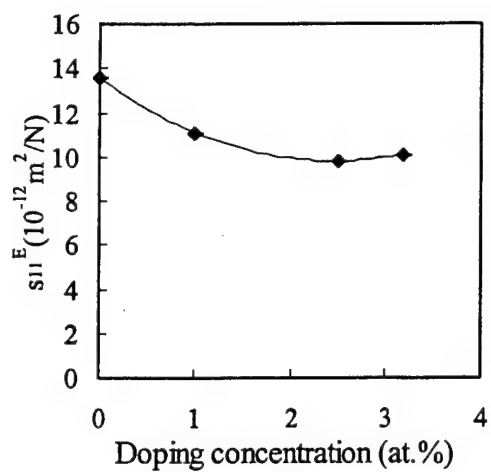




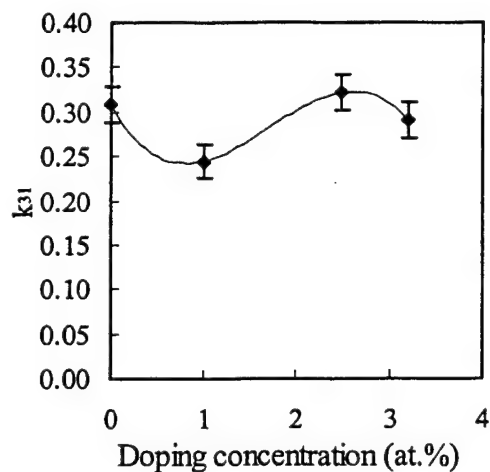
(a)



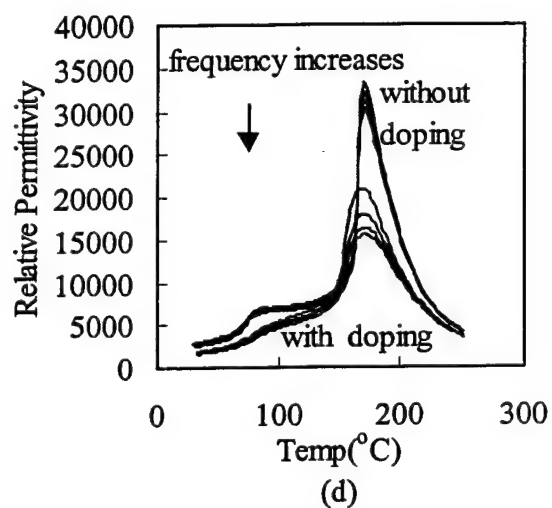
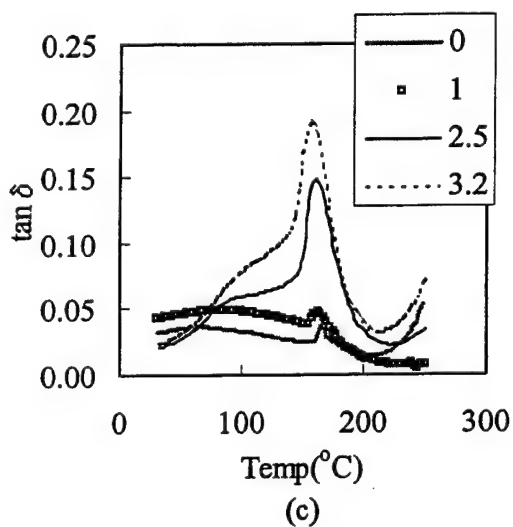
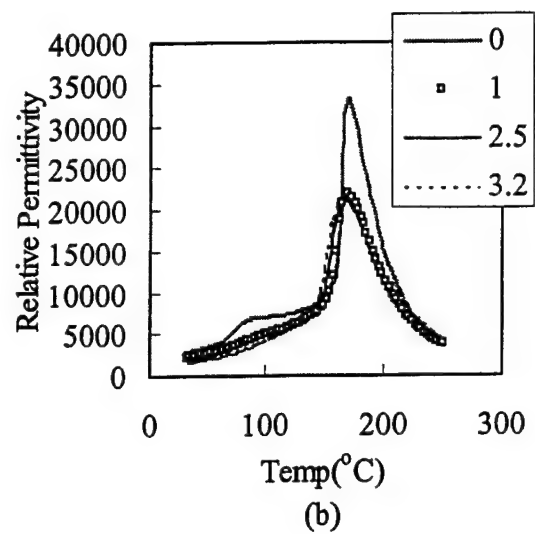
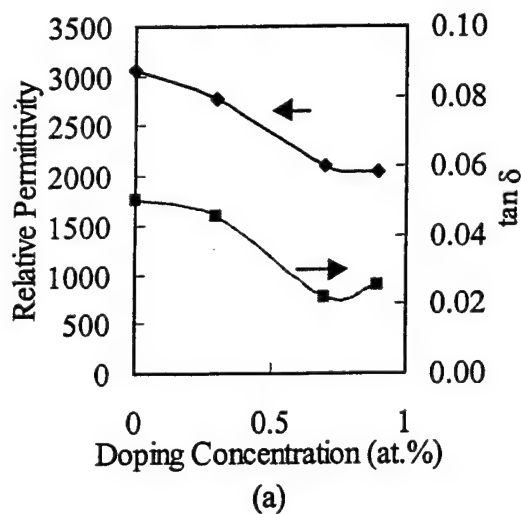
(b)

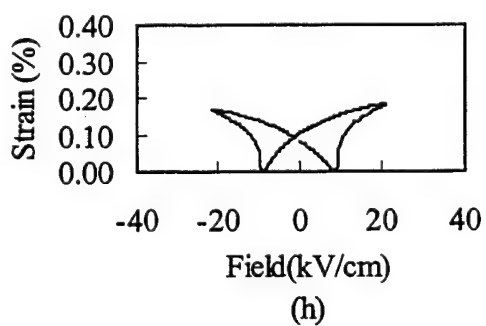
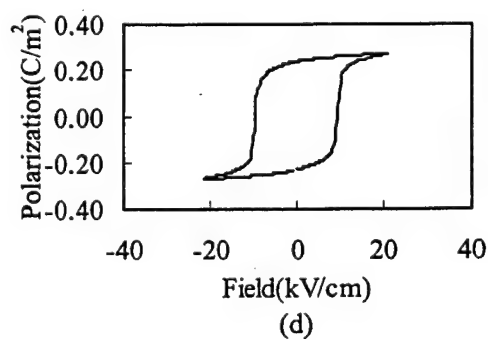
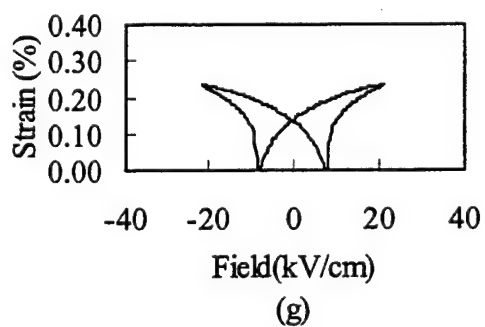
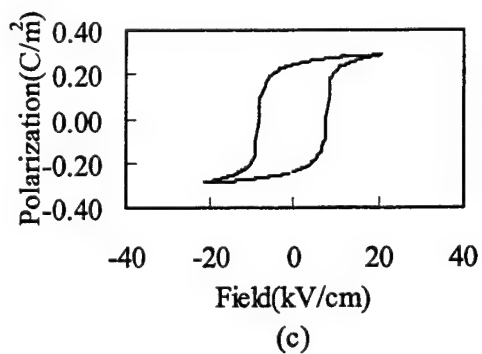
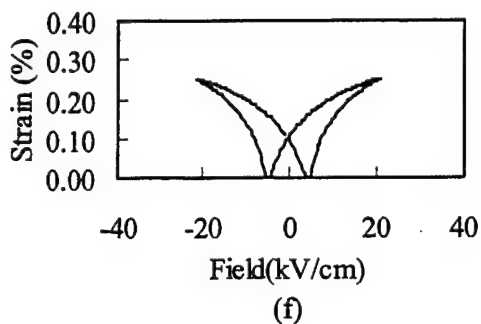
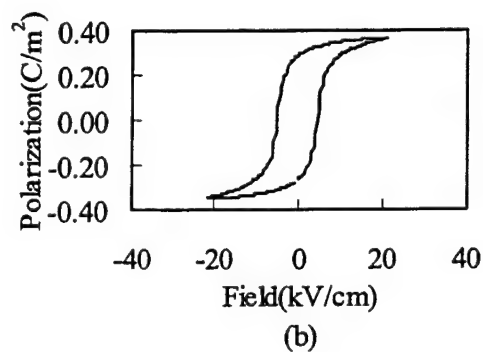
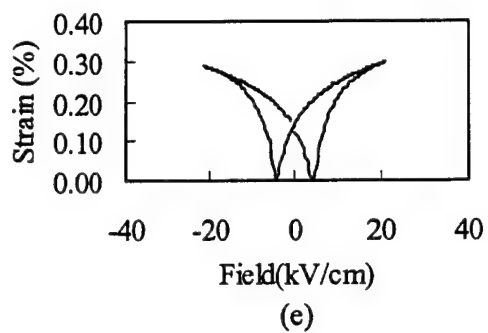
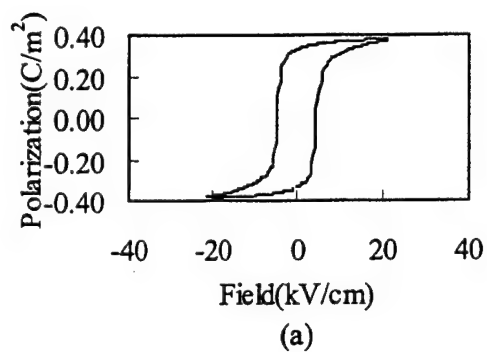


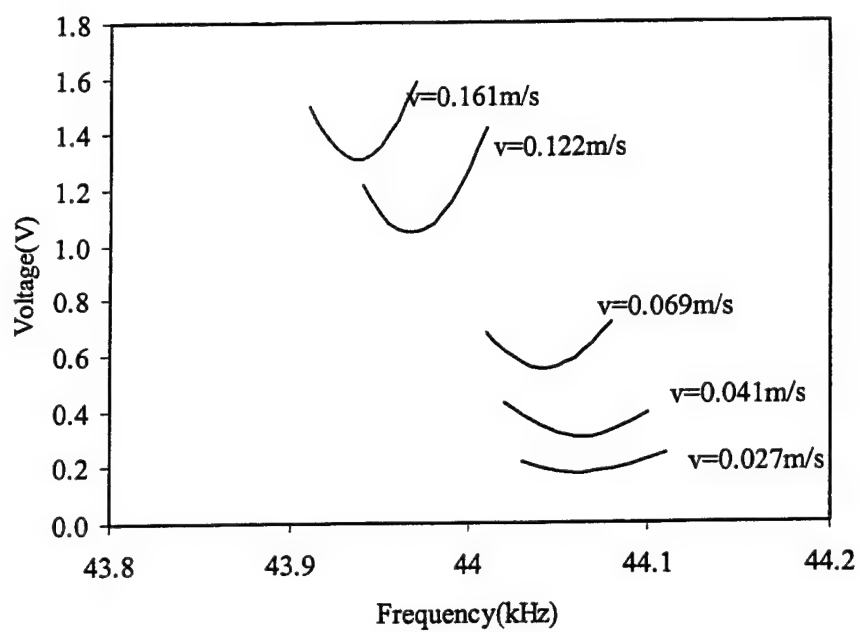
(c)



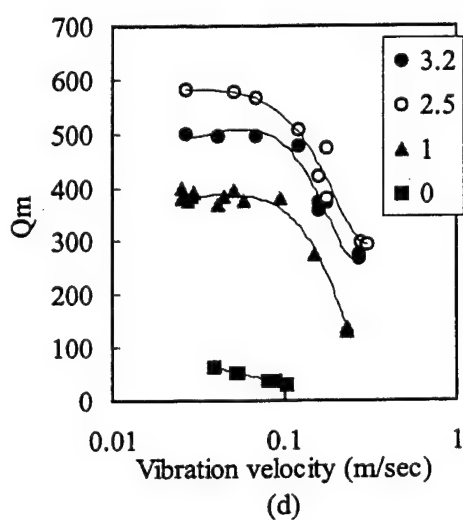
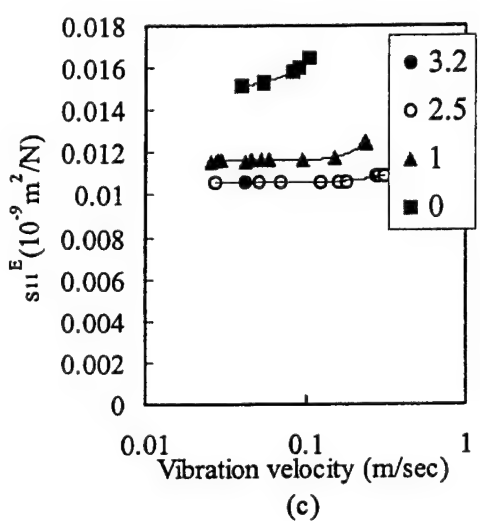
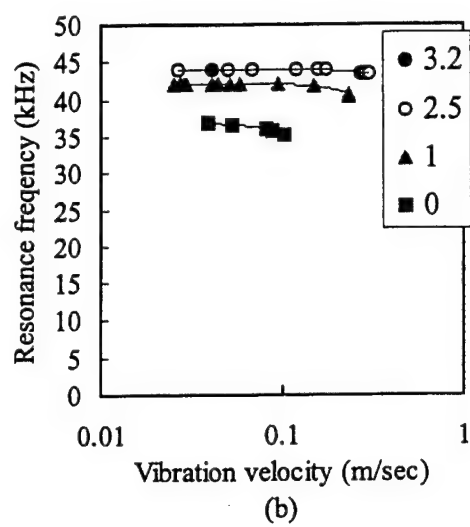
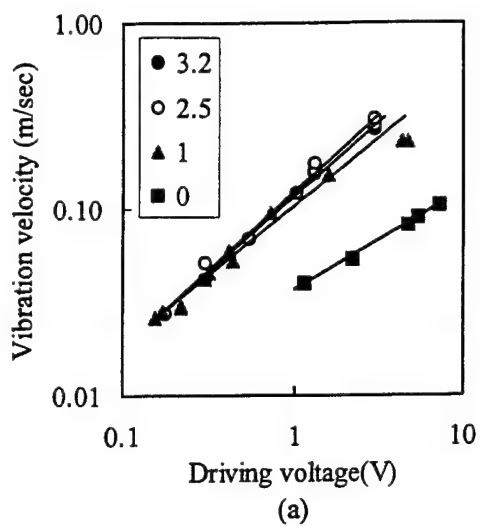
(d)

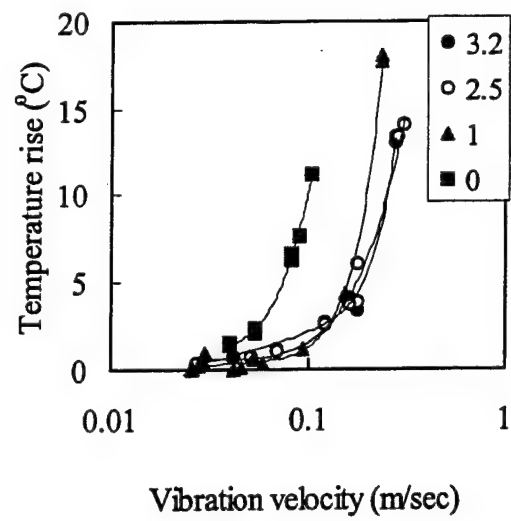












# **APPENDIX 21**

# Doping Effects in $\text{Pb}(\text{Mg}_{1/3}\text{Nb}_{2/3})\text{O}_3$ - $\text{PbTiO}_3$ Ceramics for High Power Transduction Applications

Yun-Han Chen<sup>1</sup>, Senji Hirose<sup>2</sup>, Dwight Viehland<sup>3</sup> and Kenji Uchino<sup>1</sup>

<sup>1</sup>International Center for Actuators and Transducers, Material Research Laboratory  
The Pennsylvania State University, University Park, PA 16802

<sup>2</sup>Yamagata University, Yonezawa-shi, Yamagata 992, Japan

<sup>3</sup>Code 2132; Naval Undersea Warfare Center, Newport, RI 02835

## Abstract

Piezoelectric ceramics are potential high-power electro-acoustic sources, and have been studied for many years. However, when these devices are driven under high level vibration, the electromechanical characteristics depart significantly due to the loss and nonlinear behavior in terms of elastic and dielectric properties. In this paper, we present results concerning the development of modified  $\text{Pb}(\text{Mg}_{1/3}\text{Nb}_{2/3})\text{O}_3$ - $\text{PbTiO}_3$  (PMN-PT) ceramics for high-power application. We have focused efforts on base PMN-PT compositions close to the morphotropic phase boundary. Different mono-doping have been studied to understand the doping effects on the properties of PMN-PT ceramics and, moreover, to improve the properties for the high-power application. Of all the substituents investigated in this study, Mn-doping was found the only one to improve the properties of PMN-PT significantly for high-power application by reducing the total loss (including mechanical loss as well as the dielectric loss), yet keeping the coupling factor constant. This work is supported by Office of Naval Research.

## Introduction

Piezoelectric ceramics are potential high-power electro-acoustic sources, and have been studied for many years. However, there are still some serious problems, such as the durability of the materials, and the fact that the piezoelectric data obtained for a small applied electric field becomes less relevant as the field is increased far above the general characterization condition[1,2]. Presently, the lead zirconate titanate (PZT) family of ceramics with some acceptor-type doping (Hard PZT) are the most widely used for this kind of application owing to their excellent dielectric and piezoelectric properties at the morphotropic phase boundary with the coexistence of tetragonal and rhombohedral phases, allowing increased domain reorientability and easier polarization as well as the low dielectric loss and high mechanical quality factor,  $Q_m$ , which is the inverse of the mechanical loss. However, in hard PZT, the coupling factor  $k$  is quite low and the loss still increases very fast under high-level driving[1]. Thus, investigation of other potential high  $k$  materials with more stable and reliable loss properties is important for transduction application.

The perovskite lead magnesium niobate  $\text{Pb}(\text{Mg}_{1/3}\text{Nb}_{2/3})\text{O}_3$  (PMN) is a well-known relaxor with a diffuse phase transition. The structure is pseudo-cubic with an average space group symmetry  $\text{Pm}3\text{m}$  at room temperature, with no evidence of long range ordering of the dissimilar B site cation sublattices. The disorder in the B site cation is believed to be the cause of relaxor type behavior in these materials. The piezoelectric properties of PMN can be enhanced with the addition of PT. The PMN-PT solid solution system exhibits a morphotropic phase boundary (MPB) between a pseudo-cubic and a tetragonal phase at about 30-35 mole % of PT. [3] The dielectric and piezoelectric constants for materials near the MPB are abnormally high as reported by many researchers such as Lejeune. [4] The properties of high  $k$ , high  $d$  and high energy

density PMN-PTs are very attractive for high-power applications. However, the mechanical quality factor  $Q_m$  is quite low. Although PMN-PT system has been actively studied under a small AC electric-field condition, the characterization under high power applications has seldom been performed. Furthermore, there are almost no reports about varying  $Q_m$  value in PMN-PT by composition modification. In this study, we investigated doping effects on PMN-PT based ceramics for the goal of improving the materials for high-power applications.

### Sample preparation and experimental procedure

In order to eliminate the formation of a parasitic pyrochlore phase ( $Pb_3Nb_4O_{13}$ ), the columbite precursor method proposed by Swartz and Shrout [3] was used to prepare PMN-PT on the MPB. Both A-site and B-site dopants, including the higher valence and lower valence elements were used to study the effect of doping in PMN-PT. These include La, Li, Na, K, Mn, In, Fe. Excess Mg and Nb were also studied for comparison. In the first stage, MgO and  $Nb_2O_5$  were mixed in a stoichiometric ratio, and a precursor columbite phase  $MgNb_2O_6$  was formed after calcination at  $1200^\circ\text{C}$  for 4hrs. X-ray diffraction patterns were then taken to check phase formation. In the second stage, the precursor was mixed in stoichiometric ratios with PbO and  $TiO_2$ . To insure proper mixing, both steric hinderence and electrostatic repulsion (pH adjustment by ammonia), dispersion mechanisms were required to prepare a 30 vol. % slurry with deionized water. The slurry was vibratory milled, then dried and calcined at  $700^\circ\text{C}$  for 4 hr. Calcined powders were examined by x-ray diffraction to insure phase purity. To control PbO volatility, sintering was performed in a lead rich atmosphere by placing a small amount of mixed powder of PbO and  $ZrO_2$  in a closed crucible. After sintering, the samples were polished, and gold-sputtering was used for the electrodes on both surfaces.

The dielectric properties were measured with a computer controlled automated-measurement system from room temperature to  $250^\circ\text{C}$  (HP4284A for electric measurement and FLUKE8840 with an oven for temperature controlling). The electromechanical properties were determined by measurement of the admittance spectrum under low level constant voltage using an HP4194, and by measurement of the impedance spectrum vs. different vibration velocity under constant-current driving conditions [1]. The latter method is different from the conventional impedance analyzer measurements, where the vibration velocity is significantly increased near the resonance frequency, leading to jumping and hysteresis problems in the impedance vs. frequency curve due to the nonlinearity become significant under high level driving.

### Results and discussions

#### a. Basic properties

Table I summaries the dielectric and electromechanical properties for different dopings. Data taken from previous studies of various doping elements in PZT or PMN-PT, and the radii of  $Pb(2+)$  and  $Ti(4+)$ , have also been included for reference. Effects of Na and K substituents can be seen to be almost the same. Both are from the same group (s-orbitals with 1+ valance) and substitute Pb onto the A sites which have 12-coordination. Both of these substitutents increase the quality factor  $Q_m$  a little and reduce the piezoelectric constant. Li is also from the same chemical group (s-orbital with 1+ valence), yet its ionic radii is smaller ( $0.6\text{\AA}$ ) relative to Na

( $0.95\text{\AA}$ ) and K( $1.32\text{\AA}$ ). The tolerance factor  $t = \frac{(r_{A(12-CN)} + r_{O(6-CN)})}{\sqrt{2}(r_{B(6-CN)} + r_{O(6-CN)})}$  is too small for Li to go

onto the A-sites and it is too large for it to go onto the B-sites. Consequently, the effect of Li

modification is different from Na and K doping. Fe-modification does not change the properties of PMN-PT significantly, however for the PZT system, Fe increases  $Q_m$  to more than 1000. In PZT, both B-site cation sublattice are occupied by 4+ species, while in PMN-PT occupancy is composed of multiple valent species, i.e., 2+ (Mg), 5+ (Nb), and 4+ (Ti). If Fe prefers to substitute for Mg, then, it is either a 3+ (or 2+) species on a 2+ site. In this case, it will not induce acceptor-type (or "harder") behaviors in PMN-PT, as it does in PZT. Similar effects were found in In-modified compositions, as can be seen in Table I. Excess Mg and Nb did not result in any significant effects on the properties. Possibly because concentrations of one at.% excess are too small.

Of all the substituents investigated in this study, Mn was the only one which was found to behave uniquely. Upon Mn modification, the piezoelectric constant was decreased, however the quality factor  $Q_m$  was increased significantly. The coupling coefficient  $k_{31}$  was not significantly affected by Mn modification and had a constant value of  $\sim 0.3$ . These changes in the properties make the materials more suitable for high power transducer applications. Thus, high-power measurements of Mn-modified samples will be shown in the next section.

Table I: The properties of .65PMN-.35PT with 1 at.% doping

element	La <sup>*</sup>	K	Na	Li <sup>**</sup>	Mn <sup>***</sup>	Fe <sup>****</sup>	In <sup>*****</sup>	Nb <sup>*****</sup>	Mg <sup>*****</sup>
Substitute site	A-site	A-site	A-site		B-site	B-site	B-site	B-site	B-site
Valency	+3	+1	+1	+1	+2, +3, +4, +7	+2, +3	+3	+5	+2
Behavior in PZT	Donor-like	Acceptor-like	Acceptor-like	?	Acceptor-like	Acceptor-like	Acceptor-like	Donor-like	Acceptor-like
Ionic radii(A)	1.15	1.32	.95	.6	(+7).46 (+4).6 (+3).66 (+2).8	(+3).64 (+2).74	.8	.64	.72
Curie T	50	181.23	178	178.3	175	178	187.62	185.9	189
Dielectric constant	2300	3990	4140	3260	2100	3100	3140	4050	3500
K <sub>max</sub>	23000	34800	34800	25600	21000	33000	33400	33600	38100
Dielectric loss	.025	.012	.0114	.0305	.009	.0116	.0118	.024	.02
d <sub>33</sub>	280	373	360	546	350	500	564	583	540
Q <sub>m</sub>	76	143	150	68	300	80	88	75	78

Pb (+2) 1.2A, Ti (+4) .68A

A-site cation : 12-coordinated, B-site cation : 6-coordinated

\*Used to adjust T<sub>c</sub>[3]

\*\*Used to improve the electrical resistance, reduce the sintering temperature and reduce the temperature coefficient of capacitance

\*\*\*1.Used as similar reason of Li. 2.Studied for the age effect.[6]

\*\*\*\*Can form PFN[5]

\*\*\*\*\* Can form PIN[5]

\*\*\*\*\*Can form pyrochlore[3]

\*\*\*\*\* Sintering aid, can reduce pyrochlore but induce grain growth.[3]

Figure 1 shows the temperature and frequency dependence of the dielectric constant as well as dielectric loss ( $\tan\delta$ ) for 0.65PMN-0.35PT with different substituents. Mn and Li substituents both depressed and broadened the peak dielectric constant values, shown in Fig 1(a) and (b),

even though Mn had a stronger effect. One possible reason is that they both can form a liquid phase during sintering resulting in secondary phase formation in the grain boundaries, which generally reduces the dielectric constant. However, they have very different behavior of dielectric loss (Tan Delta). While Mn substituents reduce the dielectric loss to less than 1% near room temperature, specimens with Li retain a value of 3% (Fig1 (d) and (e)). The temperature and frequency dependence of dielectric constant of Na and K-doped samples are shown in Fig1 (b). They both exhibited similar results, however Li-modification resulted in significant differences.

## b. Piezoelectric properties under a high-power driving

Heat generation is one of the big problems for materials under high-level driving. The temperature rise,  $\Delta T$ , with a specific sample due to the heat generation is proportional to the loss as follows

$$\Delta T = \frac{\omega_0 W t'}{Mc} \quad (1)$$

where  $\omega_0 W$  is dissipated vibration energy per second,  $M$  mass of the sample,  $t'$  thickness, and  $c$  the specific heat capacitance.

The dissipated-vibration-energy per second,  $\omega_0 W$  can be calculated as follows

$$\omega_0 W = \frac{1}{2} M v^2 \omega_0 Q^{-1} \quad (2)$$

and

$$Q^{-1} = Q_M^{-1} + Q_E^{-1}$$

where  $v$ , and  $\omega_0$  are vibration velocity and resonance angular respectively.

From Eqn(1) and (2), we can get

$$\Delta T = \frac{\frac{1}{2} v^2 \omega_0 Q^{-1} t'}{c} \quad (3)$$

For longitudinal  $d_{31}$  mode with both ends of the sample are mechanically free, the relationship of vibration velocity  $v$  and the driving field  $E_{d0}$  can be written as

$$v = \frac{4}{\pi} \sqrt{\frac{\epsilon_{33}^T}{\rho}} k_{31} Q E_{d0} \quad (4)$$

It can be calculated from the resonance frequency and the maximum displacement  $\xi_m$  of the ends by the following equation

$$v = \frac{1}{\sqrt{2}} \omega_r \xi_m \quad (5)$$

The result of the saturation temperature rise and the total loss increase with an increase of the vibration velocity for Mn-doped samples are shown on Fig.2(a). From Eqn. (3), the temperature

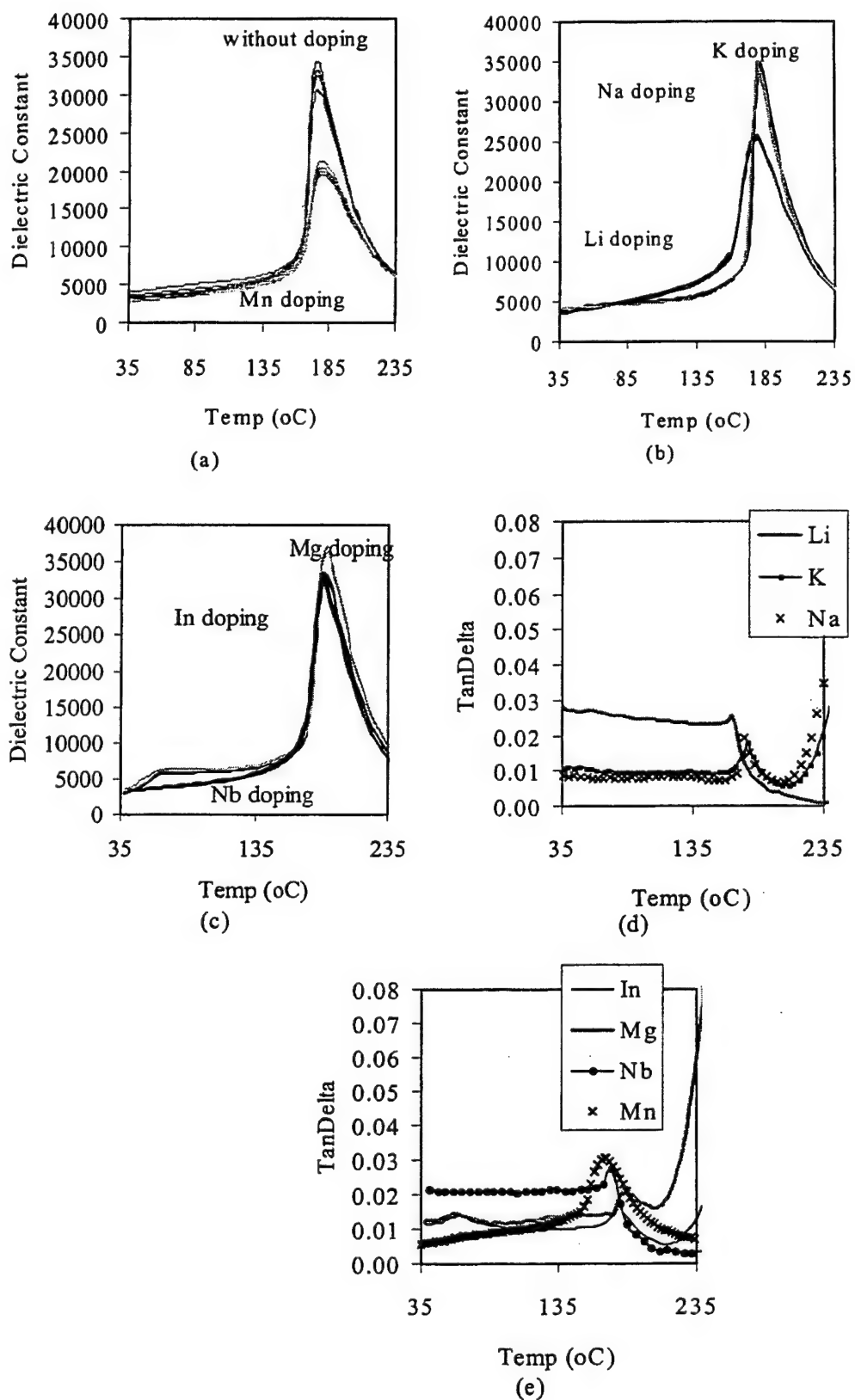


Figure 1: Dielectric constant with different frequencies (100Hz, 1kHz, and 10kHz from the highest to the lowest curve in one group) vs. temperature of  $.65\text{PMN}-.35\text{PT} + 1 \text{ at.}\%$  dopants: (a) pure and Mn, (b) K, Na, Li, (c) In, excess Mg, and excess Nb; Tan Delta vs. Temperature of  $.65\text{PMN}+.35\text{Pt} + 1 \text{ at.}\%$  dopants: (d) Li, Na, K, (e) Mn, In, excess Mg and excess Nb.



rise is proportional to the square of vibrational velocity, and the total loss. The saturation temperature was decided when the sample temperature become stable due to the balance of heat generation and radiation after a period of time when the sample driving under some vibrational velocity. Because the quality factor  $Q$  dropped significantly when the vibrational velocity  $> .2$  m/sec (referred to Fig 2(b)), the saturation temperature rise also increased much faster. The larger  $Q$  the sample has, the smaller the saturation temperature rise is.

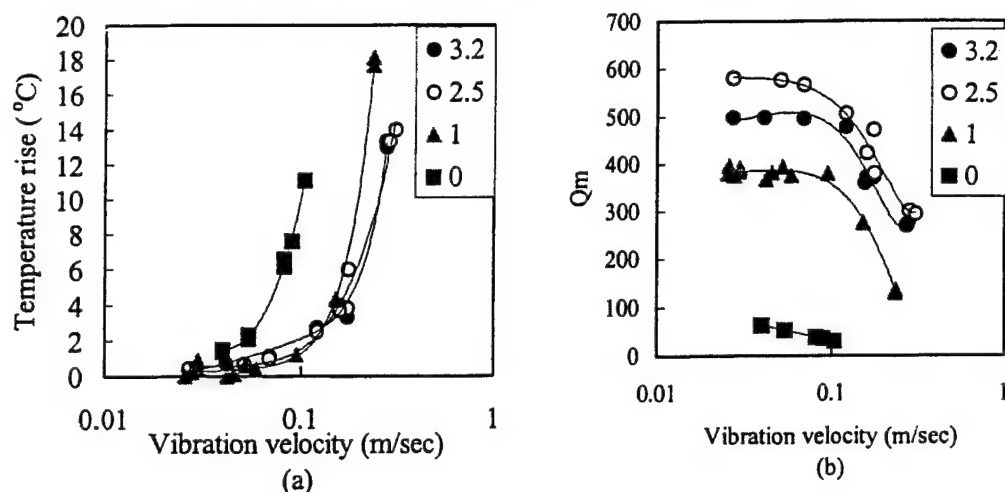


Figure 2: The vibration velocity dependence of temperature rise (a) and quality factor  $Q_m$  (b) of .65PMN-.35PT + x at.% Mn doping

### Summary

In this paper, MPB compositions of PMN-PT with various substituents were studied for high-power applications. Mn-doping was found to improve the properties of PMN-PT significantly for high-power application by reducing the total loss (including mechanical loss as well as the dielectric loss), yet keeping the coupling factor constant. It appears that Mn substituents behave as acceptors in PMN-PT ceramics, resulting in "harder" characteristics. The special effects of Mn may be related to its multiple valance states, however this needs further investigations

### Acknowledgement

This research is supported by ONR-MURI .

### REFERENCE:

1. S. Takahashi, S. Hirose, K. Uchino, *J. Am. Ceram. Soc.*, Vol. 77, 1994, p2429
2. S. Tashiro, M. Ikehiro and H. Igarashi, *Jpn. J. Appl. Phys.* Vol. 36, 1997, p3004.
3. W. Huebner, S. J. Jany, T. R. Shrout N. Kim, *Ferroelectrics*, Vol.93, 1989, p341.
4. M. Lejeune and J. P. Boilot, *Mater. Res. Bull.*, Vol. 20, 1985, p493.
5. Y. Yamashita, *Jpn. J. Appl. Phys.* Vol. 33, 1994, pp3325-3331.
6. W. Y. Pan, Q. Y. Jiang, and L. E. Cross, *Ferroelectrics*, Vol. 82, 1988, pp.111-117.

# **APPENDIX 22**

## Piezoelectric Property Enhancement in Polycrystalline Lead Zirconate Titanate by Changing Cutting Angle

多結晶ジルコン酸チタン酸鉛における切断角度変更による圧電特性の向上

Xiao-Hong DU, Qing-Ming WANG, Uma BELEGUNDU and Kenji UCHINO

International Center for Actuators and Transducers, Materials Research Laboratory  
The Pennsylvania State University, University Park, Pennsylvania 16802, USA

The effective piezoelectric strain constant  $d_{33}$  and electromechanical coupling factor  $k_{33}$  of polycrystalline lead zirconate titanate (PZT) at different cutting angles have been measured by using the IEEE standard resonance method. It was found that for tetragonal PZT 48/52, the effective  $d_{33}$  and  $k_{33}$  monotonously decrease as the cutting angle canted from the poling direction increases. However, for rhombohedral PZT 54/46, the effective  $d_{33}$  has the maximum value along a direction which is canted about 45° away from the poling direction, while the effective electromechanical coupling factor is not sensitive to the cutting direction and remains almost constant in the cutting angle range from 0° to 45°.

[Received October 29, 1998; Accepted December 3, 1998]

Key-words : Lead zirconate titanate, PZT, Piezoelectric property

Lead zirconate titanate (PZT) ceramics have been widely used in transducers and actuators due to the large piezoelectric coefficients and high electromechanical coupling factors. In these applications, the ceramic is electrically driven along a direction either parallel to the poling direction (0° cutting angle) to utilize the longitudinal extension deformation or perpendicular to the poling direction (90° cutting angle) to utilize the shear deformation. To the author's knowledge, no systematic investigations have been done to enhance the piezoelectric properties by choosing an electrical driven direction which is canted between 0° and 90° away from the poling direction. This paper presents the experimental results about such enhancement.

In the previous papers,<sup>1,2)</sup> we reported the phenomenological calculations of the piezoelectric and dielectric constants of hypothetical single crystals of PZT in different crystal orientations. For a tetragonal PZT, the effective piezoelectric constant  $d_{33}$  monotonously decreases as the crystal cutting angle from the spontaneous polarization direction [001] increases. However, for a rhombohedral PZT, the effective piezoelectric constant  $d_{33[001]}$  along the perovskite [001] direction was found to be much larger than those along the spontaneous polarization direction [111]. A similar tendency can be expected for polycrystalline samples, though the enhancement might be less significant than single crystals.

Tetragonal PZT 48/52 and rhombohedral PZT 54/46 ceramic plates with sizes about 10 mm × 10 mm × 1 mm were poled along one of the large sides, as shown in Fig. 1. Then, the plates were cut into small bars along the directions canted 0°, 15°, 30°, 45°, 60° and 75° away from the poling direction, respectively. The sizes of the samples are listed in Table 1. For each cutting direction, a plate normal to the direction was also cut for permittivity measurement. We used gold as the electrode material. The IEEE Standard resonance method<sup>3)</sup> was used to measure the

longitudinal extensional piezoelectric constant  $d_{33}$  and electromechanical coupling factor  $k_{33}$  for each bar. Figure 2 shows the values of  $d_{33}$  with respect to the cutting angles away from the poling direction. The values of  $d_{33}$  have been normalized by  $d_{33//P}$ , the  $d_{33}$  along the poling direction. Figure 3 shows the results for  $k_{33}$ . For tetragonal PZT 48/52, both  $d_{33}$  and  $k_{33}$  monotonously decrease as the cutting angle increases. However, for rhombohedral PZT 54/46,  $d_{33}$  increases as the cutting angle increases from 0° to 45°, leading 1.25 time enhancement at 45°;  $k_{33}$  is not sensitive to the cutting direction and remains almost constant in this cutting angle range. Beyond this cutting angle range, both  $d_{33}$  and  $k_{33}$  decrease as the cutting angle increases. The angle with maximum  $d_{33}$  is little smaller than the calculated angle 56°-59° for the hypothetical PZT crystals. Figure 4 shows the dielectric constants in different directions; for both rhombohedral and tetragonal PZT, the dielectric constants monotonously increase as the cutting angle increases.

In conclusion, for tetragonal PZT 48/52, the effective

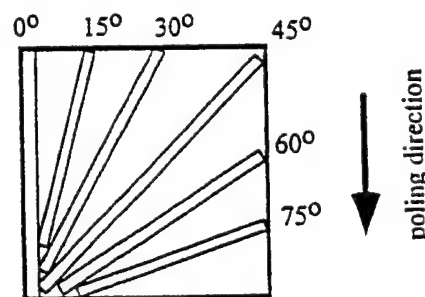


Fig. 1. Illustration of sample cutting.

Table 1. Sizes of Samples (mm)

Angles	0°	15°	30°	45°	60°	75°
PZT 54/46	10.54×0.98 ×1.04	7.05×0.67 ×1.04	8.13×0.93 ×1.04	11.40×1.12 ×1.05	7.10×0.72 ×1.05	6.80×0.64 ×1.04
PZT 48/52	10.03×0.87 ×0.98	6.87×0.65 ×1.01	7.32×0.69 ×1.01	10.03×0.97 ×1.01	6.30×0.62 ×1.00	6.52×0.58 ×1.01

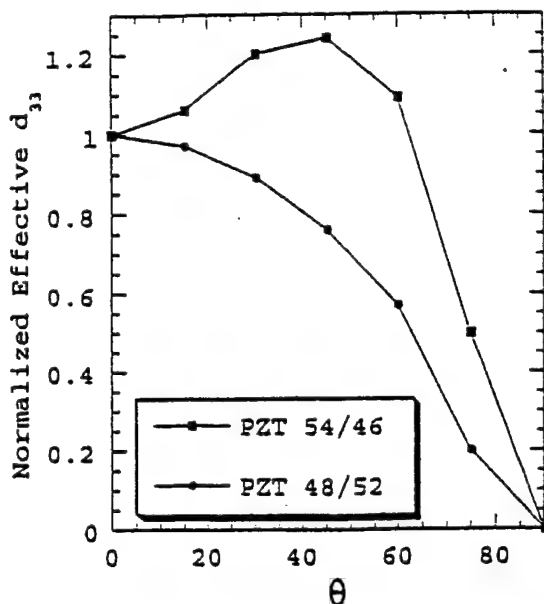


Fig. 2. The effective  $d_{33}$  normalized by  $d_{33}/P_z$ , the  $d_{33}$  along the poling direction, with respect to cutting angles from the poling direction. For tetragonal PZT 48/52,  $d_{33}/P_z = 98 \text{ pC/N}$ . For rhombohedral PZT 54/46,  $d_{33}/P_z = 148 \text{ pC/N}$ .

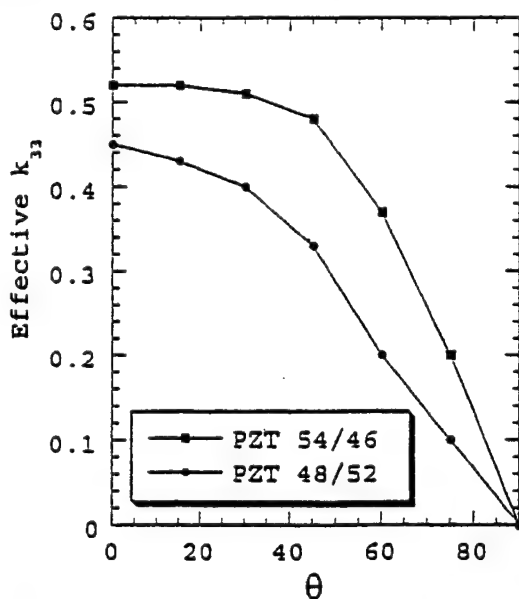


Fig. 3. The effective  $k_{33}$  with respect to cutting angles from the poling direction.

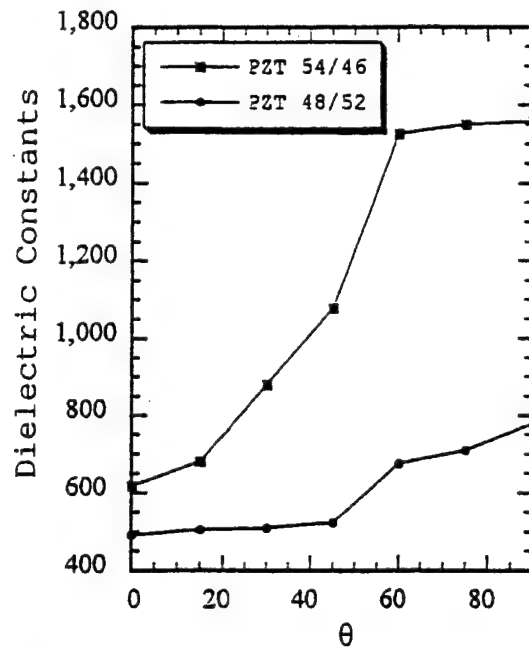


Fig. 4. The dielectric constants with respect to cutting angles from the poling direction.

piezoelectric constant  $d_{33}$  and electromechanical coupling factor  $k_{33}$  have the maximum values along the poling direction and decrease monotonously as the cutting angle from the poling direction increases. However, for rhombohedral PZT,  $d_{33}$  has the maximum value at a cutting angle about  $45^\circ$  away from the poling direction. This shows us that the enhancement of piezoelectric properties by changing the cutting direction away from the polarization direction exists not only in single crystals, but also in polycrystalline solids. By choosing an appropriate cutting direction, the piezoelectric properties can be improved.

**Acknowledgment** This work was supported by the Office of Naval Research under contract: N00014-91-J4145.

#### References

- 1) X. Du, U. Belegundu and K. Uchino, *Jpn. J. Appl. Phys.*, Part 1, 36, 5580-87 (1997).
- 2) X.-H. Du, J. Zheng, U. Belegundu and K. Uchino, *Appl. Phys. Lett.*, 72, 2421-23 (1998).
- 3) ANSI/IEEE, IEEE Standard on Piezoelectricity, Std. 176-1987, IEEE, New York (1987).

# **MATERIALS STUDIES**

***Single Crystal Systems***

# **APPENDIX 23**

## Engineered Domain Configuration in Rhombohedral PZN-PT Single Crystals and their Ferroelectric Related Properties

SATOSHI WADA<sup>a</sup>, SEUNG-EEK PARK<sup>b</sup>, LESLIE ERIC CROSS<sup>b</sup> and  
THOMAS RICHARD SHROUT<sup>b</sup>

<sup>a</sup>*Tokyo University of Agriculture & Technology, 24-16 Nakamachi 2-chome,  
Koganei, Tokyo 184-8588, JAPAN; and* <sup>b</sup>*Materials Research Laboratory,  
The Pennsylvania State University, University Park, PA 16802, USA*

The domain configuration of rhombohedral PZN-8%PT single crystals has been observed as a function of electric-field and crystallographic orientation using polarizing microscope. Although a single domain state could be achieved by applying an E-field along the rhombohedral polar direction [111], a multidomain state was observed with the removal of the E-field. This domain instability was associated with large hysteresis of the strain vs. E-field behavior. In contrast, an engineered domain configuration of [001] oriented rhombohedral crystals was found to be stable with no domain motion detectable under DC-bias, resulting in hysteresis minimized strain vs. E-field behavior. The stable engineered domain configuration under bias in multidomain [001] oriented crystals was suggested as an evidence of macroscopic symmetry 4mm out of 3m rhombohedral crystals.

**Keywords:** PZN-PT; single crystal; domain; hysteresis; macroscopic symmetry

### INTRODUCTION

In compositional engineering of conventional PZT ceramics, enhanced piezoelectric activity is achieved by adjusting  $T_c$  downward, resulting in "soft" PZT's ( $d_{33} > 500$  pC/N) with low coercivity ( $E_c \sim 5$  kV/cm). These soft PZT's are accompanied by large hysteresis in their strain vs. E-field behavior due to domain wall motion under bias, limiting applications to low frequencies. "Hard" PZTs with minimized strain vs. E-field hysteresis behavior are a consequence of acceptor dopants, constraining domain wall mobility. This non-hysteretic strain vs. E-field behavior, however, comes

with the expense of decreased piezoelectric activity ( $d_{33} \sim 200$  pC/N). Hysteresis free strain vs. E-field behavior is also expected from single domain ferroelectric crystals. Ferroelectric single crystals such as  $\text{LiNbO}_3$ , however, have not been intensively investigated for actuators because of their inherently inferior piezoelectric activity ( $d_{33} < 50$  pC/N).

Recently, ultrahigh piezoelectric properties ( $d_{33} \sim 2500$  pC/N) and large strain (1.7 %) were achieved from [001] oriented rhombohedral crystals of relaxor based ferroelectric  $\text{Pb}(\text{A}_{1/3}\text{Nb}_{2/3})\text{O}_3$  ( $\text{A} = \text{Zn}^{2+}, \text{Mg}^{2+}$ ) and its solid solution with the normal ferroelectric  $\text{PbTiO}_3$  (PT).<sup>11-14</sup> Fig. 1 presents the typical strain vs. E-field behavior observed in rhombohedral PZN-8%PT crystals. As [001] is not the polar direction, [001] poled crystals must be comprised of a multidomain state. Furthermore, these crystals are "softer" ( $E_c \sim 3$  kV/cm) than soft PZT's ( $E_c > 5$  kV/cm). However, strain values as high as 0.4 % were realized with minimized hysteresis, suggesting little domain motion under bias, a phenomenon not expected for multidomain "soft" ferroelectric crystals. In contrast, crystals oriented along [111], the polar direction of rhombohedral crystals, exhibited inferior properties such as  $d_{33} \sim 82$  pC/N. The E-field induced strain was also accompanied by large hysteresis.

In this study, the domain configuration of rhombohedral PZN-8%PT crystals was observed as a function of E-field and crystallographic orientation using a polarizing microscope. The behavior of domain wall motion will be discussed in relation to the observed hysteretic strain vs. E-field behavior.

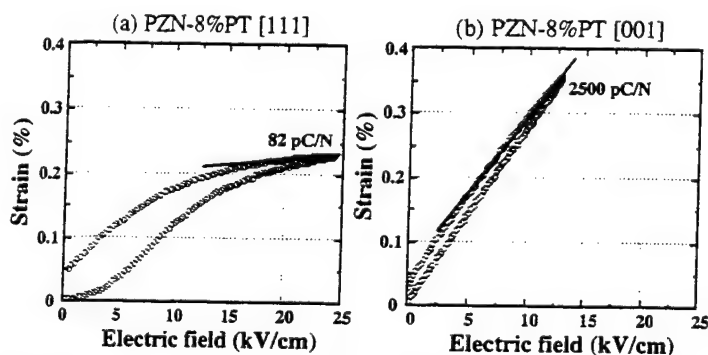


FIGURE 1 Strain vs. E-field behavior for PZN-8%PT crystals oriented along [111] and [001].



Moreover, the change of macroscopic symmetry induced by the engineered domain configuration will also be discussed.

## EXPERIMENTAL

PZN-8%PT single crystals were grown by a flux method. Further details on the crystal growth were reported elsewhere.<sup>12,51</sup> Flux grown crystals were oriented along [111] or [001] direction using a back reflection Laue camera. Crystals were heat-treated at 250 °C for 16 hr in air prior to domain observation, to remove residual stress that might result in the formation of ferroelastic domains. For in-situ domain observation under DC-bias, the sample surface was mirror-polished with the sample thickness approximately 200-300  $\mu\text{m}$  along the transmittance direction of polarized light. Gold electrodes were sputtered on both sides parallel to the polarized light. Sample width between sputtered Au electrodes was approximately 500-600  $\mu\text{m}$ . Thin samples ( $\sim 50 \mu\text{m}$ ) with mirror-finished (111) or (001) surfaces were also prepared to observe detailed domain configurations more clearly before and after E-field exposure for crystallographic interpretation. The domain configuration was observed under crossed-nicols using a Polarizing microscope (Carl Zeiss, D-7082). The application of an E-field was along the [001] or [111] direction, being normal to the polarized light, using a Trek 610A HV Amplifier.

## RESULTS AND DISCUSSION

### Domain configuration - Zero-bias state before and after E-field exposure

PZN-8%PT is compositionally located near the morphotropic phase boundary ( $\sim 9 \text{ mol}\% \text{PT}$ ) between rhombohedral phase (R3m) and tetragonal phase (P4mm) at room temperature.<sup>11</sup> PZN-8%PT undergoes two phase transitions as a function of temperature, i.e., (1) rhombohedral  $\leftrightarrow$  tetragonal phase transition around 90 °C ( $\text{PT}_{\text{R-T}}$ ), and (2) tetragonal  $\leftrightarrow$  cubic (Pm3m) phase transition around 170 °C ( $\text{PT}_{\text{T-C}}$ ). Thus, the domain configuration observed at 25 °C before E-field exposure contains domain walls originating from  $\text{PT}_{\text{T-C}}$  and  $\text{PT}_{\text{R-T}}$ . Figs. 2(a) and 3(a) show domain configurations of [111] and [001] oriented PZN-8%PT crystals before E-field exposure, respectively. Although ferroelectric domain-like pattern was obvious, crystallographic interpretation

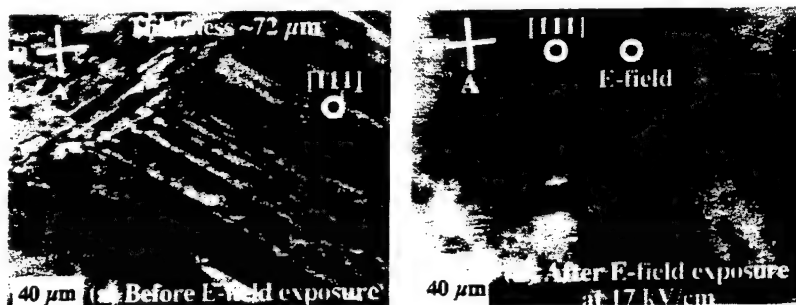


FIGURE 2 Domain configuration of  $[111]$  oriented PZN-8%PT crystals before and after poling.

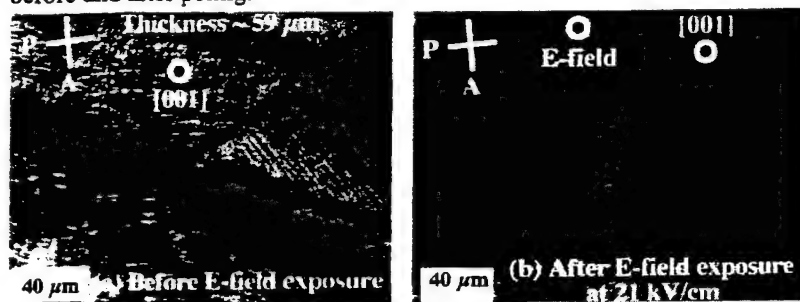


FIGURE 3 Domain configuration of  $[001]$  oriented PZN-8%PT crystals before and after poling.

was difficult due to vague domain boundaries.

Figs. 2(b) and 3(b) present the domain configurations of  $[111]$  and  $[001]$  oriented PZN-8%PT crystals after E-field ( $\sim 20$  kV/cm) exposure, respectively. In contrast to Figs. 2(a) and 3(a), E-field induced domain configuration was observed. The  $[111]$  oriented PZN-8%PT crystals (Fig. 2(b)) consisted of three kinds of the band-shaped domains with equivalent polar vectors ( $[\bar{1}11]$ ,  $[1\bar{1}1]$  and  $[11\bar{1}]$ ) in the domain with polar direction of  $[111]$ . Therefore, all domain boundaries could be interpreted as  $71^\circ$  domain walls of  $\{110\}$  planes between  $[111]$  domain and three domains with polar directions ( $[\bar{1}11]$ ,  $[1\bar{1}1]$  and  $[11\bar{1}]$ ) and  $109^\circ$  domain walls of  $\{100\}$  planes between three domains with polar directions ( $[\bar{1}11]$ ,  $[1\bar{1}1]$  and  $[11\bar{1}]$ ), consistent with crystallographic domain wall relationships.<sup>[6-7]</sup> As shown in Fig. 3(b), fiber-like domains with sharp edges on both ends were observed for  $[001]$  oriented PZN-8%PT crystals. Although crystallographic interpretation

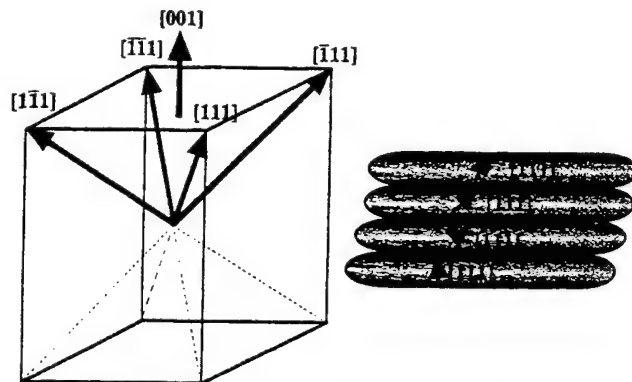


FIGURE 4. Schematic domain configuration of [001] oriented PZN-8%PT crystal.

was limited by the depth of focus of optical microscopy, each domain must have one of four possible polar vectors,  $[111]$ ,  $[111]$ ,  $[111]$  and  $[111]$  in [001] poled PZN-8%PT crystals. This configuration is schematically presented in Fig. 4. Thus, all domain boundaries could be interpreted as  $71^\circ$  domain walls of  $\{110\}$  planes and  $109^\circ$  domain walls of  $\{100\}$  planes. Similar domain configuration was also reported for pure rhombohedral PZN.[8-9]

#### In-situ domain observations

For  $[111]$  oriented PZN-8%PT crystals, the domain configuration at  $25^\circ\text{C}$  before an applied E-field is presented in Fig. 5(a). Figs. 5(b) and 5(c) exemplify the domain configuration at  $25^\circ\text{C}$  as a function of E-field, increased incrementally to 13 kV/cm. The result shown in Fig. 5 was obtained at the second measurement in the repeated cycles (1 cycle: 0 kV/cm -> 13 kV/cm -> 0 kV/cm). The domain wall density in the crystals was found to decrease with increased E-field, implying increased domain size with domain reorientation. At approximately 13 kV/cm, the PZN-8%PT crystals became nearly single domain (Fig. 5(d)), with some domain walls observed near the electrode due to crystal-electrode interfacial stresses. However, upon removal of the E-field, a multidomain state was observed as presented in Figs. 5(e) and 5(f). Domain reorientation was found to occur at 4.5 kV/cm (Fig. 5(e)), starting near the electrode. The initial multidomain state of Fig. 5(b) was completely recovered as shown in Fig. 5(f). It should be noted, however, that the domain configuration exhibited hysteresis. The domain

wall density was observed to be reduced for an equivalent E-field upon removing the E-field, the origin of hysteresis in strain vs. E-field curve shown in Fig. 1(a).

In contrast to the domain instability observed with [111] oriented PZN-8%PT crystals, [001] oriented crystals exhibited stable domain configurations as shown in Fig. 6. The result shown in Fig. 6 was obtained at the second measurement in the repeated cycles (1 cycle: 0 kV/cm  $\rightarrow$  15 kV/cm  $\rightarrow$  0

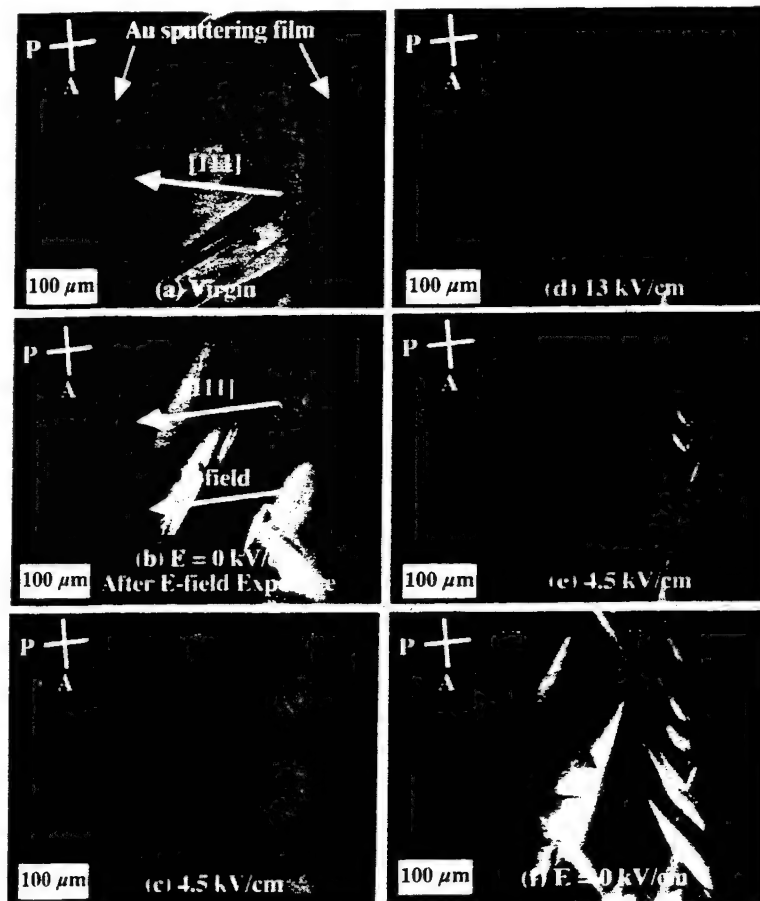


FIGURE 5 Domain configuration of [111] oriented PZN-8%PT crystal under DC-bias.

kV/cm). At the first cycle measurement, when very weak E-field below 0.2 kV/cm was applied along [001] direction of virgin crystal (Fig. 6(a)), the same domain configuration as shown in Fig. 6(b) was formed immediately. Moreover, this domain configuration did not change, although applied E-field increased under 15 kV/cm. Therefore, domain configuration did not change under DC-bias, being further evidenced by hysteresis minimized strain vs. E-field behavior in Fig. 1(b). However, if the E-field over 20

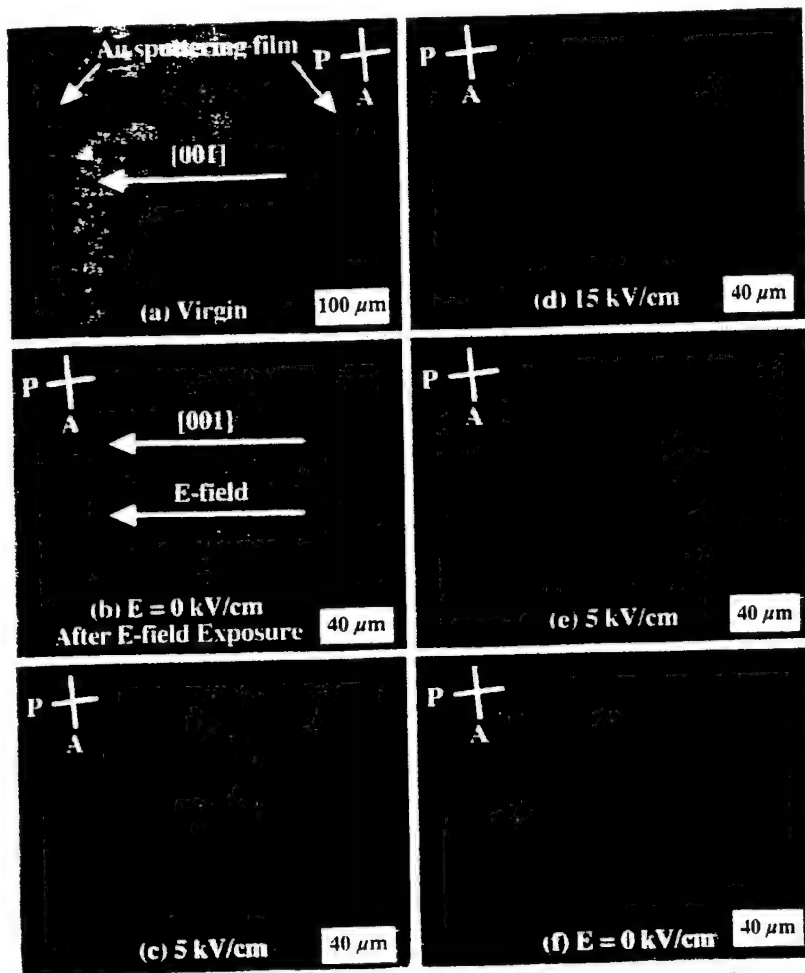


FIGURE 6 Domain configuration of [001] oriented PZN-8%PT crystal under DC-bias.

kV/cm was applied along [001] direction, the E-field induced phase transition from rhombohedral to tetragonal phase was observed and confirmed by both Polarization and strain vs. E-field curve and in-situ domain observation.

#### **Domain engineering and macroscopic symmetry**

Based on the domain observations presented in previous sections, the ability to engineer a macroscopic symmetry different from the local symmetry (lattice symmetry) is suggested, as can be found for the case of poled piezoelectric ceramics, i.e., the macroscopic symmetry being  $m$  regardless of the lattice symmetry resulting from randomly orientated grains. For ferroelectric single crystals, only single domain crystals possess macroscopic symmetry identical to the lattice symmetry. For example, unpoled tetragonal ferroelectric crystals are macroscopically  $m3m$ , if the number of each domain is equivalently distributed. As shown in Fig. 4, each domain in [001] poled crystals must have four possible polarization directions,  $[111]$ ,  $[\bar{1}11]$ ,  $[1\bar{1}1]$  and  $[\bar{1}\bar{1}1]$ . For [001] oriented crystals to exhibit a static domain configuration under DC-bias, each domain must be distributed equivalently. As a result, each domain experiences the same driving force for reorientation with respect to an applied E-field, otherwise domain reorientation under DC-bias would occur resulting in hysteresis in strain vs. E-field behavior. Therefore, the coexistence of domains with four equivalent polar vectors results in a 4-fold axis along [001], consequently resulting in the macroscopic symmetry  $4mm$  arising from the local  $3m$  symmetry.

#### **SUMMARY**

Domain configuration and ferroelectric related properties of rhombohedral PZN-8%PT crystals were investigated as a function of E-field and crystallographic orientation. In-situ domain observations revealed the domain instability for  $[111]$  oriented rhombohedral crystals, corresponding to large hysteresis of the strain vs. E-field behavior. In contrast, an engineered domain configuration of [001] oriented rhombohedral crystals was found to be stable. Domain motion was undetectable under DC-bias, resulting in hysteresis minimized strain vs. E-field behavior. Crystallographically, the macroscopic tetragonal symmetry ( $4mm$ ) arising from local rhombohedral  $3m$  symmetry resulting from the four equivalent domain state was suggested. Further detailed studies such as TEM observations are required to understand

the engineered domain observed in [001] poled PZN-8%PT crystals.

#### Acknowledgments

The authors thank Mrs. Lei for her great help with sample preparation, and also thank Dr. Fousek, Dr. Newnham, Dr. Randall and Dr. Cao for their helpful discussions and suggestions. This work has been supported by Office of Naval Research.

#### References

- [1] J. Kuwata, K. Uchino and S. Nomura, *Jpn. J. Appl. Phys.*, **21**, 1298 (1982).
- [2] S.-E. Park, M. L. Mulvihill, P. D. Lopath, M. Zipparo and T. R. Shrout, *Proceedings of the 10th IEEE International Symposium on Applications of Ferroelectrics*, Vol. I, 79 (1996).
- [3] S.-E. Park and T. R. Shrout, *J. Appl. Phys.*, **82**, 1804 (1997).
- [4] S.-E. Park and T. R. Shrout, *IEEE Trans. on Ultrasonics, Ferroelectric and Frequency Control Special Issue on Ultrasonic Transducers*, **44**, 1140 (1997).
- [5] S.-E. Park, M. L. Mulvihill, G. Risch and T. R. Shrout, *Jpn. J. Appl. Phys.*, **36**, 1154 (1997).
- [6] J. Fousek, *Czech. J. Phys.*, **B21**, 955 (1971).
- [7] E. I. Eknadiants, V. Z. Borodin, V. G. Smotrakov, V. V. Eremkin and A.N. Pinskaya, *Ferroelectrics*, **111**, 283 (1990).
- [8] S. Nomura, M. Endo and F. Kojima, *Jpn. J. Appl. Phys.*, **13** 2004 (1974).
- [9] S. Wada, S.-E. Park, L. E. Cross and T. R. Shrout, *J. Korean Phys. Soc.*, **32**, S1290 (1998).

# **APPENDIX 24**



# Electric field dependence of piezoelectric properties for rhombohedral $0.955\text{Pb}(\text{Zn}_{1/3}\text{Nb}_{2/3})\text{O}_3-0.045\text{PbTiO}_3$ single crystals

Shi-Fang Liu,<sup>a)</sup> Seung-Eek Park, Thomas R. Shrout, and L. Eric Cross

*Materials Research Laboratory, The Pennsylvania State University, University Park, Pennsylvania 16802*

(Received 24 August 1998; accepted for publication 3 December 1998)

The electric field dependence of the piezoelectric properties of rhombohedral  $0.955\text{Pb}(\text{Zn}_{1/3}\text{Nb}_{2/3})\text{O}_3-0.045\text{PbTiO}_3$  crystals were investigated as a function of orientation with respect to the prototypic (cubic) axes. For  $\langle 111 \rangle$  oriented fields, depolarization and subsequent domain reorientation resulted in an apparent maximum in the piezoelectric coefficients occurring at  $\sim 5$  kV/cm, followed by nonhysteretic  $d_{ij}$  saturation, indicating a single domain state under bias. By extrapolation, single domain values for the piezoelectric coefficients  $d_{33}$  and  $d_{31}$  were determined to be 125 and  $-35$  pC/N, respectively. The hydrostatic piezoelectric coefficient  $d_h$  for single domain crystals was calculated to be  $\sim 55$  pC/N, coincident with the experimentally determined values under hydrostatic pressure. For  $\langle 001 \rangle$  oriented fields, piezoelectric coefficients  $d_{33\langle 001 \rangle}$  and  $d_{31\langle 001 \rangle}$  as high as 2250 and  $-1000$  pC/N were determined, respectively. Although a high value of  $d_{h\langle 001 \rangle}$  ( $\sim 250$  pC/N) was expected, the experimentally determined value was only  $\sim 50$  pC/N. A change of polar vector within the crystal lattice was discussed in relation to the volume strain associated with an  $E$ -field induced phase transition and the possible origin of the discrepancy in hydrostatic  $d_h$  values. © 1999 American Institute of Physics. [S0021-8979(99)05705-9]

## I. INTRODUCTION

High levels of piezoelectric activity have been reported for single crystals in the rhombohedral ferroelectric  $\text{Pb}(\text{Zn}_{1/3}\text{Nb}_{2/3})\text{O}_3(\text{PZN})\text{:PbTiO}_3(\text{PT})$  solid solution system.<sup>1-4</sup> It must be remembered that even in ferroelectric single crystals, the piezoelectric response depends critically on its domain structure, and it is only in the single domain state, or in a carefully engineered domain state, that the properties are reproducible and age free.

In earlier studies of rhombohedral PZN-PT crystals poled along their polar axis, pseudocubic  $\langle 111 \rangle$ , Park<sup>3</sup> and Wada<sup>5</sup> presented evidence that a single domain state was not stable, indicating that previous reported piezoelectric coefficients were probably determined on partially depolarized samples. However, a stable domain state and correspondingly high level of piezoelectric activity could be achieved in nonpolar  $\langle 001 \rangle$  oriented crystals: for such crystals, a single domain state cannot be achieved.

In this article, the piezoelectric behavior as a function of field direction was investigated for rhombohedral PZN-PT, specifically, PZN-4.5%PT crystals, located at the center of the rhombohedral compositional range (0%-9% PT). Longitudinal, transverse, and hydrostatic piezoelectricity were investigated as a function of crystallographic direction and related domain configuration. Piezoelectric-domain interrelationships were established in order to obtain single domain properties for  $\langle 111 \rangle$  oriented crystals and to elucidate the induced phase transition behavior associated with these materials.

## II. EXPERIMENT

### A. Crystal growth

Crystals of  $(1-x)\text{PZN}-x\text{PT}$  were grown using the high temperature flux technique. High purity ( $>99.9\%$ ) powders of  $\text{Pb}_3\text{O}_4$ ,  $\text{ZnO}$ ,  $\text{Nb}_2\text{O}_5$ , and  $\text{TiO}_2$  (Aldrich, WI) were used. Excess  $\text{Pb}_3\text{O}_4$  was added as flux. The powders were dry mixed using a tumbling mill. The mixed powders were loaded into a platinum crucible, which was placed in an alumina crucible sealed with an alumina lid and alumina cement to minimize  $\text{PbO}$  volatilization. The alumina crucible was placed in a tube furnace and held at soak temperature ( $1100-1200^\circ\text{C}$ ), followed by slow cooling to  $900^\circ\text{C}$  at a rate of  $1-5^\circ\text{C/h}$ . The crucible was then furnace cooled to room temperature. Hot  $\text{HNO}_3$  was used to separate the crystals from the melt. Typically, crystal sizes were  $8-20$  mm. Crystal samples, oriented along the  $\langle 001 \rangle$  and  $\langle 111 \rangle$  directions using a Laue Camera, were prepared by polishing with silicon carbide and alumina polishing powders to achieve flat and parallel surfaces onto which good electrodes were deposited by sputtering.

### B. Electrical characterization

Dielectric and piezoelectric properties were measured using direct observations of strain as a function of electric field and low-field properties using the IEEE resonance technique.<sup>6</sup> The hydrostatic piezoelectric coefficient  $d_h$  was obtained by measuring the charge response under hydrostatic pressure. High-field measurements included polarization and strain hysteresis incorporated a modified Sawyer-Tower circuit and a linear variable displacement transducer (LVDT) driven by a lock-in amplifier (Stanford Research system, model SR830). Plate-shaped samples with thicknesses rang-

<sup>a)</sup>Electronic mail: sxl43@psu.edu

TABLE I. Dielectric and piezoelectric rhombohedral properties of PZN-4.5%PT crystal as a function of crystallographic orientation.

Crystal orientation	$k_{33}$	$k_{31}$	$d_{33}$ (pC/N)	$d_{31}$ (pC/N)	$d_h$ (pC/N)	$S_{11}^E$ ( $10^{-12}$ m <sup>2</sup> /N)	$S_{33}^E$ ( $10^{-12}$ m <sup>2</sup> /N)	Dielectric constant	Loss
(111)	0.41	0.17	92	-47	55	13.6	8.32	640	0.002
(001)	0.92	0.57	2280	-1015	50	71.7	120.1	5000	0.003

ing from 0.2 to 0.5 mm were employed for measurements. Electric fields as high as  $\sim 80$  kV/cm were applied using an amplified triangle or unipolar wave form at 0.2 Hz, from a Trek 609c-6 high voltage dc amplifier. During testing the samples were submerged in Fluorinert (FC-40, 3 m, St. Paul, MN), an insulating liquid, to prevent arcing.

### III. RESULTS AND DISCUSSION

#### A. Low field measurements

Table I presents dielectric and piezoelectric properties of PZN-4.5%PT crystals as a function of crystallographic orientation, measured using the IEEE standard method.<sup>6</sup> As reported by Park *et al.*,<sup>3</sup> PZN-4.5%PT crystals oriented along (001) exhibited electromechanical coupling ( $k_{33(001)}$ ) and longitudinal piezoelectric coefficients ( $d_{33(001)}$ ) as high as 92% and 2280 pC/N, respectively. A transverse piezoelectric ( $d_{31(001)}$ ) value of -1020 pC/N was also determined, as presented in Table I. Crystals oriented along their polar direction (111), however, exhibited values of  $k_{33} \sim 41\%$  and  $d_{33} \sim 92$  pC/N, significantly inferior to those oriented along (001), also reported by Kuwata *et al.*<sup>1,2</sup> and Park *et al.*<sup>3</sup>

For single domain rhombohedral crystals of symmetry  $3m$ , the hydrostatic piezoelectric coefficient  $d_h$  can be written as  $d_{33} + 2d_{31}$ , as in the case of polycrystalline piezoelectric ceramics. From Table I, the piezoelectric coefficient  $d_h$  for (111) oriented crystals results in an abnormally low and negative value of -2 pC/N. Using axis transformation for (001) oriented rhombohedral crystals, the equation  $d_{h(001)} = 1/\sqrt{3}(d_{33} + 2d_{31})$  is not applicable since a single domain state does not exist. Wada *et al.*<sup>5</sup> proposed that (001) polarized rhombohedral PZN-PT crystals possess a tetragonal macro symmetry ( $4mm$ ) with the fourfold axis along the poling direction, a consequence of an engineered domain state. Therefore, taking (001) as the new symmetric axis,  $d_{h(001)}$  can be calculated using the relation  $d_{h(001)} = d_{33(001)} + 2d_{31(001)}$ , resulting in  $d_{h(001)} \sim 250$  pC/N. However, as presented in Table I,  $d_h$  values directly measured were only 55 pC/N ((111)) and 50 pC/N ((001)). In Sec. III B, this discrepancy is discussed in relation to domain configuration and domain (in)stability.

#### B. Strain versus $E$ -field behavior for ((111)) oriented PZN-4.5%PT crystals

As the pseudocubic (111) is the polar direction for rhombohedral ferroelectric crystals, this is also the direction in which an electric field must be applied to obtain a single domain state. Figure 1 shows longitudinal/transverse strain versus unipolar  $E$ -field behavior for a (111) poled crystal. As presented, hysteresis in the strain versus  $E$ -field curves at low

fields is the result of domain instability and subsequent domain reorientation under bias.<sup>3</sup> Nearly linear and hysteresis free behavior at fields greater than 30 kV/cm indicates a single domain state. Wada *et al.*<sup>5</sup> also observed single domain behavior of (111) oriented PZN-PT rhombohedral crystals at  $E$  fields  $> 30$  kV/cm. This domain instability and subsequent difficulty in obtaining single domain crystals may be related to residual elastic strain upon poling.<sup>7</sup> As for the case of BaTiO<sub>3</sub> crystals, single domain PZN-PT crystals may require a specific elastic treatment during the poling process. The  $d_{ijs}$  of (111) oriented crystals given in Table I, therefore, are coefficients measured from partially depoled crystals, and not single domain crystals. Fundamentally, this inherent domain instability is believed to be the origin of the

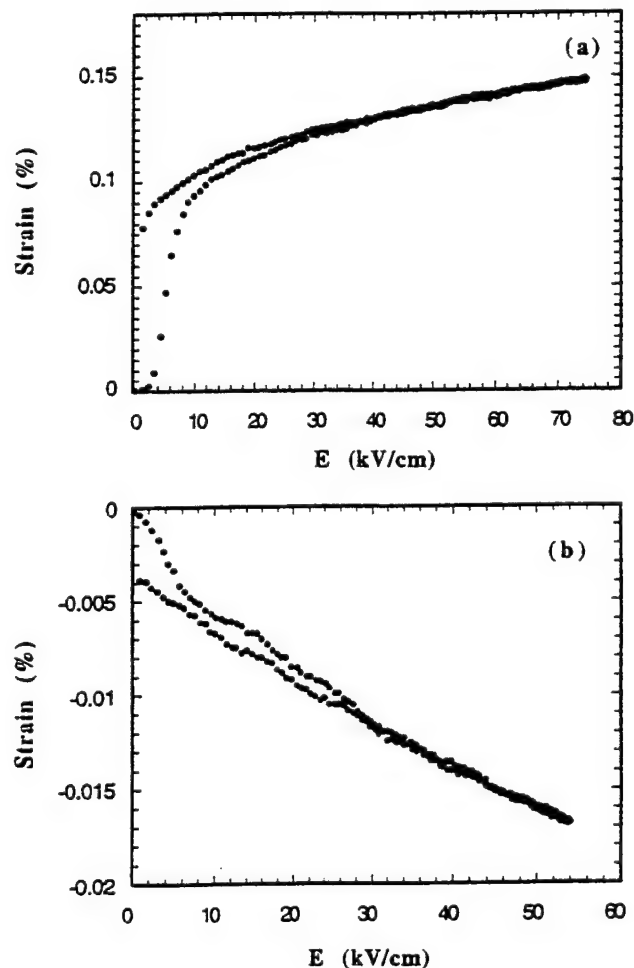


FIG. 1. Strain vs unipolar  $E$ -field behavior for (111) poled crystals: (a) longitudinal strain, (b) transverse strain.

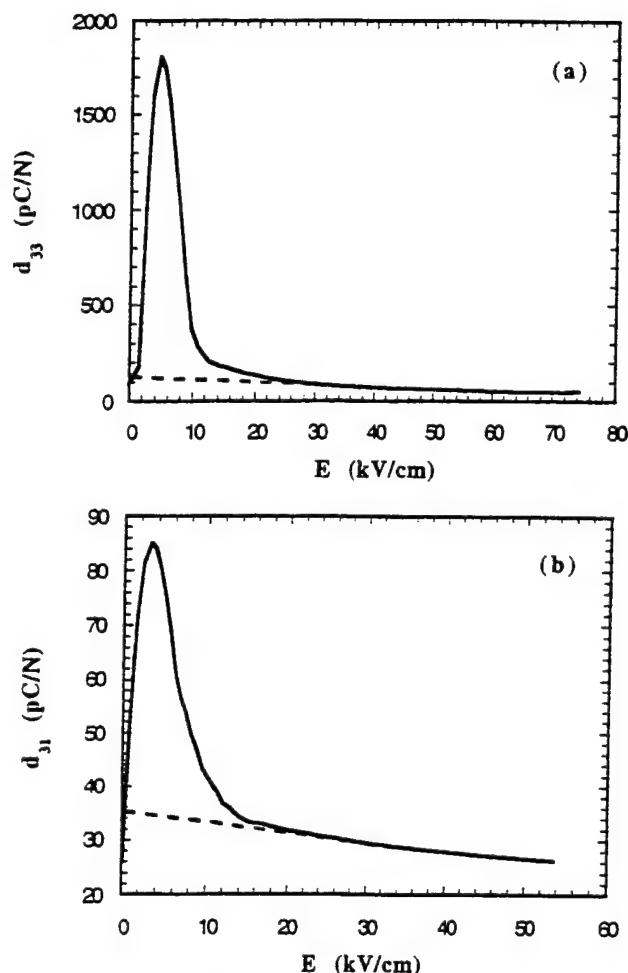


FIG. 2. Piezoelectric coefficients ( $d_{33}$  and  $d_{31}$ ) obtained from the slope of strain vs  $E$ -field curves in Fig. 1(a)  $d_{33}$ ; (b)  $d_{31}$ .

calculated negative hydrostatic  $d_h$  coefficients, since depolarization results in the longitudinal (transverse) piezoelectric coefficient to decrease (increase).

Figure 2 presents longitudinal and transverse piezoelectric coefficients ( $d_{33}$  and  $d_{31}$ ) obtained from the slope of the strain versus  $E$ -field curves in Fig. 1. The maxima in  $d_{ij}$ s at 5 kV/cm are believed to be the result of domain reorientation under bias. Since the strain versus  $E$ -field curve in Fig. 1 was hysteresis free at  $E > 30$  kV/cm,  $d_{ij}$ s at  $E > 30$  kV/cm in Fig. 2 correspond to single domain values. The piezoelectric coefficients of single domain crystals at low fields, therefore, may be extrapolated as indicated by the dashed line, resulting in  $d_{33}$  and  $d_{31}$  values of 125 and  $-35$  pC/N, respectively, being significantly different than the low field values given in Table I. It is also important to note that these values result in a  $d_h \sim 55$  pC/N, coinciding well with the experimentally determined  $d_h$  value.

### C. Strain versus $E$ -field behavior for $\langle 001 \rangle$ oriented crystals

Polarization hysteresis behavior and subsequent strain versus  $E$ -field (bipolar) curves of  $\langle 001 \rangle$  oriented PZN-4.5%PT crystals are shown in Fig. 3. Remanent polarization ( $P_r$ ) values of  $\sim 25$   $\mu\text{C}/\text{cm}^2$  for  $\langle 001 \rangle$  oriented crystals are

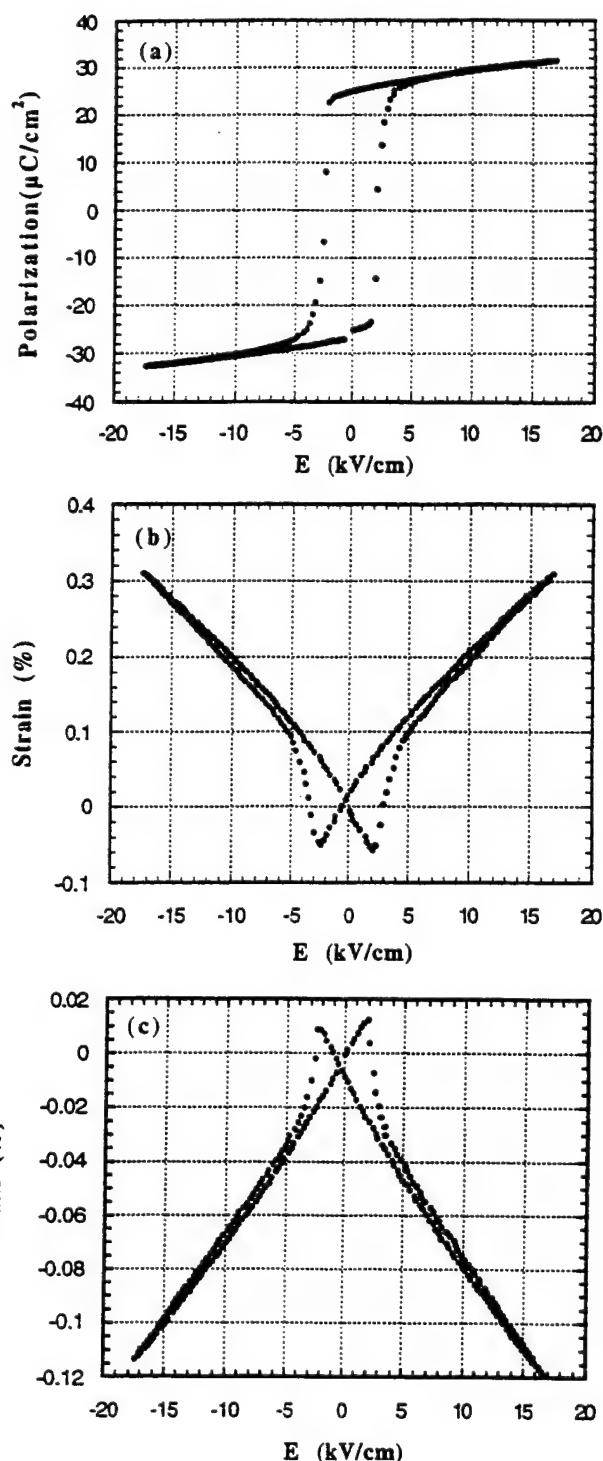


FIG. 3. Polarization and strain vs  $E$ -field (bipolar) curves for  $\langle 001 \rangle$  oriented PZN-4.5%PT crystals: (a) polarization; (b) longitudinal strain; (c) transverse strain.

reported corresponding to  $1/\sqrt{3}P_{r(111)}$ . The abrupt change in polarization at  $E_c$  is a characteristic of domain switching, as found in general for all ferroelectrics, i.e.,  $\langle 001 \rangle$  nonpolar orientation. However, a consequence of the engineered domain state is the hysteresis minimized longitudinal/transverse strain behavior (unipolar) above  $E_c$  shown in Fig. 4. The longitudinal and transverse piezoelectric coefficients  $d_{33}$  and  $d_{31}$  calculated by the slope of the strain versus

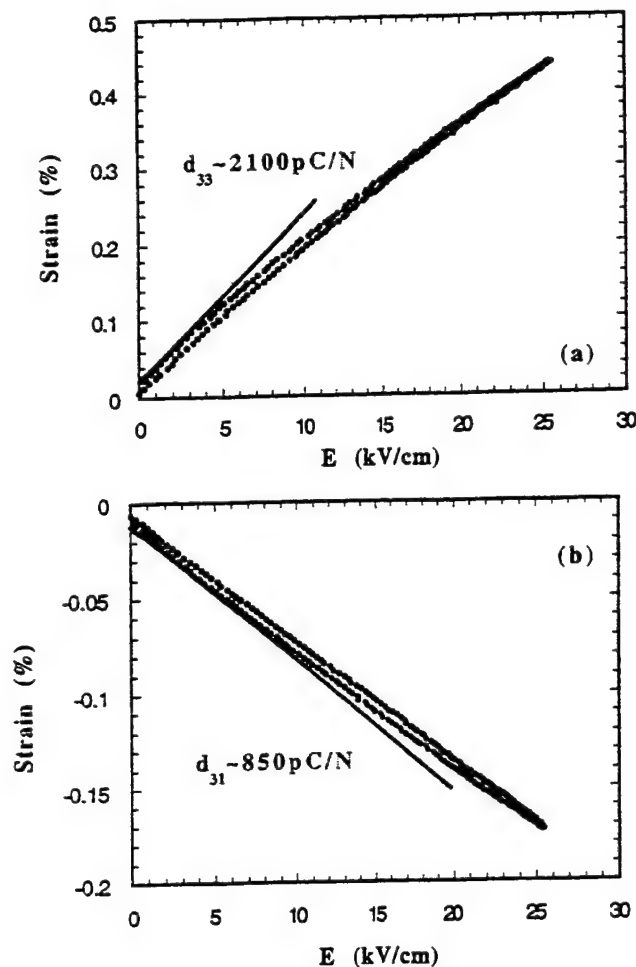


FIG. 4. Strain vs unipolar  $E$ -field behavior for  $\langle 001 \rangle$  crystals: (a) longitudinal strain; (b) transverse strain.

$E$ -field curve were  $\sim 2100$  and  $-850$  pC/N, respectively, slightly lower than that measured by the IEEE resonance technique. In regard to hydrostatic  $d_h$ , using the  $d_{33\langle 001 \rangle}$  and  $d_{31\langle 001 \rangle}$  values from Fig. 4 resulted in a calculated  $d_{h\langle 001 \rangle}$  of  $\sim 400$  pC/N, still significantly larger than that experimentally determined. Unlike  $\langle 111 \rangle$  oriented crystals, this inconsistency could not be explained by domain instability because the engineered domain configuration was stable with no or minimal domain motion under bias. It seems that the change in domain wall configuration under bias may be the underlying cause of this discrepancy. Further investigation of the domain wall state as a function of the  $E$  field is required.

#### D. $E$ -field induced phase transition

High field strain versus  $E$ -field behavior for  $\langle 001 \rangle$  oriented crystals is presented in Fig. 5. As suggested by Park<sup>3</sup> and supported using *in situ* domain observations,<sup>8</sup> the high-field phase induced at  $E$  fields  $> \sim 36$  kV/cm is believed to be a tetragonal phase. The volumetric strain associated with the induced phase transition is presented in Fig. 6. Although a volume expansion of  $\sim 0.3\%$  was associated with the induced phase transition, a decrease in volume was detected starting at 20 kV/cm. The volumetric strain may be written as follows:

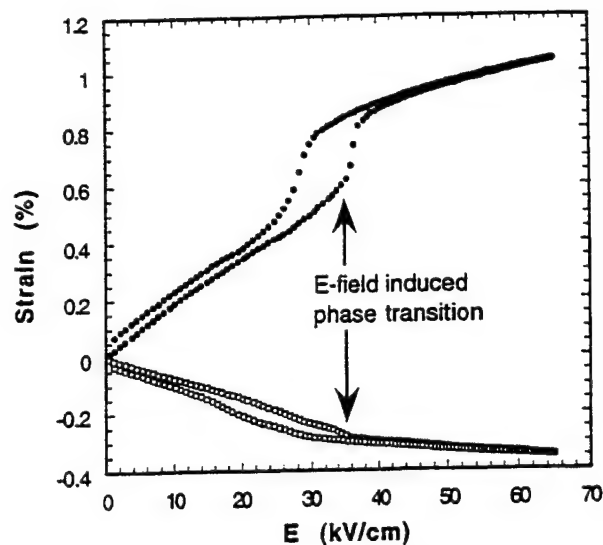


FIG. 5. High field strain vs unipolar  $E$ -field behavior for  $\langle 001 \rangle$  crystals.

$$dV/V_0 = Q_h(P_E^2 - P_L^2), \quad (1)$$

where  $V_0$  is the initial volume of the crystal,  $Q_h$  is the hydrostatic electrostrictive coefficient ( $= Q_{11} + 2Q_{12}$ ),  $P_L$  is the magnitude of zero-field spontaneous lattice polarization, and  $P_E$  is the magnitude of total lattice polarization under dc bias. Since  $Q_h$  is a material constant,<sup>9</sup> the volumetric strain is, therefore, dependent only upon the polarization change by the lattice response under bias or phase switching. It should be noted that  $P_L$  and  $P_E$  are not the apparent polarization, but the magnitude of the polar vector in the crystal lattice. For example, the apparent spontaneous polarization is a function of crystallographic direction ( $43 \mu$  and  $25 \mu\text{C}/\text{cm}^2$  for  $\langle 111 \rangle$  and  $\langle 001 \rangle$  oriented crystals, respectively), but  $P_L$  is  $43 \mu\text{C}/\text{cm}^2$ , independent of the orientation. In Eq. (1),  $P_E$  is equal to  $P_L (= P_{\langle 111 \rangle})$  under zero bias and to  $P_{\langle 001 \rangle}$  only if the entire crystal is occupied by the induced phase. The volume decrease, as shown in Fig. 6, indicates that the magnitude of the polar vector in the crystal lattice decreases during the induced phase transition. This is schematized in Fig. 7,

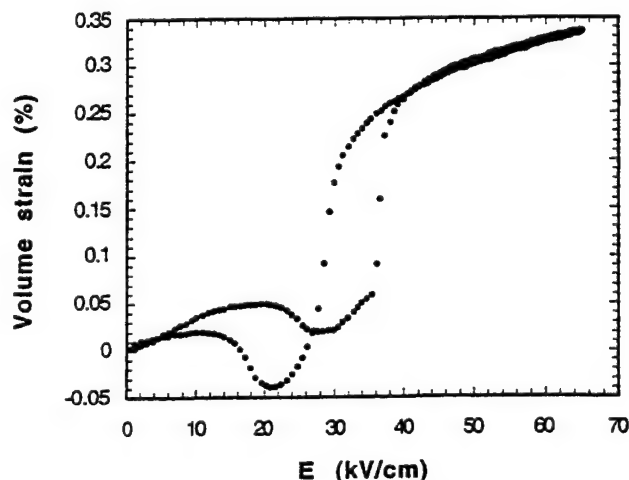


FIG. 6. Volume strain vs unipolar  $E$ -field behavior for  $\langle 001 \rangle$  crystals.

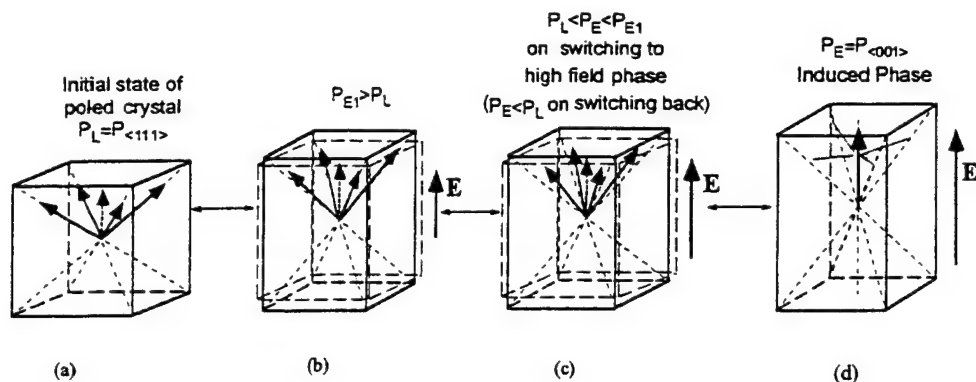


FIG. 7. Schematic of changes in polar vectors and unit cell volume for (001) oriented rhombohedral crystals under bias. Note that polar vectors are no longer along the body-diagonal direction of pseudocubic unit cell, under bias, for the engineered domain state (b) and (c).

adding an intermediate stage between Figs. 7(b) and 7(d).<sup>3</sup> The magnitude of the polar ionic shift in the crystal lattice may have to be reduced with the change of its shift direction, i.e., from  $\langle 111 \rangle$  to  $\langle 001 \rangle$ , implying the crystal symmetry becomes closer to its prototype symmetry  $m\bar{3}m$  during the induced phase transition. It is noted that the volumetric strain becomes negative on switching back to the low field phase, indicating that  $P_E$  becomes smaller than  $P_L$ . As the induced phase transition gradually occurs with nucleation and growth processes,<sup>8</sup> volumetric strain can be positive or negative depending on the nucleation and/or growth speed with respect to the  $E$ -field change rate. It is noted that under high electric field, the polar vectors no longer lie in the body-diagonal direction of the pseudocubic unit cell within the engineered domain state, as shown in Figs. 7(b) and 7(c). Further discussion associated with the changes in polarization values for domain engineered crystals will be reported elsewhere.<sup>10</sup>

#### IV. CONCLUSION

The ferroelectric related properties of rhombohedral PZN-4.5%PT crystals were investigated as a function of crystallographic direction and subsequent domain configuration. For crystals oriented along the polar  $\langle 111 \rangle$  direction, inconsistency among low field piezoelectric properties was believed to be the result of domain instability and subsequent partial depolarization. At high fields  $>30$  kV/cm, strain versus  $E$ -field curves were hysteresis free and single domain rhombohedral crystals could be ascertained. Piezoelectric coefficients  $d_{33} \sim 125$  pC/N,  $d_{31} \sim -35$  pC/N, and  $d_h \sim 55$  pC/N for single domain crystals were determined by extrapolating high field  $d_{ij}$  values. In contrast, low field strain versus  $E$ -field curves were hysteresis minimized as a result of the stable engineered domain state for  $\langle 001 \rangle$  oriented PZN-PT rhombohedral crystals. Although  $d_{h(001)}$  values of  $>200$

pC/N were expected from measured piezoelectric coefficients ( $d_{33} \sim 2280$  pC/N and  $d_{31} \sim -1020$  pC/N), the experimentally determined  $d_h$  value was only  $\sim 50$  pC/N. Further investigation of the engineered domain state(s) and domain wall modulation under bias is required to answer the origin of this inconsistency. High field strain versus  $E$ -field behavior was characterized by an induced phase transition rhombo-tetragonal, resulting in volume strain as high as 0.35%. Volume strain versus  $E$ -field curves indicated that the magnitude of polarization in the crystal lattice decreases transiently in order for the direction of ionic shift to change from  $\langle 111 \rangle$  to four-fold symmetric  $\langle 001 \rangle$  axis.

#### ACKNOWLEDGMENTS

This research has been supported by the Office of Naval Research and DARPA. The authors would like to thank Hua Lei for her help with crystal growth and sample preparation.

- <sup>1</sup>J. Kuwata, K. Uchino, and S. Nomura, *Ferroelectrics* **37**, 579 (1981).
- <sup>2</sup>J. Kuwata, K. Uchino, and S. Nomura, *Jpn. J. Appl. Phys., Part 1* **21**, 12989 (1982).
- <sup>3</sup>S.-E. Park and T. R. Shrout, *J. Appl. Phys.* **82**, 1804 (1997).
- <sup>4</sup>S.-E. Park, M. L. Mulvihill, P. D. Lopath, M. Zipparo, and T. R. Shrout, *Proc. IEEE* **1**, 79 (1996).
- <sup>5</sup>S. Wada, S.-E. Park, L. E. Cross, and T. R. Shrout, *The 8<sup>th</sup> US/Japan Seminar on Dielectric and Piezoelectric Ceramics*, October 1997, pp. 11–15.
- <sup>6</sup>*IEEE Standard on Piezoelectricity* (American National Standards Institute, Washington, D.C. 1976).
- <sup>7</sup>O. Nakano, K. Tomomatsu, S. Ajimura, A. Kurosaka, and H. Tominaga, *Jpn. J. Appl. Phys., Part 1* **31**, 3117 (1992).
- <sup>8</sup>S. Wada, S.-E. Park, L. E. Cross, and T. R. Shrout, *Proceedings of the Fifth International Symposium on Ferroic Domain and Mesoscopic Structure (ISFD-5)*, April 6–10, 1998.
- <sup>9</sup>A. E. Glazounov, J. Zhao, and Q. M. Zhang, *Proceedings of the Fifth Williamsburg Workshop of First-Principles Calculations for Ferroelectrics*, February 1–4, 1998.
- <sup>10</sup>L. E. Cross (unpublished).

# **APPENDIX 25**



# Effective material properties in twinned ferroelectric crystals

Jiří Erhart<sup>a)</sup> and Wenwu Cao<sup>b)</sup>

Materials Research Laboratory, Pennsylvania State University, University Park, Pennsylvania 16802

(Received 25 January 1999; accepted for publication 7 April 1999)

Without external fields, ferroelectric materials will have multidomain configuration in the ferroelectric state. Detailed analysis found that twinning may not be treated as random since the number of orientations for the domain walls are limited in a given symmetry change during a ferroelectric phase transition. In each finite region of a large crystal or in small crystallites, a particular set of twins is favored under certain boundary conditions, which consists of only two of the low temperature variants. Statistic models of random distribution of domains do not apply for calculating the physical properties of such twin structures. However, one could derive the two domain twin properties by using the constitutive equations and appropriate mechanical boundary considerations. This paper presents a theoretical analysis on such a two-domain twin system, including its global symmetry and effective material properties resulting from different twinning configurations. Numerical results are derived for  $\text{LiNbO}_3$  and  $\text{BaTiO}_3$ . © 1999 American Institute of Physics. [S0021-8979(99)01214-1]

## I. INTRODUCTION

The macroscopic material properties of a multidomain ferroelectric system are the collective average of individual domains. Traditionally, people took statistic average of the properties of all the low temperature variants and used the volume ratio as the weighting factor. However, in reality, different physical properties may follow different averaging rules depending on the geometric configuration. For many properties the contribution of each domain do not always coincide with their volume ratio. For example, the elastic constant of a fiber reinforced composite is much larger in the fiber length direction than in its radial direction, although the volume ratio can be the same. Similarly, in a multidomain system the contribution of each domain not only depends on the volume ratio but also on the relative geometric configuration and on the orientation of the applied external fields. Experimental evidence showed that the domains often appear in a twin band with only two variants in the set.<sup>1,2</sup> Even for a ceramic system, domains observed in each given grain are mostly twin pair sets rather than all the available variants. Such a limited variant twinning pattern is more pronounced in a single crystal system since all orientations must be coherently joined together. Each twin band often occupies a sizable volume in a large single crystal. Generally speaking, two-variant twinning is the basis of all multidomain systems in ferroelectrics.

Recent development in domain engineering of relaxor based single crystal systems (e.g., for single crystals PZN-PT, PMN-PT) produced much enhanced piezoelectric and dielectric properties.<sup>3</sup> Experimental observation showed that many engineered crystal systems have only two variants.<sup>4</sup> Even those nonpoled samples are composed of large regions of two-variant twin band structures. Experimental observa-

tion of these relaxor based single crystals revealed that the twinning mostly consists of two variant twins<sup>5,6</sup> (for PZN and for  $\text{BaTiO}_3$ ). It is also found that the orientation of the two-domain system and the selection of the variants can significantly influence the effective material properties of multidomain systems. This means that the statistical model or models, based only on the volume ratio, will not give proper prediction of the physical properties in these domain engineered crystals. Roughly speaking, the volume ratio average scheme assumed isotropic distribution of domain walls and ignored the cross coupling between different quantities of the associated domains.

If we utilize the fact that the basic domain structure only consists of two variants and they have a certain orientation relation in domain engineered crystal systems, it is possible to accurately derive the apparent macroscopic property by directly applying external loads to the system. Such a two-variant domain set can then serve as the building block for calculating properties of systems with more complex domain patterns.

The importance of calculating the effective properties of two domains lies in the fact that the macroscopic properties observed experimentally, whether from an ultrasonic method or from a resonance technique, are actually a collective contribution of the *existing* domains, not all *possible* domains. In a given domain engineered single crystal, only some of the low temperature variants can appear.

Because of the importance of predicting the effective material properties, there is vast literature on property averaging of multicomponent systems. For example, the equivalent elastic constants were previously calculated for two layer elastic system<sup>7</sup> by using the volume ratio as the weighting factor for both the stress and strain. This approach allows the calculation of elastic properties in two layer system for materials of any symmetry and any orientation between the two layers. This method was later extended to piezoelectric materials.<sup>8</sup> The dynamic approach for calculating the effec-

<sup>a)</sup>On leave from the Department of Physics, Technical University of Liberec, Liberec, Czech Republic.

<sup>b)</sup>Electronic mail: cao@math.psu.edu

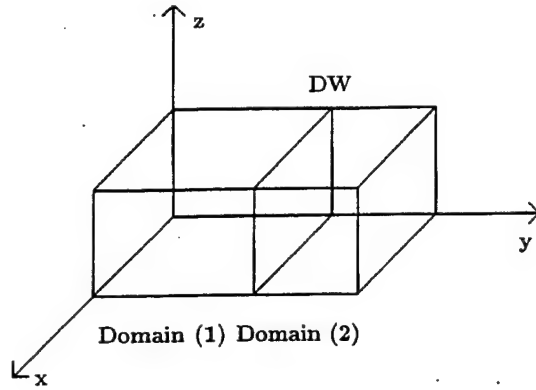


FIG. 1. The two domain system with coordinate systems chosen with the  $y$  axis perpendicular to the domain wall (DW).

tive material properties of piezoelectric layered material of arbitrary orientation<sup>9</sup> was based on the nature of acoustic wave propagation in layered material in the long-wavelength limit. It allowed explicit calculation of a complete set of all material properties. Another method for effective material property calculations is the method of effective medium which was applied to calculate the properties of polycrystalline ceramics<sup>10-12</sup> and piezoelectric composites.<sup>13,14</sup> The mechanical stress and electric field were assumed uniform in the matrix and in the inclusion (grains). The average was calculated under a number of assumptions about the space distribution and the shape of inclusions (spherical and elliptical shape). Effective material properties for 1-3 composites were calculated for 6mm symmetry as a function of volume fraction.<sup>13</sup> While all of these techniques have advantages and disadvantages in certain aspects, they have provided guidance for many particular applications and for the proper characterization of multicomponent systems of interest to a certain accuracy.

However, it is not appropriate to use the volume ratio average if there are only a limited number of domains in a system. In this paper we will try to eliminate some of those less convincing assumptions used in previous averaging methods and to develop a systematic procedure particularly applicable to a two-domain twin system. We will use different weighting factors for different physical properties based on the relative orientation to the external stress and electric field. Some quantities in each domain can be the same as in the combined twin system rather than all quantities being the weighted average. We will also give the macroscopic symmetry associated with twinning of different pairs of the low temperature variants resulting from cubic to rhombohedral and cubic to tetragonal ferroelectric phase transitions.

## II. AVERAGING OF TENSOR PROPERTIES IN A TWIN CRYSTAL

For the twinned structure under study, we assume that the two variants have a volume ratio of  $v^{(1)}$  and  $v^{(2)}$  and the domain wall (DW) is perpendicular to the  $y$  axis. Considering the unit cell of a twin structure as shown in Fig. 1, we can apply static stress and electric field to the system and use

the response to derive the effective average property of this twin crystal. For generality, we allow the crystallographic symmetry of both materials to be arbitrary, however the material properties of both domains must be expressed in the same coordinate system before performing the average. For a ferroelectric system, the material properties are represented by the elastic compliance tensor  $s^{(i)}$ , piezoelectric constant tensor  $d^{(i)}$  and dielectric constant tensor  $\epsilon^{(i)}$ , which satisfy the constitutive relations

$$\begin{pmatrix} \eta^{(i)} \\ \mathbf{D}^{(i)} \end{pmatrix} = \begin{pmatrix} s^{(i)} & d^{(i)T} \\ d^{(i)} & \epsilon^{(i)} \end{pmatrix} \begin{pmatrix} \mathbf{T}^{(i)} \\ \mathbf{E}^{(i)} \end{pmatrix} \quad (i=1,2), \quad (1)$$

where the superscripts (1) and (2) represent the quantity for domain 1 and domain 2, respectively.  $\eta^{(i)}$  and  $\mathbf{D}^{(i)}$  are the elastic strain tensor and the electric displacement vector,  $\mathbf{T}^{(i)}$  and  $\mathbf{E}^{(i)}$  are the stress and electric field, respectively. The two domains can be of different thickness, which is represented by volume ratios  $v^{(1)}$  and  $v^{(2)}$  with  $v^{(1)} + v^{(2)} = 1$ . Components of elastic strain  $\eta$  are assumed to be symmetric, while the components of elastic stress do not have this symmetry due to the cross domain coupling. The simplified notation is related to the true tensor notation in the following form:

$$T_{\lambda} = \begin{cases} T_{ij} & i=j \\ T_{ij} + T_{ji} & i \neq j \end{cases} \quad (i,j=1,2,3; \quad \lambda=1, \dots, 6). \quad (2)$$

Since the material properties are similar in magnitude for the two domains, unlike the case of polymer-ceramic composite,<sup>15,16</sup> it is reasonable to assume that the mechanical stress, strain, electric field and electric displacement in both domains are homogeneous in the equilibrium state. At equilibrium, the effective stress and strain of the twin system is symmetric and the two domains are required to form a coherent nonseparating boundary (DW) under external applied stresses. For convenience, we will use the shortened notation for all the tensor components of material properties defined by<sup>17</sup>

$$s_{\lambda\nu} = \begin{cases} s_{ijkl} & i=j, k=l \\ 2s_{ijkl} & i \neq j, k=l \\ 2s_{ijkl} & i=j, k \neq l \\ 4s_{ijkl} & i \neq j, k \neq l \end{cases} \quad (i,j,k,l=1,2,3; \quad \lambda, \nu=1, \dots, 6), \quad (3a)$$

$$d_{i\mu} = \begin{cases} d_{ijk} & j=k \\ 2d_{ijk} & j \neq k \end{cases} \quad (j,k=1,2,3; \mu=1, \dots, 6). \quad (3b)$$

The constitutive relations for each of the domains are

$$\eta_{ij}^{(n)} = d_{kij}^{(n)} E_k^{(n)} + s_{ijkl}^{(n)} T_{kl}^{(n)}, \quad (4a)$$

$$D_i^{(n)} = \epsilon_{ij}^{(n)} E_j^{(n)} + d_{ijk}^{(n)} T_{jk}^{(n)} \quad (i,j,k,l=1,2,3; n=1,2), \quad (4b)$$



where  $T_{ij}^{(n)}$  and  $E_k^{(n)}$  are the components of the elastic stress tensor and electric field vector, respectively.

Volume ratio averaging conditions can be expressed as<sup>8</sup>

$$\eta_{ij}^{\text{eff}} = v^{(1)} \eta_{ij}^{(1)} + v^{(2)} \eta_{ij}^{(2)}, \quad (5a)$$

$$T_{ij}^{\text{eff}} = v^{(1)} T_{ij}^{(1)} + v^{(2)} T_{ij}^{(2)} \quad (i, j = 1, 2, 3). \quad (5b)$$

These relations cannot hold true simultaneously for both the strain and stress as one can see from the twin structure in Fig. 1. We need to redefine the conditions for such a system for which the orientation and configuration are known. Mechanical equilibrium and nonseparable boundary conditions, i.e., the continuity of the three components of stress:  $T_{22}^{(i)}, T_{23}^{(i)}$  and  $T_{21}^{(i)}$ , six components of strain:  $\eta_{11}^{(i)}, \eta_{33}^{(i)}, \eta_{32}^{(i)}, \eta_{13}^{(i)}, \eta_{31}^{(i)}$  and  $\eta_{12}^{(i)}$ , two components of electric field,  $E_1^{(i)}$  and  $E_3^{(i)}$ , and the electric displacement  $D_2^{(i)}$ , ( $i = 1, 2$ ), lead directly to the following conditions across the domain wall:

$$\eta_{11}^{(1)} = \eta_{11}^{(2)}, \quad (6a)$$

$$\eta_{33}^{(1)} = \eta_{33}^{(2)}, \quad (6b)$$

$$\eta_{32}^{(1)} = \eta_{32}^{(2)}, \quad (6c)$$

$$\eta_{13}^{(1)} = \eta_{13}^{(2)}, \quad (6d)$$

$$\eta_{31}^{(1)} = \eta_{31}^{(2)}, \quad (6e)$$

$$\eta_{12}^{(1)} = \eta_{12}^{(2)}, \quad (6f)$$

$$D_2^{(1)} = D_2^{(2)}, \quad (6g)$$

$$T_{22}^{(1)} = T_{22}^{(2)}, \quad (6h)$$

$$T_{23}^{(1)} = T_{23}^{(2)}, \quad (6i)$$

$$T_{21}^{(1)} = T_{21}^{(2)}, \quad (6j)$$

$$E_1^{(1)} = E_1^{(2)}, \quad (6k)$$

$$E_3^{(1)} = E_3^{(2)}. \quad (6l)$$

These conditions provided different averaging rules for some components of elastic stress, strain, electric field and electric displacement.

Equations (6a)–(6l) give the relations between the elastic stress and electric field in domain 2 and domain 1. For a prescribed stress or electric field to the twinned system, one can first represent the stress and field in domains 1 and 2 using the global quantities. Then, these tensor components can be substituted into Eqs. (5a)–(5b) to find the effective material properties. The linear system of equations, Eqs. (6a)–(6l) can be solved in matrix form

$$\mathbf{b}^{(1)} \boldsymbol{\tau}^{(1)} = \mathbf{b}^{(2)} \boldsymbol{\tau}^{(2)}, \quad (7)$$

where

$$\mathbf{b}^{(i)} = \begin{pmatrix} s_{11}^{(i)} & s_{12}^{(i)} & s_{13}^{(i)} & s_{14}^{(i)} & s_{14}^{(i)} & s_{15}^{(i)} & s_{16}^{(i)} & s_{16}^{(i)} & d_{11}^{(i)} & d_{21}^{(i)} & d_{31}^{(i)} \\ 0 & 1 & 0 & 0 & 0 & 0 & 0 & 0 & 0 & 0 & 0 \\ s_{13}^{(i)} & s_{23}^{(i)} & s_{33}^{(i)} & s_{34}^{(i)} & s_{34}^{(i)} & s_{35}^{(i)} & s_{36}^{(i)} & s_{36}^{(i)} & d_{13}^{(i)} & d_{23}^{(i)} & d_{33}^{(i)} \\ 0 & 0 & 0 & 1 & 0 & 0 & 0 & 0 & 0 & 0 & 0 \\ s_{14}^{(i)} & s_{24}^{(i)} & s_{34}^{(i)} & s_{44}^{(i)} & s_{44}^{(i)} & s_{45}^{(i)} & s_{46}^{(i)} & s_{46}^{(i)} & d_{14}^{(i)} & d_{24}^{(i)} & d_{34}^{(i)} \\ s_{15}^{(i)} & s_{25}^{(i)} & s_{35}^{(i)} & s_{45}^{(i)} & s_{45}^{(i)} & s_{55}^{(i)} & s_{56}^{(i)} & s_{56}^{(i)} & d_{15}^{(i)} & d_{25}^{(i)} & d_{35}^{(i)} \\ s_{16}^{(i)} & s_{26}^{(i)} & s_{36}^{(i)} & s_{46}^{(i)} & s_{46}^{(i)} & s_{56}^{(i)} & s_{66}^{(i)} & s_{66}^{(i)} & d_{16}^{(i)} & d_{26}^{(i)} & d_{36}^{(i)} \\ 0 & 0 & 0 & 0 & 0 & 0 & 0 & 1 & 0 & 0 & 0 \\ 0 & 0 & 0 & 0 & 0 & 0 & 0 & 0 & 1 & 0 & 0 \\ d_{21}^{(i)} & d_{22}^{(i)} & d_{23}^{(i)} & d_{24}^{(i)} & d_{24}^{(i)} & d_{25}^{(i)} & d_{26}^{(i)} & d_{26}^{(i)} & \epsilon_{12}^{(i)} & \epsilon_{22}^{(i)} & \epsilon_{23}^{(i)} \\ 0 & 0 & 0 & 0 & 0 & 0 & 0 & 0 & 0 & 0 & 1 \end{pmatrix} \quad (i = 1, 2) \quad (8)$$

and transposed vector  $\boldsymbol{\tau}^{(i)}$  is given by

$$\boldsymbol{\tau}^{(i)T} = (T_{11}^{(i)}, T_{22}^{(i)}, T_{33}^{(i)}, \frac{1}{2}T_{23}^{(i)}, \frac{1}{2}T_{32}^{(i)}, \frac{1}{2}(T_{13}^{(i)} + T_{31}^{(i)}), \frac{1}{2}T_{12}^{(i)}, \frac{1}{2}T_{21}^{(i)}, E_1^{(i)}, E_2^{(i)}, E_3^{(i)}). \quad (9)$$

To find out the effective material properties of the two-domain system, we can use matrix calculations. In the examples, however, we will solve them in steps for convenience.

Nine simple loads for the two-domain system were applied to help us derive the independent effective constants. In each case, only one or two components of the load are non-zero.

#### longitudinal stress

$$\left. \begin{array}{l} 1. T_{11}^{\text{eff}} \neq 0 \\ 2. T_{22}^{\text{eff}} \neq 0 \\ 3. T_{33}^{\text{eff}} \neq 0 \end{array} \right\} \text{all other } T_{ij}^{\text{eff}} \text{ are zero and } E_i^{\text{eff}} = 0;$$

## shear stress

$$\left. \begin{array}{l} 4. T_{23}^{\text{eff}} \neq 0, T_{32}^{\text{eff}} \neq 0 \\ 5. T_{13}^{\text{eff}} \neq 0, T_{31}^{\text{eff}} \neq 0 \\ 6. T_{12}^{\text{eff}} \neq 0, T_{21}^{\text{eff}} \neq 0 \end{array} \right\} \text{all other } T_{ij}^{\text{eff}} \text{ are zero and } E_i^{\text{eff}} = 0;$$

## electric field

$$\left. \begin{array}{l} 7. E_1^{\text{eff}} \neq 0 \\ 8. E_2^{\text{eff}} \neq 0 \\ 9. E_3^{\text{eff}} \neq 0 \end{array} \right\} \text{all other } E_i^{\text{eff}} \text{ are zero and } T_{ij}^{\text{eff}} = 0.$$

The constitutive relations become relatively simple for these nine independent loads for calculating the effective material properties. Usually only one kind of material constants for the effective material is involved in each equation.

Putting each of these nine independent loads into Eqs. (6a)–(6l) and using the averaging rules, Eqs. (5a)–(5b) we obtain the linear system of equations

$$A x_i = y_i, \quad (10a)$$

$$A = A^{(1)} + \frac{v^{(1)}}{v^{(2)}} A^{(2)}, \quad (10b)$$

$$A^{(i)} = \begin{pmatrix} s_{11}^{(i)} & s_{13}^{(i)} & s_{14}^{(i)} & s_{15}^{(i)} & s_{16}^{(i)} & d_{21}^{(i)} \\ s_{13}^{(i)} & s_{33}^{(i)} & s_{34}^{(i)} & s_{35}^{(i)} & s_{36}^{(i)} & d_{23}^{(i)} \\ s_{14}^{(i)} & s_{34}^{(i)} & s_{44}^{(i)} & s_{45}^{(i)} & s_{46}^{(i)} & d_{24}^{(i)} \\ s_{15}^{(i)} & s_{35}^{(i)} & s_{45}^{(i)} & s_{55}^{(i)} & s_{56}^{(i)} & d_{25}^{(i)} \\ s_{16}^{(i)} & s_{36}^{(i)} & s_{46}^{(i)} & s_{56}^{(i)} & s_{66}^{(i)} & d_{26}^{(i)} \\ d_{21}^{(i)} & d_{23}^{(i)} & d_{24}^{(i)} & d_{25}^{(i)} & d_{26}^{(i)} & \epsilon_{22}^{(i)} \end{pmatrix} \quad (i=1,2), \quad (10c)$$

$$x_i = \begin{pmatrix} T_{11}^{(1)} \\ T_{33}^{(1)} \\ \frac{1}{2} T_{32}^{(1)} \\ \frac{1}{2} (T_{13}^{(1)} + T_{31}^{(1)}) \\ \frac{1}{2} T_{12}^{(1)} \\ E_2^{(1)} \end{pmatrix} \quad (i=1,2,\dots,9), \quad (10d)$$

$$y_1 = \frac{1}{v^{(2)}} T_{11}^{\text{eff}} \begin{pmatrix} s_{11}^{(2)} \\ s_{13}^{(2)} \\ s_{14}^{(2)} \\ s_{15}^{(2)} \\ s_{16}^{(2)} \\ d_{21}^{(2)} \end{pmatrix} \quad y_2 = T_{22}^{\text{eff}} \begin{pmatrix} s_{12}^{(2)} - s_{12}^{(1)} \\ s_{23}^{(2)} - s_{23}^{(1)} \\ s_{24}^{(2)} - s_{24}^{(1)} \\ s_{25}^{(2)} - s_{25}^{(1)} \\ s_{26}^{(2)} - s_{26}^{(1)} \\ d_{22}^{(2)} - d_{22}^{(1)} \end{pmatrix}, \quad (10e)$$

$$y_3 = \frac{1}{v^{(2)}} T_{33}^{\text{eff}} \begin{pmatrix} s_{13}^{(2)} \\ s_{33}^{(2)} \\ s_{34}^{(2)} \\ s_{35}^{(2)} \\ s_{36}^{(2)} \\ d_{23}^{(2)} \end{pmatrix}$$

$$y_4 = \frac{1}{2} T_{23}^{\text{eff}} \begin{pmatrix} \left(1 + \frac{1}{v^{(2)}}\right) s_{14}^{(2)} - s_{14}^{(1)} \\ \left(1 + \frac{1}{v^{(2)}}\right) s_{34}^{(2)} - s_{34}^{(1)} \\ \left(1 + \frac{1}{v^{(2)}}\right) s_{44}^{(2)} - s_{44}^{(1)} \\ \left(1 + \frac{1}{v^{(2)}}\right) s_{45}^{(2)} - s_{45}^{(1)} \\ \left(1 + \frac{1}{v^{(2)}}\right) s_{46}^{(2)} - s_{46}^{(1)} \\ \left(1 + \frac{1}{v^{(2)}}\right) d_{24}^{(2)} - d_{24}^{(1)} \end{pmatrix}, \quad (10f)$$

$$y_5 = \frac{1}{v^{(2)}} T_{13}^{\text{eff}} \begin{pmatrix} s_{15}^{(2)} \\ s_{35}^{(2)} \\ s_{45}^{(2)} \\ s_{55}^{(2)} \\ s_{56}^{(2)} \\ d_{25}^{(2)} \end{pmatrix}$$

$$y_6 = \frac{1}{2} T_{12}^{\text{eff}} \begin{pmatrix} \left(1 + \frac{1}{v^{(2)}}\right) s_{16}^{(2)} - s_{16}^{(1)} \\ \left(1 + \frac{1}{v^{(2)}}\right) s_{36}^{(2)} - s_{36}^{(1)} \\ \left(1 + \frac{1}{v^{(2)}}\right) s_{46}^{(2)} - s_{46}^{(1)} \\ \left(1 + \frac{1}{v^{(2)}}\right) s_{56}^{(2)} - s_{56}^{(1)} \\ \left(1 + \frac{1}{v^{(2)}}\right) s_{66}^{(2)} - s_{66}^{(1)} \\ \left(1 + \frac{1}{v^{(2)}}\right) d_{26}^{(2)} - d_{26}^{(1)} \end{pmatrix}, \quad (10g)$$

$$y_7 = E_1^{\text{eff}} \begin{pmatrix} d_{11}^{(2)} - d_{11}^{(1)} \\ d_{13}^{(2)} - d_{13}^{(1)} \\ d_{14}^{(2)} - d_{14}^{(1)} \\ d_{15}^{(2)} - d_{15}^{(1)} \\ d_{16}^{(2)} - d_{16}^{(1)} \\ \epsilon_{12}^{(2)} - \epsilon_{12}^{(1)} \end{pmatrix} \quad y_8 = \frac{1}{v^{(2)}} E_2^{\text{eff}} \begin{pmatrix} d_{21}^{(2)} \\ d_{23}^{(2)} \\ d_{24}^{(2)} \\ d_{25}^{(2)} \\ d_{26}^{(2)} \\ \epsilon_{22}^{(2)} \end{pmatrix}, \quad (10h)$$

$$y_9 = E_3^{\text{eff}} \begin{pmatrix} d_{31}^{(2)} - d_{31}^{(1)} \\ d_{33}^{(2)} - d_{33}^{(1)} \\ d_{34}^{(2)} - d_{34}^{(1)} \\ d_{35}^{(2)} - d_{35}^{(1)} \\ d_{36}^{(2)} - d_{36}^{(1)} \\ \epsilon_{23}^{(2)} - \epsilon_{23}^{(1)} \end{pmatrix}. \quad (10i)$$

The mechanical stresses  $T_{ij}^{(1)}$  and electric field  $E_2^{(1)}$  are different in general for these simple loads. Values of mechanical stress and electric field in domain 2 can be expressed from Eqs. (6a)–(6l) using values of corresponding components in domain 1. We can solve Eq. (10a) and substitute the results into Eqs. (5a)–(5b) to find the effective material properties for the two-domain system. Detailed procedure is illustrated in the example below.

### III. EXAMPLES OF TENSOR PROPERTY AVERAGING FOR A TWIN CRYSTAL WITH THE SAME VOLUME RATIOS OF THE TWO DOMAINS

As an example, we calculate the effective material properties of a  $3m$  symmetry class single crystal, such as the PZN-PT single crystal, with a set of twins containing equal volume ratios of the two domains. First of all, we need to rotate all tensor components of material properties for both domains from their own material coordinates to the same global coordinate system (material coordinate for the parent cubic structure). Components of material properties for domains 1 and 2 are rotated to the common coordinate system using matrices

$$R^{(1)} = \begin{pmatrix} \frac{1}{\sqrt{2}} & \frac{1}{\sqrt{6}} & \frac{1}{\sqrt{3}} \\ -\frac{1}{\sqrt{2}} & \frac{1}{\sqrt{6}} & \frac{1}{\sqrt{3}} \\ 0 & -\frac{2}{\sqrt{6}} & \frac{1}{\sqrt{3}} \end{pmatrix}$$

and

$$R^{(2)} = \begin{pmatrix} \frac{1}{\sqrt{2}} & \frac{1}{\sqrt{6}} & \frac{1}{\sqrt{3}} \\ -\frac{1}{\sqrt{2}} & -\frac{1}{\sqrt{6}} & -\frac{1}{\sqrt{3}} \\ 0 & -\frac{2}{\sqrt{6}} & \frac{1}{\sqrt{3}} \end{pmatrix}. \quad (11)$$

Because the prototype symmetry of the paraelectric phase is cubic, the possible DW orientations<sup>18</sup> for the two domains with polarization  $P_S[111]$  and  $P_S[\bar{1}\bar{1}\bar{1}]$  are  $[010]$  and  $[101]$ . We calculate the effective material properties for the case with DW oriented in  $[010]$ . Domains are often observed as periodic twin bands in most ferroelectric materials, therefore it is reasonable to assume the same volume ratios for the two domains, i.e.,  $v^{(1)} = v^{(2)} = \frac{1}{2}$ , the expected symmetry of such a twin structure and its effective material properties is  $mm2$ .

Independent material properties for the  $3m$  symmetry class in its own crystallographic coordinate system with the mirror symmetry plane perpendicular to the  $x$  axis can be found in published tables.<sup>17</sup>

Material properties for domain 1 in the chosen coordinate system (as plotted in Fig. 1) are

$$s'^{(1)} = \begin{pmatrix} s'_{11} & s'_{12} & s'_{12} & s'_{14} & s'_{15} & s'_{15} \\ s'_{12} & s'_{11} & s'_{12} & s'_{15} & s'_{14} & s'_{15} \\ s'_{12} & s'_{12} & s'_{11} & s'_{15} & s'_{15} & s'_{14} \\ s'_{14} & s'_{15} & s'_{15} & s'_{44} & s'_{45} & s'_{45} \\ s'_{15} & s'_{14} & s'_{15} & s'_{45} & s'_{44} & s'_{45} \\ s'_{15} & s'_{15} & s'_{14} & s'_{45} & s'_{45} & s'_{44} \end{pmatrix}, \quad (12a)$$

$$\epsilon'^{(1)} = \begin{pmatrix} \epsilon'_{11} & \epsilon'_{12} & \epsilon'_{12} \\ \epsilon'_{12} & \epsilon'_{11} & \epsilon'_{12} \\ \epsilon'_{12} & \epsilon'_{12} & \epsilon'_{11} \end{pmatrix}, \quad (12b)$$

$$d'^{(1)} = \begin{pmatrix} d'_{11} & d'_{12} & d'_{12} & d'_{14} & d'_{15} & d'_{15} \\ d'_{12} & d'_{11} & d'_{12} & d'_{15} & d'_{14} & d'_{15} \\ d'_{12} & d'_{12} & d'_{11} & d'_{15} & d'_{15} & d'_{14} \end{pmatrix}, \quad (12c)$$

while material properties for the second domain in the same coordinate system can be derived as

$$s'^{(2)} = \begin{pmatrix} s'_{11} & s'_{12} & s'_{12} & -s'_{14} & s'_{15} & -s'_{15} \\ s'_{12} & s'_{11} & s'_{12} & -s'_{15} & s'_{14} & -s'_{15} \\ s'_{12} & s'_{12} & s'_{11} & -s'_{15} & s'_{15} & -s'_{14} \\ -s'_{14} & -s'_{15} & -s'_{15} & s'_{44} & -s'_{45} & s'_{45} \\ s'_{15} & s'_{14} & s'_{15} & -s'_{45} & s'_{44} & -s'_{45} \\ -s'_{15} & -s'_{15} & -s'_{14} & s'_{45} & -s'_{45} & s'_{44} \end{pmatrix}, \quad (13a)$$

$$\epsilon'^{(2)} = \begin{pmatrix} \epsilon'_{11} & -\epsilon'_{12} & \epsilon'_{12} \\ -\epsilon'_{12} & \epsilon'_{11} & -\epsilon'_{12} \\ \epsilon'_{12} & -\epsilon'_{12} & \epsilon'_{11} \end{pmatrix}, \quad (13b)$$

$$d'^{(2)} = \begin{pmatrix} d'_{11} & d'_{12} & d'_{12} & -d'_{14} & d'_{15} & -d'_{15} \\ -d'_{12} & -d'_{11} & -d'_{12} & d'_{15} & -d'_{14} & d'_{15} \\ d'_{12} & d'_{12} & d'_{11} & -d'_{15} & d'_{15} & -d'_{14} \end{pmatrix}, \quad (13c)$$

where

$$s'_{11} = \frac{1}{9}(4s_{11} + 4s_{13} + 4\sqrt{2}s_{14} + s_{33} + 2s_{44}), \quad (14a)$$

$$s'_{12} = \frac{1}{9}(s_{11} + 3s_{12} + 4s_{13} - 2\sqrt{2}s_{14} + s_{33} - s_{44}), \quad (14b)$$

$$s'_{14} = \frac{2}{9}(s_{11} - 3s_{12} + s_{13} + \sqrt{2}s_{14} + s_{33} - s_{44}), \quad (14c)$$

$$s'_{15} = \frac{1}{9}(-4s_{11} + 2s_{13} - \sqrt{2}s_{14} + 2s_{33} + s_{44}), \quad (14d)$$

$$s'_{44} = \frac{2}{9}(5s_{11} - 3s_{12} - 4s_{13} - 4\sqrt{2}s_{14} + 2s_{33} + s_{44}), \quad (14e)$$

$$s'_{45} = \frac{1}{9}(-2s_{11} + 6s_{12} - 8s_{13} + 4\sqrt{2}s_{14} + 4s_{33} - s_{44}), \quad (14f)$$

$$d'_{11} = \frac{1}{3\sqrt{3}}(2d_{15} - 2\sqrt{2}d_{22} + 2d_{31} + d_{33}), \quad (14g)$$

$$d'_{12} = \frac{1}{3\sqrt{3}}(-d_{15} + \sqrt{2}d_{22} + 2d_{31} + d_{33}), \quad (14h)$$

$$d'_{14} = -\frac{2}{3\sqrt{3}}(d_{15} + 2\sqrt{2}d_{22} + d_{31} - d_{33}), \quad (14i)$$

$$d'_{15} = \frac{1}{3\sqrt{3}}(d_{15} + 2\sqrt{2}d_{22} - 2d_{31} + 2d_{33}), \quad (14j)$$

$$\epsilon'_{11} = \frac{1}{3}(2\epsilon_{11} + \epsilon_{33}), \quad (14k)$$

$$\epsilon'_{12} = \frac{1}{3}(-\epsilon_{11} + \epsilon_{33}). \quad (14l)$$

As an example, let us apply load 1, i.e.,  $T_{11}^{\text{eff}} \neq 0$ , other are all zero (the other loads 2–9 can be solved similarly). The corresponding matrices for the linear system are

$$\mathbf{A} = \begin{pmatrix} 2s'_{11} & 2s'_{12} & s'_{15} & 0 & 0 & 0 \\ 2s'_{12} & 2s'_{11} & s'_{15} & 0 & 0 & 0 \\ 2s'_{15} & 2s'_{15} & s'_{44} & 0 & 0 & 0 \\ 0 & 0 & 0 & s'_{44} & s'_{45} & 2d'_{15} \\ 0 & 0 & 0 & s'_{45} & s'_{44} & 2d'_{15} \\ 0 & 0 & 0 & d'_{15} & d'_{15} & 2\epsilon'_{11} \end{pmatrix}, \quad (15a)$$

$$\mathbf{x}_1 = \begin{pmatrix} T_{11}^{(1)} \\ T_{33}^{(1)} \\ T_{12}^{(1)} \\ T_{32}^{(1)} \\ T_{13}^{(1)} + T_{31}^{(1)} \\ E_2^{(1)} \end{pmatrix}, \quad (15b)$$

$$\mathbf{y}_1 = (2T_{11}^{\text{eff}}) \begin{pmatrix} s'_{11} \\ s'_{12} \\ s'_{15} \\ -s'_{14} \\ -s'_{15} \\ -d'_{12} \end{pmatrix}, \quad (15c)$$

where we reshaped matrix  $\mathbf{A}$  and vectors  $\mathbf{x}_1, \mathbf{y}_1$  for convenience. The solution of Eq. (10a) for our particular case is given by

$$T_{11}^{(1)} = T_{11}^{\text{eff}}, \quad T_{33}^{(1)} = 0, \quad T_{13}^{(1)} + T_{31}^{(1)} = 0, \quad (16)$$

$$T_{32}^{(1)} = (-2T_{11}^{\text{eff}}) \frac{\det \mathbf{B}_1}{\det \mathbf{B}}, \quad T_{12}^{(1)} = (-2T_{11}^{\text{eff}}) \frac{\det \mathbf{B}_2}{\det \mathbf{B}},$$

$$E_2^{(1)} = (-T_{11}^{\text{eff}}) \frac{\det \mathbf{B}_3}{\det \mathbf{B}}, \quad (17)$$

where

$$\mathbf{B} = \begin{pmatrix} s'_{44} & s'_{45} & d'_{15} \\ s'_{45} & s'_{44} & d'_{15} \\ d'_{15} & d'_{15} & \epsilon'_{11} \end{pmatrix}, \quad \mathbf{B}_1 = \begin{pmatrix} s'_{14} & s'_{45} & d'_{15} \\ s'_{15} & s'_{44} & d'_{15} \\ d'_{12} & d'_{15} & \epsilon'_{11} \end{pmatrix}, \quad (18)$$

$$\mathbf{B}_2 = \begin{pmatrix} s'_{44} & s'_{14} & d'_{15} \\ s'_{45} & s'_{15} & d'_{15} \\ d'_{15} & d'_{12} & \epsilon'_{11} \end{pmatrix}, \quad \mathbf{B}_3 = \begin{pmatrix} s'_{44} & s'_{45} & s'_{14} \\ s'_{45} & s'_{44} & s'_{15} \\ d'_{15} & d'_{15} & d'_{12} \end{pmatrix}. \quad (19)$$

Mechanical stresses in domain 2 are expressed as

$$T_{11}^{(2)} = T_{11}^{\text{eff}}, \quad T_{33}^{(2)} = 0, \quad T_{32}^{(2)} = -T_{32}^{(1)}, \quad (20)$$

$$T_{13}^{(2)} + T_{31}^{(2)} = 0, \quad T_{12}^{(2)} = -T_{12}^{(1)}, \quad E_2^{(2)} = -E_2^{(1)}. \quad (21)$$

Now we can substitute these expressions into the averaging conditions Eqs. (6a)–(6l) and obtain some of the effective material properties for the two-domain system. The same procedure can be applied to the other loads 2–9 and a complete set of effective material properties for the twin structure will be obtained and they are explicitly given below:

$$\mathbf{s}^{\text{eff}} = \begin{pmatrix} s_{11}^{\text{eff}} & s_{12}^{\text{eff}} & s_{13}^{\text{eff}} & 0 & s_{15}^{\text{eff}} & 0 \\ s_{12}^{\text{eff}} & s_{22}^{\text{eff}} & s_{12}^{\text{eff}} & 0 & s_{25}^{\text{eff}} & 0 \\ s_{13}^{\text{eff}} & s_{12}^{\text{eff}} & s_{11}^{\text{eff}} & 0 & s_{15}^{\text{eff}} & 0 \\ 0 & 0 & 0 & s_{44}^{\text{eff}} & 0 & s_{46}^{\text{eff}} \\ s_{15}^{\text{eff}} & s_{25}^{\text{eff}} & s_{15}^{\text{eff}} & 0 & s_{55}^{\text{eff}} & 0 \\ 0 & 0 & 0 & s_{46}^{\text{eff}} & 0 & s_{44}^{\text{eff}} \end{pmatrix}, \quad (22a)$$

$$\boldsymbol{\epsilon}^{\text{eff}} = \begin{pmatrix} \epsilon_{11}^{\text{eff}} & 0 & \epsilon_{13}^{\text{eff}} \\ 0 & \epsilon_{22}^{\text{eff}} & 0 \\ \epsilon_{13}^{\text{eff}} & 0 & \epsilon_{11}^{\text{eff}} \end{pmatrix}, \quad (22b)$$

$$\mathbf{d}^{\text{eff}} = \begin{pmatrix} d_{11}^{\text{eff}} & d_{12}^{\text{eff}} & d_{13}^{\text{eff}} & 0 & d_{15}^{\text{eff}} & 0 \\ 0 & 0 & 0 & d_{24}^{\text{eff}} & 0 & d_{24}^{\text{eff}} \\ d_{13}^{\text{eff}} & d_{12}^{\text{eff}} & d_{11}^{\text{eff}} & 0 & d_{15}^{\text{eff}} & 0 \end{pmatrix}, \quad (22c)$$

where

$$s_{11}^{\text{eff}} = s'_{11} - (s'_{14} \det \mathbf{B}_1 + s'_{15} \det \mathbf{B}_2 + d'_{12} \det \mathbf{B}_3) / \det \mathbf{B}, \quad (23a)$$

$$s_{12}^{\text{eff}} = s'_{12} - (s'_{15} \det \mathbf{B}_1 + s'_{15} \det \mathbf{B}_2 + d'_{11} \det \mathbf{B}_3) / \det \mathbf{B}, \quad (23b)$$

$$s_{13}^{\text{eff}} = s'_{12} - (s'_{15} \det \mathbf{B}_1 + s'_{14} \det \mathbf{B}_2 + d'_{12} \det \mathbf{B}_3) / \det \mathbf{B}, \quad (23c)$$

$$s_{15}^{\text{eff}} = s'_{15} - (s'_{45} \det \mathbf{B}_1 + s'_{45} \det \mathbf{B}_2 + d'_{14} \det \mathbf{B}_3) / \det \mathbf{B}, \quad (23d)$$

$$s_{22}^{\text{eff}} = s'_{11} - (s'_{15} \det \mathbf{B}_4 + s'_{15} \det \mathbf{B}_5 + d'_{11} \det \mathbf{B}_6) / \det \mathbf{B}, \quad (23e)$$

$$s_{25}^{\text{eff}} = s'_{14} - (s'_{45}\det\mathbf{B}_4 + s'_{45}\det\mathbf{B}_5 + d'_{14}\det\mathbf{B}_6)/\det\mathbf{B}, \quad (23f)$$

$$s_{44}^{\text{eff}} = s'_{44} - (s'_{14}\det\mathbf{B}_7 + s'_{15}\det\mathbf{B}_8 + s'_{45}\det\mathbf{B}_9)/\det\mathbf{B}^*, \quad (23g)$$

$$s_{46}^{\text{eff}} = s'_{45} - (s'_{15}\det\mathbf{B}_7 + s'_{14}\det\mathbf{B}_8 + s'_{45}\det\mathbf{B}_9)/\det\mathbf{B}^*, \quad (23h)$$

$$s_{55}^{\text{eff}} = s'_{44} - (s'_{45}\det\mathbf{B}_{10} + s'_{45}\det\mathbf{B}_{11} + d'_{14}\det\mathbf{B}_{12})/\det\mathbf{B}, \quad (23i)$$

$$\epsilon_{11}^{\text{eff}} = \epsilon'_{11} - (d'_{14}\det\mathbf{B}_{13} + d'_{15}\det\mathbf{B}_{14} + \epsilon'_{12}\det\mathbf{B}_{15})/\det\mathbf{B}, \quad (23j)$$

$$\epsilon_{13}^{\text{eff}} = \epsilon'_{12} - (d'_{15}\det\mathbf{B}_{13} + d'_{14}\det\mathbf{B}_{14} + \epsilon'_{12}\det\mathbf{B}_{15})/\det\mathbf{B}, \quad (23k)$$

$$\epsilon_{22}^{\text{eff}} = \epsilon'_{11} - (d'_{12}\det\mathbf{B}_{16} + d'_{12}\det\mathbf{B}_{17} + d'_{14}\det\mathbf{B}_{18})/\det\mathbf{B}^*, \quad (23l)$$

$$d_{11}^{\text{eff}} = d'_{11} - (s'_{14}\det\mathbf{B}_{13} + s'_{15}\det\mathbf{B}_{14} + d'_{12}\det\mathbf{B}_{15})/\det\mathbf{B}, \quad (23m)$$

$$d_{12}^{\text{eff}} = d'_{12} - (s'_{15}\det\mathbf{B}_{13} + s'_{15}\det\mathbf{B}_{14} + d'_{11}\det\mathbf{B}_{15})/\det\mathbf{B}, \quad (23n)$$

$$d_{13}^{\text{eff}} = d'_{12} - (s'_{15}\det\mathbf{B}_{13} + s'_{14}\det\mathbf{B}_{14} + d'_{12}\det\mathbf{B}_{15})/\det\mathbf{B}, \quad (23o)$$

$$d_{15}^{\text{eff}} = d'_{15} - (s'_{45}\det\mathbf{B}_{13} + s'_{45}\det\mathbf{B}_{14} + d'_{14}\det\mathbf{B}_{15})/\det\mathbf{B}, \quad (23p)$$

$$d_{24}^{\text{eff}} = d'_{15} - (s'_{14}\det\mathbf{B}_{16} + s'_{15}\det\mathbf{B}_{17} + s'_{45}\det\mathbf{B}_{18})/\det\mathbf{B}^*, \quad (23q)$$

where

$$\mathbf{B}^* = \begin{pmatrix} s'_{11} & s'_{12} & s'_{15} \\ s'_{12} & s'_{11} & s'_{15} \\ s'_{15} & s'_{15} & s'_{44} \end{pmatrix}, \quad \mathbf{B}_4 = \begin{pmatrix} s'_{15} & s'_{45} & d'_{15} \\ s'_{14} & s'_{44} & d'_{15} \\ d'_{11} & d'_{15} & \epsilon'_{11} \end{pmatrix}, \quad (24a)$$

$$\mathbf{B}_5 = \begin{pmatrix} s'_{44} & s'_{15} & d'_{15} \\ s'_{45} & s'_{15} & d'_{15} \\ d'_{15} & d'_{11} & \epsilon'_{11} \end{pmatrix}, \quad \mathbf{B}_6 = \begin{pmatrix} s'_{44} & s'_{45} & s'_{15} \\ s'_{45} & s'_{44} & s'_{15} \\ d'_{15} & d'_{15} & d'_{11} \end{pmatrix}, \quad (24b)$$

$$\mathbf{B}_7 = \begin{pmatrix} s'_{14} & s'_{12} & s'_{15} \\ s'_{15} & s'_{11} & s'_{15} \\ s'_{45} & s'_{15} & s'_{44} \end{pmatrix}, \quad \mathbf{B}_8 = \begin{pmatrix} s'_{11} & s'_{14} & s'_{15} \\ s'_{12} & s'_{15} & s'_{15} \\ s'_{15} & s'_{45} & s'_{44} \end{pmatrix}, \quad (24c)$$

$$\mathbf{B}_9 = \begin{pmatrix} s'_{11} & s'_{12} & s'_{14} \\ s'_{12} & s'_{11} & s'_{15} \\ s'_{15} & s'_{15} & s'_{45} \end{pmatrix}, \quad \mathbf{B}_{10} = \begin{pmatrix} s'_{45} & s'_{45} & d'_{15} \\ s'_{45} & s'_{44} & d'_{15} \\ d'_{14} & d'_{15} & \epsilon'_{11} \end{pmatrix}, \quad (24d)$$

$$\mathbf{B}_{11} = \begin{pmatrix} s'_{44} & s'_{45} & d'_{15} \\ s'_{45} & s'_{45} & d'_{15} \\ d'_{15} & d'_{14} & \epsilon'_{11} \end{pmatrix}, \quad \mathbf{B}_{12} = \begin{pmatrix} s'_{44} & s'_{45} & s'_{45} \\ s'_{45} & s'_{44} & s'_{45} \\ d'_{15} & d'_{15} & d'_{14} \end{pmatrix}, \quad (24e)$$

$$\mathbf{B}_{13} = \begin{pmatrix} d'_{14} & s'_{45} & d'_{15} \\ d'_{15} & s'_{44} & d'_{15} \\ \epsilon'_{12} & d'_{15} & \epsilon'_{11} \end{pmatrix}, \quad \mathbf{B}_{14} = \begin{pmatrix} s'_{44} & d'_{14} & d'_{15} \\ s'_{45} & d'_{15} & d'_{15} \\ d'_{15} & \epsilon'_{12} & \epsilon'_{11} \end{pmatrix}, \quad (24f)$$

$$\mathbf{B}_{15} = \begin{pmatrix} s'_{44} & s'_{45} & d'_{14} \\ s'_{45} & s'_{44} & d'_{15} \\ d'_{15} & d'_{15} & \epsilon'_{12} \end{pmatrix}, \quad \mathbf{B}_{16} = \begin{pmatrix} d'_{12} & s'_{12} & s'_{15} \\ d'_{12} & s'_{11} & s'_{15} \\ d'_{14} & s'_{15} & s'_{44} \end{pmatrix}, \quad (24g)$$

$$\mathbf{B}_{17} = \begin{pmatrix} s'_{11} & d'_{12} & s'_{15} \\ s'_{12} & d'_{12} & s'_{15} \\ s'_{15} & d'_{14} & s'_{44} \end{pmatrix}, \quad \mathbf{B}_{18} = \begin{pmatrix} s'_{11} & s'_{12} & d'_{12} \\ s'_{12} & s'_{11} & d'_{12} \\ s'_{15} & s'_{15} & d'_{14} \end{pmatrix}. \quad (24h)$$

The symmetry of these effective material properties is at least  $mm2$ . Some may show degeneracy in certain components.

Similar calculations can be carried out for any arbitrary material symmetry and arbitrary orientation of domains and DW.

#### IV. NUMERICAL EXAMPLES FOR $m3m \rightarrow 3m$ AND $m3m \rightarrow 4mm$ FERROELECTRIC SPECIES

In order to make some comparison between our method and the volume ratio weighted average, we have performed a numerical computation for two systems that have experimental data available in the single domain single crystal state. Unfortunately, the lack of experimental results prevented us from direct comparison to measured data for a two-domain twin band system. The two systems calculated represent domains formed at the ferroelectric phase transitions of  $m3m \rightarrow 3m$  and  $m3m \rightarrow 4mm$ . ( $\text{BaTiO}_3$ ) was chosen as an example for the  $m3m \rightarrow 4mm$  transition. There are unfortunately no complete data sets available for the  $m3m \rightarrow 3m$  transition. Therefore we used the numerical data of  $\text{LiNbO}_3$  in the  $3m$  phase and assumed that the domain structures could be engineered to the configurations resulting from a  $m3m \rightarrow 3m$  transition (the true phase transition of  $\text{LiNbO}_3$  is  $\bar{3}m \rightarrow 3m$  and there are only  $180^\circ$  domains in its natural  $3m$  phase).

If the effective material properties could be calculated based on volume ratio weighted average,<sup>8</sup> the effective material properties can have a very compact form. In vector notation, the effective material properties of a two-domain system are given by a  $9 \times 9$  matrix

$$\mathbf{M} = \begin{pmatrix} \mathbf{s} & \mathbf{d}^T \\ \mathbf{d} & \boldsymbol{\epsilon} \end{pmatrix}, \quad (25)$$

where  $\mathbf{s}$  is a  $6 \times 6$  matrix of the elastic compliances,  $\mathbf{d}$  is a  $6 \times 3$  matrix of piezoelectric constants and  $\boldsymbol{\epsilon}$  is a  $3 \times 3$  matrix of the dielectric constant. Because the volume ratio weighting method eliminated the cross coupling between domain 1 and domain 2 and ignored the orientation effect, the effective material properties can be simply expressed as

$$\mathbf{M} = \left( \mathbf{M}^{(1)}(\mathbf{m}^{(1)})^{-1}\mathbf{m}^{(2)} + \frac{v^{(2)}}{v^{(1)}}\mathbf{M}^{(2)} \right) \times \left( (\mathbf{m}^{(1)})^{-1}\mathbf{m}^{(2)} + \frac{v^{(2)}}{v^{(1)}}\mathbf{I} \right)^{-1}, \quad (26)$$

where  $\mathbf{M}^{(1)}$  and  $\mathbf{M}^{(2)}$  are matrices of material properties of both domains and  $\mathbf{I}$  is a  $9 \times 9$  unit matrix. The matrices  $\mathbf{m}^{(1)}$  and  $\mathbf{m}^{(2)}$  are given by

TABLE I. Effective material properties for two variant twin structure of  $\text{LiNbO}_3$  and  $\text{BaTiO}_3$ . The coordinate system is chosen in the way that the y-axis is perpendicular to the DW. Zero values of tensor components are listed by dots.

Material property	LiNbO <sub>3</sub> DW(010)				BaTiO <sub>3</sub> DW(110)				
	$P_S[111]$	$P_S[1\bar{1}1]$	This work	Ref. 8	$P_S[100]$	$P_S[010]$	This work	Ref. 8	
$S_{\alpha\beta}$ [10 <sup>-12</sup> m <sup>2</sup> N <sup>-1</sup> ]	11	5.60	5.60	5.42	5.50	7.92	7.92	7.49	7.92
	12	-1.36	-1.36	-1.10	-1.08	-1.28	-1.28	-1.71	-1.28
	13	-1.36	-1.36	-1.38	-1.46	-3.80	-3.80	-3.47	-3.79
	14	-1.35	1.35	...	...	...	...	...	...
	15	0.26	0.26	-0.49	-0.53	...	...	...	...
	16	0.26	-0.26	...	...	3.83	-3.83	...	...
	22	5.60	5.60	4.65	4.84	7.92	7.92	7.49	7.92
	23	-1.36	-1.36	-1.10	-1.08	-3.80	-3.80	-3.47	-3.79
	24	0.26	-0.26	...	...	...	...	...	...
	25	-1.35	-1.35	1.36	0.87	...	...	...	...
	26	0.26	-0.26	...	...	3.83	-3.83	...	...
	33	5.60	5.60	5.42	5.50	8.05	8.05	7.81	8.05
	34	0.26	-0.26	...	...	...	...	...	...
	35	0.26	0.26	-0.49	-0.53	...	...	...	...
	36	-1.35	1.35	...	...	-2.89	2.89	...	...
	44	15.65	15.65	15.27	15.27	13.62	13.62	11.94	11.94
	45	-0.98	0.98	...	...	4.78	-4.78	...	...
	46	-0.98	-0.98	-0.99	-0.99	...	...	...	...
	55	15.65	15.65	7.92	9.22	13.62	13.62	11.94	13.62
	56	-0.98	0.98	...	...	...	...	...	...
	66	15.65	15.65	15.27	15.27	34.23	34.23	30.63	30.63
$d_{i\alpha}$ [10 <sup>-12</sup> CN <sup>-1</sup> ]	11	16.28	16.28	11.84	15.53	-157	157	...	...
	12	-5.83	-5.83	-5.03	-3.74	121	-121	...	...
	13	-5.83	-5.83	-3.14	-6.58	24	-24	...	...
	14	-47.11	47.11	...	...	...	...	...	...
	15	26.44	26.44	23.84	20.40	...	...	...	...
	16	26.44	-26.44	...	...	-85	-85	-127	-127
	21	-5.83	5.83	...	...	121	121	130	121
	22	16.28	-16.28	...	...	-157	-157	-147	-157
	23	-5.83	5.83	...	...	24	24	17	24
	24	26.44	26.44	22.23	22.23	...	...	...	...
	25	-47.11	47.11	...	...	...	...	...	...
	26	26.44	26.44	22.23	22.23	-85	85	...	...
	31	-5.83	-5.83	-3.14	-6.58	...	...	...	...
	32	-5.83	-5.83	-5.03	-3.74	...	...	...	...
	33	16.28	16.28	11.84	15.53	...	...	...	...
	34	26.44	-26.44	...	...	-277	-277	-179	-180
	35	26.44	26.44	23.84	20.40	-277	277	...	...
	36	-47.11	47.11	...	...	...	...	...	...
$\epsilon_{ij}$ [10 <sup>-10</sup> Fm <sup>-1</sup> ]	11	3.45	3.45	1.68	3.40	135	135	24.1	24.1
	12	-0.44	0.44	...	...	-121	121	...	...
	13	-0.44	-0.44	1.04	-0.50	...	...	...	...
	22	3.45	3.45	1.91	1.92	135	135	133.3	135.5
	23	-0.44	0.44	...	...	...	...	...	...
	33	3.45	3.45	1.68	3.40	256	256	199.6	199.6

$$\mathbf{m}^{(i)} = \begin{pmatrix} s_{11}^{(i)} & s_{12}^{(i)} & s_{13}^{(i)} & s_{14}^{(i)} & s_{15}^{(i)} & s_{16}^{(i)} & d_{11}^{(i)} & d_{21}^{(i)} & d_{31}^{(i)} \\ 0 & 1 & 0 & 0 & 0 & 0 & 0 & 0 & 0 \\ s_{13}^{(i)} & s_{23}^{(i)} & s_{33}^{(i)} & s_{34}^{(i)} & s_{35}^{(i)} & s_{36}^{(i)} & d_{13}^{(i)} & d_{23}^{(i)} & d_{33}^{(i)} \\ 0 & 0 & 0 & 1 & 0 & 0 & 0 & 0 & 0 \\ s_{15}^{(i)} & s_{25}^{(i)} & s_{35}^{(i)} & s_{45}^{(i)} & s_{55}^{(i)} & s_{56}^{(i)} & d_{15}^{(i)} & d_{25}^{(i)} & d_{35}^{(i)} \\ 0 & 0 & 0 & 0 & 0 & 1 & 0 & 0 & 0 \\ 0 & 0 & 0 & 0 & 0 & 0 & 1 & 0 & 0 \\ d_{21}^{(i)} & d_{22}^{(i)} & d_{23}^{(i)} & d_{24}^{(i)} & d_{25}^{(i)} & d_{26}^{(i)} & \epsilon_{12}^{(i)} & \epsilon_{22}^{(i)} & \epsilon_{23}^{(i)} \\ 0 & 0 & 0 & 0 & 0 & 0 & 0 & 0 & 1 \end{pmatrix} \quad (i=1,2). \quad (27)$$

Numerical values for a two-domain system of engineered  $\text{LiNbO}_3$  and  $\text{BaTiO}_3$  calculated using this approach<sup>8</sup> are listed in Table I to compare with the numerical values obtained by using the method given in this paper (also listed in Table I).

It is important to point out that the global symmetry of the twin structure is maintained whether or not the intercoupling between the two domains has been considered. For the case of  $\text{LiNbO}_3$ , the symmetry belongs to the  $mm2$  class. For  $\text{BaTiO}_3$  the symmetry of the system is also  $mm2$ , but there is additional degeneracy for some material properties. They are:  $s_{44}^{\text{eff}} = s_{55}^{\text{eff}}$ . Using the method of volume ratio average,<sup>8</sup> only two of the degenerate relations  $s_{11}^{\text{eff}} = s_{22}^{\text{eff}}, s_{13}^{\text{eff}} = s_{23}^{\text{eff}}$  hold for the elastic compliance tensor.

From Table I, the difference in elastic properties calculated using these two methods is small. This is because the elastic properties of the two variants are very similar, the intercoupling effect is not significant. The difference is much larger in the piezoelectric and dielectric constants for lower symmetry systems. For  $\text{LiNbO}_3$ , the calculated piezoelectric coefficient  $d_{13}$  using these two methods differ by more than 100% and the dielectric coefficient  $\epsilon_{13}$  even have different signs. It appears that the difference becomes smaller for higher symmetry systems. For the  $4mm$  symmetry  $\text{BaTiO}_3$ , the difference is within a few percent for most of the quantities. Therefore, the volume ratio averaging method could give good predictions on the effective properties for higher symmetry systems but may run into problems for lower symmetry systems.

## V. DISCUSSION AND CONCLUSIONS

In summary, we have reported in this paper a general procedure to calculate the effective material properties of a two-variant twin structure. The method has taken into account specifically all the boundary conditions and used more realistic relations for each individual tensor component, rather than using a unified volume ratio averaging scheme. This procedure requires to solve two sets of linear systems of equations and could be easily implemented using a computer. The equations are all linear and can be solved without much difficulty.

In order to compare our method to the volume averaging scheme, we have calculated two systems with polar symme-

tries of  $3m$  and  $4mm$  using both methods. It was found that the new method gives similar results for a  $4mm$  system but predicts quite different piezoelectric and dielectric coefficients for  $3m$  systems. In some components, the difference can exceed 100%. The elastic properties, however, differ very little for both symmetries because the two types of domains are very similar in elastic properties, therefore the coupling of the two domains does not make a significant difference while performing the property average.

Two variant twins are the basis of all twin structures as revealed by all microscopy works. Properly calculated, the effective property of the two-variant twins will pave the way to calculating more precisely more complicated multidomain single crystal ferroelectric systems.

## ACKNOWLEDGMENTS

This work was supported by the National Science Foundation under Grant No. DNS 9704714 and by the Office of Naval Research under Grant Nos. N00014-98-1-0527 and N00014-96-1-1173. One of the authors (J.E.) is also grateful for partial support from the Ministry of Education of the Czech Republic (Code No. VS 96006, 1996).

<sup>1</sup>R. C. DeVries and J. E. Burke, *J. Am. Ceram. Soc.* **40**, 200 (1957).

<sup>2</sup>G. Arlt and P. Sasko, *J. Appl. Phys.* **51**, 4956 (1980).

<sup>3</sup>S. E. Park and T. Shrout, *J. Appl. Phys.* **82**, 1804 (1997).

<sup>4</sup>J. Yin and W. Cao (to be published).

<sup>5</sup>M. L. Mulvihill, L. E. Cross, W. Cao, and K. Uchino, *J. Am. Ceram. Soc.* **80**, 1462 (1997).

<sup>6</sup>M. L. Mulvihill, K. Uchino, Z. Li, and W. Cao, *Philos. Mag. B* **74**, 25 (1996).

<sup>7</sup>M. Grimsditch and F. Nizzolli, *Phys. Rev. B* **33**, 5891 (1986).

<sup>8</sup>E. Aksakaya and G. W. Farnell, *J. Appl. Phys.* **64**, 4469 (1988).

<sup>9</sup>E. Aksakaya, G. W. Farnell, and E. L. Adler, *J. Appl. Phys.* **68**, 1009 (1990).

<sup>10</sup>C.-W. Nan and D. R. Clarke, *J. Am. Ceram. Soc.* **79**, 2563 (1996).

<sup>11</sup>T. Olson and M. Avellaneda, *J. Appl. Phys.* **71**, 4455 (1992).

<sup>12</sup>N. A. Pertsev, A. G. Zembilgotov, and R. Waser, *J. Appl. Phys.* **84**, 1524 (1998).

<sup>13</sup>C.-W. Nan, *J. Appl. Phys.* **76**, 1155 (1994).

<sup>14</sup>M. L. Dunn and M. Taya, *Int. J. Solids Struct.* **30**, 161 (1993).

<sup>15</sup>W. Cao, Q. M. Zhang, and L. E. Cross, *IEEE Trans. Ultrason. Ferroelectr. Freq. Control* **40**, 103 (1993).

<sup>16</sup>W. A. Smith, A. Shaulov, and B. A. Auld, *Proceedings IEEE Ultrasonic Symposium* 1985, 642-647.

<sup>17</sup>J. F. Nye, *Physical Properties of Crystals* (Clarendon, Oxford, 1957).

<sup>18</sup>J. Fousek and V. Janovec, *J. Appl. Phys.* **40**, 135 (1969).

# **APPENDIX 26**



# Elastic, Piezoelectric, and Dielectric Properties of $0.955\text{Pb}(\text{Zn}_{1/3}\text{Nb}_{2/3})\text{O}_3\text{-}0.45\text{PbTiO}_3$ Single Crystal with Designed Multidomains

Jianhua Yin, Bei Jiang, and Wenwu Cao

**Abstract**—The elastic, piezoelectric, and dielectric properties of a  $0.955\text{Pb}(\text{Zn}_{1/3}\text{Nb}_{2/3})\text{O}_3\text{-}0.45\text{PbTiO}_3$  (PZN-4.5%PT) multi-domain single crystal, poled along [001] of the original cubic direction, have been determined experimentally using combined resonance and ultrasonic methods. At room temperature, the PZN-4.5%PT single crystal has rhombohedral symmetry. After being poled along [001], four degenerate states still remain. Statistically, such a domain-engineered crystal may be treated as having an average tetragonal symmetry, and its material constants were determined based on 4 mm symmetry. It was confirmed that the electromechanical coupling coefficient  $k_{33}$  for the domain-engineered samples is  $>90\%$ , and the piezoelectric constant  $d_{33}$  is  $>2000$  pC/N. A soft shear mode with a velocity of 700 m/s was found in the [110] direction. From the measured experimental data, the orientational dependence of phase velocities and electromechanical coupling coefficients was calculated. The results showed that the transverse and longitudinal coupling coefficients,  $k_{31}$  and  $k_{33}$ , reach their maximum along [110] and [001], respectively.

## I. INTRODUCTION

ALTHOUGH early work on  $\text{Pb}(\text{Zn}_{1/3}\text{Nb}_{2/3})\text{O}_3\text{-PbTiO}_3$  (PZN-PT) solid solution system can be dated back to the 1960s [1], [2], it was not until very recently that this relaxor-based ferroelectric single crystal system has generated a great deal of attention. It was found that the single crystal system exhibits an extraordinary large electromechanical coupling coefficient  $k_{33}$  ( $>90\%$ ) and piezoelectric coefficient  $d_{33}$  ( $>2000$  pC/N) at room temperature after being poled in [001], which is off the polarization direction of  $\langle 111 \rangle$  [3]–[5]. Considering that the best piezoelectric materials used today, the modified  $\text{Pb}(\text{Zr}_x\text{Ti}_{1-x})\text{O}_3$  (PZT), only has  $k_{33}$  of 75% and  $d_{33}$  of 700 pC/N, the new system shows a promising potential to produce higher sensitivity ultrasonic transducers with superior broadband characteristics [6], large strain actuators, and other electromechanical devices.

The physical mechanism of this multidomain system is still unclear at the moment. The lack of complete physical property data is the main hindrance for theoretical studies.

Manuscript received August 13, 1999; accepted October 7, 1999. This research was sponsored by the Office of Naval Research under Grant #N00014-98-1-0527 and the National Institutes of Health under Grant #P41 RR11795-01A1.

The authors are with the Material Research Laboratory, The Pennsylvania State University, University Park, PA 16802 (e-mail: cao@math.psu.edu).

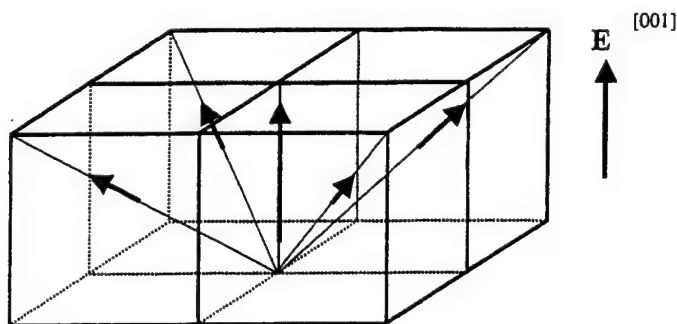


Fig. 1. Possible domain configuration and associated polarization orientation in a PZN-4.5%PT single crystal after being poled in [001] direction.

Practically, it is also very important to have a complete set of elastic, piezoelectric, and dielectric constants available. At present, only one electromechanical coupling coefficient  $k_{33}$  and one piezoelectric coefficient  $d_{33}$  have been reported [3]–[5]. The aim of this paper is to provide a complete set of such data for the PZN-4.5%PT domain-engineered single crystal. These data were obtained by using a combined method involving both pulse-echo and impedance resonance techniques.

Above  $150^\circ\text{C}$ , the crystal PZN-4.5%PT has a cubic perovskite structure with symmetry  $m\bar{3}m$  but becomes a rhombohedral ferroelectric phase with  $3m$  symmetry below the phase transition temperature [5]. When an electric poling field along [001] of the original cubic axis is applied to the crystal, a multidomain configuration can be produced (as shown in Fig. 1) consisting of four degenerate states and charged domain walls [5]. For convenience, the coordinate systems used for the orientations in this paper are all based on the high temperature cubic phase. Statistically, the poled system should have a pseudo-tetragonal 4 mm macroscopic symmetry, although the microscopic symmetry of the system is  $3m$  [5]. Our measured material properties presented in this paper are based on this 4 mm symmetry. There are total of 11 independent physical constants describing the elasto-piezo-dielectric matrices for the 4 mm symmetry [7].

The dielectric constants  $\epsilon_{11}^T$  and  $\epsilon_{33}^T$  were calculated from the low frequency capacitance using the parallel capacitor approximation. Two of the elastic compliances,  $s_{11}^E$  and  $s_{33}^D$ , and the two electromechanical coupling coefficients,  $k_{33}$  and  $k_{31}$ , were calculated from the resonance and antiresonance frequencies of the length-extensional modes

of long vibration bars. Another five elastic constants ( $c_{11}^E$ ,  $c_{12}^E$ ,  $c_{44}^E$ ,  $c_{66}^E$ , and  $c_{44}^D$ ) were determined from the measurements of phase velocities of ultrasonic waves propagating along certain orientations. Using this measurement scheme, the only samples needed are those with the orientations of  $[001]/[010]/[100]$  and  $[001]/[110]/[1\bar{1}0]$ . Thus, fewer samples are required when using this combined measurement technique [8].

For each given wave propagation direction, the relationship between the phase velocity and associated material constants can be obtained by solving the Christoffel wave equations [9], and these velocities can be measured using the pulse-echo technique [7].

## II. EXPERIMENTAL PROCEDURE

The impedance resonance method and ultrasonic pulse-echo technique, described in the IEEE standards on piezoelectricity [7], are often used to characterize material properties for piezoelectric materials [10], [11]. Theoretically, all independent elastic, piezoelectric, and dielectric constants for any crystal symmetry can be determined either by the resonance method or by the ultrasonic method, provided there are sufficient numbers of differently oriented samples. In reality, however, for materials of lower symmetry, some geometries for resonance measurements are difficult to prepare, especially when the available crystal is too small to make large aspect ratio resonators. On the other hand, because the ultrasonic technique can only measure certain elastic constants through the measurement of phase velocities, large errors can be introduced for derived material constants that are not related to pure modes. High acoustic attenuation of certain modes may also damp the propagation of ultrasonic waves in certain directions so that a complete set of material constants for low symmetry systems is also difficult to obtain using the ultrasonic method alone. In this work, we have selected only those simple pure modes in each method and combine the measured data to minimize errors in the results.

In the ferroelectric phase, the dipole in each unit cell of the PZN-4.5%PT crystal is along one of the eight  $\langle 111 \rangle$  directions. It has been shown experimentally that the crystal can hold a macroscopic polarization only when the electric field is applied along one of the six  $\langle 100 \rangle$  directions [3], [4]. After the application of a poling electric field along  $[001]$ , there are still four remaining degenerate dipole orientations. Such a poling field creates a multidomain structure with strong elastic interaction among the existing domains. Statistically, the four remaining domains have an equal possibility to form so that the global macroscopic symmetry has been assumed as 4 mm in all previous studies [5].

The as-grown crystals were first orientated using the Laue method with an accuracy of  $\pm 0.5^\circ$ . Then, each sample was cut and polished into a rectangular parallelepiped shape with three pairs of parallel surfaces. Gold electrodes were sputtered on to the  $[001]$  and  $[00\bar{1}]$  faces of each sam-

ple, and an external electric field of 1.0 to 1.5 MV/m was applied at room temperature to pole the sample. The final dimensions of the samples used for the ultrasonic measurements were about  $3 \times 3 \times 1$  mm<sup>3</sup>. For the length-extensional resonance measurements, the aspect ratio of the sample exceeded 5:1 to yield nearly pure resonance modes [7]. Several sets of samples were prepared for a consistency check. For the bar samples used in the resonance measurements, different aspect ratios were fabricated to ensure purity of the modes. In addition to samples with  $[001]/[010]/[100]$  and  $[001]/[110]/[1\bar{1}0]$  orientations, a resonance bar with its long dimension in  $[110]$  and thickness in  $[001]$  was also made to verify the anisotropy calculations.

A 15-MHz longitudinal wave transducer (Ultran Laboratories, Inc., Boalsburg, PA) and a 20-MHz shear wave transducer (Panametrics, Waltham, MA) were used for the pulse-echo measurements. The electric pulses used to excite the transducer were generated by a Panametrics 200-MHz pulser/receiver, and the time of flight between echoes was measured by using a Tektronix 460A digital oscilloscope.

For the length-extensional resonance measurements, a HP 4194A impedance/gain-phase analyzer was employed. The resonance and antiresonance frequencies corresponding to the minimum and maximum values of the impedance-frequency spectrum were obtained and used to calculate the corresponding electromechanical coupling coefficients and elastic compliance.

The dielectric measurements were carried out at 1 kHz using a Stanford Research System SR715 LCR Meter.

## III. RESULTS AND ANALYSES

Table I lists the measured phase velocities of the longitudinal and shear waves propagating along different crystal orientations in the domain engineered PZN-4.5%PT single crystals. The measured longitudinal electromechanical coupling coefficient  $k_{33}$ , the transverse coupling coefficient  $k_{31}$  in  $[110]$  and  $[100]$  directions, and the frequency constants  $2lf_r$  and  $2lf_a$  for the resonance bars are given in Table II. Here  $l$  is the length of the resonance bar, and  $f_r$  and  $f_a$  are the resonance and antiresonance frequencies, respectively, obtained from the electrical impedance spectrum. The lateral coupling coefficient  $k_{31}$  is different when the long dimension is along  $[001]$  or  $[110]$  for this system because of the anisotropy of the crystal. For comparison, the coupling coefficients and the frequency constants of PZT-5H, BaTiO<sub>3</sub> ceramic, and BaTiO<sub>3</sub> crystal are also listed in Table II. The coupling coefficients,  $k_{33}$  and  $k_{31}$ , of PZT-5H and of BaTiO<sub>3</sub> were directly taken from [12], but the other constants of these three materials were calculated using the data from the same source. The relationship between the measured phase velocities and related elastic constants were derived from the Christoffel wave equations and listed in Table III. Using the four sets of piezoelectric constitutive equations [7], a complete set of elastic, piezoelectric, and dielectric constants of a PZN-

TABLE I

MEASURED PHASE VELOCITIES (M/S) OF ULTRASONIC WAVES IN A PZN-4.5%PT CRYSTAL POLED IN [001].

$v_l^{[001]}$	$v_s^{[001]}$	$v_l^{[100]}$	$v_{s\perp}^{[100]}$	$v_{s\parallel}^{[100]}$	$v_l^{[110]}$	$v_{s\perp}^{[110]}$	$v_{s\parallel}^{[110]}$
4110	2777	3656	2755	2853	4618	668	2855

TABLE II

MEASURED ELECTROMECHANICAL COUPLING COEFFICIENTS AND FREQUENCY CONSTANTS FOR PZN-4.5%PT CRYSTAL POLED IN [001] COMPARED WITH PZT-5H AND BaTiO<sub>3</sub>.<sup>1</sup>

	$k_{31}^{[110]}$	$2lf_r$	$k_{31}^{[100]}$	$2lf_r$	$k_{33}$	$2lf_a$	$k_t$	$2lf_a$
PZN-4.5PT	0.80	2300	0.50	1210	0.90	2414	0.50	4102
BaTiO <sub>3</sub> , crystal <sup>2</sup>	0.40	5729	0.32	4542	0.56	3926	0.29	5452
BaTiO <sub>3</sub> , ceramic <sup>2</sup>	0.21	4391	0.21	4391	0.50	4971	0.43	5477
PZT-5H <sup>2</sup>	0.39	2843	0.39	2843	0.75	3851	0.60	4575

<sup>1</sup> Unit for frequency constant = Hertz · meter.<sup>2</sup>  $k_{31}$  [001] and  $k_{33}$  are from [12]. Others are calculated from the material constants in [12].

TABLE III

THE RELATIONSHIPS BETWEEN PHASE VELOCITIES AND ELASTIC CONSTANTS.

	$v_l^{[001]}$	$v_s^{[001]}$	$v_l^{[100]}$	$v_{s\perp}^{[100]}$	$v_{s\parallel}^{[100]}$	$v_l^{[110]}$	$v_{s\perp}^{[110]}$	$v_{s\parallel}^{[110]}$
$\rho v^2 =$	$c_{33}^D$	$c_{44}^E$	$c_{11}^E$	$c_{66}^E$	$c_{44}^D$	$\frac{1}{2}(c_{11}^E + c_{12}^E + 2c_{66}^E)$	$\frac{1}{2}(c_{11}^E - c_{12}^E)$	$c_{44}^D$

TABLE IV

MEASURED AND DERIVED MATERIAL PROPERTIES OF PZN-4.5%PT SINGLE CRYSTAL POLED ALONG [001].<sup>1</sup>

Elastic constants: $c_{ij}$ ( $10^{10}$ N/m <sup>2</sup> )											
$c_{11}^{E*}$	$c_{12}^E$	$c_{13}^E$	$c_{33}^E$	$c_{44}^{E*}$	$c_{66}^{E*}$	$c_{11}^D$	$c_{12}^D$	$c_{13}^D$	$c_{33}^{D*}$	$c_{44}^{D*}$	$c_{66}^D$
11.1	10.2	10.1	10.5	6.4	6.3	11.3	10.4	9.5	13.5	6.7	6.3
±0.15	±0.16	±0.15	±0.3	±0.05	±0.05	±0.15	±0.15	±0.35	±0.5	±0.05	±0.05
Elastic constants: $s_{ij}$ ( $10^{-12}$ m <sup>2</sup> /N)											
$s_{11}^{E*}$	$s_{12}^E$	$s_{13}^E$	$s_{33}^E$	$s_{44}^E$	$s_{66}^E$	$s_{11}^D$	$s_{12}^D$	$s_{13}^D$	$s_{33}^{D*}$	$s_{44}^{D*}$	$s_{66}^D$
82.0	-28.5	-51.0	108	15.6	15.9	61.5	-49.0	-9.0	20.6	14.9	15.9
±3.2	±0.9	±0.8	±0.5	±0.12	±0.18	±0.8	±0.1	±0.5	±0.8	±0.1	±0.18
Piezoelectric constants: $e$ (C/m <sup>2</sup> ), $d$ ( $10^{-12}$ C/N), $g$ ( $10^{-3}$ Vm/N), $h$ ( $10^8$ V/m)											
$e_{15}$	$e_{31}$	$e_{33}$	$d_{15}$	$d_{31}$	$d_{33}$	$g_{15}$	$g_{31}$	$g_{33}$	$h_{15}$	$h_{31}$	$h_{33}$
8.9	-3.7	15.0	140	-970	2000	5.0	-21.0	44	3.4	-4.3	17
±0.9	±1.6	±1.6	±16	±19	±75	±0.58	±0.4	±0.8	±0.4	±2.0	±1.7
Dielectric constants: $\epsilon$ ( $\epsilon_0$ ), $\beta$ ( $10^{-4}/\epsilon_0$ )											
$\epsilon_{11}^S$	$\epsilon_{33}^S$	$\epsilon_{11}^{T*}$	$\epsilon_{33}^{T*}$	$\beta_{11}^S$	$\beta_{33}^S$	$\beta_{11}^T$	$\beta_{33}^T$	$k_{15}$	$k_{31}^*$	$k_{33}^*$	$k_t^*$
3000	1000	3100	5200	3.4	10.0	3.2	1.9	0.23	0.50	0.91	0.50
±110	±45	±120	±200	±0.1	±0.5	±0.1	±0.05	±0.02	±0.01	±0.01	±0.01

<sup>1</sup> Density:  $\rho = 8310$  kg/m<sup>3</sup>.

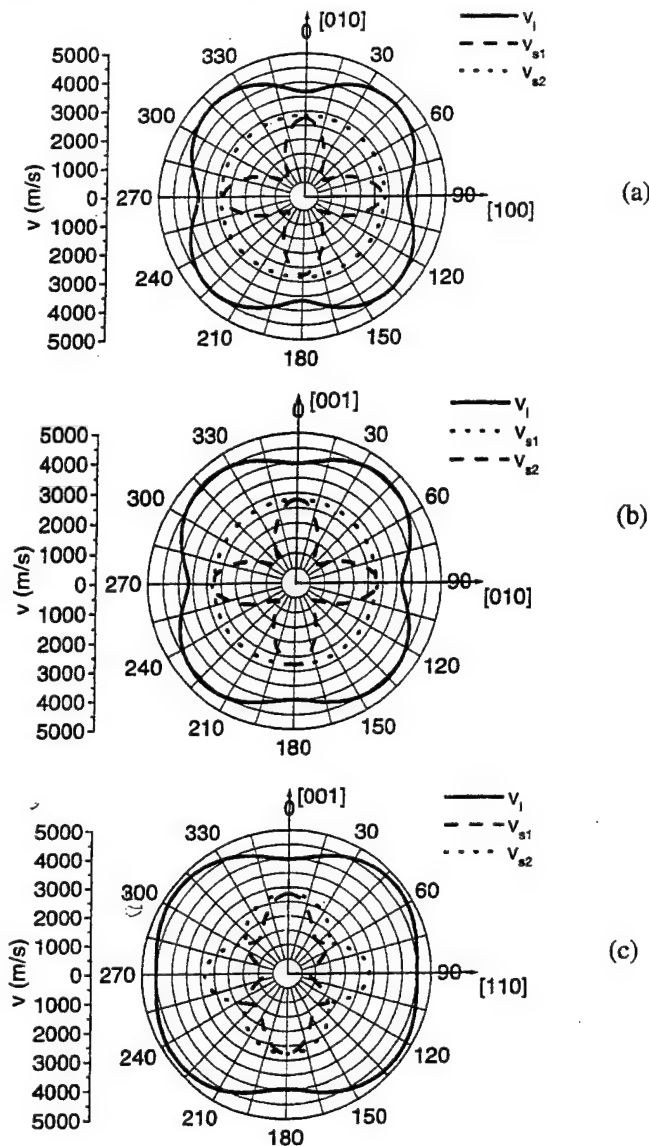


Fig. 2. Directional dependence of the longitudinal velocity,  $v_l$ , and the two shear velocities,  $v_{s1}$  and  $v_{s2}$  in a) the [100] and [010] plane, b) the [010] and [001] plane, and c) the [110] and [001] plane.

4.5%PT crystal based on the 4 mm symmetry has been derived and is given in Table IV. The independent material constants marked with a star (\*) in Table IV were measured directly; the other constants in Table IV were derived using the constitutive relations.

Our experimental results confirmed the extraordinarily large room temperature electromechanical coupling coefficient,  $k_{33} > 90\%$ , and piezoelectric constant,  $d_{33} > 2000$  pC/N, reported earlier [3]. More importantly, we have provided a complete set of material constants for this PZN-4.5%PT domain-engineered single crystal, which can be used to perform theoretical analysis and device designs. A very slow shear wave with a sound velocity of only 700 m/s propagating in [110] and polarized in  $[\bar{1}\bar{1}0]$  was observed, which implies that a "soft transverse acoustic mode" exists in this domain-engineered single crystal system.

#### IV. ERROR ANALYSIS

The errors in these measured material constants come from the following sources: 1) the use of parallel plate capacitor approximation for dielectric measurements, 2) errors in measuring the time of flight between ultrasonic echoes, 3) errors in the measurements of resonance and antiresonance frequencies and sample thickness, 4) misorientation and imperfect parallelness of sample surfaces, 5) inconsistency between different samples, and 6) numerical errors for calculating those derived constants. We have analyzed each error source to provide an estimate for the measurement errors.

Using a 15-MHz longitudinal transducer, we have quantified the error for measuring the sound velocity to be  $<1\%$  for sample with thickness  $>2$  mm. The error in the capacitance measurement is about 4%. Error from misorientation is  $<1\%$  if the misorientation is  $<2^\circ$  as analyzed subsequently. The largest error comes from the inconsistency of different samples because the properties of each sample depend strongly on the domain pattern; the domain pattern is controlled by the geometry of the sample and the poling process. This error was minimized through an oversampling scheme in the measurements.

Table V shows the velocities from several measurements in differently orientated samples. One can see that the difference among the measured velocities is  $<1\%$ . However, because the measured coupling coefficients vary from 1 to 3%, the error of the calculated coefficient  $s_{33}^E = s_{33}^D / (1 - k_{33}^2)$  [7] can be very large. This can be seen from the relative error of  $s_{33}^E$  caused by the error of  $k_{33}$ :

$$\left| \frac{\delta s_{33}^E}{s_{33}^E} \right| = \left| \frac{2k_{33}\delta k_{33}}{(1 - k_{33}^2)} \right|. \quad (1)$$

When  $k_{33}$  reaches  $> 90\%$ , the relative error of  $s_{33}^E$  calculated from this formula will be an order of magnitude larger than that of  $k_{33}$ . For instance, if  $k_{33}$  is 0.90 with a relative error of 1%, the relative error for  $s_{33}^E$  calculated from (1) will be  $>10\%$ .

Table VI gives the changes of some constants caused by a 1% change in the coupling coefficient  $k_{33}$ . Table VII lists the measured results of the length-extension modes from samples of different aspect ratios. For this system, the aspect ratio (length/width) effects come not only from the influence of mode pureness as stated in [13], but also from the change of the domain patterns. It was found that the coupling coefficient decreases if the aspect ratio decreases, but the frequency constant increases for smaller aspect ratios.

#### V. ANISOTROPY STUDY

Unlike  $\text{Pb}(\text{Zr,Ti})\text{O}_3$  ceramic samples, domain-engineered PZN-4.5%PT single crystals are anisotropic in the plane perpendicular to the poling direction. Therefore, an analysis of the directional dependence of phase velocities and

TABLE V

MEASURED PHASE VELOCITIES (M/S) OF ULTRASOUND WAVES IN A POLED PZN-4.5%PT CRYSTAL POLED ALONG [001]. THE LEFT COLUMN REPRESENTS THE NUMBER OF MEASUREMENTS. (NOTE: DATA IN THE SAME ROW DOES NOT NECESSARILY MEAN THEY ARE FROM THE SAME SAMPLE.)

Measurements (no.)	$v_l^{[001]}$	$v_s^{[001]}$	$v_l^{[100]}$	$v_{s\perp}^{[100]}$	$v_{s\parallel}^{[100]}$	$v_l^{[110]}$	$v_{s\perp}^{[110]}$	$v_{s\parallel}^{[110]}$
1	4098	2794	3611	2773	2865	4612	649	2864
2	4127	2783	3681	2737	2841	4602	667	2851
3	4122	2766	3639			4612	669	2855
4	4112	2766	3696			4648	688	2842
5	4121		3672					2870
6	4080		3640					2854
7	4123							2860
8								2847
Average	4110	2777	3656	2755	2853	4618	668	2855
Relative error (%)	0.3	0.4	0.7	0.6	0.4	0.3	1.5	0.2

TABLE VI

COMPARISON OF DERIVED CONSTANTS FOR THE TWO CASES OF  $k_{33} = 0.90$  AND  $k_{33} = 0.91$ .

$k_{33}$	$c_{13}^E$	$c_{33}^E$	$c_{13}^D$	$c_{33}^D$	$s_{11}^E$	$s_{33}^E$	$s_{33}^S$	$e_{31}$	$e_{33}$	$d_{33}$	$g_{33}$	$h_{31}$	$h_{33}$
0.91	9.6	9.5	9.3	13.0	54.1	120	890	-1.5	16.5	2100	46.4	-1.9	20.9
0.90	10.1	10.5	9.45	13.1	51.4	108	970	-3.7	15.5	2000	43.7	-4.3	17.4
$\delta^1$ (%)	1.1	5.1	10	1.6	0.8	5.1	11	8.6	85	6.3	4.9	6.0	77

<sup>1</sup> $\delta$  is relative error.

TABLE VII

EXPERIMENTAL RESULTS OBTAINED FROM THE LENGTH EXTENSIONAL RESONANCE USING SAMPLES WITH DIFFERENT ASPECT RATIOS.

$l$ (mm)	$l/w$	$f_r$ (kHz)	$f_a$ (kHz)	$k_{33}$	$2lf_a$ (Hz·m)
4.05	9.0	143.9	298.0	0.90	2414
2.90	6.3	222.5	427.5	0.88	2480
3.10	4.5	217.5	408.8	0.87	2534
3.62	3.9	202.4	372.3	0.86	2695

TABLE VIII

RELATIVE ERRORS (IN PERCENTAGES) INTRODUCED IN VELOCITIES WITH A MISORIENTATION OF  $2^\circ$ .

	$v_l^{[001]}$	$v_s^{[001]}$	$v_l^{[100]}$	$v_{s\perp}^{[100]}$	$v_{s\parallel}^{[100]}$	$v_l^{[110]}$	$v_{s\perp}^{[110]}$	$v_{s\parallel}^{[110]}$
Relative error (%)	0.2	0.4	0.3	0.5	0.5	0.06	2.0	0.2

electromechanical coupling coefficients will be very helpful to understand the nature of PZN-PT crystals. The anisotropy analysis was performed by using the measured data given in Table IV. Fig. 2 provides the directional dependence of phase velocities for sound wave propagating in the a) X-Y, b) Y-Z, and c) [110]-Z planes. The calculated results reveal that the velocities of the longitudinal waves do not change with orientation as much as that of the shear waves. As shown in Fig. 2(a), the shear wave propagating in the X-Y plane and polarized in the same plane has the strongest orientational dependence. It has a

maximum in [100] and a minimum in [110], respectively. Fig. 2(b) shows that the phase velocity of the shear wave propagating and polarizing in the Y-Z plane also changes drastically with the propagation direction. Its maximum and minimum are in [001] and [011], respectively. Therefore, the error in phase velocity measurements caused by misorientation is larger for the shear wave propagating in [110] than in other orientations. Table VIII lists the errors of the velocities for an assumed misorientation of  $2^\circ$  in the propagation directions. The maximum error from this error source is 2%.



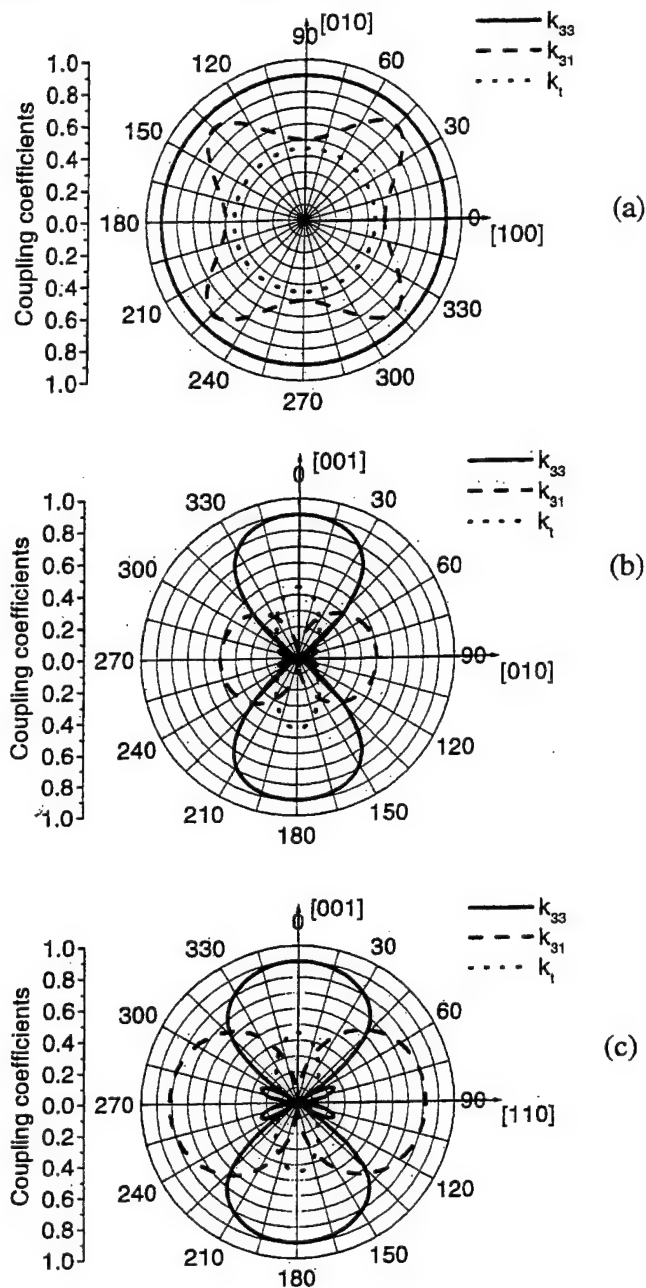


Fig. 3. Directional dependence of the coupling coefficients  $k_{33}$ ,  $k_{31}$ , and  $k_t$ , respectively, in a) the [100] and [010] plane, b) the [010] and [001] plane, and c) the [110] and [001] plane.

Fig. 3 shows the directional dependence of the electromechanical coupling coefficients  $k_{33}$  and  $k_{31}$ . The poling direction is parallel to the length direction for the  $k_{33}$  bar and perpendicular to the length direction for the  $k_{31}$  bar. The coupling coefficient  $k_{33}$  has a maximum value when the length is in [001] [Fig. 3(b)]; the coupling coefficient of  $k_{31}$  reaches the maximum when the length is in [110] direction [Fig. 3(c)]. This calculated anisotropy of the lateral coupling coefficient was verified by the direct measurement given in Table II. Fig. 3 also gives the directional dependence of  $k_t$ , the coupling coefficient of the thickness mode for a flat plate. It has a maximum in the [001] direction.

Because the 1-D formula for calculating the cou-

pling coefficient and elastic compliance from the length-extensional mode is derived based on the assumption of a long thin bar without lateral constraints, a large aspect ratio is needed to produce such decoupled modes [7]. Otherwise, the measured coupling coefficient from the resonance method will be between the value of  $k_t$  and  $k_{33}$ . In other words, the longitudinal velocity would be higher for smaller aspect ratios. These results were verified also by the experimental results given in Table VII. It is worth mentioning that some of the modes were not pure even with a very large aspect ratio for this multidomain system; therefore, it is not possible to obtain the complete set of the material properties by using the resonance technique alone.

## VI. SUMMARY AND CONCLUSIONS

The material properties of a PZN-4.5%PT single crystal poled in the [001] direction of the original cubic axes were measured using a combined method of ultrasonic and resonance techniques. The crystal symmetry of the ferroelectric state is 3m at room temperature, but the macroscopic average symmetry of the domain pattern is pseudo-tetragonal for the [001] poled samples. Rectangular parallelepiped samples with [001]/[010]/[100] and [001]/[110]/[110] orientations were made for our measurements. A complete set of elastic, piezoelectric, and dielectric constants for the PZN-4.5%PT single crystals were determined from the measured resonance frequencies, sound velocities, and low frequency capacitance values. The directional dependence of the phase velocities of the ultrasonic waves propagating in the X-Y, Y-Z, and [110]-Z planes were calculated based on the measured data. The calculated results showed that the phase velocities are strongly anisotropic for shear waves but directional dependence is relatively weaker for the longitudinal waves. A slow shear wave, about 700 m/s, was found in the [110] direction polarized in [110]. The directional dependence of the electromechanical coupling coefficients was also calculated based on the measured materials properties. It was showed that the maximum value of  $k_{33}$  is in [001], and the maximum of effective lateral coupling coefficient  $k_{31}$  is in [110]. These calculated results agree well with our experimental verifications. Detailed error analysis was performed for each measured coefficient, and it was concluded that the errors are small for directly measured quantities but relatively larger for the derived coefficients.

## ACKNOWLEDGMENTS

The crystals used for this study were provided by Drs. S. E. Park and T. R. Shrout through the Piezocrystal Resource Center of the Pennsylvania State University.

## REFERENCES

- [1] S. Nomura, T. Takahashi, and Y. Yokomizo, "Ferroelectric properties in the system  $\text{Pb}(\text{Zn}_{1/3}\text{Nb}_{2/3})\text{O}_3$ - $\text{PbTiO}_3$ ," *J. Phys. Soc. Jpn.*, vol. 27, no. 1, p. 262, 1969.
- [2] J. Kuwata, K. Uchino, and S. Nomura, "Dielectric and piezoelectric properties of 0.91PZN-0.09PT single crystals," *Jpn. J. Appl. Phys.*, vol. 21, no. 9, pp. 1298-1302, 1982.
- [3] S. E. Park, and T. R. Shrout, "Ultrahigh strain and piezoelectric behavior in relaxor based ferroelectric single crystals," *J. Appl. Phys.*, vol. 82, no. 4, pp. 1804-1811, 1997.
- [4] —, "Characteristics of relaxor-based piezoelectric single crystals for ultrasonic transducers," *IEEE Trans. Ultrason., Ferroelect., Freq. Contr.*, vol. 44, no. 5, pp. 1140-1147, 1997.
- [5] S. F. Liu, S. E. Park, T. R. Shrout, and L. E. Cross, "Electric field dependence of piezoelectric properties for rhombohedral  $0.955\text{Pb}(\text{Zn}_{1/3}\text{Nb}_{2/3})\text{O}_3$ - $0.045\text{PbTiO}_3$  single crystal," *J. Appl. Phys.*, vol. 85, no. 5, pp. 2810-2814, 1999.
- [6] S. Saitoh, T. Takeuchi, T. Kobayashi, K. Harada, S. Shimanuki, and Y. Yamashita, "A 3.7 MHz phase array probe using  $0.91\text{Pb}(\text{Zn}_{1/3}\text{Nb}_{2/3})\text{O}_3$ - $0.09\text{PbTiO}_3$  single crystal," *IEEE Trans. Ultrason., Ferroelect., Freq. Contr.*, vol. 46, no. 2, pp. 414-421, 1999.
- [7] *IEEE Standard on Piezoelectricity*, ANSI/IEEE STD. 176-1987, 1987.
- [8] S. Zhu, B. Jiang, and W. Cao, "Characterization of piezoelectric materials using ultrasonic and resonant techniques," in *Proc. SPIE, Med. Imag. 1998*, no. 3341, San Diego, CA, pp. 154-162.
- [9] B. A. Auld, *Acoustic Fields and Waves in Solids*. New York: Wiley, 1973.
- [10] A. W. Warner, M. Onoe, and G. A. Coquin, "Determination of elastic and piezoelectric constants for crystals in class(3m)," *J. Acoust. Soc. Amer.*, vol. 42, no. 6, pp. 1223-1231, 1967.
- [11] J. Kushibiki and I. Takanaga, "Elastic properties of single- and multi-domain crystals of  $\text{LiTaO}_3$ ," *J. Appl. Phys.*, vol. 81, no. 10, pp. 6906-6910, 1997.
- [12] K.-H. Hellwege, *Landolt-Bornstein Numerical Data and Functional Relationships in Science and Technology, Group III, Band 1*, Vol. 1. New York: Springer-Verlag.
- [13] W. Cao, S. N. Zhu, and B. Jiang, "Analysis of shear modes in a piezoelectric vibrator," *J. Appl. Phys.*, vol. 83, no. 8, pp. 4415-4420, 1998.

Bei Jiang received her B.A. in English from Northeast Normal University, P.R. China, in 1983 and M.Ed. from The Pennsylvania State University in 1989. She has been working in the Material Research Laboratory of Penn State as a research assistant from 1988 to 1989 and from 1996 to now. Her research interests are piezoelectric crystals and ultrasonic characterization.



Wenwu Cao received his B.S. degree in physics from Jilin University, Changchun, China, in 1982 and the Ph.D. degree in condensed matter physics from The Pennsylvania State University in 1987.

He is currently holding a joint appointment between the Department of Mathematics and the Materials Research Laboratory of The Pennsylvania State University as Associate Professor of Mathematics and Materials Science. He has conducted both theoretical and experimental research in the area of condensed matter physics and materials, including theories on proper and improper-ferroelastic phase transitions and static and dynamic properties of domains and domain walls in ferroelectric and ferroelastic materials. He has also performed measurements on second- and third-order elastic constants, linear and nonlinear dielectric constants, and piezoelectric constants in single crystals and ceramics. His current interests also include the static and dynamic behavior of piezoelectric ceramic-polymer composites, simulation design of piezoelectric sensors, transducers and actuators for underwater acoustics, and medical ultrasonic imaging as well as ultrasonic NDE and signal processing.

Dr. Cao is a member of the Society for Industrial and Applied Mathematics and the American Physical Society.



Jianhua Yin received his B.Sc., M.Sc., and Ph.D. degrees from Nanjing University, P.R. China in 1994, 1997, and 1990, respectively. He joined the Institute of Acoustics and the Department of Electronic Science and Engineering at Nanjing University in 1990. He became an Associate Professor there in 1992.

His research interests are in the field of surface acoustic wave device and its application in communication system, ultrasonic transducer, ultrasonic nondestructive evaluation, and acoustic signal processing.

Dr. Yin is a member of the Acoustic Society of China. He was a visiting researcher in Tokai University, Japan, from 1992 to 1993, and a visiting scholar in the University of Kansas from 1997 to 1998. He has been a visiting Research Associate in Material Research Laboratory at Pennsylvania State University since 1998. He is now working on the characterization of ferroelectric single crystal.

# **APPENDIX 27**



## Defect-induced Domain Configuration in Relaxor PZN Single Crystal and Its Origin

Satoshi Wada, Seung-Eek Park\*, L. Eric Cross\* and Thomas R. Shrout\*

Department of Applied Chemistry, Tokyo University of Agriculture & Technology, 24-16 Nakamachi 2-chome,  
Koganei, Tokyo 184-8588, JAPAN

Fax: 81-42-383-6134, e-mail: swada@cc.tuat.ac.jp

\*Materials Research Laboratory, The Pennsylvania State University, University Park, PA 16802-4801, U.S.A.

Fax: 1-814-865-2326, e-mail: sxp37@psu.edu

$\text{Pb}(\text{Zn}_{1/3}\text{Nb}_{2/3})\text{O}_3$  single crystal is typical relaxor ferroelectrics and has optical isotropic property. However, our PZN single crystal showed real domain configuration with very small birefringence at room temperature. This domain configuration can not satisfy crystallographic configuration, and its temperature dependence indicated that the domain configuration existed even at 200°C. Moreover, the complete same domain patterns can be always regenerated despite repeated heat annealing at 250°C. The characterization of the PZN crystal revealed that there were growth twinning structures, lattice defect, and inhomogeneity of chemical composition. Therefore, it suggests that very weak local stress field caused by these defect structure can make polar micro region ordering and thus can make the defect-induced domain configuration.

Key word: PZN single crystal, defect-induced domain configuration, polar micro region, relaxor, defect structure

### 1. INTRODUCTION

It was well known that  $\text{Pb}(\text{Zn}_{1/3}\text{Nb}_{2/3})\text{O}_3$  (=PZN) single crystal is typical relaxor ferroelectrics and has an optical isotropic property<sup>1,2</sup>. To date, many researchers have considered that a polar micro region (=PMR) must be the origin in the relaxation behavior, and PMR could also cause an optical isotropic state<sup>3</sup>. Therefore, PMR is the most important factor in the relaxation behavior. At present, there are some models about state of PMR, i.e., (i) superparaelectric model<sup>4</sup>, (ii) dipolar and spin glass model<sup>5</sup>, (iii) dipolar dielectric with random field model<sup>6</sup> and (iv) breathing model<sup>7</sup>. First three models were on the basis of flipping polar vector in PMR while the last model was on the basis of fixed polar vector. Therefore, it was very important to observe PMR directly and reveal the state of PMR. Before, it has considered that chemically ordered domain (COD) observed by TEM might be PMR, but Akbas and Devis revealed that COD did not relate with relaxation behavior, i.e., PMR<sup>10,11</sup>. Therefore, to date, no one has observed PMR directly.

Nomura et al. reported that before DC-bias exposure, pure PZN crystal showed an optical isotropic property although after DC-bias exposure, the relaxor state changed to the ferroelectric state with a normal ferroelectric domain<sup>8</sup>. However, in PZN single crystal which we grew by a flux method, a domain configuration with very low birefringence was observed clearly under crossed-nicols, as shown in Fig. 1. This domain configuration has some strange features, i.e., (1) very unclear domain wall, (2) partially curved domain wall, (3) very low birefringence, (4) unexpected angle between neighbored domain, and (5) graduation of birefringence in one domain. Moreover, it should be noted that our PZN crystal with the strange domain configuration exhibited the almost same dielectric properties as those in Yokomizo's isotropic PZN<sup>12</sup>. These results mean that the relaxation behavior in the optical isotropic PZN crystal is almost same as that in PZN crystal with the strange domain configuration, i.e.,

there is no difference between states of PMR in two PZN crystals. Therefore, it is so important to discuss about the domain configuration on the basis of crystallography, and reveal its origin.

Our objective is to clear the strange domain configuration crystallographically, and discuss about its origin. In this study, we analyze the domain configuration crystallographically, and also do in-situ domain observation as a function of temperature.

### 2. EXPERIMENTAL

PZN single crystals were grown by a conventional flux method using a PbO flux. Further details on the crystal growth were reported elsewhere<sup>12</sup>. Flux grown crystals were characterized using XRD and ICP.

These crystals were oriented along [111] direction using a back reflection Laue camera. After the orientation, the crystals were cut and polished. For in-situ domain observation from -100°C to 200°C and crystallographic interpretation, very thin crystals with thickness of around 50  $\mu\text{m}$  and two mirror-polished (111) surfaces were prepared. Domain configuration was observed under crossed-nicols at transmittance

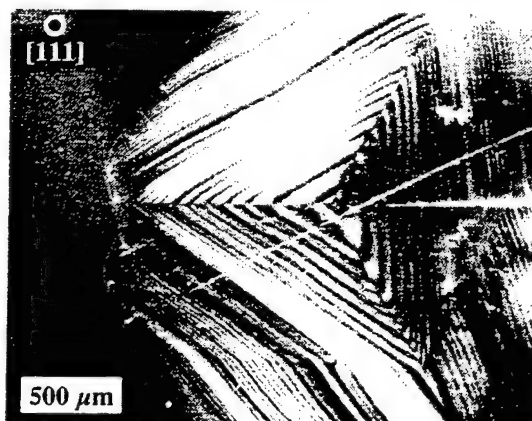


Fig. 1 Domain configuration of PZN single crystal oriented along [111].

configuration using a Polarizing microscope (Carl Zeiss, D-7082). Prior to the domain observation, all crystals were annealed at 250°C for 15hr in air in order to remove ferroelastic domains.

### 3. RESULTS AND DISCUSSION

**3.1 Characterization of PZN crystal:** Powder XRD measurement of as-grown PZN crystal indicated that an average symmetry can be assigned to rhombohedral R3m, and  $a$ -axis and  $\alpha$  is 0.4056nm and 89°55', respectively<sup>12</sup>. These lattice parameters were almost consistent with those in Yokomizo's crystal<sup>4</sup>. On the other hand, ICP measurement of the as-grown PZN crystal revealed that each wt% of lead (Pb), zinc (Zn), niobium (Nb), and oxygen (O) was 59.9, 5.7, 20.7 and 13.7, respectively, while in an ideal PZN crystal, each wt% of Pb, Zn, Nb, and O is 61.1, 6.4, 18.3 and 14.2, respectively<sup>12</sup>. This indicated that a chemical composition in the as-grown crystal is slight Nb-rich, while Yokomizo et al. grew PZN crystal with almost its stoichiometric composition<sup>4</sup>. Therefore, as considered electroneutrality condition, there must be lattice defects such as  $Nb_{Zn}^{2-}$ ,  $V_O^{\cdot-}$ ,  $V_{Nb}^{\cdot+}$ ,  $V_{Zn}^{\cdot+}$  and  $V_{Nb}^{\cdot+}$  in our PZN crystal.

Fig. 2 shows temperature dependence of dielectric constant in the as-grown PZN single crystal oriented along [111].  $T_{max}$  and dielectric constant measured at 100Hz was 134°C and around 60000, respectively, and  $T_{max}$  at various frequencies shifted to higher temperature with increasing frequency while and dielectric constant also decreased at the same time<sup>12</sup>. Moreover, the dielectric properties in our crystal were the almost same as those in Yokomizo's crystal<sup>12</sup>.

The above characterization suggested that about the average crystal structure and dielectric property, there is no difference between our and Yokomizo's crystals while about chemical composition, there is a significant difference between both crystals. Thus, it can be possible that this difference in defect structure can cause the domain configuration (Fig. 1) in our crystal while the optical isotropy in Yokomizo's crystal.

**3.2 Crystallographic domain assignment:** A crystallographic assignment of the domain configuration (Fig. 1) was done using a polarized microscope. R3m crystal can have 8 equivalent domains with polar directions of  $\langle 111 \rangle$ . Fig. 3 shows a projection of indicatrix for 8 domains on (111) plane. Under fixed crossed-nicols,  $\alpha$ ,  $\beta$  and  $\gamma$ -domains with 6 polar directions of  $[111]$ ,  $[1\bar{1}\bar{1}]$ ,  $[\bar{1}1\bar{1}]$ ,  $[1\bar{1}1]$ ,  $[\bar{1}\bar{1}1]$  and  $[11\bar{1}]$  have an extinction position by 90°, and the angle between the extinction position of these domains must be 30° or 60°, while  $\delta$ -domains with 2 polar directions of  $[111]$  and  $[\bar{1}\bar{1}\bar{1}]$  have always an optical isotropic state. Therefore, by rotating crystal under fixed crossed-nicols, we can obtain the crystallographic information about domain configuration<sup>13-14</sup>. Fig. 4 shows the crystallographic assignment performed on a part of the domain configuration in Fig. 1. The relationship between neighbored domains satisfied a crystallographic configuration in R3m ferroelectric crystal. Moreover, it

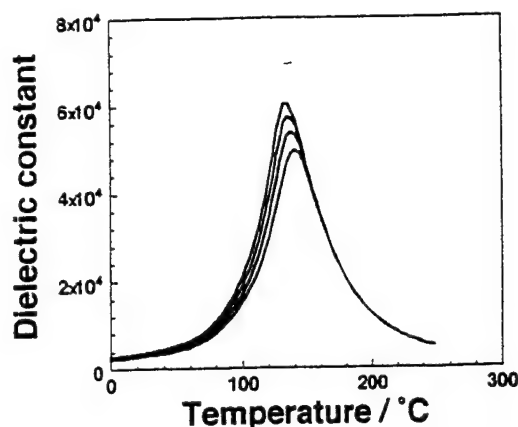


Fig. 2 Temperature dependence of dielectric constant in PZN single crystal oriented along [111].

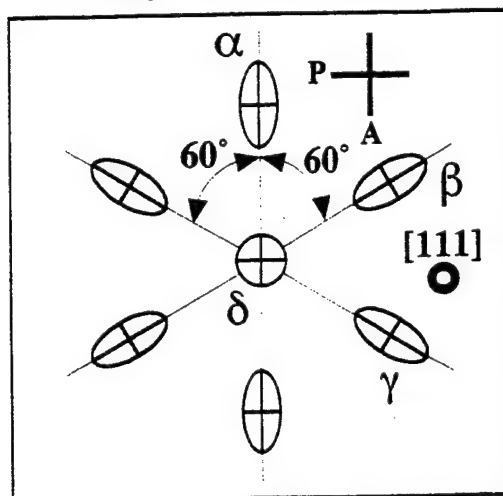


Fig. 3 Projection of indicatrix for 8 domains on (111) plane in R3m crystal.

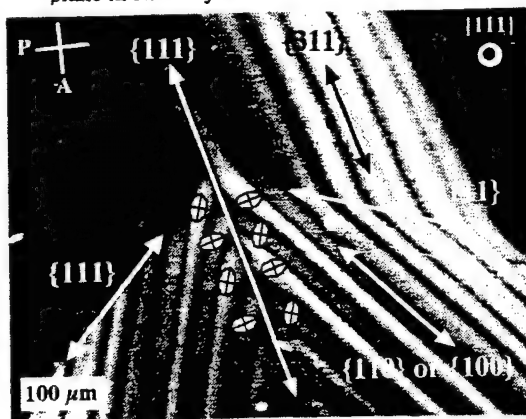


Fig. 4 Crystallographic assignment on a part of the domain configuration shown in Fig. 1.

was confirmed that there are growth twinning structures of  $\{111\}$ , 71° domain walls of  $\{100\}$  or 109° domain walls of  $\{110\}$ . However, there is still remained a significant question about crystallographic assignment, i.e., it is impossible to explain the high Miller indices of planes such as  $\{311\}$  as non-180° domain wall in R3m crystal crystallographically. Moreover, as above

mentioned, there are other questions in Fig. 1 such as (1) very unclear domain wall, (2) partially curved domain wall, (3) very low birefringence and (4) graduation from dark to bright even in one domain. Especially, it is impossible to consider one region with the graduation of birefringence as one ferroelectric domain. Therefore, the above crystallographic assignment revealed that these domains can not be regarded as a normal ferroelectric domain.

### 3.3 Temperature dependence of domain configuration:

The in-situ domain observation was done from  $-100^{\circ}\text{C}$  to  $200^{\circ}\text{C}$ . From  $25^{\circ}\text{C}$  to  $-100^{\circ}\text{C}$ , there is no change of domain configuration while its birefringence increased slightly with decreasing temperature. This slight increase of the birefringence suggests an increase of spontaneous polarization. On the other hand, from  $25^{\circ}\text{C}$  to  $200^{\circ}\text{C}$ , a drastic decrease of the birefringence was observed around  $115^{\circ}\text{C}$  while there is no change of the domain configuration as shown in Fig. 5. Pure PZN has a phase transition around  $140^{\circ}\text{C}$ . Therefore, if the domain configuration is induced on a ferroelectric phase transition from  $R3m$  to  $Pm3m$ , we can expect a disappearance of the domain configuration around  $140^{\circ}\text{C}$ . However, the domain configuration was observed even at  $200^{\circ}\text{C}$ , which means that the domain configuration is not normal ferroelectric domain.

**3.4 Domain configuration before and after poling:** Figs. 6-(a) and (b) show the domain configuration before and after poling. By the poling at  $42\text{kV/cm}$ , a normal ferroelectric domain configuration expected in  $R3m$  crystal was observed as shown in Fig. 6-(b). This detail was described elsewhere<sup>15,16</sup>. The ferroelectric domain configuration induced by poling was quite different from the domain configuration in Fig. 6-(a), and thus poling can break the strange domain configuration. However, when poled PZN crystal was annealed at  $250^{\circ}\text{C}$  for 15h, it was confirmed that the original domain configuration was regenerated completely as shown in Figs. 6-(a) and (c). Moreover, annealing at  $500^{\circ}\text{C}$  resulted in the complete regeneration of the original domain configuration. These facts suggested that the domain configuration in Fig. 6-(a) has some memory effect on its configuration. As one of factors affecting in the memory effect on the domain configuration, the defect structure is well known<sup>17</sup>. In this study, characterization of PZN crystal revealed that there were the defect structure such as the lattice defects, inhomogeneity of chemical compositions and growth twinning structures. Therefore, we must consider the defect structure as an origin of the strange domain.

**3.5 Defect-induced domain configuration:** In general, an inhomogeneously distributed defect structure can be the origin of very weak local stress field. On the other hand, relaxor material must have PMR intrinsically as the origin of relaxation behavior, and PMR is considered as the nm-sized region with flipping or fixed polar vector. Moreover, Cross proposed that PMR in relaxor can be present above  $T_{\text{max}}$ . Therefore, we propose the following model about the strange domain

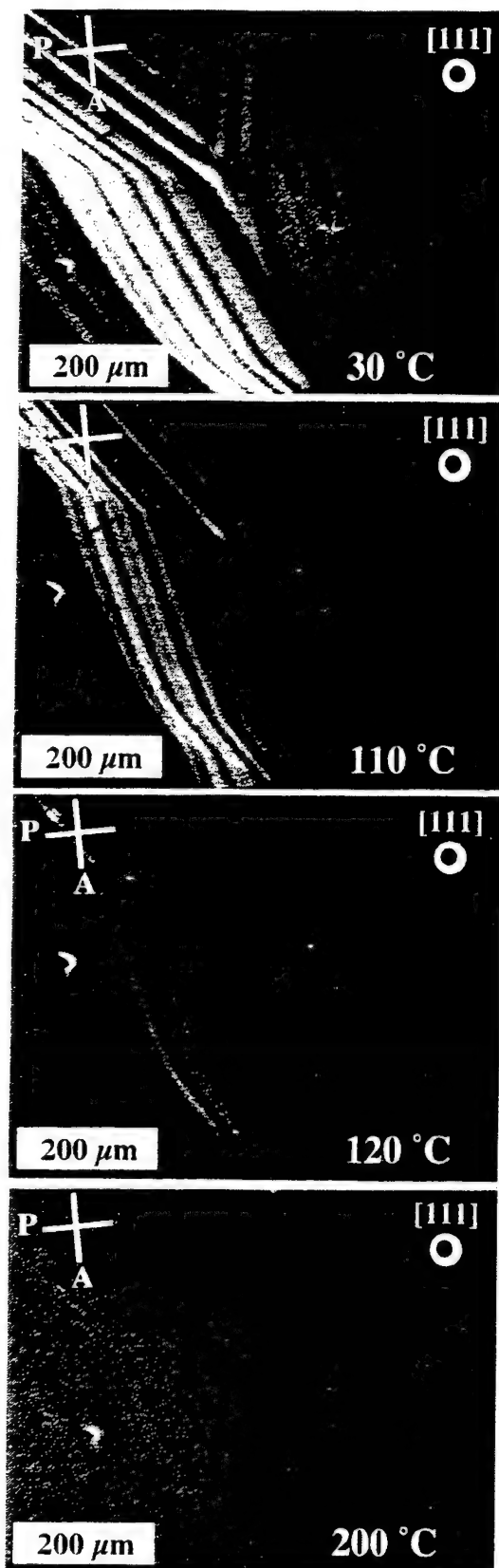


Fig. 5 Temperature dependence of the domain configuration from  $30^{\circ}\text{C}$  to  $200^{\circ}\text{C}$

configuration, i.e., the weak local stress field occurred by the inhomogeneously distributed defect structures

made polar direction of a part of PMR ordering, and thus its ordering region was observed as a domain under crossed-nicols. This model can also explain all of questions about the strange domain configuration. Now, we believe that the strange domain configuration in this study should be a defect-induced domain configuration, and the defect-induced domain configuration can be observed only in relaxor materials. This is because for an formation of the defect-induced domain configuration, the both PMR and inhomogeneously distributed defect structures must be required. Moreover, it should be noted that PMR may be first observed indirectly in this study. Therefore, it is possible that the important information about PMR can be obtained through the study about the defect-induced domain configuration, and now we are doing so.

#### 4. CONCLUSION

Our flux-grown PZN crystal exhibited the strange domain configuration with very small birefringence. The crystallographic assignment revealed that this domain configuration can not be a normal ferroelectric domain. The temperature dependence of this domain configuration indicated that the domain configuration existed even at 200°C. Moreover, the same domain patterns can be always regenerated despite of repeated heat annealing at 250°C. Our PZN crystal also included growth twinning structures, lattice defects, and an inhomogeneity of chemical composition. Therefore, it suggests that very small local stress field caused by these defect structures can make PMR ordering, and thus can make the defect-induced domain configuration. Therefore, it is possible to obtain the information about relaxation mechanism of PZN from the study about the defect-induced domain configuration. Thus, a significant decrease of the birefringence around 115°C suggested that the state of the polar vector changed remarkably.

#### 5. ACKNOWLEDGEMENTS

The authors thank Mrs. Lei and Mr. Liu for great help with PZN crystal growth, and also thank Dr. Newnham, Dr. Fousek, Dr. Cao and Dr. Randall of MRL, PennState university for helpful discussion about domain configuration.

#### References

- <sup>1</sup>V. A. Bokov and I. E. Myl'nikova, *Soviet Phys. Solid State*, **2**, 2428-31 (1961).
- <sup>2</sup>N. P. Khuchua, V. F. Bova and I. E. Myl'nikova, *Soviet Phys. Solid State*, **10**, 194-5 (1968).
- <sup>3</sup>Y. Yokomizo and S. Nomura, *J. Phys. Soc. Jpn.*, **28**, Supplement, 150-2 (1970).
- <sup>4</sup>Y. Yokomizo, T. Takahashi and S. Nomura, *J. Phys. Soc. Jpn.*, **28**, 1278-84 (1970).
- <sup>5</sup>S. Nomura, M. Endo and F. Kojima, *Jpn. J. Appl. Phys.*, **13**, 2004-8 (1974).
- <sup>6</sup>L. E. Cross, *Ferroelectrics*, **76**, 241-67 (1987).
- <sup>7</sup>D. Viehland, S. J. Jang and L. E. Cross, *J. Appl. Phys.*, **68**, 2916-21 (1990).
- <sup>8</sup>W. Kleemann, *Int. J. Mod. Phys. B*, **7**, 2469-507 (1993).
- <sup>9</sup>A. E. Glazounov and A. K. Tagantsev, *Ferroelectrics*, (1998) in press.
- <sup>10</sup>M. A. Akbas and P. K. Davies, *J. Am. Ceram. Soc.*, **80**, 2933-6 (1997).
- <sup>11</sup>P. K. Davies and M. A. Akbas, *Ferroelectrics*, (1998) in press.

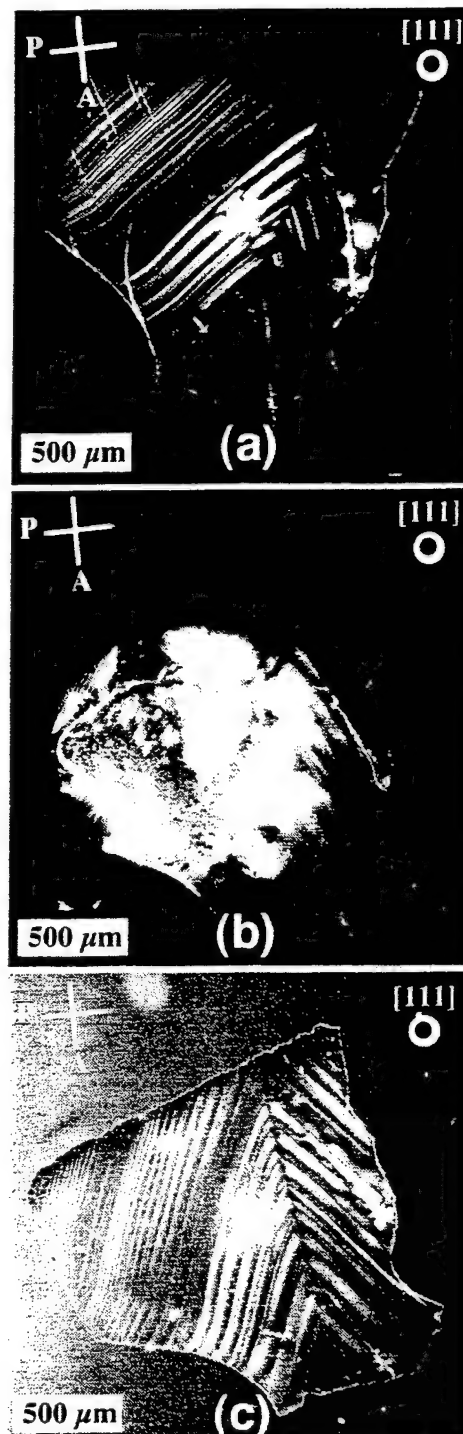


Fig. 6 Domain configuration at 25°C before poling (a), after poling at 42kV/cm (b) and after heat annealing at 250°C for 15h (c).

- <sup>12</sup>S.-E. Park, M. L. Mulvihill, G. Risch and T. R. Shrout, *Jpn. J. Appl. Phys.*, **36**, 1154-8 (1997).
- <sup>13</sup>J. Fousek, *Czech. J. Phys.*, **B21**, 955-68 (1971).
- <sup>14</sup>E. I. Eknadiousiants, V. Z. Borodin, V. G. Smotrakov, V. V. Eremkin and A.N. Pinskaya, *Ferroelectrics*, **111**, 283-9 (1990).
- <sup>15</sup>S. Wada, S.-E. Park, L. E. Cross and T. R. Shrout, *J. Korean Phys. Soc.*, **32**, S1290-3 (1998).
- <sup>16</sup>S. Wada, S.-E. Park, L. E. Cross and T. R. Shrout, *Ferroelectrics*, (1998) in press.
- <sup>17</sup>W. Cao, *Phase Trans.*, **55**, 69-78 (1995).

# **APPENDIX 28**

Switching Current In  $\text{Pb}(\text{Zn}_{1/3}\text{Nb}_{2/3})\text{O}_3$  -  $\text{PbTiO}_3$  Single Crystals  
Uma Belegundu, Xiaohong Du and Kenji Uchino  
International Center for Actuators Transducers  
Materials Research Laboratory, Pennsylvania State University  
University Park PA 16803, USA

*Abstract: Switching current measurements have been carried out on relaxor ferroelectric single crystal - pure PZN, and the solid solution  $(1-x)\text{Pb}(\text{Zn}_{1/3}\text{Nb}_{2/3})\text{O}_3 - x\text{PbTiO}_3$  with  $x = 0.04, 0.09, 0.10$ . Measurements have been done for crystallographic directions  $[001]$  and  $[111]$  for all these compositions. Switching times versus the applied field showed the following results. Pure PZN along  $[111]$  and  $0.90\text{PZN} - 0.10\text{PT}$  along  $[001]$ , and  $[111]$  showed an exponential dependence. Along  $[001]$  the PZN showed a linear fit. For solid solution single crystals -  $0.96\text{PZN} - 0.04\text{PT}$  and  $0.91\text{PZN} - 0.09\text{PT}$ , a linear fit was obtained for the reciprocal switch times versus applied field for both the directions. If we draw a parallel picture with the reported barium titanate data, it appears that the polarization reversal is controlled by nucleation along  $[111]$  - spontaneous direction for PZN and  $[001]$ ,  $[111]$  for  $0.90\text{PZN} - 0.10\text{PT}$ . The mobility of the reversed domains controls the reversal along  $[001]$  for PZN and the solid solution single crystals with rhombohedral composition along  $[001]$  and  $[111]$ . The transient current curves showed two maximum points for crystals with  $x = 0.04$  and  $0.09$ . This is attributed to the co-existence of the two phases in  $0.96\text{PZN} - 0.04\text{PT}$  and  $0.91\text{PZN} - 0.09\text{PT}$  crystals.*

## INTRODUCTION

Measurement of switching current to study the polarization reversal phenomena<sup>1</sup> is well known. In this method, a series of symmetric bipolar voltage pulse which produces polarization reversal is applied to the crystal and the transient current measured across a resistor connected in series with the sample. Information on polarization reversal processes was obtained by switching current measurements for  $\text{BaTiO}_3$  (BT)<sup>2,3</sup>. These measurements for BT showed that the total polarization reversal time depends on the applied field.

Such transient current studies have not been carried out on relaxor ferroelectric single crystals such as  $\text{Pb}(\text{Zn}_{1/3}\text{Nb}_{2/3})\text{O}_3$  (PZN) and their solid solutions with  $\text{PbTiO}_3$  (PT). In this paper, the experimental results of switching current measurements for PZN, PZN - PT single crystals and their dependence on crystal orientation are presented. Their switching behavior is examined in terms of the presently accepted model of domain nucleation and growth.

Single crystals of  $0.91\text{PZN} - 0.09\text{PT}$  are known to show very high values of electromechanical coupling factor  $k_{33}$  of 92-95 % and piezoelectric constant  $d_{33}$  of  $2500 \text{ pC/N}^{4,5}$ . In this system, PZN having rhombohedral symmetry is a relaxor ferroelectric material which undergoes a diffuse phase (frequency dependent) transition around  $140^\circ\text{C}$ . On the other hand lead titanate PT having a tetragonal symmetry is a normal ferroelectric with a sharp phase transition at  $490^\circ\text{C}$ . These two composition form a solid solution system with a morphotropic phase boundary (MPB) around  $0.91\text{PZN} - 0.09\text{PT}$ . It has to be mentioned that the giant values of  $k_{33}$  and  $d_{33}$  are obtained for crystals with rhombohedral composition with spontaneous polarization along  $[111]$  is poled along  $[001]$ . This direction is the spontaneous polarization direction for tetragonal crystals.

## EXPERIMENTAL DETAILS

All the single crystals PZN and  $(1-x)\text{PZN} - x\text{PT}$  used for the measurements were grown the lab by the flux method. The crystal direction  $[001]$  and  $[111]$  were determined by Laue back reflection method. The crystals were then cut and polished to form rectangular plates with the desired orientation perpendicular to major faces. The thickness of all the samples varied from  $0.20 \text{ mm} - 0.23 \text{ mm}$  and the area was around  $4\text{mm} \times 1.3\text{mm}$ . Sputtered gold was used as electrodes. A function synthesizer (DF -194 digital function synthesizer) in conjunction with an amplifier was used to apply rectangular pulses of one second duration to the sample. A resistor of  $150 \text{ ohms}$  was used in series with the sample and voltage across it was measured using oscilloscope for determining the switching current. A representative switching current obtained when a positive pulse is applied to the sample is shown in Fig. 1. The normal displacement



current transient obtained when the second positive pulse is applied is also shown in the same figure. This displacement current is subtracted to obtain the actual switching current. The fields applied ranged from 3-36 kV/cm. The switching time is defined here as the time taken for the current to reduce from maximum to 1/10 of the maximum. The field was applied along [001] and [111] crystallographic directions. All these crystals have rhombohedral compositions. The spontaneous polarization for rhombohedral composition is along [111] and that for tetragonal is along [001] respectively.

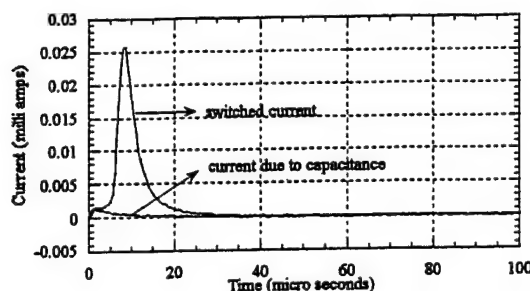


Fig.1 A representative switching and the corresponding displacement current. The two are subtracted to get the actual switching current.

## RESULTS

Figure 2 shows the transient current associated with switching for PZN, 0.96PZN -0.04PT and 0.91PZN - 0.09PT single crystals. We will name them crystals A, B and C for discussion purposes. It has to be mentioned that the time scale for all the curves are not same, they vary from 2.5 millisecond (for low field) to 100 microsecond for high applied electric field. Hence no unit has been mentioned in the figure. These curves are overlapped only for comparison. However, each curve is considered separately for calculation of the switching time. Looking at this data for spontaneous polarization direction [111], the crystals B and C showed a double maximum in the switching current curve. For crystals B, having 0.04 PT at low field values (5 - 9 kV/cm) the first peak was much higher in magnitude than the second peak. As the field is increased, the second peak increases in magnitude and finally only one peak is observed. For crystals C having 0.09PT, similar variation of second peak overtaking the magnitude of the first peak was observed. However, two distinct peaks were present even at high fields. Such a behavior was not observed for pure PZN crystal with field along [111] direction. For field applied along [001] -the spontaneous polarization direction for tetragonal crystals, no such double maximum in the switching curve was observed for pure PZN (crystal A) and crystal B. The crystal C showed a double maximum at low field values. The curve corresponding to 26kV/cm for 0.91PZN - 0.09PT with field along [001] shows the field induced phase transition from rhombohedral to tetragonal.

This leads us to believe that the presence of two peaks is due to the co-existence of both rhombohedral and tetragonal phases in these crystals. It is difficult to associate a particular peak with either rhombohedral or tetragonal composition. The two parameters -the component of electric field along a crystallographic direction and the volume fraction of the second phase present may also need to be considered in explaining the presence of the double peaks. More detailed work is continuing and will be reported shortly.

The reciprocal switching time as a function of applied field is shown in Fig. 3. For pure PZN (crystal A), linear dependence was observed along [001] and exponential dependence along [111] direction. The figure shows a linear variation with different slopes at low and high field values for the crystals B, C and both the directions [111] and [001]. It appears that a linear law can describe the switching process

$$\frac{1}{t} = \frac{\mu}{d} E \quad (1)$$

where  $t$  is the switching time,  $d$  the thickness of the crystal,  $\mu$  is the mobility of the moving domain wall,  $E$  is the applied field. However, there is a change in the slope at a certain applied field for all the crystals. At higher fields, the curve becomes almost horizontal to field axis.

## DISCUSSION

From the published data<sup>2,3,6,7</sup> for  $\text{BaTiO}_3$  (BT), the switching current shows an exponential dependence on applied field at small field values. The dependence becomes linear as the applied field is increased. On the basis of these results, it was suggested that the polarization reversal for BT at small-applied fields is controlled by nucleation rate of the reversed domains. At higher field, the mobility of the reversed domains controls the reversal mechanism.

We now compare this with the present data for relaxor based single crystals of PZN, 0.96PZN - 0.04PT and 0.91PZN - 0.09PT. The field was applied along [001] and [111] - the spontaneous direction for rhombohedral and tetragonal compositions.

For PZN along [111] the dependence of switching time on applied field was exponential. Along [001], the dependence was linear. If we draw a parallel picture with the barium titanate data, it appears that the polarization reversal is controlled by nucleation along [111] and the mobility of the reversed domains along [001].

For solid solution single crystals 0.96PZN - 0.04PT and 0.91PZN - 0.09PT, a piecewise linear fit was obtained for the reciprocal switch times versus applied field. Unlike the barium titanate, no exponential dependence was observed at small field values. Assuming the model of domain nucleation and motion, it appears that the polarization reversal in these crystals is controlled by the forward motion of the domains.

A double maximum observed in the switched current is attributed to the co-existence of the two phases in 0.96PZN - 0.04PT and 0.91PZN - 0.09PT crystals. This was not observed in PZN crystal.

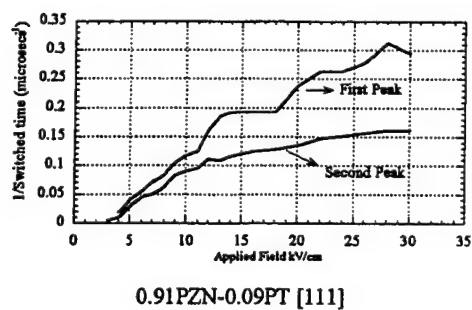
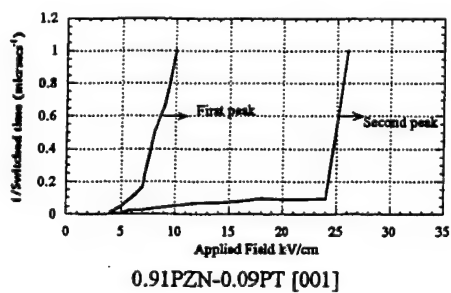
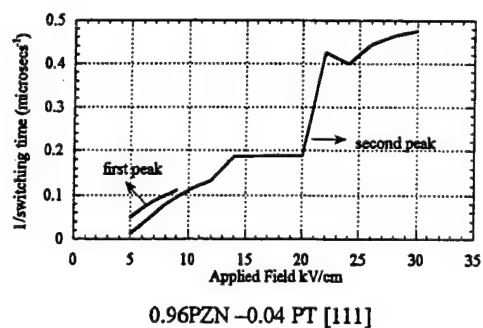
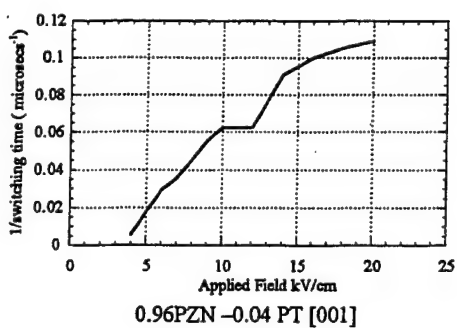
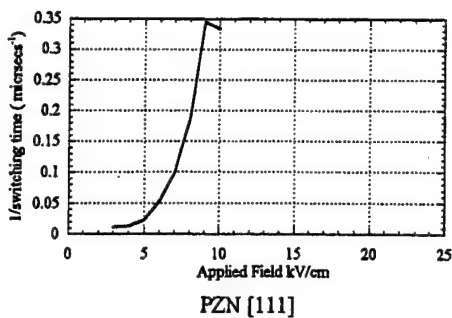
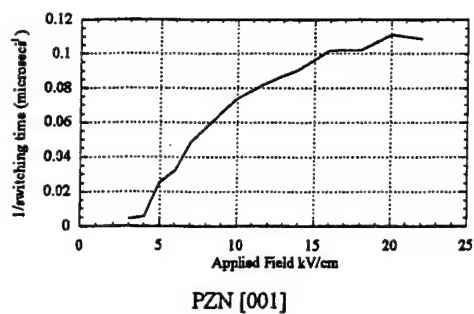
## ACKNOWLEDGEMENT

This work is supported by Office of Naval Research through contract # N00014-91-J-4145

## REFERENCES

- 1) F. Jona and G. Shirane, "Ferroelectric Crystals" Dover Publications Inc. p172 (1993)
- 2) W. J. Merz, Phys. Rev., v 95, p690 (1954)
- 3) R. C. Miller and A. Savage, Phys. Rev., v 112, p755 (1958)
- 4) J. Kuwata, K. Uchino and S. Nomura, Ferroelectrics, v 37, p579 (1981)
- 5) S. E. Park and T. R. Shrout, J. Mater. Res. Innovations vol.1, p20 (1997)
- 6) W. J. Merz, J. Appl. Phys. v 27, p938 (1956)
- 7) H. L. Stadler, J. Appl. Phys. v29, p1485 (1958)





# **APPENDIX 29**

# Crystallographically engineered BaTiO<sub>3</sub> single crystals for high-performance piezoelectrics

Seung-Eek Park,<sup>a)</sup> Satoshi Wada,<sup>b)</sup> L. E. Cross, and Thomas R. Shrout  
*Materials Research Laboratory, The Pennsylvania State University, University Park, Pennsylvania 16802*

(Received 11 March 1999; accepted for publication 27 May 1999)

Dielectric and piezoelectric properties of BaTiO<sub>3</sub> single crystals polarized along the  $\langle 001 \rangle$  crystallographic axes were investigated as a function of temperature and dc bias. Electromechanical coupling ( $k_{33}$ )  $\sim 85\%$  and piezoelectric coefficients ( $d_{33}$ )  $\sim 500$  pC/N, better or comparable to those of lead-based Pb(Zr, Ti)O<sub>3</sub> (PZT), were found from  $\langle 001 \rangle$ -oriented orthorhombic crystals at 0 °C, as a result of crystallographic engineering. A rhombohedral BaTiO<sub>3</sub> crystal polarized along  $\langle 001 \rangle$  also exhibited enhanced piezoelectric performance, i.e.,  $k_{33} \sim 79\%$  and  $d_{33} \sim 400$  pC/N at  $-90$  °C, superior to PZTs at the same temperature. It was found that the crystal structure determined the (in)stability of the engineered domain state in BaTiO<sub>3</sub> single crystals. Rhombohedral (3m) crystals at  $-100$  °C exhibited a stable domain configuration, whereas depoling occurred in crystals in the adjacent orthorhombic phase upon removal of the  $E$  field. © 1999 American Institute of Physics. [S0021-8979(99)04517-X]

## I. INTRODUCTION

Recent innovations in regard to relaxor-based single-crystal piezoelectrics such as Pb(Zn<sub>1/3</sub>Nb<sub>2/3</sub>)O<sub>3</sub>, Pb(Mg<sub>1/3</sub>Nb<sub>2/3</sub>)O<sub>3</sub>, and their solid solution with PbTiO<sub>3</sub> are based on crystallographic engineering associated with an engineered domain state and crystal anisotropy, which is not achievable in polycrystalline ceramics. Longitudinal coupling coefficients ( $k_{33}$ ) as high as 94%, piezoelectric coefficients ( $d_{33}$ )  $> 2500$  pC/N with strain levels exceeding 1.7% (Refs. 1–3) were recognized by electrically polarizing relaxor-based rhombohedral single crystals along their nonpolar pseudocubic  $\langle 001 \rangle$  direction. In contrast, rhombohedral crystals poled along their polar direction  $\langle 111 \rangle$  exhibited significantly inferior properties, i.e.,  $k_{33} < 50\%$  and  $d_{33} \sim 100$  pC/N.<sup>2,4</sup>

In addition to ultrahigh piezoelectric performance, strain versus  $E$ -field behavior with minimal hysteresis, and low dielectric loss ( $< 1\%$ ), was another important characteristic of the crystallographically engineered relaxor-based single crystals.<sup>2</sup> a consequence of four equally populated rhombohedral types of domains.<sup>5</sup> Although in a multidomain state, the stable domain configuration resulted in materials with enhanced reliability, i.e., no degradation detected after more than  $10^7$  cycles of unipolar driving at high fields ( $> 50$  kV/cm, 1 kHz).<sup>6</sup> From a crystallographic point of view, it was suggested<sup>5,7,8</sup> that the macroscopic symmetry of rhombohedral relaxor ferroelectric crystals poled, or dc biased along  $\langle 001 \rangle$ , should be 4 mm, describing the macrosymmetry of an entire single crystal composed of a stable engineered domain configuration.

Based on the concept of crystallographic engineering used in relaxor ferroelectric single crystals, single crystals or

epitaxial forms of any known ferroelectric materials should exhibit significant enhancement in electromechanical performance at temperature or composition close to an appropriate phase transition. It was the objective of this work, therefore, to apply the concept of crystallographic engineering to normal ferroelectric crystals such as BaTiO<sub>3</sub>, and to evaluate the possibility of enhanced piezoelectric performance. Low-temperature phases of BaTiO<sub>3</sub> single crystals, such as orthorhombic and rhombohedral, were poled along  $\langle 001 \rangle$  to induce an engineered domain state. The obtained piezoelectric properties were compared with values predicted by axis transformation for single-domain BaTiO<sub>3</sub> crystals using the Devonshire theory.<sup>9</sup>

## II. EXPERIMENTAL PROCEDURE

Samples for measuring dielectric and piezoelectric properties were prepared using commercially available BaTiO<sub>3</sub> single crystals (optical grade, Fujikura Ltd.) grown by the top-seeded solution growth (TSSG) technique. According to company brochures and the related report,<sup>10</sup> concentration of impurities such as Cr, Mn, Co, Ni, Fe, and Cu was less than 3 ppm. Individual crystals were oriented along their pseudocubic  $\langle 001 \rangle$  axis using a Laue back-reflection camera.

For electrical characterization, samples were prepared by polishing with silicon carbide and alumina polishing powders to achieve flat and parallel surfaces. Gold electrodes were sputtered on both sides of the samples. Prior to electrical characterization, all samples were heat treated at 250 °C for 14 h to eliminate residual stresses induced during sample preparation. For low-field measurements using the IEEE resonance technique,<sup>11</sup> samples were poled either by field cooling (10 kV/cm) from 150 °C or by applying 40 kV/cm at room temperature.

Low-temperature properties under dc bias were measured using an HP4194 impedance analyzer in conjunction with a computer-controlled temperature chamber (Delta De-

<sup>a)</sup>Electronic mail: sxp37@psu.edu

<sup>b)</sup>Current Address: Department of Applied Chemistry, Tokyo University of Agriculture and Technology, 24-16, Nakamachi 2-chome, Koganei, Tokyo 184-8588, Japan.

TABLE I. Phase transitions of BaTiO<sub>3</sub> crystal as a function of temperature.

Temperature range	>130 °C	120 to 0 °C	0 to -90 °C	<-90 °C
Primitive cell symmetry	Cubic	Tetragonal	Pseudomonoclinic (orthorhombic <sup>a</sup> )	Rhombohedral
Point group	m3m	4mm	mm2	3m
Macrosymmetry <sup>b</sup>	...	4mm	4mm	4mm

<sup>a</sup>Unit-cell symmetry.<sup>b</sup>Under dc bias along (001).

sign Inc., model MK 2300) and a dc bias blocking circuit with a maximum capacity of 1000 V. For longitudinal piezoelectric coefficient ( $d_{33}$ ) determination, bar-shape samples of  $0.4 \times 0.4 \times 1.6$  mm in length were prepared. High-field measurements included polarization and strain hysteresis using a modified Sawyer-Tower circuit and a linear variable differential transducer (LVDT) driven by a lock-in amplifier (Stanford Research Systems, model SR830). Plate-shape samples with thickness ranging from 0.2 to 0.5 mm were used. Electric fields as high as  $\sim 140$  kV/cm were applied using an amplified unipolar wave form at 0.1 Hz, from a Trek 609C-6 high-voltage dc amplifier. During testing the samples were submerged in Fluorinert (FC-40, 3M, St. Paul, MN), an insulating liquid, to prevent arcing.

### III. RESULTS AND DISCUSSION

Table I summarizes the phase transitions of BaTiO<sub>3</sub>. As considered in the phenomenological theory by Devonshire,<sup>12</sup> the unit-cell symmetry dictates the direction of the polar shift, i.e., orthogonal (4mm), face diagonal (mm2), and body diagonal (3m), based on the primitive perovskite cell. When an  $E$  field is applied along an orthogonal direction at various temperatures, a single-domain state may be achieved only for tetragonal crystals. In contrast, in orthorhombic as well as in rhombohedral crystals, four polarization directions ( $\langle 101 \rangle$ ,  $\langle 011 \rangle$ ,  $\langle -101 \rangle$ ,  $\langle 0-11 \rangle$  and  $\langle 111 \rangle$ ,  $\langle -111 \rangle$ ,  $\langle 1-11 \rangle$ ,  $\langle -1-11 \rangle$ , respectively) are energetically equivalent and four types of domains will be equally populated under the  $\langle 001 \rangle$   $E$  field. Using analogy with rhombohedral relaxor ferroelectric single crystals,<sup>5,7</sup> we propose that this configuration should result in a macroscopic symmetry 4mm, as shown in Table I. It is interesting to note that the crystal macrosymmetry retains 4mm regardless of lattice symmetry changes, under the  $\langle 001 \rangle$   $E$  field. The macroscopic symmetry of crystals at zero  $E$  field that were exposed to the  $\langle 001 \rangle$   $E$  field was determined by the stability of the engineered domain configuration. A certain magnitude of the  $\langle 001 \rangle$   $E$  field will ultimately induce the phase transition into a single-domain tetragonal phase. Details on the  $E$ -field-induced phase transition can be found elsewhere.<sup>8,13</sup> Details on domain (in)stability will be discussed in the following sections.

Figure 1 presents longitudinal electromechanical coupling coefficients ( $k_{33}$ ) as a function of temperature for the  $\langle 001 \rangle$ -poled BaTiO<sub>3</sub> crystal under dc bias. At room temperature, the value of  $k_{33}$  increased from  $\sim 0.53$  (0 kV/cm) to 0.65 (6 kV/cm) as a result of the domain reorientation in the crystal, which had been partially depoled due to domain in-

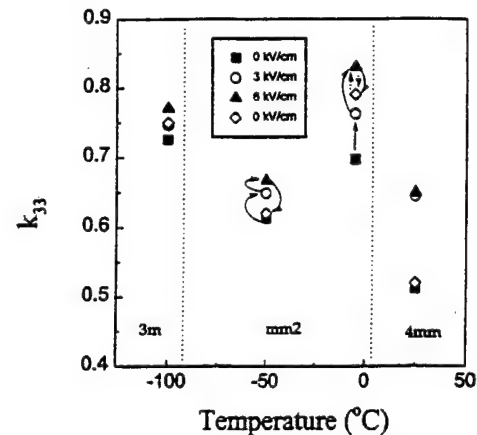


FIG. 1.  $k_{33}$  as a function of temperature for the  $\langle 001 \rangle$ -poled BaTiO<sub>3</sub> crystal under various dc bias. (solid arrows: first cycle, dashed arrows: second cycle).

stability. Regardless of the magnitude of the dc bias, the initial partially depoled state reappeared upon removal of the  $E$  field. It is important to note that  $k_{33} \sim 0.53$  (0 kV/cm), a value from the partially depoled crystals in this work, corresponds to values reported earlier, i.e.,  $\sim 0.56$  (Ref. 14) and  $\sim 0.55$  (Ref. 15) for tetragonal BaTiO<sub>3</sub> crystals, suggesting that they were not those of single-domain crystals.

At lower temperatures,  $k_{33}$  was also found to be dependent on the dc bias due to crystal depoling as a result of phase transitions as well as domain instability. Figure 2 shows  $k_{33}$  as a function of the  $E$  field for orthorhombic crystals ( $-5$  °C).  $k_{33} \sim 0.7$  initially detected at 0 kV/cm increased with increasing bias, to a value of  $k_{33}$  as high as 0.83 at 6 kV/cm. After  $E$ -field exposure, the unbiased  $k_{33}$  value was as high as 0.79, being a starting point for the second cycle (dashed arrows in Fig. 1). The initial lower value for the first cycle (solid arrows in Fig. 1) must be a consequence of partial depoling caused by the tetragonal-orthorhombic phase transition. It is noted that when the  $E$  field was constant at 6 kV/cm, the  $k_{33}$  value increased from 0.79 to 0.83, indicating that higher  $k_{33}$ 's may be obtained under larger dc bias. Similar behavior was observed for rhombohedral crystals at  $-100$  °C, with maximum  $k_{33}$  as high as 0.78 at 6 kV/cm.

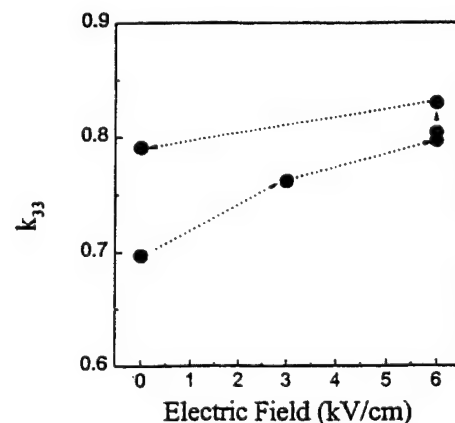


FIG. 2.  $k_{33}$  as a function of dc-bias (first cycle) for the  $\langle 001 \rangle$ -oriented BaTiO<sub>3</sub> crystal at  $-5$  °C.

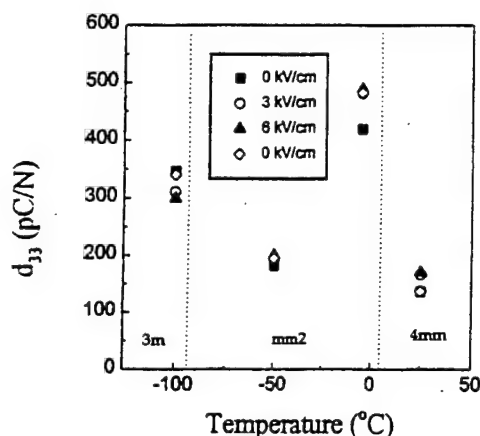


FIG. 3.  $d_{33}$  as a function of temperature for the (001)-poled BaTiO<sub>3</sub> crystal under various dc bias, measured using the IEEE standard method.

Note that these  $k_{33}$  values of BaTiO<sub>3</sub> crystals are larger than room-temperature  $k_{33}$  values of Pb-based polycrystalline Pb(Zr,Ti)O<sub>3</sub> (PZTs) (0.5–0.75), the current piezoelectric material of choice.

Piezoelectric coefficients ( $d_{33}$ ) versus dc bias at various temperatures are shown in Fig. 3. For the (001)-poled BaTiO<sub>3</sub> crystals, change in  $d_{33}$  as a function of the (001)  $E$  field was not as significant as in the case of  $k_{33}$ , as evident from the equation,

$$d_{33} = k_{33} \sqrt{(\epsilon_{33}^T s_{33}^E)}, \quad (1)$$

with  $\epsilon_{33}^T$  (free-dielectric permittivity) quickly decreasing with increased  $E$  field while  $k_{33}$  increased and  $s_{33}^E$  (elastic compliance) remained almost constant as demonstrated in Fig. 4. It is noted that the  $d_{33}$  value of  $\sim 490$  pC/N, which was measured at  $-5^\circ\text{C}$  is comparable to the room-temperature  $d_{33}$  values of the PZTs. Rhombohedral BaTiO<sub>3</sub> crystals at  $-100^\circ\text{C}$  exhibited  $d_{33}$ 's as high as 350 pC/N, also larger than that of polycrystalline PZTs at the same temperature.<sup>16</sup>

In regard to domain instability in single crystals,  $d_{33}$  was also determined directly from strain versus  $E$ -field curves. Figure 5 presents strain versus unipolar  $E$ -field behavior for the (001)-poled BaTiO<sub>3</sub> crystals at various temperatures.

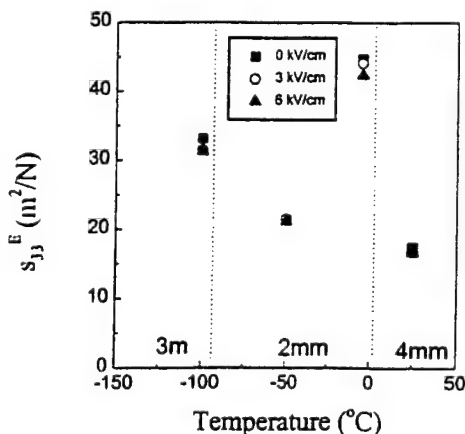


FIG. 4.  $s_{33}^E$  as a function of temperature for the (001)-poled BaTiO<sub>3</sub> crystals under various dc bias.

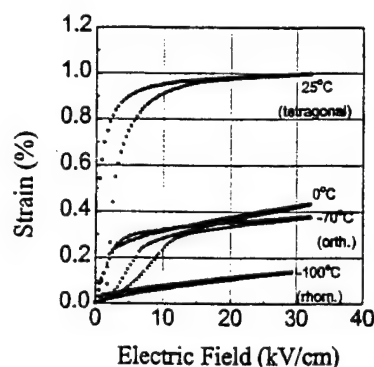


FIG. 5. Strain vs  $E$ -field behavior (unipolar) for the (001)-oriented BaTiO<sub>3</sub> crystal.

Room-temperature strain values (unipolar) as high as 1% were quite surprising, considering that a total 1.07% strain is involved with the full spontaneous ferroelectric strain ( $c/a-1$ ) of BaTiO<sub>3</sub> crystals at room temperature. This ultra-high unipolar strain behavior, although unusable for practical actuation, indicates that crystal depoling involved almost full  $90^\circ$  domain switching rather than  $180^\circ$  switching upon the removal of the  $E$  field. Although still not completely clear, it is suspected that the very small amount of compressive force under the probe of the LVDT (see the experimental procedure) might cause this depoling behavior. The single-domain state of the tetragonal crystals, reflected by nonhysteretic strain versus  $E$ -field behavior, could be achieved at  $E$  fields  $> \sim 10$  kV/cm at room temperature as shown in Fig. 5, with  $d_{33} \sim 128$  pC/N values determined at 20 kV/cm.

The hysteresis ( $E < 10$  kV/cm) found in the orthorhombic crystal (0 and  $-70^\circ\text{C}$  in Fig. 5) was also ascribed to domain instability. In contrast, the engineered domain state of rhombohedral crystals ( $-100^\circ\text{C}$ ) was found to be stable, as can be seen in Fig. 5, retaining macrosymmetry 4mm over the full range (unipolar) of the  $E$  field. Note that relaxor-based single crystals with a stable engineered domain state were also rhombohedral. Although further study is required to clarify the relationship between the crystal structure and the engineered domain state, it is suggested that lattice symmetry determines the (in)stability of the domain configuration. Rhombic lattice distortion might be critical to stabilize the engineered domain state in (001)-poled ferroelectric crystals. However, depoling affected by the weak uniaxial stress described above may also be noted. Only in the (001)-poled rhombohedral crystals is the domain configuration unaffected by uniaxial stress along (001).

Nonhysteretic regions of the strain versus  $E$ -field ( $E > 10$  kV/cm) curves are presented in Fig. 6. Apparent  $d_{33}$ 's calculated from such nonhysteretic regions of the strain versus  $E$ -field curves are plotted in Fig. 7. The  $d_{33}$  values in Fig. 7 confirm those (Fig. 3) obtained from the IEEE standard technique under bias (6 kV/cm).

According to Devonshire,<sup>9</sup>  $d_{33}$  values of single-domain BaTiO<sub>3</sub> crystals under weak field or stress can be calculated using the following equations:

$$d_{33} = 2\epsilon_0 Q_{11} \eta_{33} P_3,$$

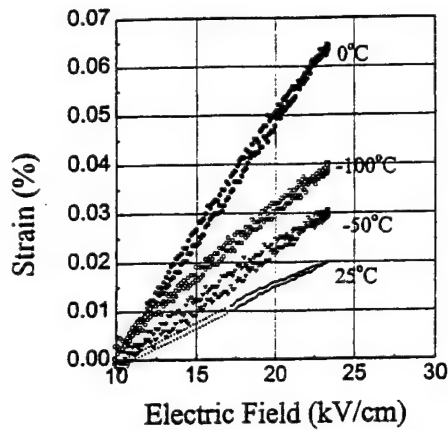


FIG. 6. Nonhysteretic portion of strain vs  $E$ -field curves (unipolar) for the  $\langle 001 \rangle$ -oriented BaTiO<sub>3</sub> crystal.

where  $P_3 = P_s$  (spontaneous polarization),  
for tetragonal crystals, (2)

$$d_{33} = 2\epsilon_0(Q_{11}\eta_{33} + Q_{12}\eta_{23})P_3,$$

where  $P_3 = P_s/\sqrt{2}$ , for orthorhombic crystals. (3)

$$d_{33} = 2\epsilon_0(Q_{11}\eta_{11} + 2Q_{12}\eta_{12})P_3,$$

where  $P_3 = P_s/\sqrt{3}$ , for rhombohedral crystals. (4)

where  $\epsilon_0$  is the permittivity of free space,  $Q_{ij}$  the electrostrictive coefficients, and  $\eta_{ij}$  the dielectric susceptibility. For crystallographically engineered orthorhombic and rhombohedral crystals with engineered multidomain states, however, the lattice symmetry is expected to change under higher  $\langle 001 \rangle$   $E$  field. For instance, orthorhombic and rhombohedral lattices strained by the  $\langle 001 \rangle$   $E$  field lack two-fold and three-fold symmetry, respectively. Microscopically, this results in pseudomonoclinic symmetry with  $P_1^2 \neq P_2^2$ , and  $P_1^2 = P_2^2 \neq P_3^2$  for orthorhombic and rhombohedral crystals, respectively. For the engineered domain state under the  $\langle 001 \rangle$   $E$  field, therefore, Eqs. (3) and (4) are rewritten as

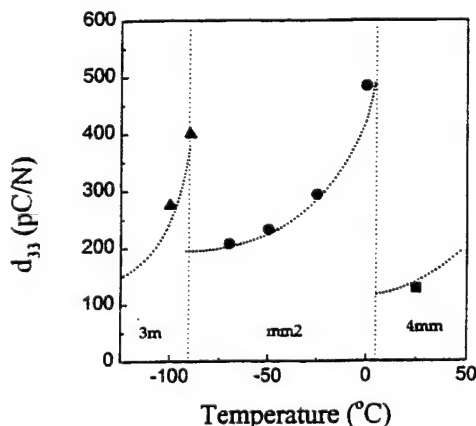


FIG. 7.  $d_{33}$  of the  $\langle 001 \rangle$ -oriented BaTiO<sub>3</sub> crystal, calculated from the slope of strain vs  $E$ -field curves in Fig. 6 (dashed lines: calculated values for single-domain BaTiO<sub>3</sub> crystals).

$$d_{33} = 2\epsilon_0(Q_{11}\eta_{33}P_3 + Q_{12}\eta_{23}P_1),$$

for orthorhombic crystals, (5)

$$d_{33} = 2\epsilon_0(Q_{11}\eta_{11}P_3 + 2Q_{12}\eta_{12}P_1),$$

for rhombohedral crystals. (6)

Although crystallographically engineered BaTiO<sub>3</sub> crystals consist of an engineered multidomain state,  $d_{33}$  based on Eqs. (5) and (6) could not be calculated due to the lack of experimental data. The authors' efforts to obtain experimental data for the engineered domain state are ongoing. In this work instead, the  $d_{33}$  values calculated for single-domain BaTiO<sub>3</sub> crystals under weak field are plotted on Fig. 7 (dashed line). The measured  $d_{33}$  values [see specifically the orthorhombic (mm2) range] fit well to the theoretical values for single-domain crystals derived in this way, suggesting that  $P_3/P_1$  is not large at the field levels used in this work, and/or may be compensated by changes in  $\eta_{ij}$ . Although further research is required, it may be suggested that intrinsic effects are the major contribution to large piezoelectric coefficients and subsequent shape changes of BaTiO<sub>3</sub> crystals, on the basis of the curve fit in Fig. 7.

#### IV. CONCLUSION

BaTiO<sub>3</sub> single crystals are promising candidates for high-performance nonlead piezoelectrics at low temperatures. Crystallographic engineering, by polarizing crystals under dc bias toward the nonpolar  $\langle 001 \rangle$  direction, resulted in orthorhombic and rhombohedral crystals with macroscopic symmetry 4mm. Piezoelectric properties with an electromechanical coupling coefficient ( $k_{33}$ )  $\sim 85\%$  and piezoelectric coefficient ( $d_{33}$ )  $\sim 500$  pC/N, better or comparable to those of PZTs were obtained from orthorhombic crystals at 0 °C. At  $-90$  °C, rhombohedral BaTiO<sub>3</sub> crystals with  $k_{33} \sim 79\%$  and  $d_{33} \sim 400$  pC/N were found to be superior to PZTs at the same temperature. The stability of the engineered domain state in BaTiO<sub>3</sub> crystals was dependent upon the crystal structure. Although possessing the same macroscopic symmetry 4mm, rhombohedral (3m) crystals ( $-100$  °C) exhibited a stable domain configuration whereas the adjacent orthorhombic state ( $-70$  °C) was depoled. A possible role of weak uniaxial stress in the depoling must be further examined. The intrinsic piezoelectric response could explain most of the measured values.

Orthorhombic or rhombohedral BaTiO<sub>3</sub>, stabilized by proper dopants such as zirconium, are expected to be a high-performance nonlead piezoelectric in single-crystal or epitaxial form at room temperature.

#### ACKNOWLEDGMENTS

This work has been supported by DARPA and the Office of Naval Research. The authors would like to thank Hua Lei for her help with sample preparation.

<sup>1</sup>J. Kuwata, K. Uchino, and S. Nomura, Jpn. J. Appl. Phys., Part I 21, 1298 (1982).

<sup>2</sup>S.-E. Park and T. R. Shrout, IEEE Trans. Ultrason. Ferroelectr. Freq. Control 44, 1140 (1997).

- <sup>3</sup>S.-E. Park and T. R. Shrout, *J. Appl. Phys.* **82**, 1804 (1997).
- <sup>4</sup>S.-E. Park, M. Mulvihill, G. Risch, M. Zipparo, and T. R. Shrout, *Proceedings of the 10th IEEE International Symposium on the Application of Ferroelectrics* **1**, 79 (1996).
- <sup>5</sup>S. Wada, S.-E. Park, L. E. Cross, and T. R. Shrout, *J. Korean Phys. Soc.* **32**, 1290 (1998).
- <sup>6</sup>S.-E. Park, V. Vedula, M.-J. Pan, W. S. Hackenberger, P. Pertsch, and T. R. Shrout, in *Effect of Prestress on the Strain Behavior of Relaxor-based Single Crystals*, SPIE's 5th Annual International Symposium on Smart Structures and Materials, San Diego, CA, March 1998.
- <sup>7</sup>S.-E. Park and T. R. Shrout, in *Relaxor-based Ferroelectric Single Crystals with High Piezoelectric Performance*, Proceedings of the 8th U.S.-Japan Seminar on Dielectric and Piezoelectric Ceramic Thin Films, pp. 235-241, Plymouth, MA, October 1997.
- <sup>8</sup>S.-F. Liu, S.-E. Park, T. R. Shrout, and L. E. Cross, *J. Appl. Phys.* **85**, 2810 (1999).
- <sup>9</sup>A. F. Devonshire, *Philos. Mag.* **42**, 1065 (1951).
- <sup>10</sup>S. Ajumura, K. Tomomatu, O. Nakao, A. Kurosaka, H. Tominaga, and O. Fukuda, *J. Opt. Soc. Am. B* **9**, 1609 (1992).
- <sup>11</sup>IEEE Standard on Piezoelectricity, American National Standards Institute, 1976.
- <sup>12</sup>A. F. Devonshire, *Philos. Mag.* **40**, 1040 (1951).
- <sup>13</sup>D.-S. Paik, S.-E. Park, S. Wada, S.-F. Liu, and T. R. Shrout, *J. Appl. Phys.* **85**, 1080 (1999).
- <sup>14</sup>B. Jaffe, W. R. Cook, and H. L. Jaffe, *Piezoelectric Ceramics* (Academic, New York, 1971).
- <sup>15</sup>M. Zgonik, P. Bernasconi, M. Duelli, R. Schlessner, and P. Gunter, *Phys. Rev. B* **50**, 5941 (1994).
- <sup>16</sup>X. L. Zhang, Z. X. Chen, L. E. Cross, and W. A. Schulze, *J. Mater. Sci.* **18**, 968 (1983).

# **APPENDIX 30**





ELSEVIER

August 1999

Materials Letters 40 (1999) 109–113

**MATERIALS  
LETTERS**

www.elsevier.com/locate/matlet

## Crystal orientation dependence of piezoelectric properties of single crystal barium titanate

Xiao-hong Du, Qing-Ming Wang, Uma Belegundu, Amar Bhalla<sup>\*</sup>, Kenji Uchino<sup>1</sup>

*International Center for Actuators and Transducers, Materials Research Laboratory, The Pennsylvania State University, University Park, PA 16802, USA*

Received 27 October 1998; received in revised form 27 January 1999; accepted 29 January 1999

### Abstract

The dielectric and piezoelectric constants of single crystal barium titanate have been theoretically calculated and experimentally measured for different cutting orientation directions. The dielectric constant rapidly increases as the cutting direction deviates away from the unique spontaneous polarization direction [001]. The effective piezoelectric strain constant  $d_{33}$  exhibits the same trend in the range from 0° to 50° away from the polarization direction and has the maximum value more than 3.5 times larger than its value along the polarization direction. The electromechanical coupling factor  $k_{33}$  is also enhanced by choosing a cutting direction canted away from the polarization direction. © 1999 Elsevier Science B.V. All rights reserved.

PACS: 77.22 – d; 77.84 – S; 77.84 Dy

**Keywords:** Barium titanate; BaTiO<sub>3</sub>; Single crystal; Orientation dependence; Piezoelectric; Dielectric properties

### 1. Introduction

In our previous papers, the orientation dependence of piezoelectric and dielectric properties for lead zirconate titanate (PZT) has been theoretically studied [1,2]. It was found that for tetragonal PZT, the effective piezoelectric constant  $d_{33}$  and electromechanical coupling factor  $k_{33}$  have the maximum values along the spontaneous polarization; however, for rhombohedral PZT, the maximum values of  $d_{33}$  and  $k_{33}$  are not along the polarization, but in a direction canted from 50° to 60° away from the

polarization direction. For both rhombohedral and tetragonal PZT, the dielectric constant monotonously increases as the cut-angle from the spontaneous polarization direction increases [1,2].

In this paper, we investigated theoretically and experimentally the crystal orientation dependence of the piezoelectric properties of single crystal barium titanate (BT). Due to its large dielectric constants, barium titanate ceramics and crystals are best optional materials for capacitors and barium titanate thin films are highly potential for applications in dynamic random access memory devices [3]. However, the utilization of its piezoelectric properties has been limited because of its relatively small piezoelectric constant along its spontaneous polarization

<sup>\*</sup> Corresponding author

<sup>1</sup> E-mail: kenjiuchino@psu.edu.

direction [001]. Nevertheless, our recent study shows that single crystal barium titanate has an effective piezoelectric constant  $d_{33}$  as large as 250 (pC/N), which is comparable to that of PZT, if the electrical driving direction is canted about 50° away from the spontaneous polarization direction [001]. These results indicate that BT may be a good substitution for PZT in some application fields where lead-containing materials are undesirable.

## 2. Theoretical calculation

In our theoretical calculations, the elastic, dielectric, and piezoelectric constant values we used have previously been published [4]. For an arbitrary cutting orientation, the corresponding values of these constants can be obtained by performing tensor calculations [5,6]. The details of the calculations have been described in Ref. [1]. The calculated results are shown in Figs. 1(a) and 2(a). In these figures, the absolute values of  $d_{33}$  and  $k_{33}$  along an arbitrary direction are represented by the distance from the origin to the surface of the graph along that direction. The cross sections are also shown in Figs. 1(b) and 2(b). From these figures, we can see that the maximum values of  $d_{33}$  and  $k_{33}$  can be obtained in the directions canted 52° and 47°, respectively, away from the polarization direction. The  $d_{33}$  and  $k_{33}$  values are enhanced along the cubic perovskite [111] direction. The  $d_{33}$  of 250 (pC/N) for this canted angle is about 3.5 times larger than the  $d_{33}$  along the polarization direction. It is interesting that the orientation dependence of  $d_{33}$  and  $k_{33}$  in BT is very different from the situation for tetragonal PZT that always exhibits maximum values of  $d_{33}$  and  $k_{33}$  along the spontaneous polarization direction [001]. The main reason for this is the very large  $d_{15}$  of BT.

## 3. Experiment

For convenience,  $d_{33}(\theta)$  is used to denote the value of the effective  $d_{33}$  along a direction canted an angle  $\theta$  away from the spontaneous polarization direction [001]. For example,  $d_{33}(0)$  means the value of  $d_{33}$  along [001], and  $d_{33}(45)$  means the value of effective  $d_{33}$  along the direction canted 45° away

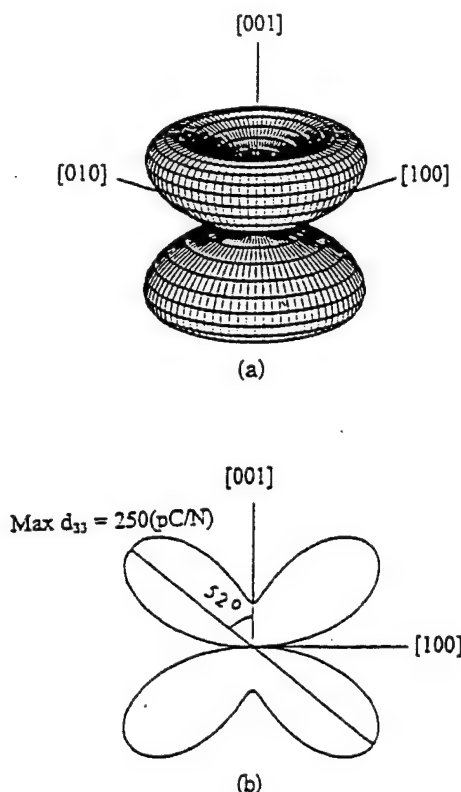


Fig. 1. (a) Effective piezoelectric constants  $d_{33}$  of a single crystal barium titanate. (b) The cross-section curve when the figure in (a) is cut by the (010) plane.

from [001]. This notation is also used for the other property coefficients, such as dielectric constants and electromechanical coupling factors.

Barium titanate single crystals were first poled along the perovskite [001] direction. The following two methods were used to observe the orientation dependence of  $d_{33}$ : (i) the conventional resonance method for a length-extensional bar [7], and (ii)  $d_{33}$ -meter to quickly check the orientation dependence of  $d_{33}$ . Method 2 is an easy way to observe the distribution of  $d_{33}(\theta)$  with respect to angle  $\theta$ : i.e., the normalized value  $d_{33}(\theta)/d_{33}(0)$  with respect to  $\theta$ .

### 3.1. Method 1

A poled single crystal of BT was cut into four small bars along the directions canted 0°, 45°, 50°, and 60° from the [001] direction, respectively. After

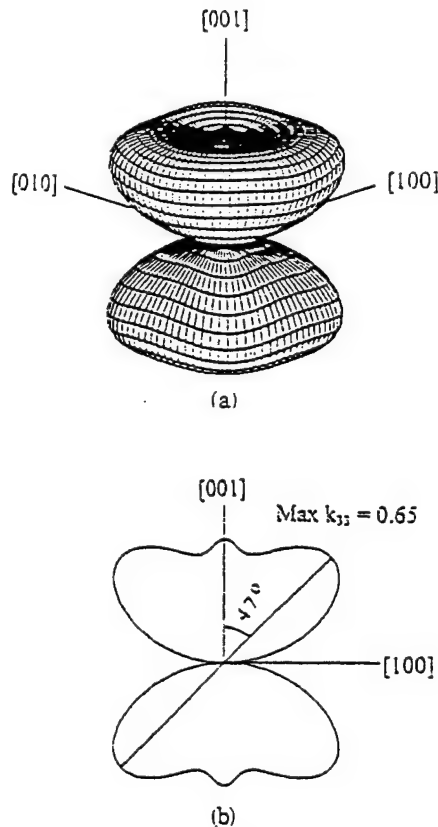


Fig. 2. (a) Effective electromechanical coupling factor  $k_{33}$  of a single crystal barium titanate. (b) The cross-section curve when the figure in (a) is cut by the (010) plane.

the samples were polished and electrodes formed by sputtering, resonance and anti-resonance frequencies were determined with an impedance analyzer (HP4194A). From these measurements,  $d_{33}(\theta)$ ,  $k_{33}(\theta)$ , and  $s_{33}(\theta)$  were determined, using the approach described in the IEEE standards [7]. A plate normal to each direction was also cut for determining the dielectric constant in the respective orientation. The results are shown in Table 1. The values of  $\epsilon_{33}$ ,  $k_{33}$ , and  $d_{33}(\theta)/d_{33}(0)$  are also plotted in Figs. 3–5 for comparison. The value of  $d_{33}(0)$  in Table 1 is lower than the published data (Schaefer et al.) [4]. This was due to the depoling of the sample during the orientation and cutting process. It was not convenient to pole the samples after they were cut along directions which were canted away from [001]. After finishing the above measurements, the sample at  $0^\circ$  was poled again. The  $d_{33}(0)$  and  $k_{33}(0)$  recovered

Table 1

Constants  $d_{33}$ ,  $k_{33}$ ,  $\epsilon_{33}$ , and  $s_{33}$  in different directions

Constants	$0^\circ$	$45^\circ$	$50^\circ$	$60^\circ$
$d_{33}$ (pC/N)	24.69 <sup>a</sup>	85.72	129.44	95.4
$k_{33}$	0.2	0.264	0.33	0.246
$\epsilon_{33}$	103	1795	2873	2263
$s_{33}$ ( $\times 10^{-3}$ /GPa)	17.56	6.63	5.94	7.47

<sup>a</sup> Values on fully poled sample of BT as reported in Ref. [4] are:  $d_{33} = 68.5$  (pC/N),  $\epsilon_{33} = 130$ , and  $s_{33} = 14.95$  ( $\times 10^{-3}$ /GPa).

their original values 75.58 pC/N and 0.6, respectively. In spite of the depoling of sample,  $d_{33}(50)$  is still much larger than the  $d_{33}(0)$  that was measured by Schaefer et al.

### 3.2. Method 2

Fig. 6 illustrates the simple approach for those measurements. A poled crystal of BT was polished in a cylindrical shape with its axis perpendicular to [001]. A dial, marked in angular degrees, was attached to one end of this cylinder. The test probes of a  $d_{33}$ -meter were placed at an appropriate place on the cylinder to measure the  $d_{33}$  values. The cylinder

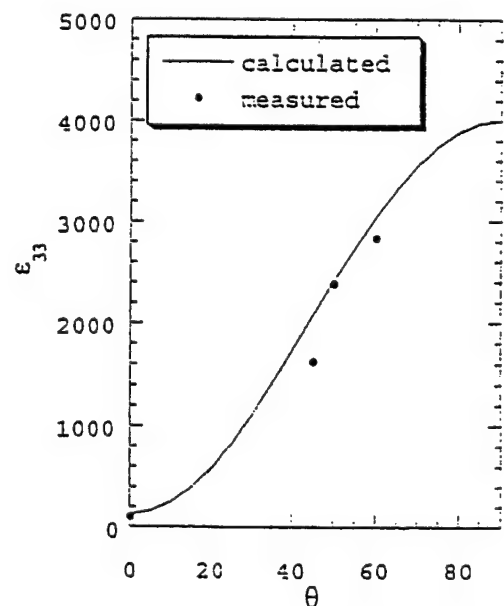


Fig. 3. Dielectric constants of a single crystal barium titanate for different cutting angles. The solid line is obtained by calculations using the data from Schaefer et al. [4].

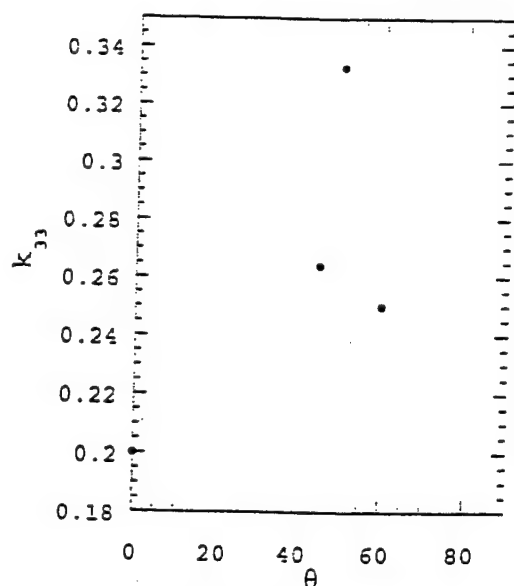


Fig. 4. Effective electromechanical coupling factor  $k_{33}$  of a single crystal barium titanate for different cutting angles.

was rotated when  $d_{33}(\theta)$  was measured for each  $\theta$  angle (which could be read from the dial). The

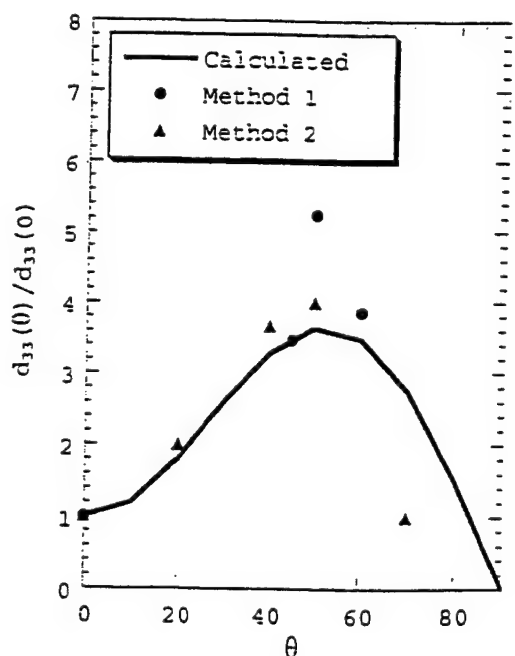


Fig. 5. Normalized piezoelectric constant  $d_{33}(\theta)/d_{33}(0)$  of a single crystal barium titanate for different cutting angles. The solid line is obtained by calculations using the data from Schaefer et al. [4].

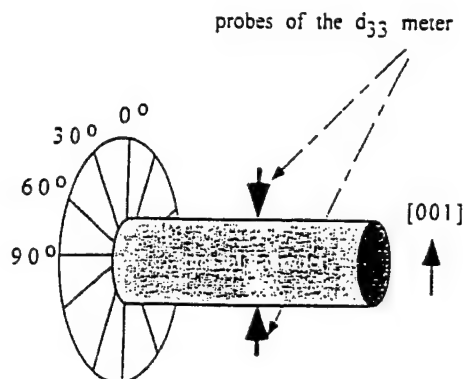


Fig. 6. Illustration of Method 2, showing the position of the probes.

normalized values of  $d_{33}(\theta)/d_{33}(0)$  are plotted as shown in Fig. 5.

#### 4. Discussions and conclusions

Fig. 3 shows that the dielectric constant has its minimum value along the polarization direction and rapidly increases as the cutting angle from the spontaneous polarization direction increases. For effective  $d_{33}$ , theoretical and experimental results show that more than a 3.5 times enhancement can be obtained by choosing a cutting direction canted about  $50^\circ$  from the spontaneous polarization direction [001], as shown in Fig. 5. In this direction,  $k_{33}$  is also substantially improved (Fig. 4).

These results imply that the piezoelectric properties can be greatly enhanced by adopting the [111] orientation for barium titanate single crystals or thin films. The [111]-oriented BT has a large  $d_{33}$  which is comparable with that of PZT. This provides another option for actuator and transducer applications, especially for applications where non-lead containing materials are desirable.

#### Acknowledgements

The authors gratefully acknowledge the financial support from the Office of Naval Research under contract N00014-91-J-4145.

## References

- [1] X. Du, U. Belegundu, K. Uchino, *Jpn. J. Appl. Phys.* 36 (1997) 5580, Part I.
- [2] X. Du, J. Zheng, U. Belegundu, K. Uchino, *Appl. Phys. Lett.* 72 (1998) 2421.
- [3] D. Kim, S. Lee, Y. Park, S. Park, *Jpn. J. Appl. Phys.* 34 (1995) L1564.
- [4] A. Schaefer, H. Schmitt, A. Dorr, *Ferroelectric* 69 (1986) 253.
- [5] J.F. Nye, *Physical Properties of Crystals*, Oxford, England, 1957.
- [6] W.G. Cady, *Piezoelectricity*, Vol. 1, Dover, New York, 1964, p. 65.
- [7] ANSI/IEEE, *IEEE Standard on Piezoelectricity*, Std 176-1987, IEEE, New York, 1987.

# **APPENDIX 31**

# Linear Electro-optic Effect of 0.88Pb(Zn<sub>1/3</sub>Nb<sub>2/3</sub>)O<sub>3</sub>–0.12PbTiO<sub>3</sub> Single Crystal

Yu LU, Zhong-Yang CHENG, Seung-Eek PARK, Shi-Fang LIU and Qiming ZHANG\*

Materials Research Laboratory and Department of Electrical Engineering, The Pennsylvania State University,  
 University Park, PA 16802, USA

(Received August 23, 1999; accepted for publication October 14, 1999)

The linear electro-optic (E-O) coefficients of poled 0.88Pb(Zn<sub>1/3</sub>Nb<sub>2/3</sub>)O<sub>3</sub>–0.12PbTiO<sub>3</sub> single crystal were characterized using an automated scanning Mach-Zehnder interferometer and the senarmont compensator method at room temperature. They were obtained at a wavelength of 632.8 nm:  $r_{33} = 134$  pm/V,  $r_{13} = 7$  pm/V,  $r_{51} = 462$  pm/V, and  $r_c = 131$  pm/V respectively and the refractive indices:  $n_e = 2.57$  and  $n_o = 2.46$ . The large  $r_{51}$  coefficient compared with  $r_{33}$  is caused by the high dielectric constant at perpendicular to the polar-axis compared with the dielectric constant along the  $c$ -axis. Comparison with the quadratic E-O coefficients measured at near and above the Curie temperature suggests that the values of the quadratic E-O coefficients measured earlier may be smaller than the intrinsic ones due to the influence of micro-polar regions. The development of an automated scanning Mach-Zehnder interferometer, which is less susceptible to the errors caused by the laser intensity fluctuation and drifting in the optical path length in the system, is also described.

KEYWORDS: ferroelectric, electro-optic, refractive index, interferometer

## 1. Introduction

Ferroelectric crystals, such as LiNbO<sub>3</sub> and KH<sub>2</sub>PO<sub>4</sub> (KDP), are widely used in electro-optic (E-O) devices such as electro-optic modulators, electro-optic switches, and light valves.<sup>1,2</sup> More recently, there is an increased interest in the relaxor ferroelectric crystal Pb(Zn<sub>1/3</sub>Nb<sub>2/3</sub>)O<sub>3</sub>–PbTiO<sub>3</sub> (PZN–PT), which over a broad composition range possesses a very high electromechanical coupling factor, piezoelectric coefficients, and field induced strain response.<sup>3–7</sup> A uniqueness of this crystal system is that relatively high quality single crystals can be grown at compositions near the tetragonal-rhombohedral morphotropic phase boundary (MPB). It is well known that many of the material responses exhibit increased activity near a MPB.<sup>8,9</sup> In this paper, we report the result of the linear E-O coefficients in 0.88PZN–0.12PT single crystal, which is near the MPB on the tetragonal side.<sup>3,5</sup>

The E-O effect describes the change of refractive index  $\Delta n_{ij}$  due to the applied field:

$$\Delta n_{ij} = -\frac{1}{2}n_{ij}^3 \left( \sum_{j=1}^3 r_{ijk} E_k + \sum_{j,k=1}^3 R_{ijkl} E_k E_l \right) \quad (1)$$

where  $r_{ijk}$  and  $R_{ijkl}$  are linear and quadratic E-O coefficients, respectively. The quadratic coefficients for PZN–PT crystals at temperatures near and above the dielectric constant maximum have been characterized earlier, and in this paper all three non-zero linear E-O coefficients ( $r_{33} = r_{333}$ ,  $r_{13} = r_{113}$ , and  $r_{51} = r_{311}$ ) were measured for 0.88PZN–0.12PT in the ferroelectric tetragonal phase (room temperature).<sup>10</sup> The comparison of the two results, indicates that the coefficients measured at the high temperature phase may be affected by the relaxor ferroelectric nature of the PZN–PT system, and will be discussed in the paper. In addition, we will also report briefly a modified interferometric method for the characterization of these coefficients, which is based on the dynamic scanning concept.

## 2. Experimental

### 2.1 0.88PZN–0.12PT single crystal and related E-O coefficients

The 0.88PZN–0.12PT crystal used in this study was grown using the high temperature flux method.<sup>3,6,11</sup> It is known that 0.88PZN–0.12PT has a tetragonal structure at room temperature and that the spontaneous polarization is along (001) ( $c$ -axis) direction.<sup>3–5</sup> The single crystal sample was oriented along the (001) direction using a Laue camera, then the (100) faces were polished to optical quality. The sample was poled at a temperature of 230°C, which is much higher than the paraelectric to ferroelectric phase transition temperature, with an electric field of 5 kV/cm for 30 min. Then, the sample was slowly cooled down to room temperature under the electric field. It was found that poling at room temperature resulted in fractures in the sample since the domain switch induces very large strain, expansion along the poling direction. The dimension of the sample is  $1.35 \times 3.35 \times 4.83$  mm<sup>3</sup> and the poling field was applied across the 3.35 mm thickness.

For the tetragonal symmetry, there are three non-zero E-O coefficients, i.e.,  $r_{33}$ ,  $r_{13}$ , and  $r_{51}$ . In this study,  $r_{33}$  and  $r_{13}$  were measured using an interferometric method, where the applied field  $E_3$  is along the  $c$ -axis and the light passes through the sample along the (100) axis ( $a$ -axis),

$$\Delta n_e = -n_e^3 r_{33} E_3 / 2 \quad (2a)$$

$$\Delta n_o = -n_o^3 r_{13} E_3 / 2 \quad (2b)$$

where  $n_o$  and  $n_e$  denote the refractive index perpendicular and parallel to the  $c$ -axis, respectively. In the  $r_{33}$  measurement, the polarization direction of the laser beam is along the  $c$ -axis and in measuring  $r_{13}$ , the polarization direction is perpendicular to the  $c$ -axis.

For the PZN–PT crystal studied, the  $E_3$  field will also induce a change in the sample thickness along the path of the laser beam due to the piezoelectric effect,<sup>12</sup>

$$\Delta l_1 = d_{31} E_3 l_1$$

where  $l_1$  is the thickness of the crystal along the beam path and  $d_{31}$  is the piezoelectric coefficient. Hence, the total measured optical path length change in the interferometric method

\*To whom correspondence should be addressed. E-mail: qxz1@psu.edu

is  $\Delta n_i \cdot l_i + (n_i - 1) \cdot \Delta l_i$ .

The E-O coefficient  $r_{31} (\Delta(1/\pi_{31}^2) = \Delta(1/\pi_{31}^2) = r_{31} E_1)$  was measured by the Senarmont compensator method, where the applied field  $E_1$  is along the (010) axis perpendicular to both the  $c$ -axis and the light propagation direction.<sup>13)</sup> The polarization direction of the laser beam is canted  $45^\circ$  with respect to the  $c$ -axis. In the  $r_{31}$  measurement, there is no correction due to the piezoelectric effect.

Using the Senarmont compensator method, the E-O coefficient  $r_e$ , which is defined as  $r_e = r_{33} - \pi_0^3 r_{13}/\pi_0^3$  and determines the half-wave voltage of the material, was also measured.<sup>13,14)</sup>

## 2.2 Operation principle of scanning Mach-Zehnder interferometer for E-O coefficient measurement

Shown in Fig. 1 is a typical Mach-Zehnder interferometer.<sup>15)</sup> The interference pattern at the detection point depends on the optic path length difference ( $\Phi = 2\pi(n_R l_R - n_S l_S)/\lambda$ , where  $n$  and  $l$  are the refractive indices and the path lengths respectively, R and S in subscript expresses the reference and signal arms, respectively) between the signal and reference beams,

$$I = I_1 + I_2 + 2\sqrt{I_1 I_2} \cos(\Phi) \\ = \frac{1}{2}(I_{\max} + I_{\min}) + \frac{1}{2}(I_{\max} - I_{\min}) \cos(\Phi) \quad (3)$$

where  $I_{\max} = (\sqrt{I_1} + \sqrt{I_2})^2$  and  $I_{\min} = (\sqrt{I_1} - \sqrt{I_2})^2$  are the maximum and minimum intensities of interference fringes, respectively, and  $I_1$  and  $I_2$  are the light intensities of signal beam and reference beam, respectively. From eq. (3), one can find that when  $\Phi$  has a small change ( $\Delta\Phi$ ) around  $\Phi_0 = (m + 1/2)\pi$ ,  $m = 0, \pm 1, \dots$ ,  $\cos(\Phi_0 + \Delta\Phi) \approx \pm \Delta\Phi$ , and the  $\pm$  signs depend on the value of  $m$ , and

$$\Delta I = I - \frac{1}{2}(I_{\max} + I_{\min}) = \pm \frac{1}{2}(I_{\max} - I_{\min}) \Delta\Phi. \quad (4)$$

Hence, by stabilizing the system at  $\Phi_0$  (working point), the change of interference intensity will depend linearly on the change of the optic path length. When this change is measured by a photo-detector, eq. (4) can be converted into the voltage form as:

$$\Delta\Phi = \frac{v_{\text{out}}}{(V_{\max} - V_{\min})/2} = \frac{v_{\text{out}}}{V_{p-p}/2}. \quad (5)$$

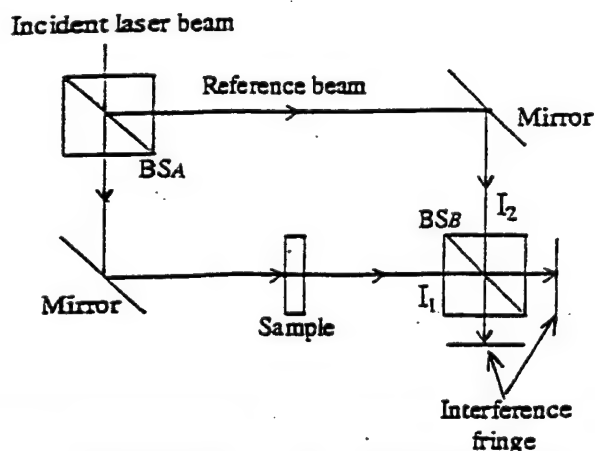


Fig. 1. Schematic drawing of a typical Mach-Zehnder interferometer.

Where  $v_{\text{out}}$  corresponds to  $\Delta I$ ,  $V_{\max}$  and  $V_{\min}$  correspond to  $I_{\max}$  and  $I_{\min}$  respectively and  $\Delta\Phi = 2\pi\Delta(nl)/\lambda$ . For E-O or piezoelectric coefficient measurement under an ac electric field of frequency ( $f_0$ ), a lock-in amplifier can be used to measure  $v_{\text{out}}$  which yields a high sensitivity of the system in resolving the change in  $\Delta\Phi$ .

However, in developing a computer controlled experimental set-up to measure the change in the optic path length (and hence  $\Delta\Phi$ ), we found that the approach of stabilizing the system near the working point (by using a feedback loop to control the path length of the reference arm) is not convenient. The change in the incident light intensity and other factors such as air turbulence in the system and the variation of the light absorption in the sample due to thermal and electric field can cause shift in the working point light intensity.<sup>16)</sup> As a result, the stabilized experimental point will be no longer at  $\Phi_0$ . Furthermore, those changes will also result in changes in  $I_{\max}$  and  $I_{\min}$ , causing errors in the experimental results on  $\Delta(nl)$ .

If instead of stabilizing the system at any specific point, an optic translation stage is used to drive a slow change in the path length  $l_R$  of the reference arm,  $\Phi$  will be changed continuously. As a result, the interference intensity will change with time, from which  $I_{\max}$  and  $I_{\min}$  can be measured readily. If an AC electric field with a frequency  $f_0$  is applied to a sample which causes a small change (much smaller than the wave length) in the optic path length in the signal arm, the change in the phase  $\Phi$  will be  $\Phi_{\text{ref}} + \Delta\Phi$ . The resulting signal will be:

$$I = \frac{1}{2}(I_{\max} + I_{\min}) + \frac{1}{2}(I_{\max} - I_{\min}) \cos(\Phi_{\text{ref}} + \Delta\Phi) \quad (6)$$

where  $\Phi_{\text{ref}}$  describes the drifting in the phase caused by the optic path length change of the reference arm and also in the signal arm due to slow drifting, and  $\Delta\Phi$  is the phase change caused by the sample due to the applied AC electric field. Since  $\Delta\Phi$  is very small, one can get

$$I = \left( \frac{1}{2}(I_{\max} + I_{\min}) + \frac{1}{2}(I_{\max} - I_{\min}) \cos \Phi_{\text{ref}} \right) \\ - \left( \frac{1}{2}(I_{\max} - I_{\min}) \sin \Phi_{\text{ref}} \right) \Delta\Phi. \quad (7)$$

Therefore, when  $\Phi_{\text{ref}} = (m + 1/2)\pi$ , eq. (7) is reduced to eq. (4). When  $\Phi_{\text{ref}} = m\pi$ , the second term on the right hand side of the equation is zero and the first term yields  $I_{\max}$  and  $I_{\min}$ . Thus,  $V_{p-p}/2$  can be obtained. Hence, in one scanning period of the reference beam, all the quantities in eq. (5) can be determined and yield  $\Delta\Phi$ . Clearly, even if  $v_{\text{out}}$ ,  $V_{\max}$  and  $V_{\min}$  may vary due to various noise sources, the corresponding variation in  $\Delta\Phi$  which is the ratio between them [eq. (5)] will be much smaller. This has been verified experimentally. In addition, the data accuracy can be improved further by averaging  $\Delta\Phi$  thus obtained over long time period.

Based on these considerations, a Mach-Zehnder interferometer with the reference arm scanned was developed to measure E-O or piezoelectric coefficients (as schematically shown in Fig. 2). In this scanning Mach-Zehnder interferometer, the reference mirror is driven by a servo-transducer made of piezoelectric material. In experiments for E-O or piezoelectric measurement,  $f_0$  typically runs from 100 Hz to 100 kHz, and the corresponding scan frequency may be varied from 0.003 Hz to 3 Hz to satisfy the condition that the scanning fre-



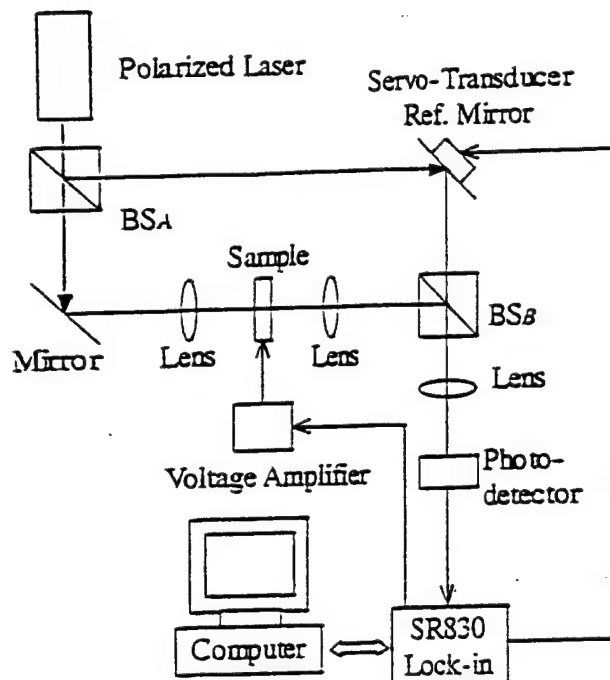


Fig. 2. Schematic drawing of the setup of the automated scanning Mach-Zehnder interferometer developed for E-O measurement.

quency is much lower than the signal frequency. Both the AC and DC components of the photo-detector output are transmitted to a digital lock-in amplifier (SRS SR830). A computer is used to control the system and acquire the data from the SR830 through a GPIB cable. The system can be controlled easily by the computer over a long time period. The computer software was programmed using LabView 4.1.

### 3. Experiment Results and Discussion

#### 3.1 Experimental results

For the 0.88PZN-0.12PT single crystal used in this experiment, no data of the refractive index at room temperature were available. Hence, the first step is to measure these indices. Although the refractive index can be measured by the minimum deviation method, the sample needs to be made into a wedge shape.<sup>14,15</sup> In order to measure the E-O coefficients, the sample has to be reshaped to a rectangular parallelepiped. Because of the relatively small size sample, instead, Brewster's angle method was used in which only one reflection surface is required.<sup>14,15</sup> Hence the sample used in the refractive index measurement can also be used directly in E-O measurement.

Brewster's angle ( $\theta_B$ ) is the incident angle at which the reflection intensity is zero for polarized light with the polarization direction parallel to the incident plane. The relationship between the refractive index and  $\theta_B$  is:  $n = \tan \theta_B$ . By changing the orientation of the crystal with respect to the linearly polarized incident laser beam, both  $n_o$  and  $n_e$  can be determined. The obtained  $\theta_B$  for the PZN-PT crystal are  $68.75^\circ$  and  $67.84^\circ$ , yielding  $n_o = 2.57 \pm 0.01$  and  $n_e = 2.46 \pm 0.01$  at 632.8 nm wavelength for the sample at room temperature.

To facilitate the discussion, apparent E-O coefficients  $r_{13}^*$  and  $r_{33}^*$  are introduced here to denote the coefficients obtained directly from  $\Delta\Phi$  without the correction of the piezoelectric effect.

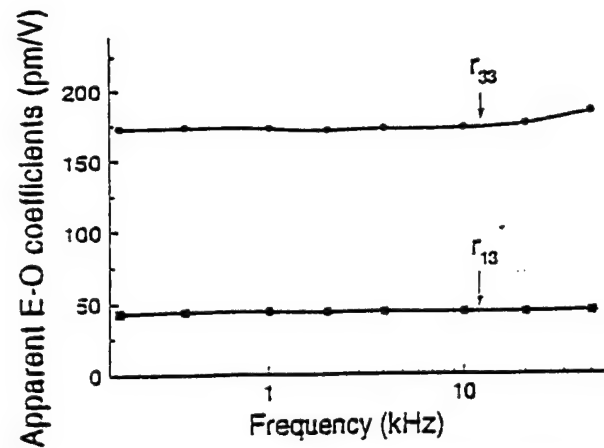


Fig. 3. Apparent E-O coefficients ( $r_{33}^*$  and  $r_{13}^*$ ) measured at different frequencies for 0.88PZN-0.12PT single crystal at room temperature.

$$\Delta(n_e L) = \frac{\lambda}{2\pi} \Delta\Phi = r_{33}^* n_e^3 l E_3 / 2$$

or

$$\Delta(n_o L) = \frac{\lambda}{2\pi} \Delta\Phi = -r_{13}^* n_o^3 l E_3 / 2$$

The apparent E-O coefficients  $r_{13}^*$  and  $r_{33}^*$  are measured separately for the sample under a stress free condition. For a piezoelectric material, it is well known that there are serious resonance frequencies at which the electric field induced strain can no longer be described by the linear piezoelectric equation.<sup>12</sup> This certainly imposes frequency windows in which the E-O coefficient can be measured reliably. In addition, any mechanical resonance in the sample holding system can also cause error in the measurement. In this study, the frequency window used is from 200 Hz to 40 kHz, well below the first (lowest) resonance frequency ( $f_r$ ) which is at several hundreds kHz. To ensure the weak field condition in the measurement, the applied field is about 15 V/cm which is also well below the room temperature coercive field of about 5 kV/cm.

The results for  $r_{13}^*$  and  $r_{33}^*$  are shown in Fig. 3. In the frequency range measured, there is no large change of the E-O coefficients with frequency and the average values of  $r_{13}^*$  and  $r_{33}^*$  are  $44 \pm 1$  pm/V and  $173 \pm 4$  pm/V, respectively. A mechanical resonance due to the sample holding system was observed at frequencies above 40 kHz which affects the data acquired near 40 kHz.

To subtract the piezoelectric effect, the piezoelectric  $d_{31}$  coefficient was measured using a single beam laser interferometer:  $d_{31} = -210 \pm 10$  pm/V. From  $r_{33} = r_{33}^* + 2(n_e - 1)d_{31}/n_e^3$  and  $r_{13} = r_{13}^* + 2(n_o - 1)d_{31}/n_o^3$ , the E-O coefficients  $r_{33}$  and  $r_{13}$  are obtained:  $r_{33} = 134 \pm 5$  pm/V and  $r_{13} = 7 \pm 2$  pm/V at 632.8 nm wavelength for 0.88PZN-0.12PT at room temperature.

One of the concerns in the single crystal PZN-PT is the imperfect poling which results in residual domains in the sample. This will affect the measured E-O coefficients. In order to check this, the E-O coefficients under high DC bias field were measured. In the experiment, an oil chamber was built so that the sample can be immersed in an insulation oil which prevents electric breakdown through air when the sample is subject to a high DC voltage. Shown in Fig. 4 are the apparent E-O coefficients  $r_{13}^*$  and  $r_{33}^*$  measured at 1 kHz as a func-

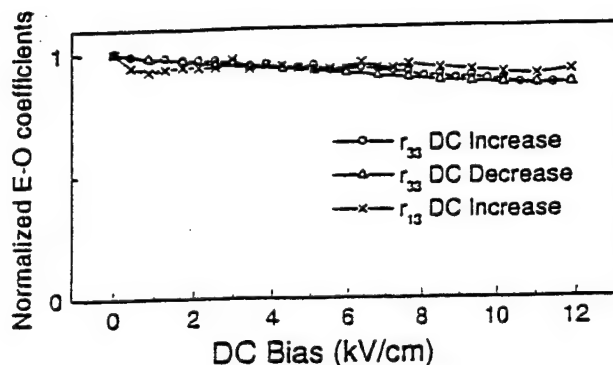


Fig. 4. The E-O coefficients as a function of the DC electric bias field for 0.88PZN-0.12PT single crystal at room temperature.

tion of a DC bias field which is applied parallel to the original poling direction up to 15 kV/cm, much higher than the room temperature coercive field. Apparently, the measured coefficients do not show much change with a DC bias field (except a small decrease which is expected) and as the bias field is reduced to zero, the E-O coefficients return to their original values. The results indicate that the sample used in this study was properly poled.

The  $r_{51}$  coefficient measured by the senarmont compensator method is  $r_{51} = 462$  pm/V which is much larger than  $r_{33}$  and in the frequency range measured. (below 40 kHz),  $r_{51}$  does not show much change with frequency.

Using the senarmont compensator method, the E-O coefficient  $r_c$  was also characterized. The coefficient measured direct from the experiment data is the apparent coefficient  $r_c^*$  which is

$$r_c^* = r_{33}^* - \frac{n_o^3}{n_e^3} r_{13}^* = r_c + \frac{2(n_e - n_o)}{n_e^3} d_{31}. \quad (8)$$

Because the difference between  $n_e$  and  $n_o$  is very small, the piezoelectric effect [the second term on the right hand side of eq. (8)] has much less effect on  $r_c$  compared with  $r_{13}$  and  $r_{33}$ . The measured value of  $r_c^*$  for the sample under stress free condition used above is 128 pm/V. The corresponding coefficient after the correction of the piezoelectric effect is  $r_c = 131$  pm/V.

From measured values of  $n_e$ ,  $n_o$ ,  $r_{13}$  and  $r_{33}$ , the E-O coefficient  $r_c$  can also be deduced from  $r_c = r_{33} - n_o^3 r_{13} / n_e^3$ . From the measured results of  $n_e$ ,  $n_o$ ,  $r_{13}^*$  and  $r_{33}^*$ , the calculated  $r_c^*$  is 124 pm/V, which is very close to 128 pm/V measured directly using the Senarmont compensator method.

A qualitative aging experiment was also performed on the E-O coefficients and it was found that even the poled sample was used for various other measurements, the E-O coefficients were nearly the same when measured after 3 months. Therefore the optical coefficients reported here are the stable material properties of 0.88PZN-0.12PT single crystal.

### 3.2 Discussion

At this point, it is interesting to compare the results obtained here with those reported earlier. For example, the quadratic E-O coefficients  $g_{11} - g_{12}$  and  $g_{44}$  were measured by Nomura *et al.* [ $\Delta n_{ij} = -(1/2)n_{ij}^3 \sum_{k,l=1}^3 g_{ijkl} P_k P_l$ , where  $P_k$  is the polarization component along the  $k$ -direction].<sup>10)</sup> Since in ferroelectric single crystals, the linear E-O effect can

be regarded as a polarization biased quadratic E-O effect,<sup>17)</sup> the relationships between the linear E-O coefficients and the quadratic E-O coefficients are:

$$r_{33} - r_{13} = 2K_{33}\epsilon_0 P_s (g_{11} - g_{12}) \quad (9a)$$

$$r_{51} = K_{11}\epsilon_0 P_s g_{44} \quad (9b)$$

where  $g_{11} = g_{1111}$ ,  $g_{12} = g_{1122}$ , and  $g_{44} = 2g_{2323}$ ,  $K_{33}$  and  $K_{11}$  are the dielectric constant along the  $c$ -axis and  $a$ -axis, respectively,  $P_s$  is the spontaneous polarization, and  $\epsilon_0 = 8.85 \times 10^{-12}$  F/m is the vacuum permittivity.

For the crystal investigated here, at room temperature the dielectric constant was measured to be:  $K_{33} = 710$  and  $K_{11} = 7630$ . From the data of ref. 10,  $g_{11} - g_{12} = 0.013$  m<sup>3</sup>/C<sup>2</sup> and  $g_{44} = 0.009$  m<sup>3</sup>/C<sup>2</sup>. Hence, the ratio of  $(r_{33} - r_{13})/r_{51}$  is equal to  $2K_{33}(g_{11} - g_{12})/K_{11}g_{44} = 0.269$  using the dielectric constant measured here and the  $g$  coefficients of ref. 10. Using the value of the  $r$  coefficients measured here yields the ratio of  $(r_{33} - r_{13})/r_{51} = 0.275$ . The agreement between the values obtained using two sets of data is surprisingly good.

The results from the two sets of data can also be compared directly if the spontaneous polarization  $P_s$  is known. From the room temperature polarization hysteresis loop,  $P_s$  is extrapolated:  $P_s = 40$   $\mu$ C/cm<sup>2</sup>. Substituting  $P_s$  and other data to the right hand sides of eq. (9) yields  $r_{33} - r_{13} = 65.3$  pm/V and  $r_{51} = 243$  pm/V. The results show that the linear E-O coefficients deduced from the quadratic E-O coefficients measured at temperatures near and above the dielectric constant maximum are about half of the values of the corresponding coefficients measured directly at poled samples (127 pm/V and 462 pm/V, respectively). In other words, either  $P_s$  and/or the  $g$  coefficients used in eq. (9) are smaller than the intrinsic values. Although one cannot rule out that the intrinsic  $P_s$  value for the crystal studied may be higher than 40  $\mu$ C/cm<sup>2</sup>, the difference will not be large enough to account for the discrepancy observed here.

In studies of the relaxor ferroelectric Pb(Mg<sub>1/3</sub>Nb<sub>2/3</sub>)O<sub>3</sub>-PbTiO<sub>3</sub> system, it was found that the electrostrictive coefficients measured at near and above the dielectric constant maximum are much smaller than the intrinsic values.<sup>18,19)</sup> This is caused by the fact that in a relaxor ferroelectric system, the response of the local polar regions under external electric field includes the orientation of the polar regions and the motion of the interface between the non-polar area and the polar region.<sup>20)</sup> All these responses contribute to the polarization, but do not totally contribute to the strain responses.<sup>19)</sup> PZN-PT is also a typical relaxor ferroelectric system when the PT content is less than 10% and the evolution from a relaxor ferroelectric to a normal ferroelectric is a gradual process covering a broad composition range.<sup>4,21)</sup> For the composition studied here, it is still quite close to the MPB and hence will possess many features resembling a relaxor ferroelectric. For example, if there is a 180° local polar region reorientation, it will not cause a large change in the quadratic E-O coefficient in spite of the fact that there is a large polarization change. On the other hand, this response will influence  $g_{11} - g_{12}$  and  $g_{44}$  in a similar way which will not affect the ratio between them as observed here. (The ratio of  $(r_{33} - r_{13})/r_{51}$  measured here is the same as the ratio of  $2K_{33}(g_{11} - g_{12})/K_{11}g_{44}$  deduced from the  $g$ -coefficients). Thus, the observed discrepancy be-

Table I. Properties characterized in this study for 0.88PZN-0.12PT single crystal.

---

$n_o = 2.57$ , $n_e = 2.46$ , $r_{33} = 134$ pm/V, $r_{13} = 7$ pm/V, $r_c = 131$ pm/V, $r_{31} = 462$ pm/V (all measured at 633 nm wavelength)	
$d_{31} = -210$ pm/V, $K_{33} = 710$ , $K_{11} = 7630$ , $P_s = 40$ $\mu\text{C}/\text{cm}^2$	

---

between the measured linear E-O coefficients and the calculated ones from the quadratic E-O coefficients is reasonable. That is, when the measurement is performed at near the dielectric constant maximum where there is a strong contribution of the polarization responses from the local polar regions, the response of the local polar regions in relaxor systems will make the measured quadratic E-O coefficients deviating from their intrinsic values. By applying a high external field to remove this mesoscopic polarization inhomogeneity in the material, one may be able to obtain the intrinsic coefficients as observed in PMN-PT system.<sup>19,22)</sup>

In Table I, the material properties characterized in this study are summarized.

#### 4. Summary and Acknowledgement

Using the newly developed automated scanning Mach-Zehnder interferometer and the Senarmont compensator method, the linear E-O coefficients of 0.88PZN-0.12PT single crystal were measured at room temperature. It is found that the coefficients measured using the interferometer method and the Senarmont compensator method are in excellent accord. It is also found that the ratio of  $(r_{33} - r_{13})/r_{31}$  measured here is also in very good accord with that deduced from the quadratic E-O coefficients measured earlier. However, in comparing the absolute values of the linear E-O coefficients measured here with that deduced from the quadratic E-O coefficients, it was found that the quadratic coefficients measured earlier at temperatures near the dielectric constant maximum may be substantially smaller than the intrinsic values of these coefficients due to the existence of mesoscopic polar regions and their different contributions to the polariza-

tion response and E-O response.

This work was supported by the Office of Naval Research under Contract No: N00014-98-1-0527.

- 1) M. E. Lines and A. M. Glass: *Principles and Applications of Ferroelectrics and Related Materials* (Clarendon Press, Oxford 1977).
- 2) L. J. Pinson: *Electro-optics* (John Wiley & Sons, New York, 1985).
- 3) J. Kuwata, K. Uchino and S. Nomura: *Jpn. J. Appl. Phys.* 21 (1982) 1298.
- 4) J. Kuwata, K. Uchino and S. Nomura: *Ferroelectrics* 37 (1981) 579.
- 5) S.-E. Park and T. Shrotr: *J. Appl. Phys.* 82 (1997) 1304.
- 6) S.-F. Liu, S.-E. Park, T. R. Shrotr and L. E. Cross: *J. Appl. Phys.* 85 (1999) 2810.
- 7) S.-E. Park and T. R. Shrotr: *Mater. Res. Innov.* 1 (1997) 20.
- 8) B. Jaffe, W. R. Cook and H. Jaffe: *Piezoelectric Ceramics* (Academic Press, New York, 1971).
- 9) T. Mitsui and S. Nomura: *Ferroelectric and Related Materials* (Springer-Verlag, Berlin, 1981).
- 10) S. Nomura, H. Arima and F. Kojima: *Jpn. J. Appl. Phys.* 12 (1973) 531.
- 11) S.-F. Liu: unpublished.
- 12) IEEE Standard Board: An American National Standard, IEEE Standard on Piezoelectricity, ANSI/IEEE Std. 176 (1987).
- 13) A. R. Johnson and J. M. Weingart: *J. Opt. Soc. Am.* 55 (1965) 823.
- 14) D. McHenry: Dr. Thesis. Solid State Science, The Pennsylvania State University (1992).
- 15) F. W. Sears: *Optics* (Addison-Wesley, Cambridge, 1956).
- 16) T. Kwaijtaal, B. J. Luymes and G. A. Pijll: *J. Phys. D* 13 (1980) 1005.
- 17) F. Jona and G. Shirane: *Ferroelectric Crystals* (Dover, New York 1993).
- 18) J. Zhao, A. Glazonov, Q. M. Zhang and B. Toby: *Appl. Phys. Lett.* 72 (1998) 1048.
- 19) Q. M. Zhang and J. Zhao: *Appl. Phys. Lett.* 71 (1997) 1649.
- 20) Z.-Y. Cheng, R. S. Kanyar, X. Yao and A. S. Bhalla: *Phys. Rev. B* 57 (1998) 8166.
- 21) A. Halliyal, U. Kumar, R. E. Newnham and L. E. Cross: *J. Am. Ceram. Soc.* 70 (1987) 119.
- 22) J. Zhao: Dr. Thesis. Solid State Science, The Pennsylvania State University (1998).

# **MATERIALS STUDIES**

***High Strain Polymers***

# **APPENDIX 32**

# Polarization and structural properties of high-energy electron irradiated poly(vinylidene fluoride-trifluoroethylene) copolymer films

Vivek Bharti,<sup>a)</sup> H. S. Xu, G. Shanthi, and Q. M. Zhang

*Materials Research Laboratory, The Pennsylvania State University, University Park, Pennsylvania 16802*

Kuming Liang

*ATL Echo Ultrasound, Reedsville, Pennsylvania 17084*

(Received 2 June 1999; accepted for publication 29 September 1999)

The effect of high-energy electron irradiation on structural and polarization properties of 50/50 mol% copolymer of poly(vinylidene fluoride-trifluoroethylene) was investigated for both mechanically stretched and unstretched films. Although stretching can significantly enhance the polarization and dielectric responses in unirradiated films, it was observed that this enhancement was not significant in irradiated films. In addition, the polarization in both types of films after irradiation can be described quite well by a logarithmic mixing law of composites, which consist of crystallites embedded in an amorphous matrix with nearly the same fitting parameters. On the other hand, the enhancement of the mechanical properties from stretching persists after the irradiation, and the elastic modulus along the stretching direction remains high after irradiation in comparison with unstretched films. It was found that the dielectric dispersion in both types of films after irradiation fits well to the Vogel-Fulcher law. It was also observed that the crystallinity decreases and the crosslinking coefficient increases continuously with dose. However, there was no direct one to one type relationship between the crystallinity and the crosslinking coefficient. Although stretching can reduce the rate of crosslinking, the reduction of crystallinity with dose for stretched and unstretched films does not show a marked difference. © 2000 American Institute of Physics. [S0021-8979(00)08501-7]

## I. INTRODUCTION

Since the discovery of ferroelectricity in the vinylidene fluoride-trifluoroethylene copolymers P(VDF-TrFE), extensive research has been carried out to understand the ferroelectric behavior, to enhance the electromechanical properties, and to establish structure-property relationship.<sup>1-4</sup> It is well known that the electromechanical properties are highly dependent upon the structural parameters such as molecular orientation, crystallinity, and the state of polarization.<sup>4-6</sup> Various methods such as high temperature annealing,<sup>7</sup> stretching, and high electric field poling<sup>8-10</sup> have been employed to introduce high degree of crystallinity and perfect alignment of dipoles in polymer films.

We have shown recently that under proper electron irradiation treatment, P(VDF-TrFE) copolymers can exhibit massive electrostrictive strain with high elastic energy density.<sup>11,12</sup> It was also observed that a piezoelectric state can be induced in this copolymer under a dc electric bias field with a piezoelectric constant approaching those of the current piezoceramic materials.<sup>13</sup> In addition, the irradiation treatment was found to convert the polymer from a normal ferroelectric to a relaxor ferroelectric exhibiting a broad dielectric relaxation peak following Vogel-Fulcher law,<sup>14</sup> as observed in the inorganic ferroelectric relaxors like lead magnesium niobate (PMN).<sup>15,16</sup> These distinct features make this material very attractive for a broad range of applications such as transducers, actuators, and sensors,<sup>17,18</sup> and also for

the fundamental study of ferroelectric systems with frozen-in defects and frustrations.<sup>16</sup>

It was observed that the electromechanical properties of irradiated copolymers depend crucially on the processing conditions both prior and during the irradiation. For example, by mechanically stretching the copolymer films prior to the irradiation, the electric field induced strain and electromechanical coupling coefficient can become much higher along the stretching direction in comparison to the thickness direction or unstretched films. Furthermore, the changes in the phase transition properties with irradiation doses can also be affected markedly by stretching.<sup>13</sup> These findings raise the questions of what are the structural reasons behind the observed phenomena, and how the field induced strain and other electromechanical properties can be improved further.

For the P(VDF-TrFE) copolymers, it is well known that depending upon the molar content ratios of VDF ( $x$ ) and TrFE ( $1-x$ ) and on crystallization conditions, the copolymer can crystallize into polar ( $\beta$  phase) and nonpolar ( $\alpha$  phase).<sup>19</sup> The ferroelectric  $\beta$  phase consists of the polar packing of zigzag chains, while the  $\alpha$  phase is constructed with an arrangement of antiparallel  $TGTG'$  chains. For copolymers containing a VDF content of less than about 85%, the ferroelectric-paraelectric (F-P) transition lies below their melting temperature. At temperatures higher than the transition temperature (Curie temperature), the  $\beta$  phase is converted into a paraelectric phase with a random mixture of  $TG$ ,  $TG'$ , and  $TTTG$  conformations.

<sup>a)</sup>Electronic mail: vxh5@psu.edu



The effect of high-energy radiation such as gamma rays and electron beams on polymeric material has been intensively studied over the past several decades.<sup>20-22</sup> It was found that the  $\gamma$  irradiation improves the piezoelectric retention characteristics in uniaxially stretched and poled PVDF films.<sup>23</sup> It was observed that under very specific electron irradiation conditions, the P(VDF-TrFE) copolymer undergoes a solid phase transformation from the ferroelectric phase to a structure similar to the paraelectric phase.<sup>24</sup> Marked changes in the dielectric and mechanical properties in irradiated copolymers were also observed.<sup>25,26</sup> At high electron doses, P(VDF-TrFE) loses all crystallinity and becomes an amorphous polymer.<sup>24</sup> Although these studies provide useful results regarding changes in the crystalline phase and morphology of the VDF based polymers, no attempt has been made to investigate the changes in the ferroelectric response, and to link the structural changes to the changes in functional properties which are of most interest from both applied and fundamental points of view.

In this article, we will examine the evolution in the ferroelectric behavior of P(VDF-TrFE) copolymer with irradiation, and link them to the chemical and morphological changes in the copolymer due to irradiation. It is of great interest to understand the structural reasons for the appearance of relaxor ferroelectric behavior and directions for the further improvement of electro-mechanical properties in the irradiated copolymers. The composition chosen for this study is P(VDF-TrFE), 50/50 mol % copolymer. It was shown that among the compositions available to us and investigated earlier (50/50, 65/35, and 70/30 mol %), it is the only composition that can be converted to the relaxor ferroelectric by 2.55 MeV energy electrons in both stretched and unstretched films. One of the objectives here is to investigate the differences between unstretched and stretched films in various properties pertinent to the relaxor ferroelectric behavior and electromechanical responses in irradiated films. In parallel with the measurement of polarization hysteresis and dielectric properties, wide angle x-ray diffraction, thermal property measurement (differential scanning calorimeter, DSC data), crosslinking coefficient, and elastic modulus were also used to characterize the structural and morphological changes in the irradiated copolymer.

## II. EXPERIMENT

The P(VDF-TrFE) 50/50 mol % copolymer powder was supplied by Solvay and Cie, Bruxelles, Belgium, and the copolymer has a mean molecular weight of 200 000. The films were prepared by pressing the copolymer powder between aluminum foil at 215 °C and then cooled down to room temperature, either by quenching the sandwich in ice water or by slow cooling. The stretched films were prepared by uniaxially stretching the quenched films up to five times of their initial length at 25 °C. In order to improve the crystallinity, the stretched films were annealed under the clamped condition in a vacuum oven at 140 °C for 16 h. The electron irradiation was carried out in a nitrogen atmosphere with

2.55 MeV electrons at 95 °C with different irradiation doses, ranging from 40 to 100 Mrad. The film thickness ranged from 25 to 30  $\mu\text{m}$ .

The samples used for dielectric constant and polarization hysteresis measurement were sputtered with gold electrodes on both surfaces. The polarization hysteresis loops were measured using the Sawyer-Tower technique. An external electric field was applied in the form of triangular waveform with a frequency of 10 Hz and an amplitude of 160 MV/m. The dielectric measurements were carried out using a dielectric analyzer (TA instrument, Model No. 2870) in a frequency range from 30 Hz to 100 kHz and in a temperature interval of -60 to 120 °C. The DSC measurements were taken using a differential scanning calorimeter (TA instrument, Model No. 2010) at a scanning rate of 10 °C/min under a nitrogen atmosphere. The x-ray patterns were taken at room temperature (20 °C) using a Scintag diffractometer (model PAD-V) with Ni filtered Cu  $K\alpha$  radiation. The elastic modulus of the films was measured along the film direction (perpendicular to the film thickness) using a Dynamic Mechanical Analyzer (TA instruments, Model No. 2890) in a temperature range from -60 to 90 °C at 10 Hz frequency.

The measurement on the crosslinking factor was performed by measuring the gel content of irradiated films using the American standard test method (D2765-95) by placing the samples inside a Soxhlet Extractor and extracting with the methyl ethyl ketone at its boiling point for 12 h. After measuring the gel content, these films were kept in dimethyl foramide solution for ten days at room temperature in order to reach their equilibrium degree of swelling. The average molecular weight between crosslinks ( $M_c$ ), which is the representative of the crosslinking density was calculated using the following equations:

$$M_c = \frac{-\rho_2 V_1 \phi_2^{1/3}}{\ln(1 - \phi_2) + \phi_2 + \chi_1 \phi_2^2} \quad (1)$$

where  $\rho_2$  is the density of the polymer before swelling,  $V_1$  is the molar volume of solvent,  $\chi_1$  is the polymer-solvent interaction parameter, and  $\phi_2$  is the volume fraction of the polymer which is defined as

$$\phi_2 = \frac{W_2 / \rho_2}{W_1 / \rho_1 + W_2 / \rho_2} \quad (2)$$

where  $W_1$  and  $W_2$  are the weights of the polymer and solvent, and  $\rho_1$  and  $\rho_2$  are the densities of the polymer and solvent, respectively.<sup>27</sup>

## III. EXPERIMENTAL RESULTS AND DISCUSSION

### A. Polarization responses, x-ray, DSC, and crosslinking coefficient measurements on irradiated copolymers

#### 1. Polarization responses

Figures 1(a) and 1(b) compare the polarization hysteresis loops measured at room temperature, for unstretched and stretched films, as a function of irradiation dose. As can be seen, for unirradiated films, the polarization level of the stretched film is much higher in comparison to the unstretched films although it will be shown later that there is

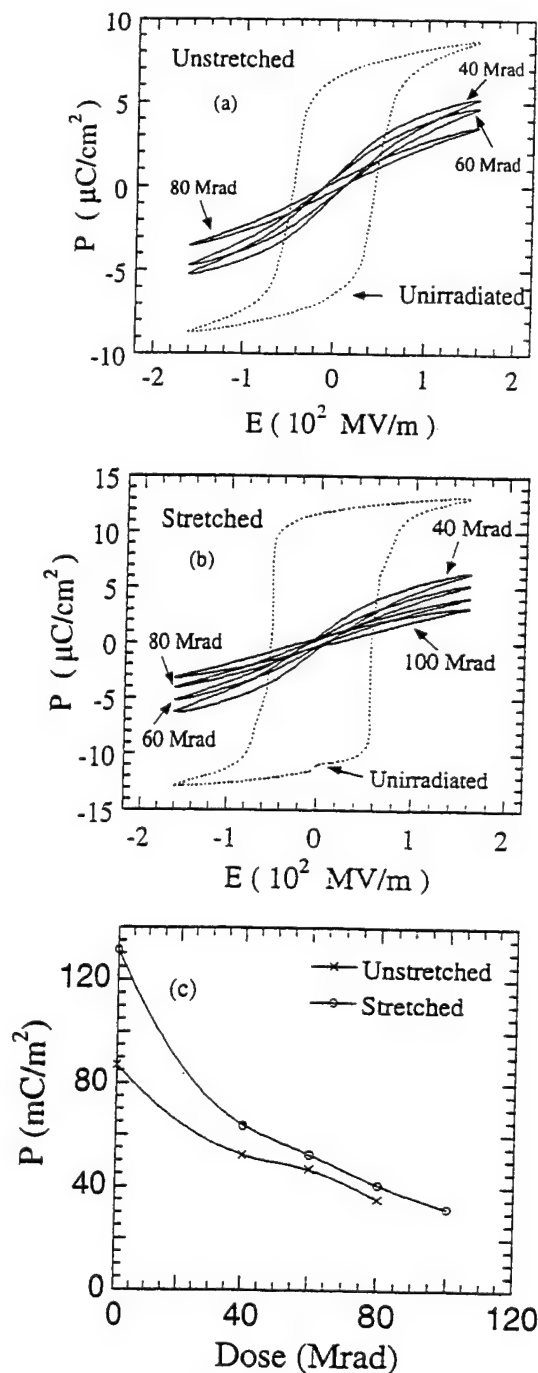


FIG. 1. Change in the polarization hysteresis loops measured for (a) unstretched, and (b) stretched, P(VDF-TrFE) 50/50 mol % copolymer films, unirradiated and irradiated at 95 °C with different doses. (c) Variation of polarization ( $P$ ) induced under the 160 MV/m electric field [obtained from (a) and (b)] with the irradiation dose.

not a large difference in the crystallinity between the two groups of samples. The result agrees with earlier studies and it arises due to a higher degree of crystalline orientation in the stretched films than in unstretched ones.<sup>28</sup>

After irradiation, the polarization hysteresis is reduced markedly for both unstretched and stretched films. The change of the field induced polarization  $P$  under 160 MV/m field as a function of dose is summarized in Fig. 1(c). For irradiated films, it can be seen clearly that there is not a large difference in the induced polarization level between the

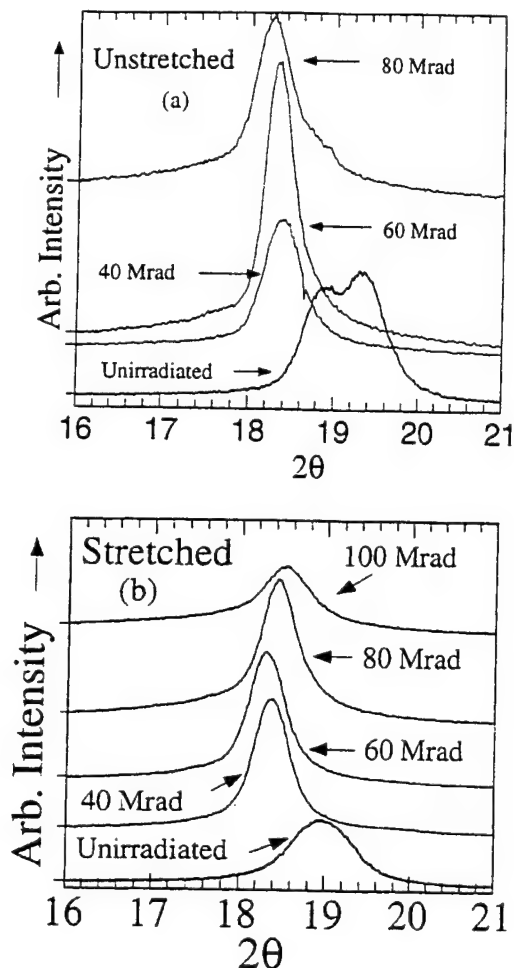


FIG. 2. X-ray diffraction pattern of (a) unstretched, and (b) stretched, P(VDF-TrFE) 50/50 mol % copolymer films irradiated with different doses at 95 °C.

stretched and unstretched ones after 40 Mrad irradiation. This is in sharp contrast with the unirradiated films where the stretched film exhibits a substantially higher polarization compared with the unstretched one. These results show that the enhancement of the polarization due to alignment of crystallites induced by stretching is nearly eliminated as a consequence of the irradiation. On the other hand, both DMA data (Figs. 9 and 10) and electric field induced strain data<sup>13</sup> show that the irradiation does not change the chain orientation markedly in stretched samples, at least in the range of 40 and 60 Mrad doses. Therefore, the large reduction of the polarization in stretched films due to irradiation suggests that the irradiation randomizes the crystallite orientation in directions perpendicular to the chain stretching direction.

## 2. X-ray results

Figures 2(a) and 2(b) present x-ray patterns of (200) and (110) reflections obtained from unstretched and stretched films irradiated under different doses. As expected, the unirradiated unstretched films exhibit two peaks at 4.72 and 4.59 Å ( $2\theta = 18.79^\circ$  and  $19.28^\circ$ ). The peak at 4.72 Å is from the hexagonal packing of 3/1-helical chains generated by TG and TG' defects, which are due to the presence of domain patterns and the second is due to similarly packed trans-



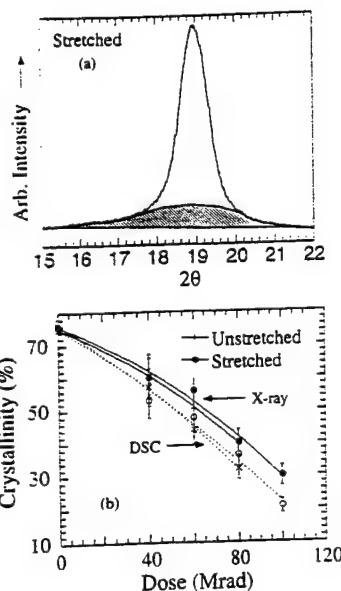


FIG. 3. (a) X-ray scan from unirradiated, stretched P(VDF-TrFE) 50/50 mol % copolymer films used to illustrate the calculation of crystallinity. The amorphous and crystalline regions were separated by fitting the Lorentzian function and are represented by shaded and nonshaded area respectively. (b) Change in the crystallinity with the irradiation dose calculated from x-ray [Figs. 2(a) and 2(b)] and DSC [Figs. 4(a) and 4(b)]. The symbols here are the data points and lines are drawn to guide points.

planar chains.<sup>19,29</sup> However, the stretched films show only one broad peak at 4.68 Å spacing and therefore, it indicates that the stretching not only eliminates the chain segments containing 3/1 helical conformation, but also packs more closely the chain segments that already are in the transplanar conformation.<sup>30</sup> The similar effect can also be observed by poling the unstretched films.<sup>30</sup> The broadening of the x-ray peak, in unirradiated films after stretching [Fig. 2(b)], suggests that in addition to reduction in the crystallite sizes, stretching also induces additional domain boundaries parallel to the polymer chains. This results in a reduction in the size of the coherent x-ray diffraction region for the (200) and (110) reflections.

After 40 Mrad of irradiation, only one peak is observed at a lower angle for both the unstretched and stretched films and thus clearly indicates the expansion of the lattice due to the introduction of defects in the crystalline phase during the irradiation. This is responsible for the observed change in the polarization hysteresis from a typical normal ferroelectric hysteresis loop to a slim polarization loop. After 60 Mrad irradiation, the peak appears at 4.84 Å for both unstretched and stretched films. The corresponding lattice spacing is close to the paraelectric phase as determined from x-ray data taken above the Curie temperature for unirradiated copolymer films and therefore, indicate the conversion of ferroelectric to a paraelectric-like phase at this dose.<sup>30</sup> It should be pointed out that, although macroscopically (from x-ray diffraction), the phase after irradiation is paraelectric like, the observed broad dielectric constant peak with Vogel-Fulcher dielectric dispersion behavior suggests that the phase resembles a relaxor ferroelectric with local polar regions (polar glass system).<sup>11</sup> The x-ray peaks become relatively more intense after 60 Mrad irradiation for unstretched films and after

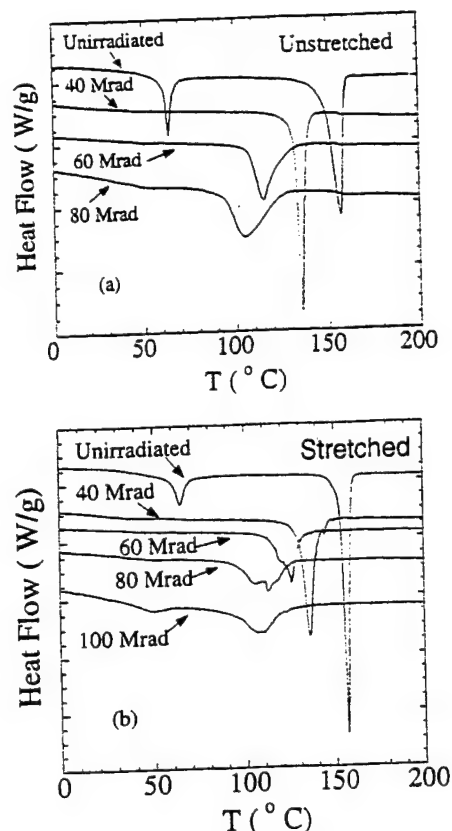


FIG. 4. DSC thermogram of (a) unstretched, and (b) stretched, P(VDF-TrFE) 50/50 mol % copolymer unirradiated, and irradiated with different doses at 95 °C.

80 Mrad irradiation for stretched films in comparison to the unirradiated films and the films irradiated with lower doses. The increase in the coherence length of x-ray diffraction is due to the disappearance of the macroscopic ferroelectric ordering.

Interestingly, at higher doses the x-ray peak moves back to higher angle and concomitantly the peak broadens, indicating the reduction of the crystallite size. The cause for the contraction in the lattice spacing between polymer chains is unclear. It might be related to the nature of the defects induced during the irradiation, which depend on the boundary conditions of the crystalline-amorphous interface and crystallite size. At high irradiation doses, the crystallite size becomes quite small and the shape of the x-ray peak becomes Lorentz type suggesting that the crystallite-amorphous interface is also quite diffused. In addition, peak area analysis, as shown in Fig. 3(a), indicates that at doses of 80 Mrad or higher, the crystallinity of the copolymer has been reduced to less than half as compared with the unirradiated films [Fig. 3(b)].

### 3. DSC results

In order to further quantify the change in the transitional behavior in irradiated samples, a DSC measurement was conducted on these samples. As expected, the thermal properties of the copolymer undergo a significant change after irradiation. Figures 4(a) and 4(b) summarize the DSC results obtained from unstretched and stretched copolymer films, re-

spectively. Being ferroelectric in nature, before irradiation both unstretched and stretched films exhibit two peaks. The peak at 63 °C is due to ferroelectric to paraelectric (F-P) transition, while the peak at 157 °C is due to the melting of crystals.<sup>31</sup> For unirradiated films, the crystal melting peak for stretched films is sharper and more intense than unstretched films and thus, reflects a higher crystalline ordering for stretched films. After the irradiation, the temperature and the enthalpy of the melting peak decrease continuously with the irradiation dose for both unstretched and stretched films. Assuming that the enthalpy of the melting is directly proportional to the crystallinity in the sample, the change of crystallinity with dose can be deduced<sup>32,33</sup> and is presented in Fig. 3(b). Clearly, the change of crystallinity with the dose acquired from the x-ray data, is consistent with that from the DSC data, although the DSC data yield a slightly lower crystallinity.

It is well known that the morphology of P(VDF-TrFE) copolymers is that of crystallites embedded in an amorphous matrix, which is analogous to a composite structure.<sup>4</sup> It is interesting to compare the results obtained here on the polarization and crystallinity (approximately the volume fraction of the crystallites in the polymer). Figure 5(a) presents the polarization  $P$  induced by 160 MV/m field as a function of crystallinity, which is taken from the averaged value of the DSC and x-ray data. Apparently, the initial drops of the crystallinity at low dose range (40 Mrad) causes a large reduction in the polarization in both stretched and unstretched films. As has been pointed out, the initial precipitant decrease of the polarization in the stretched films is also partly caused by the reduction in the crystallite orientation in the irradiation process. Therefore, if the crystallinity of the polymer under 40 Mrad dose can be raised, due to the high ratio of the polarization/crystallinity for the copolymer studied here at this particular dose the polarization level can be improved markedly, especially in stretched films.

For a composite system, there are many relationships describing the dependence of the dielectric properties of a composite with the properties of constituents. It was found that the logarithmic law of mixing of composites can fit most of the experimental data well,<sup>19</sup>

$$\log P = \nu_c \log P_c + (1 - \nu_c) \log P_a, \quad (3)$$

where  $P$  is the total polarization,  $P_c$  and  $P_a$  are the averaged polarizations of the crystallites and amorphous regions, respectively, and  $\nu_c$  is the crystallinity. The fitting of the data in Fig. 5(a) is shown in figure 5(b) where for the stretched films the data point from the unirradiated stretched film is not included because of its high crystallite orientation effect. Clearly, Eq. (3) fits the data quite well for both stretched and unstretched films. Surprisingly, the slopes of the curves from the two sets of data are nearly the same, indicating that  $P_c/P_a$  is nearly the same for both stretched and unstretched films. The parameters obtained in the fitting are,  $P_c = 144.5 \text{ mC/m}^2$  and  $P_a = 15.5 \text{ mC/m}^2$  for unstretched films, while for stretched films,  $P_c = 151.6 \text{ mC/m}^2$  and  $P_a = 18.4 \text{ mC/m}^2$ . The fact that  $P_c$  from irradiated stretched

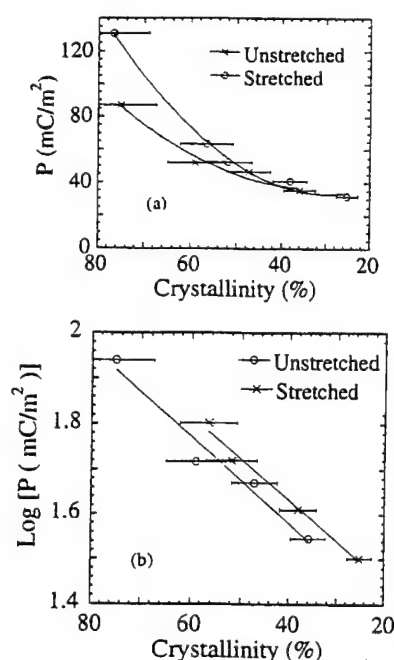


FIG. 5. (a) Change in polarization ( $P$ ) induced by 160 MV/m electric field with the averaged value of crystallinity obtained from the x-ray and DSC data [Fig. 3(b)]. (b) Fitting of the logarithmic law for unstretched and stretched P(VDF-TrFE) 50/50 mol % copolymer films after 40 Mrad irradiation at 95 °C. The solid line is the fitting and points are the experimental data obtained from (a).

films is only about 5% higher than that in unstretched films confirms that stretching does not have a marked effect on the polarization level in irradiated films.

In addition to the reduction of the crystallinity, the DSC peak associated with melting of crystals also broadens with doses. This indicates the presence of broad distribution in crystallite sizes and crystal ordering in irradiated films, which is due to the lattice defects and crosslinking in the copolymer.

In contrast to the DSC peak of the melting process for unirradiated films, the peak of F-P transition for the unstretched film is sharper with a higher transition enthalpy in comparison with the stretched film. This shows that the stretching process does introduce defects in the crystalline region, which have a much stronger effect on the polar ordering, but have a minimum effect on the crystalline ordering.

Consistent with the polarization data where there is very weak hysteresis for film irradiated with 40 Mrad dose, the DSC data show that the F-P phase transition peak almost disappears upon 40 Mrad irradiation for both stretched and unstretched films. Interestingly, a broad DSC peak reappears at temperatures near the original F-P transition peak position of unirradiated films when the dose is increased to 80 Mrad and beyond. This is consistent with the x-ray data where at high doses the x-ray peak moves back to higher angle. The finding here indicates that the structural defects introduced by irradiation in the crystalline region depends on the crystallite size and also the boundary conditions at the crystalline-amorphous interface.

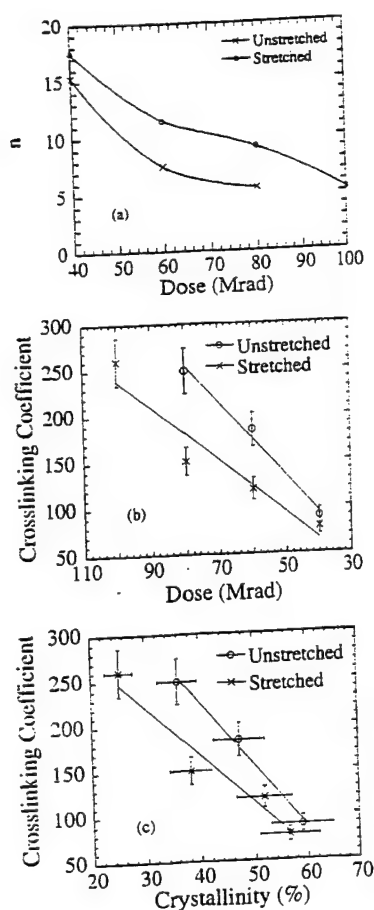


FIG. 6. (a) Variation in the number of repeating units ( $n$ ) between two crosslinks for unstretched and stretched P(VDF-TrFE) 50/50 mol % copolymer films irradiated with different doses at 95 °C. (b) Change in the crosslinking coefficient with (b) doses and (c) averaged value of crystallinity obtained from the x-ray and DSC data [Fig. 3(b)]. for unstretched and stretched P(VDF-TrFE) 50/50 mol % copolymer films irradiated at 95 °C. The solid lines are drawn to guide eyes.

#### 4. Crosslinking coefficient measurements results

Crosslinking coefficient (or crosslinking density) was measured to provide information on the effect of crosslinking on the properties investigated here. Figure 6(a) presents the change in the number of repeating units ( $n$ ) between two crosslink points along the chain in unit of  $-\text{CH}_2-\text{CF}_2-\text{CHF}-\text{CF}_2-$  as a function of dose for both stretched and unstretched films. The lower the value of  $n$  corresponds to the greater value of the crosslinking density. Clearly, with the same dose, the crosslinking density is much lower in the stretched films compared with unstretched films. In Fig. 6(b), the crosslinking coefficient, which is the number of crosslink per chain, is presented as a function of irradiation dose. For both unstretched and stretched films, the crosslinking coefficient increases with dose. The rate of the increase in the crosslinking coefficient for the stretched films at doses below 80 Mrad is a much lower than for the unstretched films. This indicates that the chain orientation introduced by stretching reduces the rate of crosslinking in the irradiation process. However, at doses from 80 to 100 Mrad, the rate of the crosslinking coefficient with dose for stretched films becomes higher than that for unstretched films. As has been shown, irradiation randomizes the orientation (crystal-

lites and polymer chains) induced by stretching, at high dosages the local chain orientation in stretched films may not be very much different from that in unstretched films.

Presented in Fig. 6(c) is the crosslinking coefficient as a function of crystallinity for the two sets of samples investigated. For both unstretched and stretched films, the crosslinking coefficient increases in proportion to the decrease in the crystallinity. Furthermore, even with the same crystallinity, the crosslinking coefficient of unstretched films is higher than that in stretched films. In other words, the reduction of the crystallinity in the copolymer under irradiation is not directly controlled by the crosslinking density, but it is expected that the crosslinking process has a significant role here in the conversion from the crystalline to amorphous phase.

The influence of crosslinking density on the ferroelectric behavior and polar ordering in the crystalline region is not clear. From the data presented, it seems that as far as the field induced polarization is concerned, the effect of crosslinking density is not significant and direct. However, the crosslinking density should have a direct effect on the crystallite size, which may affect the polar response in the copolymer when the size of crystallites becomes small.

### B. Dielectric and mechanical responses and relaxations

#### 1. Dielectric responses

To further elucidate the change in the ferroelectric related properties in the irradiated films, the weak field dielectric constant was measured on irradiated films as a function of irradiation dose. Figures 7(a) and 7(b) show the temperature dependence of the dielectric constant at 1 kHz for the films irradiated for different doses. Before irradiation, the dielectric constant for stretched films is higher than that of unstretched films, which is consistent with the polarization result and arises due to the higher dipolar orientation in the stretched films. After the irradiation, the dielectric peak of both unstretched and stretched films shifts towards a lower temperature in comparison to respective unirradiated film and therefore, increases the room temperature dielectric constant remarkably. In addition, the dielectric peak after irradiation becomes broader and exhibits a strong frequency dispersion [Fig. 8(a)]. As shown in Figs. 8(b) and 8(c) for both stretched and unstretched irradiated films, the dispersion follows Vogel-Fulcher law, an empirical law which holds for the systems undergoing freezing below certain temperature,  $T_f$ , such as glassy and relaxor ferroelectric materials.<sup>15</sup>

$$f = f_0 \exp \left[ \frac{-U}{k(T - T_f)} \right], \quad (4)$$

where  $T$  is the dielectric constant peak temperature,  $f$  is the corresponding frequency, and  $k$  is the Boltzmann constant. The fitting parameters obtained are summarized in Table I. If we regard that the Vogel-Fulcher law describes a thermally activated process with the activation energy approaching to infinity at  $T_f$ , Eq. (4) can be rewritten as,  $f = f_0 \times \exp(-\alpha/kT)$ , where for the polarization freezing process,  $\alpha = UT/(T - T_f)$  which leads to Vogel-Fulcher law. Hence,  $U$  is directly related to the activation energy  $\alpha$ .<sup>15</sup> The param-

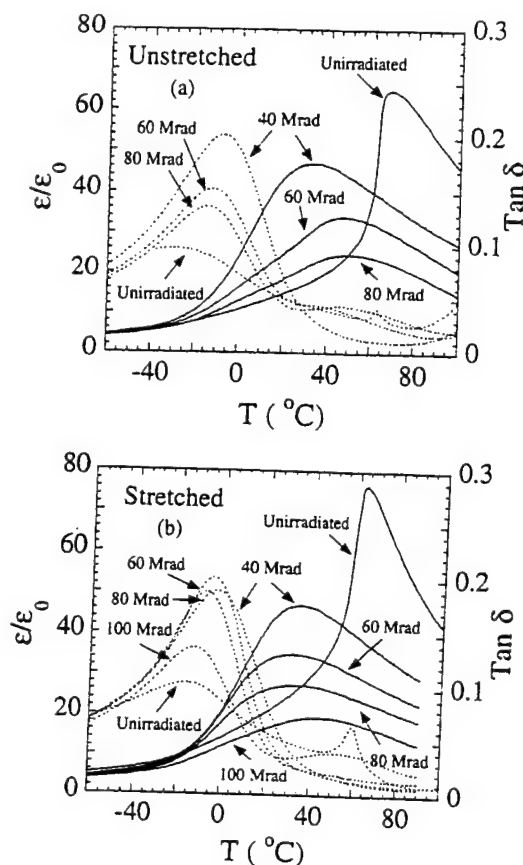


FIG. 7. Change in the dielectric constant (solid lines) and tangent loss (broken lines) measured at 1 kHz frequency as a function of temperature for P(VDF-TrFE) 50/50 mol % (a) unstretched, and (b) stretched films irradiated at 95 °C with different doses.

eter  $U$  for unstretched films and stretched films shows quite different values and it is higher in unstretched films than that in the corresponding stretched films. In addition, as the dose increases,  $U$  decreases monotonically.

Therefore, both the polarization and dielectric constant data suggest that the irradiation destroys the ferroelectric ordering and breaks the macro-polar domains into micropolar regions. The observed V-F type relaxation suggests that these local polar regions couple to each other and this coupling becomes stronger with the decreasing temperature. The decrease of  $U$  with the dose indicates the reduction in the polar-region size with irradiation. The observed upward shifting of  $T_f$  at high dosage suggests that the average polar ordering in these regions increases, which is consistent with the x-ray and DSC data presented.

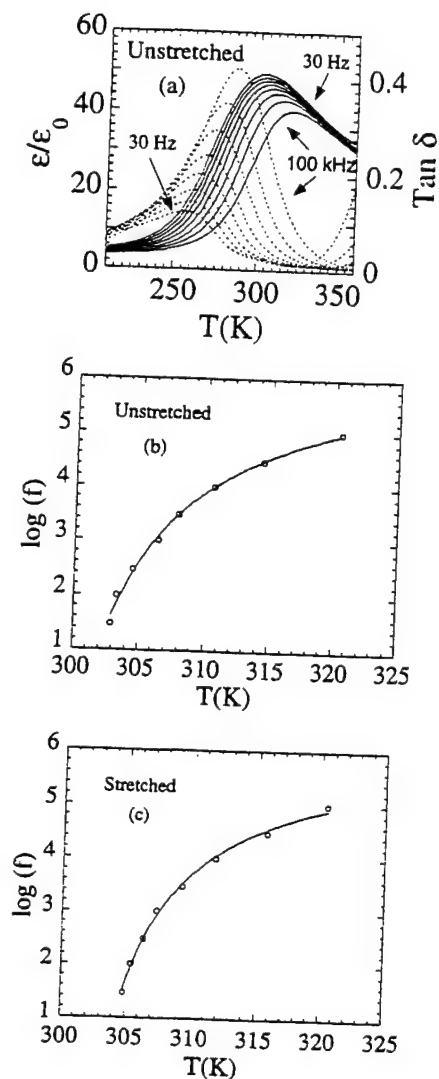


FIG. 8. (a) Dielectric constant (solid lines) and dielectric loss (broken lines) as a function of temperature for unstretched P(VDF-TrFE) 50/50 mol % copolymer films after 40 Mrad irradiation at 95 °C. The measuring frequencies (from top to bottom for dielectric constant and from bottom to top for dielectric loss) 30 Hz, 100 Hz, 300 Hz, 1 kHz, 3 kHz, 10 kHz, 30 kHz, and 100 kHz. Fitting of Vogel-Fulcher law for (b) unstretched, and (c) stretched P(VDF-TrFE) 50/50 mol % copolymer films after 40 Mrad irradiation at 95 °C. The solid line is the fitting and the circles are the experimental data.

## 2. Elastic responses

For electromechanical transduction applications, mechanical properties are of great importance. They also provide valuable information on the structural and relaxation processes in the material. Presented in Figs. 9 and 10 are the elastic modulus of unstretched and stretched films respec-

TABLE I. Fitting parameters of the V-F law for P(VDF-TrFE) 50/50 mol % irradiated copolymer.

Dose	Unstretched films			Stretched films		
	Crystallinity	$U$ ( $10^{-3}$ eV)	$T_f$ (K)	Crystallinity	$U$ ( $10^{-3}$ eV)	$T_f$ (K)
40	0.59	3.6	294.5	0.57	2.4	298.8
60	0.47	2.0	314	0.52	1.2	299.3
80	0.36	1.62	310	0.38	0.55	304
100				0.25	0.47	316

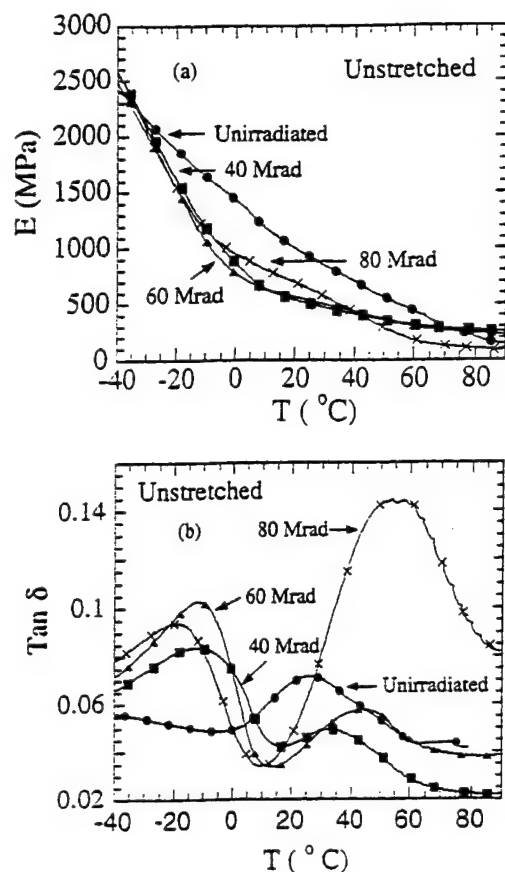


FIG. 9. Change in the (a) elastic modulus and (b) mechanical loss as a function of temperature for unstretched P(VDF-TrFE) 50/50 mol % copolymer, unirradiated, and irradiated at 95 °C with different irradiation doses.

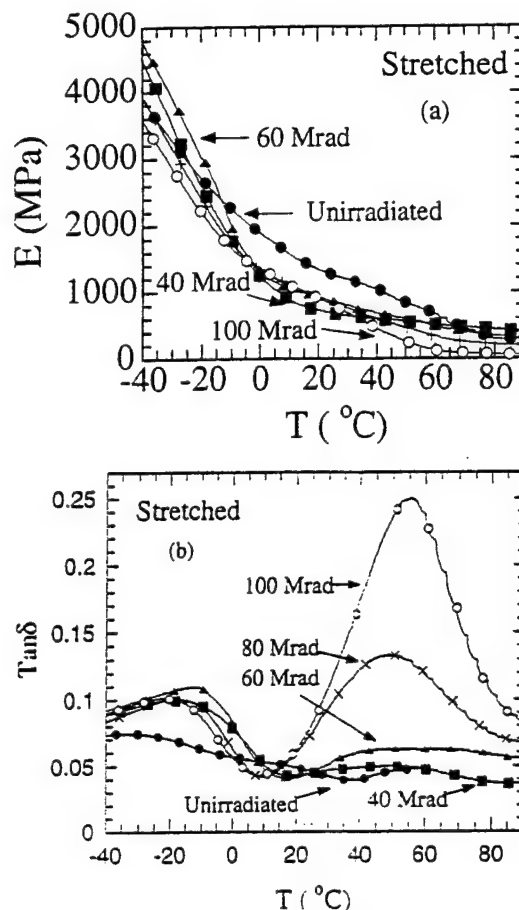


FIG. 10. Change in the (a) elastic modulus and (b) mechanical loss as a function of temperature for stretched P(VDF-TrFE) 50/50 mol % copolymer, unirradiated, and irradiated at 95 °C with different irradiation doses.

tively. For stretched films, only the modulus along the stretching direction is shown. As expected, stretched films [Fig. 10(a)] exhibit higher elastic modulus in the stretching direction in comparison to the unstretched films [Fig. 9(a)], which is due to the alignment of chains. After the irradiation, the elastic modulus is found to decrease with the irradiation dose in most of the temperature region. However, at low temperatures (below the glass transition, about  $-30$  °C), due to the crosslinking, the irradiated films exhibit higher modulus than unirradiated films. It is also interesting to note that for unstretched films irradiated with 40 and 60 Mrad and for stretched films irradiated with 40 Mrad dose, at temperatures above 10 and to 90 °C, which is the upper temperature range measured, the elastic modulus shows a very weak temperature dependence compared with unirradiated films. Above these doses, the films exhibit an increased room temperature modulus, presumably due to increased crosslinking density. The modulus decreases with temperature with a noticeable relaxation step at temperatures near 40 °C. In addition, after the irradiation, the elastic modulus of stretched films along the stretching direction remains higher compared with unstretched films (except at 100 Mrad).

We now discuss the relaxation processes in the films studied where the data from both the mechanical and dielectric losses will be used. In P(VDF-TrFE) copolymers, it is known that several relaxations exist, which depend on the molecular relaxations in amorphous, crystalline, and at the

crystal-amorphous interfaces.<sup>34</sup> Dielectric responses are from those relaxations in which motions of dipoles are involved, while the motions related to mechanical relaxations can be due to the non-polar processes. Therefore, as shown in an earlier study, the loss peak from the mechanical data may not be at the same temperature and frequency position as that from the dielectric data.<sup>35</sup>

In the temperature range studied, the mechanical tangent loss exhibits two relaxation peaks. Before irradiation two weak peaks around  $-40$  °C ( $\beta$ ) and  $30$  °C ( $\alpha$ ) are observed in unstretched films, which have been attributed in earlier studies to the molecular relaxation in amorphous and crystalline regions and/or crystalline amorphous interface boundaries [Fig. 9(b)]. While for unirradiated stretched films, these peaks are much weaker [Fig. 10(b)] due to the alignment of polymer chains. These mechanical relaxation peaks may be compared with the dielectric loss peaks [Figs. 7(a) and 7(b)]. A broad dielectric loss peak can be seen at temperatures near  $-30$  °C and a weak sharp peak at near  $65$  °C for unstretched films. For stretched films, a broad dielectric loss peak is at about  $-20$  °C and a relatively sharp loss peak at  $60$  °C. We believe that the sharp peak seen in the dielectric loss is associated with the F-P transition, which is not detected in the mechanical loss data and is also different from the high temperature broad relaxation seen in the mechanical loss data.



For irradiated films, the observed low temperature mechanical loss peak is mainly due to the glass transition in the polymer while the dielectric loss peak seems to be dominated by the frozen process of the polar regions, which diminishes in size as the dose increases (or the crystallinity decreases). The contribution of the glass transition to the dielectric loss is much weaker compared to the frozen process of the polar regions. On the other hand, the frozen process of the polar regions does not have a marked effect on the elastic properties, which is analogous to the DSC results.

The high temperature mechanical loss peak (at  $>30^\circ\text{C}$ ) does not show much increase for both stretched and unstretched films at doses of 40 and 60 Mrad [Fig. 9(b) and 10(b)] compared with unirradiated films. A large increase of loss peak is seen for films irradiated at 80 and 100 Mrad. In contrast, the dielectric loss peak for this relaxation is very weak. These results suggest that the relaxation process associated with this peak ( $\alpha$ ) is mainly due to the motions involving large chain segments. Therefore, at high doses with increased crosslinking density and diminishing crystallinity, a strong mechanical relaxation will occur resulting in a drop of the elastic modulus with a temperature, as observed near  $40^\circ\text{C}$  for unstretched films irradiated with 80 Mrad dose, and stretched films irradiated with 80 and 100 Mrad doses, and corresponding strong mechanical loss peaks.

#### IV. SUMMARY

The experimental results presented can be summarized as the following:

(1) The high-energy electron irradiation converts the polarization loop of the copolymer studied from the one with large hysteresis to a slim loop. The dielectric dispersion in the irradiated samples can be described well by the V-F law for both stretched and unstretched samples.

(2) Although in unirradiated samples, the polarization level and dielectric constant can be substantially increased by stretching but for irradiated films at doses above 40 Mrad, the induced polarization level does not show a large difference between stretched and unstretched films.

(3) In both stretched and unstretched samples, the dependence of the induced polarization  $P$  on crystallinity  $\nu_c$  can be described quite well by the logarithmic law of two component composites, indicating that the morphology of the irradiated copolymer consists of micropolar regions embedded in an amorphous matrix. The results also indicate that because of the high ratio of  $\Delta P/\Delta \nu_c$  at the low dose region, an increase in the crystallinity will result in a large increase in  $P$ .

(4) Although the irradiation nearly eliminates the enhanced polarization and dielectric response induced by stretching, the elastic modulus of stretched films remains higher compared with unstretched ones after the irradiation (at least for doses below 80 Mrad, indicating the difference in the molecular segment motions to the mechanical and electric responses. Similar differences between the electric and mechanical responses are also observed for the molecular relaxation processes in the copolymer.

(5) For unirradiated films, stretching improves the crystalline ordering while reduces the ferroelectric ordering as suggested by the DSC and x-ray data.

(6) Stretching can have a marked effect in reducing the crosslinking rate in the irradiation process and correspondingly, the crosslinking density of stretched samples is lower than that of unstretched samples. On the other hand, the crystallinity of stretched samples is nearly the same as that of unstretched films at the same irradiation dose. The reduction of crystallinity with irradiation does not have a direct link to the crosslinking process.

Therefore, during irradiation the changes in the structure and phase transition properties are mainly controlled by the two processes: one is the introduction of polarization defects which is responsible for the conversion from a normal ferroelectric to a relaxor ferroelectric phase and the other is the amorphization of the copolymer, which reduces the overall polar responses in the material. How to reduce the rate of the second process is crucial in order to further improve the electromechanical responses in the copolymer.

#### ACKNOWLEDGMENTS

The authors wish to thank Z.-Y. Cheng, R. Ting, and T. Ramontowski for stimulating discussions. This work was supported by the Office of Naval Research through Grant No. N00014-97-1-0900 and the National Science Foundation through Grant No. ECS-9710459.

- <sup>1</sup>T. Furukawa, *Adv. Colloid Interface Sci.* **71-72**, 183 (1997).
- <sup>2</sup>K. Tashiro and M. Kobayashi, *Phase Transit.* **18**, 213 (1989).
- <sup>3</sup>A. J. Lovinger, G. E. Johnson, H. E. Bair, and E. W. Anderson, *J. Appl. Phys.* **56**, 2412 (1984).
- <sup>4</sup>T. T. Wang, J. M. Herbert, and A. M. Glass, *The Application of Ferroelectric Polymers* (Blackie, Chapman and Hall, New York, 1988).
- <sup>5</sup>H. Ohigashi, K. Omote, and T. Gomyo, *Appl. Phys. Lett.* **66**, 3281 (1995).
- <sup>6</sup>K. Omote, H. Ohigashi, and K. Koga, *J. Appl. Phys.* **81**, 2760 (1997).
- <sup>7</sup>J. S. Green, B. L. Farmer, and J. F. Rabolt, *J. Appl. Phys.* **60**, 2690 (1986).
- <sup>8</sup>H. Ohigashi and K. Koga, *Jpn. J. Appl. Phys., Part 2* **21**, L455 (1982).
- <sup>9</sup>M. A. Marcus, *IEEE Trans. Electr. Insul.* **EI-21**, 519 (1986).
- <sup>10</sup>V. Bharti, T. Kaura, and R. Nath, *IEEE Trans. Dielectr. Electr. Insul.* **2**, 1106 (1995).
- <sup>11</sup>Q. M. Zhang, V. Bharti, and X. Zhao, *Science* **280**, 2101 (1998).
- <sup>12</sup>V. Bharti, X.-Z. Zhao, and Q. M. Zhang, *Mater. Res. Innovat.* **2**, 57 (1998).
- <sup>13</sup>Z.-Y. Cheng, T.-B. Xu, V. Bharti, S. Wang, and Q. M. Zhang, *Appl. Phys. Lett.* **74**, 1901 (1999).
- <sup>14</sup>H. Vogel, *Z. Phys.* **22**, 645 (1921); G. S. Fulcher, *J. Am. Ceram. Soc.* **8**, 339 (1925).
- <sup>15</sup>D. Viehland, S. J. Jang, and L. E. Cross, *J. Appl. Phys.* **68**, 2916 (1990).
- <sup>16</sup>L. E. Cross, *Ferroelectrics* **151**, 305 (1994).
- <sup>17</sup>L. E. Cross, *Jpn. J. Appl. Phys., Part 1* **34**, 2525 (1995).
- <sup>18</sup>K. Uchino, *Piezoelectric Actuators and Ultrasonic Motors* (Kluwer, Dordrecht, 1996).
- <sup>19</sup>H. S. Nalwa, *Ferroelectric Polymers* (Dekker, New York, 1995), Chaps. 2 and 11.
- <sup>20</sup>B. J. Lyons, *Radiat. Phys. Chem.* **45**, 159 (1995).
- <sup>21</sup>A. Chapiro, *Radiation Chemistry of Polymeric Systems* (Interscience, New York, 1962).
- <sup>22</sup>A. Charlesby, *Atomic Radiation and Polymers* (Pergamon, London, 1960).
- <sup>23</sup>T. T. Wang, *Ferroelectrics* **41**, 213 (1982).
- <sup>24</sup>A. J. Lovinger, *Macromolecules* **18**, 910 (1985).
- <sup>25</sup>B. Daudin, M. Dubus, and J. F. Legrand, *J. Appl. Phys.* **62**, 994 (1987).
- <sup>26</sup>F. Macchi, B. Daudin, J. Hillairet, J. Lauzier, J. B. N'goma, J. Y. Cavaille, and J. F. Legrand, *Nucl. Instrum. Methods Phys. Res. B* **46**, 334 (1990).
- <sup>27</sup>E. A. Collins, J. Bares, and F. W. Billmeyer, Jr., *Experiments in Polymer Science* (Wiley, New York, 1973).

- <sup>28</sup>V. Bharti, T. Kaura, and R. Nath, *IEEE Trans. Dielectr. Electr. Insul.* **4**, 738 (1997).
- <sup>29</sup>K. Tashiro, K. Takano, M. Kobayashi, Y. Chatani, and H. Tadokoro, *Ferroelectrics* **57**, 297 (1984).
- <sup>30</sup>A. J. Lovinger, T. Furukawa, G. T. Davis, and M. G. Broadhurst, *Polymer* **24**, 1233 (1983).
- <sup>31</sup>T. Yamada, T. Ueda, and T. Kitayama, *J. Appl. Phys.* **52**, 948 (1981).
- <sup>32</sup>T. Yagi, *Polym. J. (Tokyo)* **12**, 9 (1980).
- <sup>33</sup>K. Nakagawa and Y. Ishida, *J. Polym. Sci., Polym. Phys. Ed.* **11**, 2143 (1973).
- <sup>34</sup>T. Yagi, M. Tatemato, and J. Sako, *Polym. J. (Tokyo)* **12**, 209 (1980).
- <sup>35</sup>Q. M. Zhang, J. Su, C. H. Kim, R. Ting, and R. Capps, *J. Appl. Phys.* **81**, 2770 (1997).

# **APPENDIX 33**



# Transverse strain responses in the electrostrictive poly(vinylidene fluoride-trifluorethylene) copolymer

Z.-Y. Cheng, T.-B. Xu, Vivek Bharti, Shexi Wang, and Q. M. Zhang<sup>a)</sup>

Materials Research Laboratory and Department of Electrical Engineering, The Pennsylvania State University, University Park, Pennsylvania 16802

(Received 1 December 1998; accepted for publication 3 February 1999)

A large transverse electrostrictive strain  $S_1$  with a high elastic strain energy density is observed along the drawing direction in the stretched poly(vinylidene fluoride-trifluorethylene) copolymer film under a proper electron irradiation treatment condition, which results in a ratio of  $|S_1/S_3|$  larger than 1 where  $S_3$  is the longitudinal strain. In contrast, unstretched films generate a relatively small transverse strain with a small ratio of  $|S_1/S_3|$  ( $\sim 0.25$ ). Hence, in this copolymer system, the ratio of  $|S_1/S_3|$  can be varied over a broad range. In addition, a large volume strain, which amounts to about half of the longitudinal strain, is observed in the films investigated. © 1999 American Institute of Physics. [S0003-6951(99)03513-5]

Electroactive polymers with high strain response and high elastic energy density are very attractive for actuator and transducer technologies because of their mechanical flexibility, conformability, shock resistance, and low acoustic impedance.<sup>1</sup> Depending on application, either the longitudinal, or transverse strains, parallel to and perpendicular to the applied electric field, or both (volume strain) are utilized. In many applications, it is also highly desirable that a material can produce a high strain anisotropy, for example, a large longitudinal strain and a weak transverse strain response. This can be made use of to reduce the unwanted mechanical coupling or interference between different directions and to improve device reliability. Recently, we reported the finding that in the modified poly(vinylidene fluoride-trifluorethylene) (PVDF-TrFE) copolymer, a large longitudinal electrostrictive strain ( $S_3$ ) can be achieved.<sup>2,3</sup> In this letter, we present the observation of large transverse strain responses ( $S_1$ ) with an elastic energy density higher than that from  $S_3$  in this class of electrostrictive polymer.

The strain responses of the P(VDF-TrFE) copolymer at compositions of 50/50, 65/35, and 72/28 mol % were evaluated initially in this investigation. It was found that among them the copolymer 65/35 generated the highest transverse strain, and subsequently, a more detailed measurement was carried out on this composition on the ratio of  $|S_1/S_3|$ , volume strain, and other related properties. The results of this study will be reported in this letter.

The copolymers were from Solvay & Cie of Belgium. Thin films (about 20  $\mu\text{m}$  thick) were made using the solvent (DMF) cast method. Two types of films were used in the investigation, unstretched and stretched films. Unstretched films were directly annealed at 140 °C in a vacuum for 12 h after cast to remove residual solvent and improve the crystallinity. After annealing, the polarization hysteresis loop was measured, which has a remanent polarization, 71 mC/m<sup>2</sup>. The stretched films were prepared by uniaxially stretching the film at a temperature between 25 and 50 °C with a stretching ratio of five times. The films were annealed

afterwards at 140 °C in a vacuum for 12 h. For the stretched films, the measured remanent polarization is 117.6 mC/m<sup>2</sup>. The electron irradiation was carried out at N<sub>2</sub> atmosphere at temperatures ranging from room temperature to 120 °C with 3 MeV energy-level electrons. Au electrodes were sputtered on both surfaces of the film. The dielectric constant and elastic modulus were measured using a dielectric analyzer and a dynamic mechanical analyzer (TA Instrument, DEA2870 and DMA 2980), respectively. The transverse strain was characterized using a cantilever-based dilatometer and the longitudinal strain was measured by a piezoelectric bimorph-based dilatometer.<sup>4,5</sup> The frequency for the strain measurement is from 1 to 10 Hz and all the strain measurements were taken at room temperature.

Shown in Fig. 1 are the transverse and longitudinal strains of two unstretched films, one irradiated with a 140 Mrad dose at room temperature and the other with a 60 Mrad dose at 120 °C. The data in Fig. 1 are plotted as the ampli-

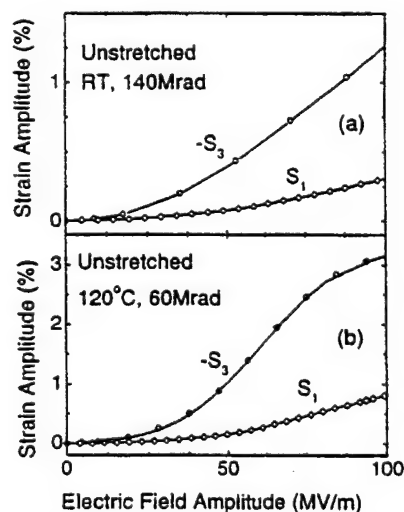


FIG. 1. The amplitude of electrostrictive longitudinal ( $S_3$ ) and transverse strain ( $S_1$ ) as a function of the amplitude of the applied field. The films were irradiated at room temperature with a 140 Mrad dose (a) and at 120 °C with a 60 Mrad dose (b), respectively. The data points are shown in the figure and the solid curves are drawn to guide the eyes.

<sup>a)</sup>Corresponding author. Electronic mail address: qxzl@psu.edu

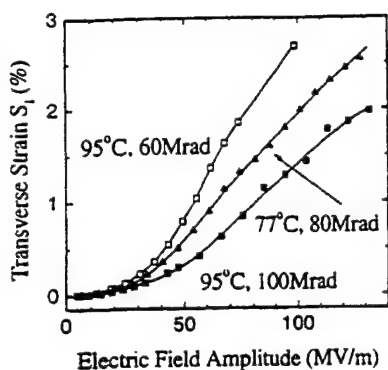


FIG. 2. The amplitude of transverse electrostrictive strain for stretched films measured along the drawing direction as a function of the amplitude of the applied field. The irradiation conditions are shown in the figure and the solid lines are drawn to guide the eyes.

tude of induced strain versus the amplitude of applied field. It should be mentioned that the film irradiated at 120 °C with the 60 Mrad dose shows the highest longitudinal strain among the films investigated when the applied field is 100 MV/m or lower.<sup>3</sup> One interesting feature of Fig. 1 is that in spite of a large difference in the strain levels between the two films, the ratio of  $|S_1/S_3|$  is nearly the same for both films (at 0.25). For most of the unstretched films examined, this ratio is in the range from 0.25 to 0.33, which is smaller than those in the conventional piezoceramics where the ratio is at about 0.4 or higher.<sup>6</sup> For P(VDF-TrFE), it is known that a change in polarization will result in a strain along the polymer chain direction in the opposite sign to that perpendicular to the chain direction. It is this cancellation effect of these two strains that produces a small transverse strain in the unstretched films. From the data in Fig. 1(b), the volume strain can be determined:  $S_v = -1.5\%$  under a field of 100 MV/m, which is about half of the longitudinal strain. The electrostrictive coefficients  $Q$  ( $S_i = Q_{i3}P^2$ , where  $P$  is the polarization,  $S_i$  is the strain, and  $i=1,3$ ) for the same film is also determined:  $Q_{33} = -12 \text{ m}^4/\text{C}^2$ ,  $Q_{13} = 3 \text{ m}^4/\text{C}^2$ , and  $Q_h = -6 \text{ m}^4/\text{C}^2$ , where  $Q_h (= Q_{33} + 2Q_{13})$  is the hydrostatic electrostrictive coefficient.

In contrast to the results in Fig. 1, the stretched films exhibit a much higher transverse strain response when measured along the stretching direction, and the results are presented in Fig. 2 where the data is presented as the amplitude of induced strain versus the amplitude of applied field. At 100 MV/m driving field, the transverse strain  $S_1$  can reach 2.7% for films irradiated at 95 °C with the 60 Mrad dose. At higher dosages, the strain is reduced, while at lower dosages, strain hysteresis was observed. The comparison between  $S_3$  and  $S_1$  is made in Fig. 3, and for the two films shown in Fig. 3 the ratio of  $|S_1/S_3|$  is 1.03 for the film irradiated at 95 °C with 60 Mrad and 0.8 for the film irradiated at 77 °C with 80 Mrad. Hence, the stretched films can have a transverse strain, the magnitude of which approaches that of the longitudinal strain. It is well known that uniaxial stretching of P(VDF-TrFE) copolymer films aligns the polymer chains along the drawing direction, which enhances the strain response in that direction.<sup>7</sup> The electrostrictive coefficients for the film irradiated at 95 °C with 60 Mrad, which exhibits the highest transverse strain among the films examined (under a field of

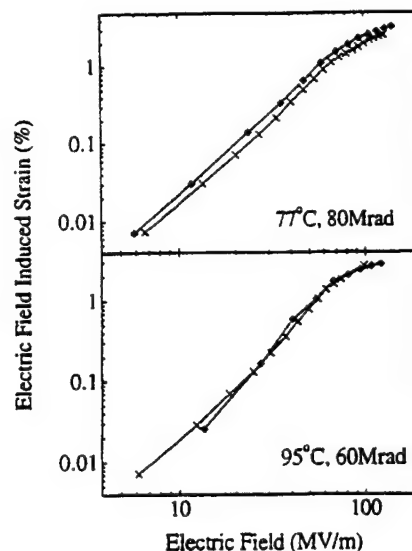


FIG. 3. Comparison between the transverse strain along the stretching direction ( $S_1$  shown as crosses) and the longitudinal strain ( $S_3$  shown as the diamond) for the stretched films. The solid curves are drawn to guide the eyes.

100 MV/m or lower), are evaluated:  $Q_{33} = -4.8 \text{ m}^4/\text{C}^2$  and  $Q_{13} = 4.9 \text{ m}^4/\text{C}^2$ .

To determine the elastic energy density, which is an important parameter for many actuator and transducer applications, the elastic modulus of these films was measured. The data for the unstretched film irradiated at 120 °C with the 60 Mrad dose and for the stretched film irradiated at 95 °C with 60 Mrad along the drawing direction are presented in Fig. 4. Clearly, the elastic modulus  $Y$  for the stretched film along the drawing direction is much higher than that of the unstretched film. At room temperature (20 °C), the stretched film has a modulus of 1.3 GPa, while the modulus for the unstretched film is 0.4 GPa. Based on these numbers, the elastic energy density of the two films, along with other data obtained here, are listed in Table I, where  $YS_i^2/2$  is the volumetric energy density (related to the device volume) and  $YS_i^2/2\rho$  is the gravimetric energy density (related to device weight),  $\rho$  is the density, and  $S_i$  is the strain level under 100 MV/m applied field along either the thickness ( $i=3$ ) or drawing direction ( $i=1$ ). Apparently, these strain levels and energy densities are improved markedly compared with the conventional piezoceramic and magnetostrictive materials and are

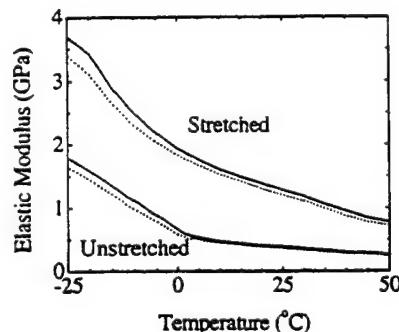


FIG. 4. The elastic modulus as a function of temperature for the stretched (irradiated at 95 °C with 60 Mrad) and the unstretched (irradiated at 120 °C with 60 Mrad) films. The dots and solid lines are the data measured at 1 and 10 Hz, respectively.

TABLE I. Summary of the electrostrictive properties of the 65/35 copolymer. The data were measured at a field of 100 MV/m.

	$S_3$ (%)	$S_1$ (%)	$S_v$ (%)	$Y$	$YS_1^2/2$ (J/cm <sup>3</sup> )	$YS_1^2/2\rho$ (J/kg)
Unstretched and irradiated at 120 °C with 60 Mrad <sup>a</sup>	-3.1	0.8	-1.5	0.4	0.19	95
Stretched and irradiated at 95 °C with 60 Mrad <sup>b</sup>	-2.6	2.7		1.3	0.47	237

<sup>a</sup>The energy density is calculated for the longitudinal strain  $S_3$ .<sup>b</sup>The energy density is calculated for the transverse strain along the drawing direction  $S_1$ .

several orders of magnitude better than those of the conventional P(VDF-TrFE) piezopolymers.<sup>2,8,9</sup> In addition, because of the high elastic modulus along the drawing direction, the elastic energy density is much higher along that direction compared with that along the thickness direction. It should also be pointed out that although the films reported here show a high value of strain and strain energy density under a field of 100 MV/m and a high ratio of induced strain/applied field, they are not the ones which generate the highest strain level and strain energy density under higher fields (>150 MV/m). In other words, the films capable of generating the highest strain are not the ones yielding the highest ratio of strain/applied field.

In our earlier publication, it has been shown that the irradiation transforms the polymer from a normal ferroelectric into a relaxor ferroelectric, which has a microscopic structure consisting of local polar regions (all transbonds) embedded in a nonpolar matrix.<sup>2</sup> The strain and polarization response can be from the expansion and contraction of these regions (similar to the transformation between a ferroelectric and paraelectric phase), from the reorientation of these regions, and from the pure dielectric response.<sup>10</sup> In addition, for polymers, the Maxwell stress effect, which is the deformation due to the electrostatic force, may also be significant.<sup>10,11</sup> For the unstretched film irradiated at 120 °C with 60 Mrad, the longitudinal strain due to the Maxwell stress effect is below 1% at 100 MV/m, which is much below the measured strain of -3.1% at this field. For the stretched films, the large strain and high elastic modulus along the stretching direction also rule out a large contribution from the Maxwell stress effect.

It is interesting to compare the results obtained here with the lattice strains in the crystalline region related to the para-to-ferro-electric-phase transition. For the P(VDF-TrFE)

65/35 copolymer, it has been shown that the averaged strain perpendicular to the chain direction is about -8% and along the molecular chain is about 10% when transformed from the high-temperature paraelectric to low-temperature ferroelectric phase, which results in a volume strain of about -6%.<sup>7,12</sup> Apparently, the strain obtained here is much lower than these values, which is partly due to the fact that the material has a semicrystalline morphology and the crystallinity of the films at the doses used here is below 50 vol %. In addition, the orientation of the local polar regions in the films is also spread out over a broad direction, which may reduce the averaged strain response and favor the reorientation of the polar regions under applied fields. For the reorientation of local polar regions in a nonpolar matrix, it will not generate much volume strain on the average.<sup>13</sup> Hence, the relatively large value of  $S_v$  observed in unstretched films indicates that the expansion and contraction of local polar regions (local transformation between polar and nonpolar phases) makes a significant contribution to the polarization and strain response. Interestingly, for stretched films, we also observed a volume strain which is about half of the longitudinal strain. On the other hand, the ratio of  $S_v/S_3 \sim 0.5$ , which is below the single-crystal value, may suggest that the reorientation of the local polar regions also contributes to the polarization and strain responses significantly.

Thanks are due to R. Y. Ting, J. Lindberg, G. Kavarnos, T. Ramotowski, and F. Tito for stimulating discussions. The financial support of this work by the Office of Naval Research under Grant No. N00014-97-1-0900 and NSF through Grant No. ECS-9710459 is greatly appreciated.

<sup>1</sup> T. T. Wang, J. M. Herbert, and A. M. Glass, *Applications of Ferroelectric Polymers* (Chapman and Hall, New York, 1988).<sup>2</sup> Q. M. Cheng, V. Bharti, and X. Zhao, *Science* **280**, 2101 (1998).<sup>3</sup> X. Zhao, V. Bharti, and Q. M. Zhang, *Appl. Phys. Lett.* **73**, 2054 (1998).<sup>4</sup> J. Su, P. Moses, and Q. M. Zhang, *Rev. Sci. Instrum.* **69**, 2480 (1998).<sup>5</sup> T.-B. Xu (unpublished).<sup>6</sup> B. Jaffe, W. Cook, and H. Jaffe, *Piezoelectric Ceramics* (Academic, New York, 1971).<sup>7</sup> T. Furukawa, *Phase Transit.* **18**, 143 (1989).<sup>8</sup> H. Wang, Q. M. Zhang, L. E. Cross, and A. O. Sykes, *J. Appl. Phys.* **74**, 3394 (1993).<sup>9</sup> T. Furukawa and N. Seo, *Jpn. J. Appl. Phys., Part 1* **29**, 675 (1990).<sup>10</sup> Z.-Y. Cheng (unpublished).<sup>11</sup> G. Kloos, *J. Phys. D* **28**, 939 (1995).<sup>12</sup> K. Tashiro, K. Takano, M. Kobayashi, Y. Chatani, and H. Tadokoro, *Ferroelectrics* **57**, 297 (1984).<sup>13</sup> Q. M. Zhang, H. Wang, N. Kim, and L. E. Cross, *J. Appl. Phys.* **75**, 454 (1994).

# **APPENDIX 34**

# Transverse strain responses in electrostrictive poly(vinylidene fluoride-trifluoroethylene) films and development of a dilatometer for the measurement

Z.-Y. Cheng, Vivek Bharti, T.-B. Xu, Shexi Wang, and Q. M. Zhang<sup>a)</sup>  
*Materials Research Laboratory, The Pennsylvania State University, University Park, Pennsylvania 16802*

T. Ramotowski and F. Tito  
*Naval Undersea Warfare Center, Newport, Rhode Island 02841*

R. Ting  
*Chemistry Department, University of Central Florida, Orlando, Florida 32816*

(Received 21 January 1999; accepted for publication 5 May 1999)

A dilatometer based on the cantilever beam concept has been developed. The dilatometer is easy to use and capable of measuring transverse strain response of soft polymer films in a broad strain range (from  $10^{-7}$  to  $10^{-1}$ ) without mechanical constraining of the sample. It is capable of detecting strain over a relatively wide frequency range from mHz to above 100 Hz under different load and temperature. Using the setup, the electric field induced transverse strains of the electrostrictive poly(vinylidene fluoride-trifluoroethylene) copolymer films were characterized which shows that a large transverse strain can be achieved in this class of polymer. In addition, the effect of mechanical tensile load on the transverse strain was also evaluated and the results show that the strain response will be affected by the load. However, depending on the load level, the strain response of the polymer film under a given electric field may increase or decrease with load. Based on the phenomenological theory, it is shown that for a ferroelectric based material, the mechanical load will shift the Curie temperature. Hence, to a large extent, the change of the strain response with load observed here can be understood by linking it to the strain change with temperature. © 1999 American Institute of Physics. [S0021-8979(99)00716-1]

## I. INTRODUCTION

Recently, it was found that a very large longitudinal electrostrictive strain (more than 4.5%) can be achieved in poly(vinylidene fluoride-trifluoroethylene) [P(VDF-TrFE)] copolymers under a proper electron irradiation treatment.<sup>1,2</sup> Furthermore, because of the relatively high elastic modulus, the polymer also exhibits a high elastic energy density which is crucial for many electromechanical actuator and transducer applications. These features represent a significant improvement in the electromechanical performance of this new material over the conventional electroactive ceramics and polymers.

For electromechanical applications,<sup>3</sup> in addition to the longitudinal response, the transverse response is also of great importance. In many devices operated in the longitudinal mode, a weak transverse strain response is desired which can reduce the mode coupling between the thickness direction and lateral directions for a thickness resonator or improve the device reliability. On the other hand, transverse strain responses are utilized in many areas and because the applied electric field is perpendicular to the strain direction, it offers a convenient means in generating actuation over large distances without the need to raise the driving voltage.

In this article, we report the measurement of transverse strain response in the newly developed electrostrictive

P(VDF-TrFE) copolymers. In order to characterize the strain response to high fields ( $\sim 50$  MV/m) without application of high voltages, thin polymer films of thickness about 20  $\mu\text{m}$  were used. One of the challenges in characterizing transverse strain response in thin polymer films is to measure the strain response in free-standing form over a broad range without introducing constraints.

In general, the strain measurement techniques can be grouped into two categories: contact methods and noncontact methods.<sup>4</sup> The contact methods such as strain gauge and linear variable differential transformer (LVDT) which are used for transverse strain measurement in inorganic materials will impose severe constraints on polymer films due to low elastic modulus of polymers compared with inorganic materials.

For the noncontact method, although in principle laser dilatometer can be used to characterize the transverse strain response in polymer films, to reflect the laser beam mirrors are needed on two ends of the film which is a very difficult task. In addition, the sample holding is another challenge for a soft polymer film.<sup>5</sup> Optical microscope offers a convenient means to characterize the transverse strain response.<sup>6</sup> However, its resolution is limited so that it cannot be used at low strain response region. In the case when a high applied electric field is required, and hence, the polymer film is immersed in insulation oil to increase the breakdown voltage, the operation of an optical microscope to obtain reliable results is quite difficult. In fact, these two methods have been tested and considered for transverse strain measurement of

<sup>a)</sup>Corresponding author, electronic mail: qxz1@psu.edu

newly developed polymer films and no satisfactory results can be obtained.

From both the application and fundamental understanding points of view, the electromechanical properties of an electroactive material under mechanical loads are important parameters. Thus, in developing a new technique or setup for characterizing the electromechanical behavior of materials, the capability of the setup working when the material is under mechanical loads should be an important concern.

In this article, we will first discuss the development of a new setup which is simple, convenient to use, versatile, and capable of measuring transverse strain response of polymer films over a broad strain range. The performance of setup was evaluated using the electric field induced transverse strains of both piezoelectric and electrostrictive polymeric films and the results show that the setup is capable of characterizing transverse strain responses of polymer films with a high sensitivity over a relatively wide frequency range (from near static to above 100 Hz). The electric field induced transverse strains of electron irradiated (PVDF-TrFE) 65/35 mol % copolymer films under different load conditions are also presented, which illustrates that for ferroelectric based electroactive materials, the main effect of external mechanical loads on the electromechanical responses can be understood from the shift of the ferroelectric-paraelectric transition temperature caused by the loads.

## II. DILATOMETER FOR TRANSVERSE STRAIN MEASUREMENT IN POLYMER FILMS

The setup developed for characterizing transverse strain response of polymer films is shown schematically in Fig. 1(a). The key part of the setup is a plastic cantilever which holds the polymer film to be measured under a slight tension as shown in Fig. 1(b). As seen from the figure, the polymer film to be tested has one end clamped at a solid base (fixed) and the other end attached to the free end of the plastic cantilever which is fixed at a solid base. When the polymer film is subjected to an electric field, its expansion and contraction cause the free end of the plastic cantilever to move which can be detected using optical technique. In the current setup, a photonic sensor (Model 2000, MTI Instruments) is employed. However, if needed, a laser dilatometer can be used here to probe the movement of the free end of the cantilever which will yield a great sensitivity. This is one of the advantages of this setup, that is, the displacement probe and mechanical holding part are two separate units and can be changed separately without affecting the other part.

The photonic sensor with the optic probe (MTI 2032R) has two sensitivity ranges: the sensitivity for range 1 is 0.019  $\mu\text{m}/\text{mV}$  and for range 2 is 0.137  $\mu\text{m}/\text{mV}$ . All the measurements were conducted at ac mode. The output signal of the photonic sensor was measured/recorded through a lock-in amplifier (SRS Model SR 830 DSP) at small strain region and/or a digital oscilloscope (LeCroy 9310A) at high strain region of polymer films. The output signal noise of the photonic sensor, whose working frequency is from dc to 100 kHz, is about 10 mV<sub>r-p</sub>. The working frequency of the lock-in amplifier is from 0.005 Hz to 100 kHz. The lock-in

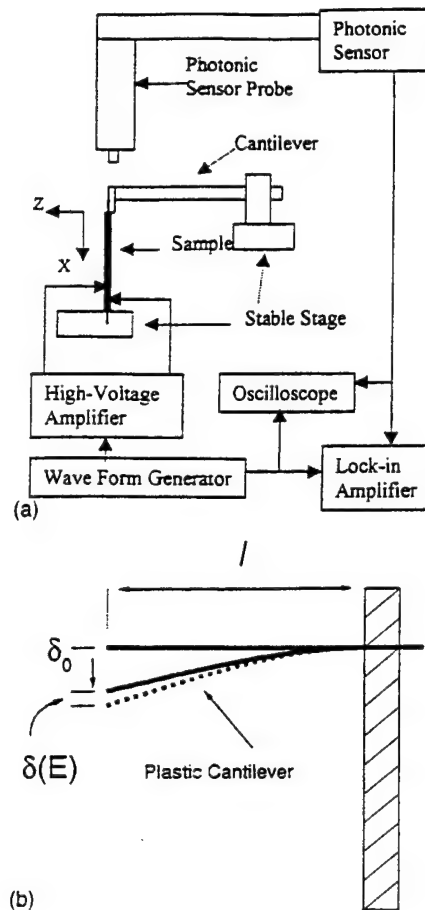


FIG. 1. Schematic of the setup (a), where the stable stage can move along  $x$ - $y$ - $z$  directions as well as rotate about the  $x$  axis. The displacement of cantilever's free end (b). In the experiment,  $\delta_0$  and  $\delta(E)$  are much smaller than  $l$ , the length of the cantilever.

amplifier has a dynamic reserve greater than 100 dB which makes it possible to measure a signal of a few  $\mu\text{V}$  in a 10 mV noise background.

We now proceed to describe the details of the setup. The symbols used are summarized here. For the polymer film under test,  $L$  is the length,  $t$  is the thickness,  $A$  is the cross section area, and  $E_s$  is the elastic modulus in the transverse direction. The typical values of  $t$ ,  $A$ , and  $L$  are about 20  $\mu\text{m}$ ,  $6 \times 10^{-2} \text{ mm}^2$ , and 12–15 mm, respectively. For the plastic cantilever,  $l$  is the length,  $h$  is the thickness,  $b$  is the lateral width, and  $E_c$  is the elastic modulus. For the data presented in this section, the values of  $b$ ,  $h$ , and  $l$  are about 6, 0.8, and 80 mm, respectively. The typical value of  $\delta_0$ , which is the static displacement of cantilever's free end from its equilibrium position as shown in Fig. 1(b), is 2 mm. The elastic modulus of the plastic cantilever used is about 5 GPa. For the plastic cantilever with one end firmly fixed, the deflection  $\delta_0$  at the free end will generate a static force ( $F$ ) which are related to each other as<sup>7</sup>

$$\delta_0 = \frac{1}{3} \frac{Fl^3}{E_c I}, \quad (1)$$

where  $I$  (in  $\text{m}^4$ ) is the inertia moment of the cantilever,



$$I = \frac{1}{12}bh^3. \quad (2)$$

Combining the two equations yields

$$\delta_0 = 4 \frac{Fl^3}{E_Cbh^3} \quad (3a)$$

or

$$F = \frac{E_Cbh^3}{4l^3} \delta_0. \quad (3b)$$

Because the polymer film is directly attached to the free end of the cantilever, this force will act as a static tensile load to the polymer film. Apparently, Eq. (3) shows that by adjusting  $\delta_0$ ,  $h$ , and other parameters of the cantilever, the mechanical load can be varied over a wide range. This is another advantage of this setup.

As the polymer film is subjected to an ac electric field, its expansion and contraction will induce a corresponding ac motion in the free end of the cantilever as shown by the dashed lines in Fig. 1(b). As long as this displacement  $\delta(E)$  is in the range " $\delta_0 + \delta(E) > 0$ ," the strain response of the film can be measured. For the piezoelectric PVDF and electrostrictive P(VDF-TrFE) copolymer films studied here,  $\delta(E)$  is in the range from 0 to  $-0.4$  mm. As the polymer film extends or contracts under applied fields, the free end of the cantilever will move as

$$\delta(E) = -L[d_{13}E + M_{13}E^2] - \frac{L}{AE_S} \frac{E_Cbh^3}{4l^3} \delta(E), \quad (4)$$

where  $E$  is the applied electric field (along the thickness direction, three-direction),  $d_{31}E$  describes the piezoelectric effect, and  $M_{13}E^2$  the electrostrictive effect in the polymer film, respectively.<sup>8</sup> The last term in Eq. (4) is due to the dynamic load from the cantilever since a change in  $\delta$  will cause change in the force level at the free end of the cantilever as shown in Eq. (3). In fact, this term can be made use of to evaluate the change of the elastic modulus of the polymer film with external load. The measured transverse strain response of the polymer film is

$$S(E) = \frac{-\delta(E_3)}{L} = \frac{d_{13}E + M_{13}E^2}{1 + \Delta}, \quad (5)$$

$$\Delta = \frac{S_0L}{\delta_0} = \frac{E_Cbh^3}{4l^3} \frac{L}{AE_S},$$

where,  $\Delta > 0$ ,  $S_0$  is the static strain of the sample corresponding to the static load originated from the static displacement ( $\delta_0$ ) of cantilever's free end. In the current setup,  $\Delta$  is much smaller than 1 (on the order of 0.001) and hence, the strain response can be linked directly to the piezoelectric and electrostrictive coefficients of the polymer evaluated, i.e.,

$$S(E) = d_{31}E + M_{13}E^2. \quad (6)$$

Equation (6) expresses the transverse strain response under an external electric field  $E$  for a film under a constant mechanical stress. In present case, the constant stress on the sample originates from the static force which is determined by the static displacement ( $\delta_0$ ) of cantilever's free end as

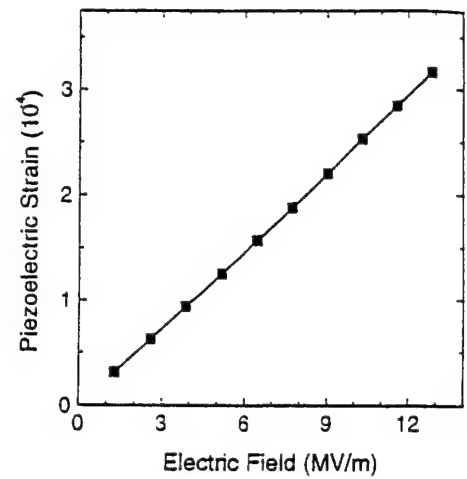


FIG. 2. Transverse strain of pure PVDF piezoelectric film under different electric fields of 1 Hz at room temperature.

shown in Eq. (3). Since, for most electroactive materials, both  $d_{13}$  and  $M_{13}$  will depend on the stress (load),<sup>9,10</sup> the dilatometer can be used to characterize the electromechanical properties of polymeric films under different load conditions.

In the case of a sample possessing electrostrictive and piezoelectric activities, it is hard to separate the contribution from the electrostrictive and piezoelectric effects using an oscilloscope. However, one can still use a lock-in amplifier to separate and identify the contribution to the strain response from the electrostrictive and piezoelectric effects, respectively. If the applied electric field on the sample is a sine wave, the first-harmonic response of the lock-in amplifier is corresponding to the contribution from the piezoelectric effect, while the second harmonic response of the lock-in amplifier is corresponding to the contribution from the electrostrictive effect.

In the setup, special consideration and design were made so that the film under test can be immersed in an oil chamber, which serves to increase the breakdown electric field so that the measurement can be carried out to high fields. Thus, the temperature of the sample is the same as the temperature of the oil. Since the temperature of the oil can be easily changed, the setup can be used to evaluate the transverse strain responses of polymer films with temperature. During the development of the setup, it was found that in order to reduce the error in the measured strain response, it is necessary to keep the film flat. Therefore, a stage which is capable of translating the cantilever in three orthogonal directions as well as rotation in one of the axes is used.

The setup is calibrated using a commercial piezoelectric PVDF film whose  $d_{31}$  value is known. As shown in Fig. 2, the strain versus applied field exhibits a linear curve, indicating the response is piezoelectric as expected. The piezoelectric coefficient  $d_{13}$  is determined through the electric field strength and measured transverse strain. The results are consistent with the value from the manufacturer.

The displacement sensitivity was also evaluated using the newly developed electrostrictive P(VDF-TrFE) 65/35 mol % copolymer and the results are presented in Fig. 3. The data were obtained at 1 Hz applied field with the time con-

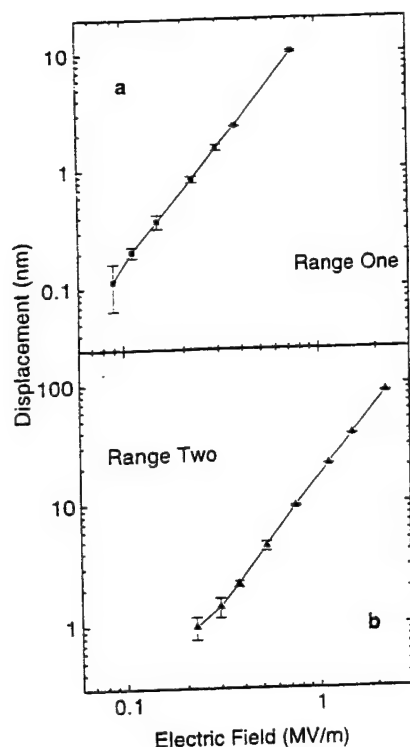


FIG. 3. Displacement sensitivity of the system when the photonic sensor is in the range one and two.

stant of 30 s for the lock-in amplifier. For the range 1 of the photonic sensor, the lowest measurable displacement is about 0.1 nm, while for the range 2, it is about 1 nm. Considering a fact that  $L \approx 10$  mm, the results indicate that the setup is capable of measuring transverse strain to  $10^{-7}$  range. On the other hand, the photonic sensor used here can measure displacement up to 0.7 mm range which corresponds to a strain in polymer films of 0.07. However, photonic sensors with the upper range to more than 5 mm is commercially available. Clearly, the separation of the sample holding unit and displacement sensing unit in the set up enables us to characterize the strain in polymer films over a very wide range. In addition, the linear log-log plot of the data in Fig. 3 implies that the strain response of the polymer follows  $S(E) = M_{13}E^n$  relation (power law) and slopes yield  $n = 1.99$  and  $n = 2.08$ , respectively, which is consistent with the longitudinal strain data on the similar films measured in the low field range ( $< 10$  MV/m) and shows that the response is electrostrictive ( $n = 2$ ).<sup>2</sup> The electrostrictive coefficient  $M_{13}$  calculated from the data in Fig. 3 is  $1.9 \times 10^{-18} \text{ m}^2/\text{V}^2$ .

The operation frequency range is another concern when developing a strain measurement set up. At the low frequency end, the frequency limit depends on the frequency range of a lock-in amplifier and the strain level of the sample. The limiting frequency for the former is 0.005 Hz in the present system. And the later is caused by the increased noise of the environment which has approximately  $1/f$  spectrum, where  $f$  is frequency. On the high frequency end, the operation frequency is limited by the resonance frequency ( $f_1$ ) of the cantilever. The lowest resonance frequency of a cantilever with one end fixed and the other free is given by<sup>11</sup>

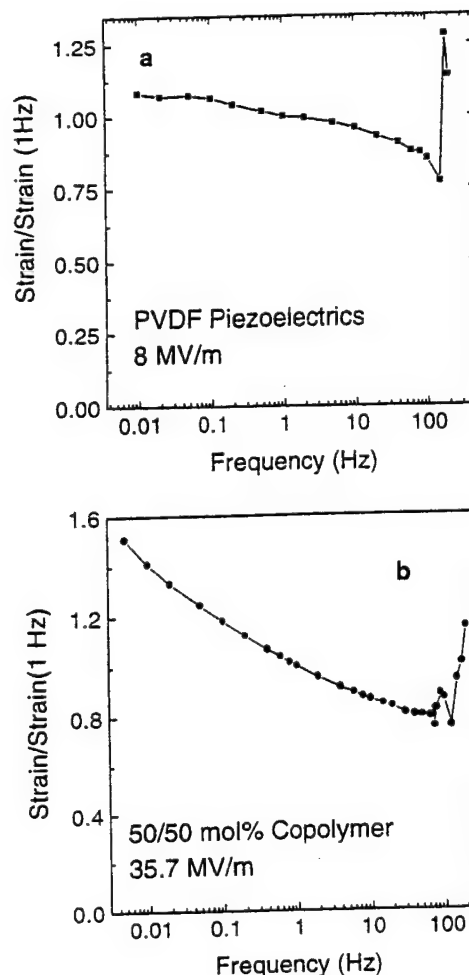


FIG. 4. Frequency dependence of the electric field induced transverse strain of a PVDF piezoelectric film and (b) P(VDF-TrFE) electrostrictive film under a constant electric field.

$$f_1 = 0.16154 \frac{h}{l^2} \sqrt{\frac{E_c}{\rho}}, \quad (7a)$$

while the lowest resonance frequency of a cantilever with two ends fixed is determined by<sup>11</sup>

$$f'_1 = 1.0279 \frac{h}{l^2} \sqrt{\frac{E_c}{\rho}}, \quad (7b)$$

where  $\rho$  (in  $\text{kg}/\text{m}^3$ ) is the density of the plastic probe used. Since in our setup, one end of the cantilever is fixed firmly at a base and another end is not totally free (attached to the polymer film), the resonance frequency should be somehow in between the  $f_1$  and  $f'_1$  of Eq. (7).

Therefore, as the polymer film is driven electrically with increasing frequency, a series of resonance in the cantilever will be excited. For example, the frequency response data using the commercial piezoelectric PVDF film as the polymer sample attached to the cantilever probe is presented in Fig. 4(a). A resonance was observed at a frequency of the ac driving electric field at about 170 Hz for a cantilever beam with  $\rho = 1.47 \times 10^3 \text{ kg}/\text{m}^3$  and  $E_c = 5 \text{ GPa}$ , and the result is in accord with what was expected from Eq. (7). The weak frequency dependence of the piezoelectric coefficient at frequencies below 50 Hz as shown in Fig. 4(a) is consistent



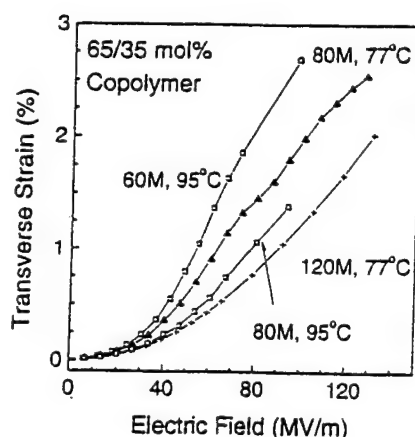


FIG. 5. Electric field dependence of the transverse strain measured at room temperature for stretched 65/35 mol % P(VDF-TrFE) copolymer films under different electron irradiation conditions.

with what measured in a thick copolymer sample (mm thickness) of P(VDF-TrFE) 75/25 mol % piezoelectric copolymer.<sup>5</sup> With the same probe, the frequency dependence of transverse strain response of a newly developed electrostrictive copolymer film under a field of 35.7 MV/m [P(VDF-TrFE) 50/50 mol % irradiated at 95 °C with 100 Mrad dose] was also characterized. As shown in Fig. 4(b), there is a resonance at a frequency near 90 Hz of the ac driving electric field. The apparent lowering of the resonance frequency here is caused by the electrostrictive response of the polymer film ( $S = ME^2$ ) which generates a mechanical motion of  $2f$  frequency when the driving electric field has a frequency  $f$ . Apparently, at below 50 Hz, the effect of the resonance to the measured data is negligible here. By adjusting the dimension of the cantilever probe, one can raise the resonance frequency to above 500 Hz which makes it possible to characterize the transverse strain response of a polymer film up to more than 100 Hz if needed.

### III. TRANSVERSE STRAIN RESPONSE OF IRRADIATED P(VDF-TRFE) 65/35 COPOLYMER

In this section, the change of the transverse strain of stretched films ( $5\times$  stretching ratio) of P(VDF-TrFE) 65/35 copolymer with mechanical load was evaluated. Shown in Fig. 5 is the transverse strain response as a function of applied field measured at room temperature for films with different irradiation conditions under load free condition. Clearly, the response depends strongly on the irradiation condition.

With regard to electroactive materials for electromechanical applications, although the electric field induced strain response at load free condition is important to understand and to characterize the materials behavior, the material response when subjected to external load is crucial for most of the device applications. Needless to say, the information is also valuable from a basic understanding point of view. Here, the film irradiated at 95 °C with 60 Mrad dosage is examined under different mechanical load conditions, since this is the one that exhibits the best transverse strain response at load free condition as seen from Fig. 5. In order to vary

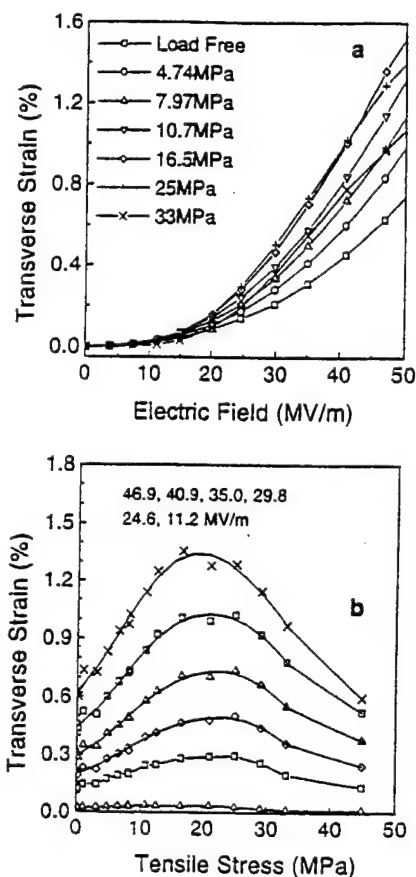


FIG. 6. Load effect on the electric field induced transverse strain response measured at room temperature with applied electric field of 1 Hz for 65/35 mol % P(VDF-TrFE) copolymer film irradiated at 95 °C with 60 Mrad dosage (a). The relation between the strain response and electric field for films under different loads (b). The relation between strain response and static load for films at different electric field strengths. Symbols in figure express the measured data, while solid lines in figure are drawn to guide eyes.

the mechanical load over a broad range, plastic cantilever beams with thickness from 0.8 to 4 mm were used. The  $E_c$  of the plastic trips is from 2.5 to 6 GPa. In addition, the static displacement ( $\delta_0$ ) of cantilever's free end was varied from 2 to 6 mm. Thus, the static tensile load on the polymer film can change from nearly zero to more than 45 MPa.

The relation between the electric field and the transverse strain response for the sample under different static tensions is shown in Fig. 6(a). The static tension dependence of electric field induced strain for the same material at different external electric fields is shown in Fig. 6(b). In these experiments, the load (stress) was along the stretching direction of the copolymer film and the transverse strain was also measured along the stretching direction. Although the strain response of a sample at the same electric field strongly depends on the static tension, it is found that the strain response for the sample under different static load conditions still linearly depends on the square of the electric field strength. This is what is expected from the electrostrictive effect.<sup>1,2</sup> However, the electrostrictive coefficient depends strongly on the static load.

The results in Fig. 6 indicate that for a given field, the transverse strain increases with load initially and then decreases with the load after reaching the maximum. For the

polymer studied here, the electric field induced strain response mainly originates from the phase changes from a non-polar to a polar phase under external electric field.<sup>1,12,13</sup> Hence, this load dependence behavior can be understood based on how this change is affected by the load.

Before the electron irradiation, the copolymer exhibits typical first-order phase transition from para- to ferro-electric phase.<sup>1,14</sup> However, after the electron irradiation, the physical properties of the copolymer are very similar to that of relaxor ferroelectrics. For example, the dielectric constant maximum temperature ( $T_m$ ) and dielectric loss maximum temperature ( $T_m'$ ) are strongly dependent on the frequency; and at the same frequency  $T_m$  is higher than  $T_m'$ .<sup>1</sup> These are the basic features of dielectric relation phenomena observed in relaxor ferroelectrics.<sup>15</sup> In addition, it was found that the relation between  $T_m$  and frequency for these copolymers follows well the Vogel–Fulcher law.<sup>1,16</sup> The Vogel–Fulcher law was widely used in relaxor ferroelectrics to express the relation between  $T_m$  and frequency.<sup>17</sup> More importantly, it was found that these copolymers exhibit a slim polarization hysteresis loop, that the remanent polarization gradually increase with decreasing temperature, and that the ferroelectric state can be observed at low temperature.<sup>1,17</sup> These are exactly the polarization behaviors observed in relaxor ferroelectrics.<sup>18</sup> With regard to the ferroelectric behavior of the relaxor ferroelectrics, it is found that the depolarization temperature ( $T_d$ ) is generally lower than  $T_m$  by a few tens degrees.<sup>19</sup> It was found that  $T_d$  for the copolymer studied here is about 40–60 °C lower than  $T_m$ .<sup>16</sup>

For relaxor ferroelectrics, it is known that the local phase transition temperature (or the freezing temperature of the polar region) is distributed in a very broad range and that the density of the frozen polar regions increases with decreasing temperature.<sup>18,19</sup> In addition, the volume density of the frozen polar regions increases with external electric field, which is also called the electric field induced phase transition.<sup>19</sup> That is why the large electrostrictive coefficient was obtained in relaxor ferroelectrics.<sup>20</sup> Therefore, the dielectric behavior and the electric field induced strain response strongly depends on the temperature. It is believed that the density of the frozen polar region is relatively higher and the interaction between the frozen polar regions is still not high at temperatures near  $T_m$ .<sup>19</sup> However, at temperatures lower than  $T_d$ , most of the polar regions are frozen and the interaction among the frozen polar regions is relatively high. Thus, both  $T_m$  and  $T_d$  can be used as parameters to characterize the average phase transition temperature of local transition between para- and ferroelectric phases. For the material studied here, the  $T_m$  is about 27 °C at 30 Hz as measured from the dielectric data.<sup>21</sup> It has been observed that for the relaxor ferroelectrics under a relatively high driving electric field, the induced strain increases as the temperature is lowered towards  $T_d$ .<sup>22</sup> However, as the temperature is lowered further, the strain response will decrease due to increased 180° domain wall motions associated with the macropolarization switching.

Based on Devonshire phenomenological theory, for a ferroelectric material under a stress  $X_i$  and with a polarization ( $P_3$ ) along “3” direction, if only consider the contribu-

tion to the free energy of the system from the electrostrictive effect (first order approximate),<sup>23</sup> the shift of phase transition temperature with stress is

$$\Delta T = 2\varepsilon_0 C Q_{i3} X_i, \quad (8)$$

where  $\Delta T = T_c(X_i) - T_c(0)$ ,  $\varepsilon_0 = 8.85 \times 10^{-12}$  F/m,  $C$  is the Curie–Weiss constant,  $Q_{i3}$  is the electrostrictive coefficients defined as  $S_i = Q_{i3} P_3^2$ , and  $T_c$  is the Curie temperature. Although the Eq. (8) is written for a single-crystal normal ferroelectrics, the trend should be the same also for the relaxor ferroelectrics considering the microstructure of the relaxor ferroelectrics. For relaxor ferroelectrics, the stress will shift both  $T_m$  and  $T_d$  and the direction of the shifting will depend on the sign of  $Q$ , the electrostrictive coefficient. For the polymer investigated here,  $Q_{i3} > 0$  and the applied stress is  $X_i > 0$ . Thus, Eq. (8) shows that  $\Delta T > 0$ . That is, both  $T_m$  and  $T_d$  of the sample will move to a higher temperature with the tensile load.

This result indicates that the measured strain responses at room temperature for films under different load are, to a large extent, equivalent to the strain responses measured at different temperatures under stress free condition. Since  $T_m$  for the polymer under free stress condition is close to room temperature, the measured strain response will increase with tensile stress. This is what was obtained at the low load range as shown in Fig. 6. However, as the load increases further which moves  $T_d$  to higher than room temperature, the strain response will decrease. Below  $T_d$ , most of polar regions are frozen and the interaction among the frozen polar regions is very high. Thus, the contribution to the electric field induced strain from the para- to ferro-electric phase transition decreases. This is why the electrostrictive response decreases with load in the high load region as shown in Fig. 6.

#### IV. SUMMARY

A new dilatometer is developed for characterizing the electric field induced transverse strain of free-standing polymer films under different load conditions and at different temperatures. The setup is easy to use, can be operated in a broad strain range with high sensitivity, and has a reasonable operation frequency range, from mHz to above 100 Hz. Using the dilatometer, the electric field induced transverse strains of high energy electron irradiated P(VDF-TrFE) films were characterized. It was found that a high transverse strain response can be achieved in this class of material which depends crucially on the irradiation condition. It was also found that the field induced strain will change with external load. For example, for P(VDF-TrFE) 65/35 mol % copolymer irradiated at 95 °C with 60 Mrad dosage, the transverse strain measured at room temperature increases with tensile load initially until a load near 15 MPa, beyond that the strain decreases slowly with the load. Based on Devonshire phenomenological theory, it can be shown that for the polymer investigated here, the tensile stress will favor the low temperature phase and the change of the strain with load can be understood qualitatively from the shifting of  $T_m$  and  $T_d$  due to the load. In general, for ferroelectric based materials, the

dependence of strain response with load can be understood from the shifting of the Curie temperature with stress.

## ACKNOWLEDGMENTS

This work was supported by the National Science Foundation through Grant No ECS-9710459 and the Office of Naval Research through Grant No N00014-97-1-0900.

- <sup>1</sup>Q. M. Zhang, V. Bharti, and X. Zhao, *Science* **280**, 2101 (1998).
- <sup>2</sup>X. Zhao, V. Bharti, Q. M. Zhang, T. Romotowski, F. Tito, and R. Ting, *Appl. Phys. Lett.* **73**, 2054 (1998).
- <sup>3</sup>J. M. Herbert, *Ferroelectric Transducers and Sensors* (Gordon and Breach, New York, 1984).
- <sup>4</sup>J. Su, P. Moses, and Q. M. Zhang, *Rev. Sci. Instrum.* **69**, 2480 (1998).
- <sup>5</sup>H. Wang, Ph.D. thesis, The Pennsylvania State University, 1994.
- <sup>6</sup>R. E. Pelrine, R. D. Kornbluh, and J. P. Joseph, *Sens. Actuators A* **64**, 77 (1998).
- <sup>7</sup>K. Lingaiah, *Machine Design Data Handbook* (McGraw-Hill, New York, 1994).
- <sup>8</sup>IRE Standards on Piezoelectric Crystals, *Proc. IRE* **49**, 1169 (1961).
- <sup>9</sup>Q. M. Zhang, W. Y. Pan, S. J. Jang, and L. E. Cross, *Ferroelectrics* **88**, 147 (1988).
- <sup>10</sup>J. Zhao et al., *Appl. Phys. Lett.* (to be published).
- <sup>11</sup>J. Merhaut, *Theory of Electroacoustics* (McGraw-Hill, New York, 1981).
- <sup>12</sup>Z.-Y. Cheng, T.-B. Xu, V. Bharti, S. Wang, and Q. M. Zhang, *Appl. Phys. Lett.* **74**, 1901 (1999).
- <sup>13</sup>K. Tashiro, in *Ferroelectric Polymers*, edited by H. S. Nalwa (Dekker, New York, 1995), pp. 63-181.
- <sup>14</sup>T. Furukawa, *Phase Transit.* **18**, 143 (1989).
- <sup>15</sup>Z.-Y. Cheng, R. S. Katiyar, X. Yao, and A. Guo, *Phys. Rev. B* **55**, 8165 (1997).
- <sup>16</sup>V. Bharti, Z.-X. Zhao, Q. M. Zhang, T. Romotowski, F. Tito, and R. Ting, *Mater. Res. Innovat.* **2**, 57 (1998).
- <sup>17</sup>D. Viehland, S. J. Jang, L. E. Cross, and M. Wutting, *J. Appl. Phys.* **68**, 2916 (1990).
- <sup>18</sup>L. E. Cross, *Ferroelectrics* **76**, 241 (1987).
- <sup>19</sup>Z.-Y. Cheng, R. S. Katiyar, X. Yao, and A. S. Bhalla, *Phys. Rev. B* **57**, 8166 (1998).
- <sup>20</sup>K. Uchino and S. Nomura, *J. Mater. Sci.* **16**, 569 (1981).
- <sup>21</sup>Q. M. Zhang (unpublished).
- <sup>22</sup>J. Zhao, Q. M. Zhang, N. Kim, and T. Shrout, *Jpn. J. Appl. Phys., Part 1* **34**, 5658 (1995).
- <sup>23</sup>M. E. Lines and A. M. Glass, *Principles and Applications of Ferroelectrics and Related Materials* (Oxford University Press, New York, 1977).

# **APPENDIX 35**

# High electrostrictive strain under high mechanical stress in electron-irradiated poly(vinylidene fluoride-trifluoroethylene) copolymer

Vivek Bharti, Z.-Y. Cheng, S. Gross, T.-B. Xu, and Q. M. Zhang

*Materials Research Laboratory, Pennsylvania State University, University Park, Pennsylvania 16802*

(Received 9 July 1999; accepted for publication 27 August 1999)

In this letter, we show that the electric field induced strain in the electron irradiated poly(vinylidene fluoride-trifluoroethylene) copolymer can generate high strain even under a high mechanical stress. The observed change in strain with stress is due to the electrostrictive coupling of the local polarization with stress, and can be directly related to the change of the induced strain with temperature. The results indicate that the field induced strain observed in the films investigated is indeed from the local polarization regions in the material, and is electrostrictive in nature. © 1999 American Institute of Physics. [S0003-6951(99)03743-2]

Polymers which can generate high electric field induced strain are very attractive for a broad range of applications such as artificial muscles, robots, ultrasonic transducers for medical diagnosis, sonar, and active control of mechanical systems.<sup>1</sup> It was found recently that under a proper electron irradiation treatment, a massive electrostrictive strain can be induced in poly(vinylidene fluoride-trifluoroethylene) [P(VDF-TrFE)] copolymers. Because of the high elastic modulus of the material, it also possesses a high elastic energy density.<sup>2-5</sup> Being a polymeric material, the electromechanical response under high mechanical load is always a concern, that is, whether the material can maintain the strain level when subject to high external stresses. For example, several polymers such as polyurethane, polybutadiene, silicone rubber etc. were observed to generate very high electric field induced strains up to  $\sim 10\%$ .<sup>2-5</sup> But due to the fact that these materials have a very low elastic modulus and the strain is caused by the Maxwell stress effect, the elastic energy density of these polymers is low and the strain diminishes even under the mechanical constraints of the metal electrodes deposited on the samples.<sup>5</sup> In this letter, we demonstrate that the irradiated P(VDF-TrFE) copolymer films can generate a high strain under a high external load. In addition, the experimental results also show that due to the ferroelectric nature of the material, the mechanical load effect on the field induced strain can be directly linked to the variation of the strain with temperature.

The PVDF( $x$ )-TrFE( $1-x$ ) copolymer with  $x=65$  mol % was chosen for this study. Among the compositions investigated, this composition showed the highest electrostrictive strain in both the longitudinal and transverse directions (parallel and perpendicular to the applied electric field). The copolymer powder was purchased from Solvay and Cie, Bruxelles, Belgium. The unstretched and uniaxially stretched ( $4.5\times$ ) films of thickness  $\sim 20$ – $30\ \mu\text{m}$  were prepared by melt pressing and solution casting methods, respectively. In order to improve the crystallinity and also to remove residual solvent, the films were annealed in a vacuum oven at  $140^\circ\text{C}$  for 16 h. These films were irradiated in a nitrogen atmosphere with 2.55 MeV electrons at  $95^\circ\text{C}$  and with a 60 Mrad dose.

A cantilever based dilatometer was used to measure the

strain along the stretching direction (transverse strain,  $S_1$ ) at different tensile stresses ( $\sigma_T$ ) applied in the same direction.<sup>4</sup> The strain along the thickness direction (longitudinal strain,  $S_3$ ) was measured at different hydrostatic pressures ( $\sigma_h$ ) using a piezoelectric bimorph based sensor.<sup>9</sup> In this setup, one end of the piezoelectric bimorph was fixed while the other was in contact with the sample. Under an ac electric field, the expansion and contraction along the sample thickness direction generate the corresponding bending motion in the bimorph sensor. Through the piezoelectric effect, an electrical output voltage which is proportional to the bending of bimorph is observed. Both the setups were designed and developed specifically for strain measurements in polymer films under load. In both cases, the ac electric field is applied along the film thickness with frequencies ranging from 1 to 10 Hz.

Since the magnitude of the transverse strain is higher for stretched films in comparison to unstretched films, the 65/35 stretched films were used to measure the transverse strain at different tensile stresses along the stretching direction. As can be seen from Fig. 1, under a constant electric field, the transverse strain initially increases with the load and reaches to a maximum at the tensile stress of about 20 MPa. Upon further increase of the load, the field induced strain is reduced. One important result revealed by the data is that even under a tensile stress of 45 MPa, the strain generated is still nearly the same as that it was without load, indicating that the material has a very high load capability.

The longitudinal strain for unstretched 65/35 mol % films as a function of hydrostatic pressure was measured and the data is presented in Fig. 2. As can be seen, at low driving electric fields, the strain does not change much with pressure. On the other hand, for high fields it shows increases with pressure. Due to the limitation of the experimental setup, we could not apply pressure higher than 8.2 MPa.

The results from both experiments clearly demonstrate that the electrostrictive P(VDF-TrFE) copolymer has a high load capability and maintains its strain level even under a very high mechanical load, which is in contrast to many other polymeric materials.<sup>6-9</sup> However, the increase of the field induced strain with load and the strain maximum observed in Fig. 1 seems to be puzzling. In the following, we

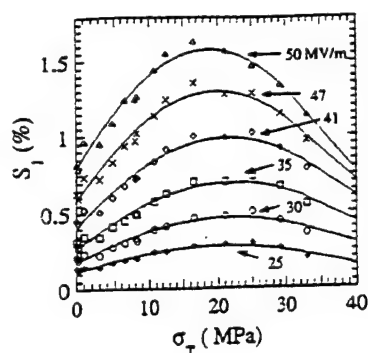


FIG. 1. Effect of tensile stress ( $\sigma_T$ ) on electric field induced transverse strain ( $S_1$ ) measured at room temperature under different driving electric field strengths.

will be showing that the observed phenomena can be understood by considering the electrostrictive coupling of the local polarization with stress in this relaxor ferroelectric material.

It is well known that the unirradiated P(VDF-TrFE) 65/35 mol % copolymer is a normal ferroelectric polymer with a Curie temperature near 70 °C.<sup>10</sup> After the irradiation, we have shown that the material is transformed into a relaxor ferroelectric, which exhibits a large electrostrictive strain.<sup>2</sup> According to the Landau-Devonshire phenomenological theory, when a normal ferroelectric material is subjected to an external stress, its Curie point will shift, which can be described as<sup>11,12</sup>

$$\Delta T = 2 \epsilon_0 C Q \Delta \sigma, \quad (1)$$

where  $\Delta T$  is the shift of the Curie temperature,  $\epsilon_0$  is permittivity in free space,  $C$  is Curie-Weiss constant,  $\sigma$  is the applied stress, and  $Q$  is electrostrictive coefficient. Therefore, depending on the sign of the electrostrictive coefficient and the applied stress, the shift of the Curie point can be either positive (to higher temperature) or negative (to lower temperature). For a relaxor ferroelectric, if we use the simple Smolensky model<sup>13</sup> that a relaxor ferroelectric can be regarded as consisting of local polar regions with different Curie points over a broad temperature range, Eq. (1) can still be used to provide a qualitative understanding of the data.

For the irradiated P(VDF-TrFE) copolymer, it is also shown that the strain is proportional to the square of the induced polarization  $P$ :<sup>2</sup>

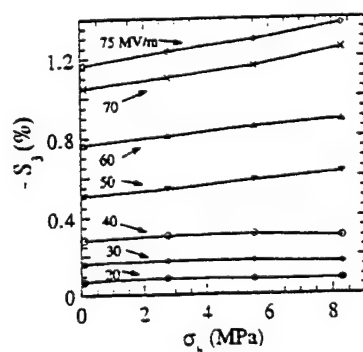


FIG. 2. Effect of hydrostatic pressure ( $\sigma_h$ ) on electric field induced longitudinal strain ( $S_3$ ) measured at room temperature under different driving electric field strengths.

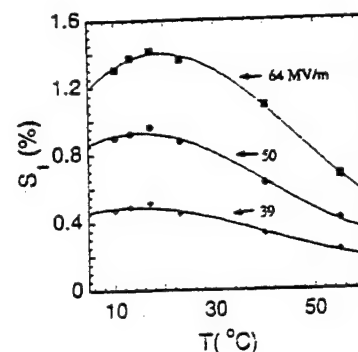


FIG. 3. Variation in electric field induced transverse strain ( $S_1$ ) as a function of temperature measured under stress free conditions at different electric field strengths.

$$S = Q P^2. \quad (2)$$

The relevant electrostrictive coefficients used in Eq. (1) for the irradiated copolymer are:  $Q_{13}$  (transverse coefficient, related to the transverse tensile stress) and  $Q_h$  (volume coefficient, related to the hydrostatic pressure). From early experimental results, it has been shown that  $Q_{13} > 0$  and  $Q_h < 0$ .<sup>5</sup> Therefore, under a transverse tensile stress,  $\Delta \sigma_T > 0$ , and Eq. (1) dictates that the applied tensile stress will shift the Curie temperature downwards. In an analogy, under hydrostatic pressure,  $\Delta \sigma_h < 0$ , and with increased pressure, the Curie temperature will also move downwards. Combining this with the results in Figs. 1 and 2 suggests that at temperatures near room temperature, both the longitudinal and transverse strains of the samples studied should increase as the temperature is reduced and will reach to a maximum at a temperature below room temperature.

Figures 3 and 4 present the temperature dependence of the transverse strain for the stretched film and the longitudinal strain for the unstretched film measured under stress free conditions at a field range similar to those used in Figs. 1 and 2. Figure 3 shows that for the transverse strain measured in the stretched sample, there is a broad maximum at a temperature near 17 °C in the electric field range measured, which seems to be consistent with the data in Fig. 1. For the longitudinal strain, the temperature limitation of the setup prevents the experiment from being performed below room temperature, and the results in Fig. 4 are consistent with the data in Fig. 2. That is, the field induced strain decreases with

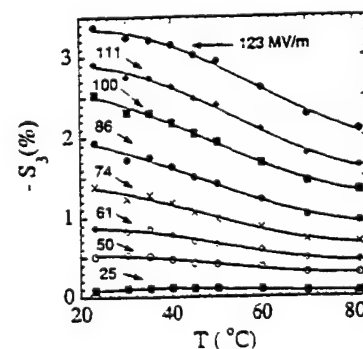


FIG. 4. Variation in electric field induced longitudinal strain ( $S_3$ ) as a function of temperature measured under stress free condition at different electric field strengths.

temperature. It should be pointed out that due to the nature of relaxor ferroelectric material, the induced strain changes with stress or temperature are also dependent on the level of the driving electric field. For the unstretched sample, the data in Fig. 4 seems to indicate that there is a weak strain maximum at a temperature near 35 °C when the measurement was made under a field of 25 MV/m.

From the data presented in Figs. 1 and 3 for the stretched films and in Figs. 2 and 4 for unstretched films, one may obtain the effective electrostrictive coefficients using Eq. (1) if the Curie-Weiss constants are known for the two samples. Using the Curie-Weiss relation,  $\epsilon = C/(T - T_c)$ , where  $\epsilon$  is the permittivity of the material,<sup>12</sup> the values of the Curie-Weiss constants ( $C = 4002$  and  $3475$ ) and Curie-Weiss temperatures ( $T_c = 10.24$  and  $28$  °C) were calculated for unirradiated stretched and unstretched films, respectively. These values are found to be close to the values reported by others.<sup>10</sup> The value of  $Q_{13} = 4.6 \text{ m}^4/\text{C}^2$  is calculated from Eq. (1) using  $\Delta T = 6$  °C (Fig. 3) and  $\Delta \sigma_T = 18.4 \text{ MPa}$  (Fig. 1), which is very close to the value of  $Q_{13} = 4.9 \text{ m}^4/\text{C}^2$  obtained directly from the strain and polarization using Eq. (2).<sup>5</sup> Although for a system as complicated as the irradiated P(VDF-TrFE) copolymer, we do not expect that the analysis presented can be used quantitatively, the consistency in the effective electrostrictive coefficient obtained from the two sets of data does indicate that the observed change of the induced strain with stress is due to the electrostrictive coupling of the local polarization with stress in this material. For unstretched films, by comparing the slopes from the curves under 75 MV/m in Fig. 2 and under 74 MV/m in Fig. 4, we obtain  $Q_h = -10.8 \text{ m}^4/\text{C}^2$  which is also consistent with  $Q_h = -6 \text{ m}^4/\text{C}^2$  obtained directly from the measured volume

strain with polarization.<sup>5</sup> The results obtained here clearly indicate that the field induced strain is due to the local polarization in the material and is electrostrictive in nature. The data presented show that the variation of the field induced strain with stress can be related qualitatively to the change in strain with temperature through Eq. (1) even for a complicated system such as the relaxor ferroelectric P(VDF-TrFE) copolymer. Furthermore, the data show that the electrostrictive strain from the irradiated P(VDF-TrFE) copolymer has a high load capability.

This work was supported by DARPA (Grant No. N00173-99-C-2003), NSF (Grant No. ECS-9710459), and ONR (Grant No. N00014-97-1-0667). The authors also wish to thank A. Glazov for stimulating discussions.

<sup>1</sup>T. T. Wang, J. M. Herbert, and A. M. Glass, *The Application of Ferroelectric Polymers* (Blackie, Chapman and Hall, New York, 1988).

<sup>2</sup>Q. M. Zhang, V. Bharti, and X. Zhao, *Science* **280**, 2101 (1998).

<sup>3</sup>V. Bharti, X.-Z. Zhao, and Q. M. Zhang, *Mat. Res. Innovat.* **2**, 57 (1998).

<sup>4</sup>Z.-Y. Cheng, V. Bharti, T.-B. Xu, S. Wang, and Q. M. Zhang, *J. Appl. Phys.* **86**, 2208 (1999).

<sup>5</sup>Z.-Y. Cheng, T.-B. Xu, V. Bharti, S. Wang, and Q. M. Zhang, *Appl. Phys. Lett.* **74**, 1901 (1999).

<sup>6</sup>R. E. Peirine, R. D. Kornbluh, and J. P. Joseph, *Sens. Actuators A* **64**, 77 (1998).

<sup>7</sup>J. Su, Q. M. Zhang, and R. Y. Ting, *Appl. Phys. Lett.* **71**, 386 (1997).

<sup>8</sup>M. Zhenyi, J. I. Scheinbeim, J. W. Lee, and B. A. Newman, *J. Polym. Sci., Part B: Polym. Phys.* **32**, 2721 (1994).

<sup>9</sup>J. Su, P. Moses, and Q. M. Zhang, *Rev. Sci. Instrum.* **69**, 2480 (1998).

<sup>10</sup>T. Furukawa, *Phase Transit.* **18**, 143 (1989).

<sup>11</sup>M. E. Lines and A. M. Glass, *Principal and Applications of Ferroelectrics and Related Materials* (Oxford University Press, New York, 1977).

<sup>12</sup>A. F. Devonshire, *Philos. Mag.* **3**, 85 (1954).

<sup>13</sup>G. A. Smolensky, *J. Phys. Soc. Jpn.* **28**, 26 (1970).



# **TRANSDUCER STUDIES**

***Composite Transducers***



# **APPENDIX 36**

# Resonance modes and losses in 1-3 piezocomposites for ultrasonic transducer applications

Xuecang Geng<sup>a)</sup> and Q. M. Zhang

*Materials Research Laboratory and Department of Electrical Engineering, The Pennsylvania State University, University Park, Pennsylvania 16802*

(Received 13 July 1998; accepted for publication 28 October 1998)

The article presents the results of a recent investigation on the ultrasonic performance of 1-3 piezocomposites. Using a guided wave approach, the electromechanical properties of the thickness resonance are modeled and the results are compared with the experimental data. The influence of various losses in a 1-3 composite on the dispersion curves and the quality factor for the thickness mode is examined. It is found that the reduction in the quality factor of a composite compared with piezoceramic is mainly due to the acoustic coupling between the two constituents. Even for a composite with the mechanical  $Q$  of the polymer higher than that of the ceramic, the mechanical  $Q$  of the composite is still lower than that of the ceramic except when the ceramic volume content is very low. Hence, in most of piezoceramic polymer composites, the mechanical  $Q$  of the ceramic phase plays a major role in determining the quality factor of a 1-3 composite transducer. For the lateral modes in a 1-3 composite, it is found experimentally that the frequencies of the two lowest lateral modes can be determined approximately by the shear wave velocity and the width of the polymer gap over a broad ceramic volume fraction range, suggesting that they correspond to the half-wave standing waves in the polymer gap. © 1999 American Institute of Physics. [S0021-8979(99)08603-X]

## I. INTRODUCTION

Piezoceramic polymer composites offer many advantages over single phase materials for many transducer applications such as underwater sonar, ultrasonic imaging for medical and NDE applications, and stress sensors.<sup>1,2</sup> The complementary properties of the polymer and ceramic phases in the electric and mechanical responses make it possible to tune the composite properties over a wide range. On the other hand, in order to fully make use of these advantages and to reduce the manufacture costs of composite, it is necessary and still a challenge to establish a quantitatively structure-property relationship which links various design parameters in the constituents to the final device performance and reveals new properties of composites that are absent in single phase materials.

In the past two decades, a great deal of effort has been devoted to analyze and model the transducer performance of piezocomposites.<sup>3-9</sup> The model (quasi-static model) developed by Smith and Auld<sup>3</sup> and Hashimoto and Yamaguchi<sup>4</sup> based on the isostrain and isostress concepts in treating the coupling between the constituent phases provided a qualitative prediction on the effective piezoelectric properties of 1-3 composites as a thickness resonator. It was shown from the model that the thickness coupling factor  $k_t$  of a composite can approach the longitudinal coupling factor  $k_{33}^I$  of the piezoceramic rod, which agrees with experiments for composites with a high aspect ratio  $d/t$ , where  $t$  is the thickness and  $d$  is the periodicity of the composites. Because of its simplicity, the quasi-static model offers a convenient means for a

quick estimation of the composite parameters. Auld *et al.* pointed out the existence of the stop band edge resonance in both 2-2 and 1-3 composites due to the periodic arrangement of the ceramic elements in these composites.<sup>5,6</sup> However, in order to address quantitatively many realistic issues of a composite material such as the influence of the aspect ratio and shape of the ceramic rod in a 1-3 composite on the performance, finite element method (FEM) is often used.<sup>7-9</sup>

More recently, based on the guided wave approach, an analytical model was developed which is capable of treating many practical issues related to the ultrasonic performance of a 2-2 composite. By combining this with the eigenmode expansion, the ultrasonic properties of a finite thickness 2-2 composite can be analyzed quantitatively and many new features were predicted and confirmed experimentally.<sup>10,11</sup> Clearly, the model results offer many new physical insights into the ultrasonic performance of a 2-2 piezocomposite. It is the purpose of this work to explore the possibility of using similar approach to 1-3 piezocomposites.

In this article, a simplified wave propagation model will be used to analyze the ultrasonic properties related to the thickness resonance of 1-3 composites and the results will be compared with experiment. Comparison will also be made with the quasi-static model to show the range of its validity. Since the mechanical  $Q$  of a composite is an important parameter in determining the bandwidth of the transducer made from it, experiment and model analysis are also made to show that the mechanical  $Q$  of a composite is not a simple extrapolation between the two end constituent phases (i.e., ceramic and polymer) and can be much smaller than those of both constituents. In addition, experimental results will be presented regarding the frequencies of the lateral modes and

<sup>a)</sup>Current address: Blarek, Inc. State College, PA 16801.

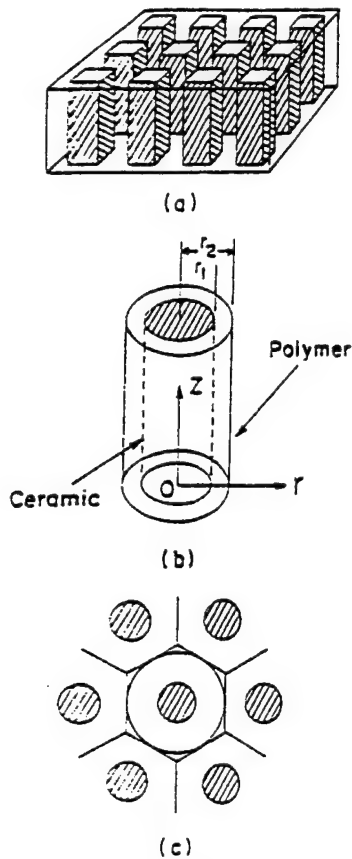


FIG. 1. (a) Schematic drawing of a 1-3 piezocomposite having a square unit cell. (b) A concentric unit cell and the coordinate system for a 1-3 composite ( $d=2r_2$ ). (c) Schematic drawing of a 1-3 composite with ceramic rods arranged in a hexagonal periodic array. A concentric unit cell may be used to approximate hexagonal unit cell as shown.

it will be shown that simple relationships exist between the frequencies positions of these modes and the parameters of the polymer matrix.

## II. SAMPLE PREPARATION

In order to compare the model results with experiment, 1-3 piezocomposites with different ceramic volume fractions were prepared by a dice and fill method. The ceramic used was the commercial PZT-5H disk and the polymer matrix was Spurr epoxy.<sup>12</sup> In the fabrication of 1-3 composites, PZT-5H ceramic disk was first diced in one direction periodically by Isomet 1000 dicing saw and the ceramic volume fraction is determined by the ratio of the kerf width/period. For example, for a 1-3 composite with 40.5% ceramic volume content, the periodicity is 1.024 mm and the kerf width is 0.355 mm. After the dicing, the sample was carefully cleaned by acetone, and the Spurr epoxy was then filled into the kerf. Any possible gas bubbles in the polymer were removed by placing the sample in a vacuum for more than an hour. The polymer matrix was then cured at 50 °C in the oven for 8 h. After curing, the sample was cut in the perpendicular direction to the first cut with the periodicity and the kerf the same as the first cut, and then cleaned, filled with epoxy and cured. Because the ceramic may be partially de-poled in the process of cutting, curing and polishing, the final 1-3 composite was repoled in 70 °C oil for 5 min under a 2

kV/mm dc electric field. Different thickness samples were used to vary the thickness resonance frequency and the electric impedance was measured by an HP 4194 Impedance Analyzer.

## III. WAVE PROPAGATION IN AN UNBOUNDED 1-3 PIEZOCOMPOSITE

In general, a 1-3 composite, such as shown in Fig. 1(a), has a three-dimensional structure and although its dynamic behavior can be treated using the approach in Refs. 13 and 14, the mathematics involved is quite complicated and cumbersome. To simplify the mathematics of the analysis, we will investigate the possibility of using the concentric unit cell Fig. 1(b), which is an approximation to the unit cell of a 1-3 composite having the ceramic rods arranged in a hexagonal lattice as schematically drawn in Fig. 1(c), to analyze the ultrasonic properties of a 1-3 composite at the thickness resonance. Such an approximation reduces the problem to a two-dimensional one which is much simpler and as will be shown in the article the model results on the thickness resonance compare quite well with experimental data.

The cylindrical coordinate system is chosen for the unit cell shown in Fig. 1(b) where the  $z$  axis is along the poling direction of the piezoceramic rod, the  $r$  axis is along the radial direction and the  $\theta$  axis is perpendicular to the  $r$ - $z$  plane, respectively. Because of the axial symmetry, the governing equations become<sup>15</sup>

$$\frac{\partial T_{rr}}{\partial r} - \frac{\partial T_{rz}}{\partial z} - \frac{1}{r}(T_{rr} - T_{\theta\theta}) = \rho \frac{\partial^2 u_r}{\partial t^2}, \quad (1a)$$

$$\frac{\partial T_{rz}}{\partial r} + \frac{T_{rz}}{r} + \frac{\partial T_{zz}}{\partial z} = \rho \frac{\partial^2 u_z}{\partial t^2}, \quad (1b)$$

$$\frac{\partial D_r}{\partial r} - \frac{1}{r}D_r + \frac{\partial D_z}{\partial z} = 0. \quad (1c)$$

The symbols adopted in this article are summarized as follows:  $T_{ij}$  and  $S_{ij}$  are the stress and strain tensor components,  $u_i$  is the elastic displacement vector,  $\rho$  is the density,  $D_i$  is the electric displacement vector, and  $E_i$  the electric field. The relevant material coefficients are:  $e_{ij}$  is the piezoelectric coefficient,  $c_{ij}$  is the elastic stiffness, and  $\epsilon_i$  the dielectric permittivity. Equation (1) holds for both polymer and piezoceramic phases.

The constitutive equations for the piezoceramic in the cylindrical coordinate system are

$$T_{rr} = c_{11}^E \frac{\partial u_r}{\partial r} - c_{12}^E \frac{u_r}{r} + c_{13}^E \frac{\partial u_z}{\partial z} - e_{31} E_z, \quad (2a)$$

$$T_{\theta\theta} = c_{12}^E \frac{\partial u_r}{\partial r} - c_{11}^E \frac{u_r}{r} + c_{13}^E \frac{\partial u_z}{\partial z} - e_{31} E_z, \quad (2b)$$

$$T_{zz} = c_{13}^E \frac{\partial u_r}{\partial r} - c_{13}^E \frac{u_r}{r} + c_{33}^E \frac{\partial u_z}{\partial z} - e_{33} E_z. \quad (2c)$$

$$T_{rz} = c_{14}^E \left( \frac{\partial u_r}{\partial z} + \frac{\partial u_z}{\partial r} \right) - e_{15} E_r, \quad (2d)$$

$$D_r = e_{15} \left( \frac{\partial u_r}{\partial z} + \frac{\partial u_z}{\partial r} \right) + \epsilon_{11}^S E_r, \quad (2e)$$

$$D_z = e_{31} \left( \frac{\partial u_r}{\partial r} + \frac{u_r}{r} \right) + e_{33} \frac{\partial u_z}{\partial z} + \epsilon_{33}^S E_z. \quad (2f)$$

For the polymer phase,  $e_{ki}$  in Eq. (2) is zero. The superscripts  $E$  and  $S$  indicate that the coefficients are under the constant electric field and constant strain conditions, respectively. Under the quasi-electrostatic approximation, the electric field  $E$  is related to the electrical potential  $\Phi$

$$\vec{E} = -\nabla \Phi. \quad (3)$$

Combining Eqs. (1), (2), and (3) yields differential equations governing the elastic displacement  $u_r$ ,  $u_z$ , and the electrical potential  $\Phi$  in the piezoceramic rod and in the polymer, respectively.<sup>11</sup> The general solutions for the piezoelectric active modes in the ceramic rod have the form:

$$[M_{ij}] = \begin{bmatrix} c_{33}^E \beta^2 + c_{44}^E h^2 - \rho \omega^2 & (c_{13}^E + c_{44}^E) h \beta & e_{33} \beta^2 - e_{15} h^2 \\ (c_{13}^E + c_{44}^E) h \beta & c_{11}^E h^2 + c_{44}^E \beta^2 - \rho \omega^2 & (e_{15} - e_{31}) h \beta \\ e_{33} \beta^2 + e_{15} h^2 & (e_{15} + e_{31}) h \beta & -(\epsilon_{11}^E h^2 + \epsilon_{33}^E \beta^2) \end{bmatrix} \quad (4)$$

(where  $h$  is replaced by  $h_i^c$  for  $i=1, 2$ , and  $3$ , respectively). The time-dependent term  $\exp(-j\omega t)$  is omitted in Eq. (4), where  $\omega$  is the angular frequency.<sup>11</sup>  $R_i^c$  are the coefficients to be determined from the boundary conditions.

Similarly, the solutions for the polymer phase can be obtained<sup>11</sup>

$$u_z^p = \sum_i f_i^p [R_i^p J_0(h_i^p r) + Q_i^p Y_0(h_i^p r)] \sin(\beta z),$$

$$u_r^p = \sum_i g_i^p [R_i^p J_1(h_i^p r) + Q_i^p Y_1(h_i^p r)] \cos(\beta z), \quad (6)$$

$$\Phi^p = [C_1^p J_0(h_3^p r) + C_2^p Y_0(h_3^p r)] \sin(\beta z),$$

where  $i=1, 2$ , and the superscript  $p$  denotes the polymer. For a nonslippery interface between the ceramic and polymer,  $\beta$  in the polymer should be the same as that in the ceramic.  $Y_0$  and  $Y_1$  are the zeroth-order and first-order Hankel function.  $f_i^p$  and  $g_i^p$  are the cofactors of  $A_{k1}(i)$ ,  $A_{k2}(i)$  of Eq. (5) with all the material parameters replaced by those of polymer phase, and

$$(h_1^p)^2 = (k_L^p)^2 - \beta^2, \quad (h_2^p)^2 = (k_T^p)^2 - \beta^2, \quad \text{and} \quad (h_3^p)^2 = -\beta^2. \quad (7)$$

where  $k_L^p = \omega / v_L^p$ ,  $k_T^p = \omega / v_T^p$ ,  $v_L^p$  and  $v_T^p$  are the longitudinal and shear wave velocities in the polymer phase, respectively.  $R_i^p$ ,  $Q_i^p$ ,  $C_1^p$ , and  $C_2^p$  are the coefficients to be determined by the boundary conditions.

$$u_z^c = \sum_i R_i^c f_i^c J_0(h_i^c r) \sin(\beta z).$$

$$u_r^c = \sum_i R_i^c g_i^c J_1(h_i^c r) \cos(\beta z). \quad (4)$$

$$\Phi^c = \sum_i R_i^c t_i^c J_0(h_i^c r) \sin(\beta z).$$

where  $i$  runs from 1 to 3 and the superscript  $c$  denotes the ceramic.  $J_0$  and  $J_1$  are zeroth-order and first-order Bessel function.  $\beta$  is the wave vector component along the  $z$  direction ( $\beta = 2\pi/\lambda$ , where  $\lambda$  is the wavelength along the same direction) and  $h_i$  is the wave vector perpendicular to that direction. For each  $\beta$ , there are three  $h$ ,  $h_1^c$ ,  $h_2^c$ , and  $h_3^c$ , corresponding to the quasi-electromagnetic, quasi-longitudinal, and quasi-shear waves in the piezoceramic rod, respectively.  $f_i^c$ ,  $g_i^c$  and  $t_i^c$  are the cofactors of  $A_{k1}(i)$ ,  $A_{k2}(i)$ , and  $A_{k3}(i)$  of the determinant:

The expressions of the stresses and the electric displacement in the ceramic rod and the polymer phase can be obtained by substituting the equations of the elastic displacement and electric potential into the constitutive equations [Eq. (2) for the ceramic rod].<sup>11</sup>

The boundary conditions at the ceramic polymer interface ( $r=r_1$ ) are

$$u_r^c = u_r^p, \quad u_z^c = u_z^p, \quad T_{rr}^c = T_{rr}^p, \quad T_{rz}^c = T_{rz}^p, \quad (8a)$$

$$\Phi^c = \Phi^p, \quad D_r^c = D_r^p, \quad (8b)$$

and the symmetry conditions at  $r=r_2$  require

$$T_{rz}^p = 0, \quad u_r^p = 0, \quad D_r^p = 0. \quad (8c)$$

From Eq. (8), the relationship between  $\omega$  and  $\beta$ , the dispersion relations, can be determined. For each pair of  $\omega$  and  $\beta$ , the relationships among  $R_i^c$ ,  $R_j^p$ ,  $Q_j^p$ , and  $C_j^p$  [in Eqs. (4) and (6)] can be obtained.<sup>11</sup>

#### IV. EFFECTIVE ELECTROMECHANICAL PROPERTIES OF A 1-3 PIEZOCOMPOSITE

The longitudinal wave velocity of a 1-3 piezocomposite is determined from the dispersion curves using  $V_{ph} = \omega/\beta$ . Presented in Fig. 2(a) is the comparison of the theoretical and experimental results of the longitudinal wave velocity  $V^D$  as a function of  $d/t$  ( $t$  is the thickness of the composite and  $d=2r_2$ , and at the thickness resonance  $\beta=2\pi/\lambda=\pi/t$ ) for a 1-3 piezocomposite with 40% ceramic volume fraction. In this article, except otherwise specified, the composites

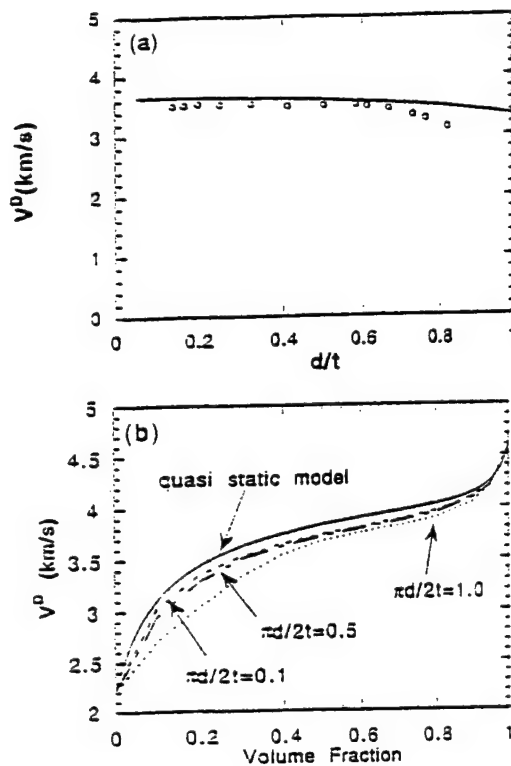


FIG. 2. (a) Longitudinal wave velocity of a 1-3 piezocomposite with 40% ceramic content as a function of  $d/t$ . The open circles are the experimental results and solid line is from the model. (b) The longitudinal wave velocity is a function of ceramic volume fraction for composites with different  $d/t$  derived from the model. For the comparison, the result from the quasi-static model is also included.

have PZT-5H as the piezoceramic and Spurr epoxy as polymer matrix.<sup>12</sup> The parameters of the PZT-5H piezoceramic and the Spurr epoxy are presented in Table I, where the real part of the material parameters is from Ref. 16. The experimental results are obtained by the resonance method using HP4194 Impedance Analyzer from 1-3 piezocomposite plates with different thickness  $t$  (the sample thickness  $t$  ranges from 0.5 to 5 mm) and  $V^D = 2 f_p t$  ( $f_p$  is the parallel resonance frequency). The agreement is very good for  $d/t$  less than 0.65. At  $d/t$  higher than 0.65, the theoretical results deviate from the experimental values, which is due to the concentric unit cell approximation used in the analysis which cannot treat the mode coupling correctly.

Shown in Fig. 2(b) is the dependence of the longitudinal wave velocity on ceramic volume fraction for a 1-3 piezocomposite with different ratio of  $d/t$ . The lowering of  $V^D$  for  $d/t = 0.63$  shown at the low ceramic volume content region (at the ceramic volume content less than 40%) in the figure is due to the coupling of the thickness mode with the lateral mode. For composites with higher ceramic volume content, this coupling will occur at higher  $d/t$  and correspondingly, the lowering of  $V^D$  will occur at higher values of  $d/t$ . Away from the coupling region (in practical design, the frequency of the first lateral mode is chosen to be at twice that of the thickness mode),  $V^D$  exhibits very little dependence on  $d/t$  which is consistent with the data in Fig. 2(a) and earlier experiment results.<sup>17</sup> For the comparison,  $V^D$  from quasi-static model are also shown in Fig. 2(b).<sup>3,4</sup> And  $V^D$  derived

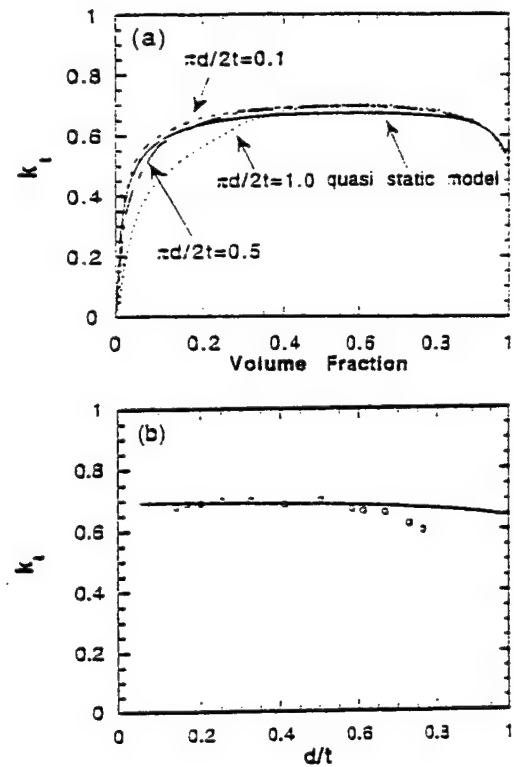


FIG. 3. (a) Electromechanical coupling coefficient  $k_t$  as a function of ceramic volume fraction for composites with different  $d/t$  derived from the model. For the comparison, the result from the quasi-static model is also included as the solid line. (b) The electromechanical coupling coefficient  $k_t$  of a 1-3 piezocomposite with 40% ceramic content as a function of  $d/t$ . The open circles are the experimental results and solid line is from the model.

from the quasi-static model is higher than that determined from this model and experimental data.

The thickness mode electromechanical coupling coefficient of a 1-3 piezocomposite is derived in the model from<sup>16</sup>

$$k_t^2 = 1 - \left( \frac{v_t^E}{v_t^D} \right)^2 \quad (9)$$

where  $v_t^E$  and  $v_t^D$  are the longitudinal wave velocity under constant  $E$  and constant  $D$  conditions, respectively. Presented in Fig. 3(a) is the dependence of  $k_t$  on ceramic volume fraction for a 1-3 piezocomposite with different  $d/t$ . Again, the reduction in  $k_t$  at the low ceramic volume fraction region for the curve with  $d/t = 0.63$  is due to the coupling to the lateral mode. At  $d/t$  away from the coupling region,  $k_t$  exhibits very little dispersion. For the comparison, the results from the quasi-static model is also presented in the figure and  $k_t$  from the quasi-static model is less than that from this model even when  $d/t$  approaches zero, where the thickness of the composite is much larger than the period.

The thickness coupling factor for a 1-3 piezocomposite with 40% ceramic volume content was evaluated experimentally using the relation:<sup>18</sup>

$$k_t^2 = \frac{\pi f_s}{2 f_p} \tan \left( \frac{\pi f_p - f_s}{2 f_p} \right) \quad (10)$$

where  $f_s$  and  $f_p$  are the series and the parallel resonance frequencies of the 1-3 piezocomposite plate, respectively. The dependence of the theoretical and experimental electro-

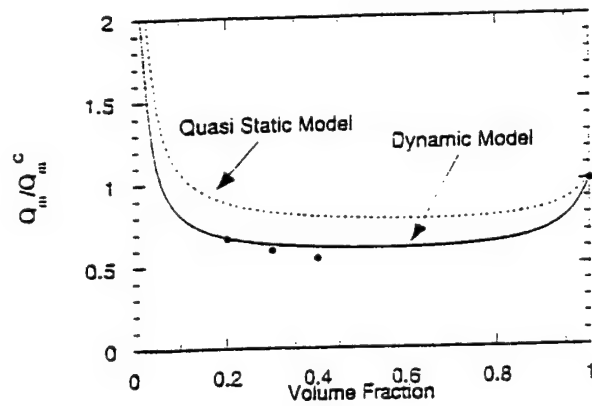


FIG. 4. Quality factor  $Q_m$  of 1-3 piezocomposites as a function of ceramic volume fraction.  $Q_m$  is evaluated at  $d/t=0.063$  and  $f=117$  kHz ( $\eta_{11}=20.7$  N/m<sup>2</sup> s and  $\eta_{33}=11.0$  N/m<sup>2</sup> s for the polymer).  $Q_m^c$  is the quality factor for the piezoceramic (poled PZT-5H). The result from the quasi-static model is included as the dashed line. The experimental data are represented as black dots.

mechanical coupling coefficient  $k_t$  on the aspect ratio  $d/t$  is shown in Fig. 3(b) for composites with 40% ceramic content. The agreement between the two is excellent for  $d/t$  less than 0.65. At  $d/t$  above 0.65, the deviation of the theoretical value from the experimental one is due to the concentric unit cell approximation used in the model which cannot describe the mode coupling between thickness mode and lateral mode correctly.

## V. LOSSES IN 1-3 PIEZOCOMPOSITES

In the previous sections, the losses in the materials have not been included in the analysis. However, as has been demonstrated in many experiments, loss in a 1-3 piezocomposite is much higher and hence the mechanical  $Q$  is much lower than that in piezoceramic. Therefore, it is very important to include the losses in the analysis. For practical transducer applications, a material with a mechanical  $Q$  much lower than that of piezoceramics is desirable in order to broaden the transducer bandwidth.

In general, there are three types of losses in a piezoelectric material, i.e., mechanical loss, dielectric loss, and piezoelectric loss. In the polymer phase, there are only mechanical loss and dielectric loss. The losses in the ceramic phase can be expressed by complex constants.<sup>19</sup>

$$\begin{aligned} c_{ij}^E &= c_{ij}^{E'} + j c_{ij}^{E''}, \\ e_{ij} &= e_{ij}' + j e_{ij}'', \end{aligned} \quad (11)$$

$$\epsilon_{ij}^S = \epsilon_{ij}' - j \epsilon_{ij}''$$

and the losses in the polymer phase can be expressed as

$$c_{ij} = c_{ij}' + j c_{ij}'', \quad (12)$$

$$\epsilon = \epsilon' - j \epsilon''.$$

From the fact that the attenuation in piezoceramic is proportional to frequency, the imaginary part of the parameters in ceramic can be assumed constants.<sup>20</sup> While in the polymer phase, the main loss mechanism is due to viscosity, therefore,  $c_{ij}'' = \omega \eta_{ij}$ , where  $\eta_{ij}$  is the viscosity coefficient of the polymer.

The quality factor  $Q$  (or the mechanical  $Q$ ) for the thickness mode of a 1-3 piezocomposite is evaluated from the dispersion curves using the relation:

$$Q = \frac{\beta_r}{2\beta_i}, \quad (13)$$

where  $\beta_r$  and  $\beta_i$  are the real and imaginary part of the wave vector  $\beta$ , respectively. Presented in Fig. 4 is the  $Q$  of a 1-3 piezocomposite as a function of ceramic volume fraction evaluated at  $d/t=0.063$ . The loss parameters used in the calculation are those of PZT-5H for the ceramic phase and Spurr epoxy for the polymer (listed in Table I). Those parameters are obtained from several sources: the dielectric losses for the PZT-5H ceramic and the elastic losses in Spurr epoxy were measured here; the elastic losses and the piezoelectric losses for the PZT-5H ceramic are taken from Refs. 21 and 22. The elastic loss for the polymer is evaluated at 117 kHz which yields a mechanical  $Q=2.22 \times 10^3$  for the polymer (which seems to be very high, however, it was derived directly from measured viscosity coefficient  $\eta$  at 2.5 MHz). The mechanical  $Q$  in the polymer phase is inversely proportional to frequency while in the ceramic phase it is a constant.

The results in Fig. 4 show that the quality factor of a 1-3 piezocomposite is less than that of both the ceramic and polymer for the composites evaluated. For the comparison, the quality factor for the thickness mode of several 1-3 composites with different ceramic content and single phase PZT-5H ceramic plate was experimentally determined.<sup>18</sup> The experiment data are also presented in the figure which is consistent with the theoretical results. The result here is quite different from the real part of the elastic constant of a 1-3 composite which always lies in between the two end phases. This is also in contrary to the common belief that the low

TABLE I. Material parameters for the PZT-5H and Spurr epoxy used in the model calculation.

Ceramic: $c_{11}^E = 12.72 \times 10^{10} (1.0 + j 8.0 \times 10^{-3})$ N/m <sup>2</sup> , $c_{33}^E = 11.74 \times 10^{10} (1.0 + j 8.0 \times 10^{-3})$ N/m <sup>2</sup> , $c_{12}^E = 7.95 \times 10^{10} (1.0 - j 6.5 \times 10^{-3})$ N/m <sup>2</sup> , $c_{13}^E = 8.47 \times 10^{10} (1.0 - j 6.5 \times 10^{-3})$ N/m <sup>2</sup> , $c_{22}^E = 2.3 \times 10^{10} (1.0 - j 1.2 \times 10^{-3})$ N/m <sup>2</sup> , $e_{11}^S = 1700 \epsilon_0 (1.0 - j 2.7 \times 10^{-2})$ , $e_{33}^S = 1470 \epsilon_0 (1.0 - j 2.7 \times 10^{-2})$ , $e_{31} = 23.09 (1.0 - j 5.4 \times 10^{-3})$ C/m <sup>2</sup> , $e_{13} = 17.0 (1.0 - j 5.0 \times 10^{-3})$ C/m <sup>2</sup> , $e_{31} = -6.6 (1.0 - j 7.2 \times 10^{-3})$ C/m <sup>2</sup> , $\rho^c = 7500$ kg/m <sup>3</sup> , Polymer: $c_{11}^p = 5.41 \times 10^9$ N/m <sup>2</sup> , $c_{33}^p = 1.307 \times 10^9$ N/m <sup>2</sup> , $\eta_{11} = 20.74$ N/m <sup>2</sup> s, $\eta_{33} = 11.0$ N/m <sup>2</sup> s; $\epsilon_{11}^p = 4.0 \epsilon_0$ , $\rho^p = 1100$ kg/m <sup>3</sup> .	
---	--

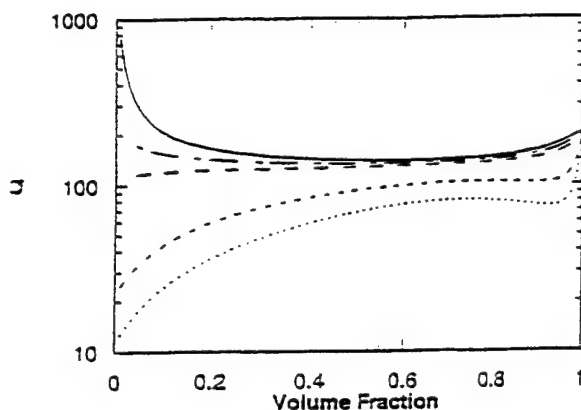


FIG. 5. Influence of elastic loss of polymer on the quality factor of a 1-3 piezocomposite as a function of ceramic volume fraction, where  $Q_m^p$  for each curve (from top to bottom) is 2220, 222, 111, 22.2, and 11.1, respectively. The losses for the ceramic phase is from depoled PZT-5H which piezoelectric coefficients are zero.

mechanical  $Q$  in a 1-3 composite is a result of the loss in the polymer phase. In fact, in the composite evaluated, the mechanical  $Q$  of the polymer phase (Spurr epoxy) is much higher than that of the piezoceramic, while the  $Q$  of the 1-3 composite is lower than that of the piezoceramic. The similar conclusion can also be obtained from the quasi-static model, which is presented in Fig. 4, where the quality factor is equal to  $1/\tan \delta$  of  $\bar{c}_{33}^D$  (the effective elastic constant of the composite at the constant electric displacement  $D$ ).

To examine whether the observed effect is due to the piezoelectric coupling, the quality factor for a 1-3 composite without piezoelectricity is also derived and the results are presented in Fig. 5 where the parameters are taken from Spurr epoxy and unpoled PZT-5H ceramic (no piezoelectric effect) and the mechanical  $Q$  of the ceramic is about 200. Apparently, the quality factor here is still less than that of both ceramic and polymer when the  $Q$  of the polymer phase is larger than that of the ceramic. On the other hand, when the  $Q$  of the polymer phase becomes smaller than that of the ceramic, the quality factor of the composite lies between that of the polymer and ceramic.

To elucidate how different losses of the ceramic phase in a composite influence the quality factor of the composite transducer, calculation is carried out for model composites with different losses in the ceramic. Presented in Fig. 6 are the results for a 1-3 piezoceramic composite in which the piezoceramic has dielectric loss only (no piezoelectric and elastic losses) and piezoelectric loss only (the dielectric and elastic losses are assumed to be zero). In both cases, the trend of quality factor with the ceramic volume fraction is quite similar to those in the pure elastic case as shown in Fig. 5. Apparently, through the piezoelectric coupling in the material, both the piezoelectric and dielectric losses reduces the mechanical  $Q$  of a 1-3 composite. It should be pointed out that in general, a piezoelectric loss may not imply a real energy loss. Although for the materials examined here, the piezoelectric loss reduces the mechanical  $Q$  of the thickness resonance mode, it can also be an energy gain in other cases which means an increase in the mechanical  $Q$ , as has been pointed out by Holland.<sup>22</sup>

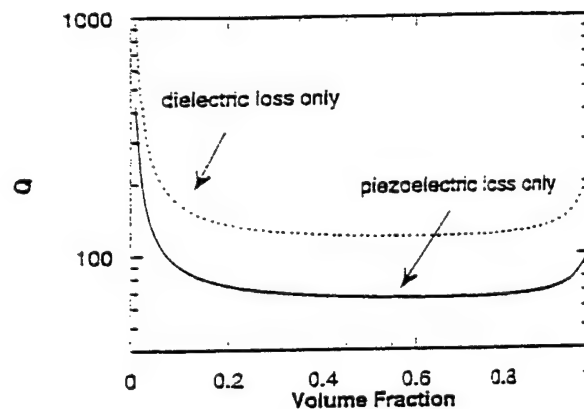


FIG. 6. Contribution of dielectric loss (no elastic and piezoelectric losses) and piezoelectric loss (no dielectric and elastic loss) of piezoceramic to the quality factor of a 1-3 piezocomposite as a function of ceramic volume fraction, where the  $\tan \delta$  of dielectric constant is 2% and the  $\tan \delta$  of the piezoelectric coefficient  $e_{33}$  is 2%. The curves are evaluated at  $d/t=0.063$  and  $Q_m = 2220$  for polymer.

Presented in Fig. 7(a) are the results when all the losses in a 1-3 composite are included (data in Table I), where the different polymer loss can be corresponding to different thickness resonance frequency. Since the elastic loss in a polymer increases linearly with frequency, different level of polymer loss may be obtained by using composite samples with different thickness mode resonance frequencies. It can

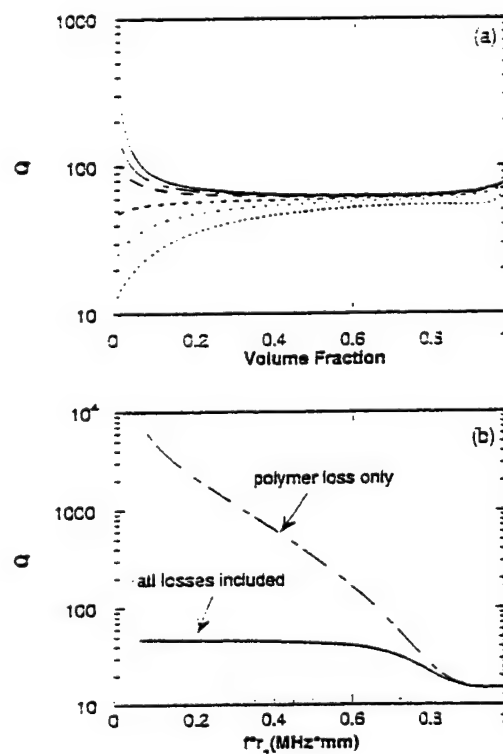


FIG. 7. (a) Quality factor of a 1-3 piezocomposite with both the elastic loss of the polymer and the elastic, dielectric, and piezoelectric losses of the piezoceramic, where the quality factor  $Q_m^p$  (polymer) for each curve (from the top to the bottom) is 2220, 222, 111, 44.4, 22.2, and 11.1, respectively. (b) Quality factor of a 1-3 composite with 40% ceramic content as a function of frequency when the loss is from the polymer only (dashed line) and when all the losses are included (solid line).



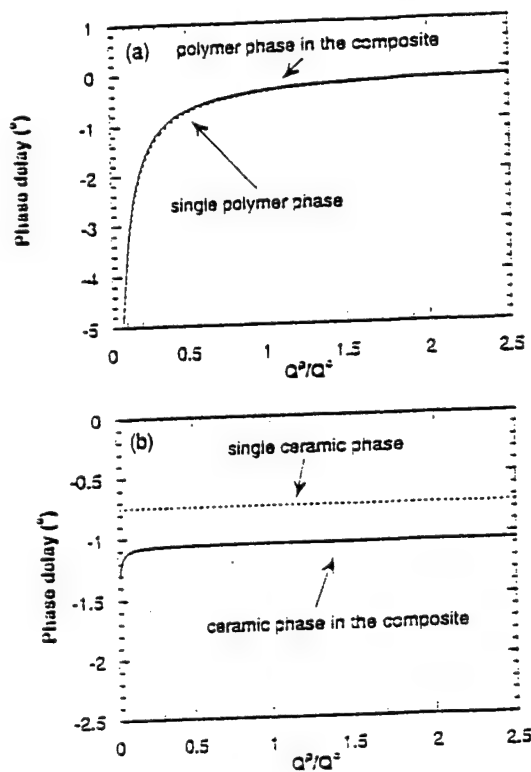


FIG. 3. (a) Comparison of the phase delay between the strain and stress in polymer as a single phase material (dashed line) and in composite (solid line). (b) Comparison of the phase delay between the strain and stress in ceramic as a single phase material (dashed line) and in composite (solid line). Apparently, by compositing, the phase delay in the polymer is reduced while in the ceramic, it is increased. The ceramic volume content is 10%.

be seen that at high ceramic volume content (for example,  $>40\%$ ), the polymer loss does not have a significant effect on the quality factor of a composite transducer. For example, as the mechanical  $Q$  of the polymer is reduced from more than 2000 down to about 10, the  $Q$  of the composite changes only from about 63 to 47 for a composite of 40% ceramic volume content. On the other hand, the losses in the ceramic phase seem to play more important role in determining the mechanical  $Q$  of the composite. To illustrate that, in Fig. 7(b), the  $Q$  for a composite with losses from the polymer phase only, i.e., there is no loss in the piezoceramic, and for a composite with all the losses included is plotted as a function of frequency, where the ceramic volume content is 40% and the quality factor of the ceramic (PZT-5H) is 75. Since the quality factor is defined as the ratio of stored mechanical energy vs. mechanical energy loss in one cycle and as seen from Table I, the elastic constants of the ceramic are more than ten times higher than those of the polymer, only when the loss in the polymer becomes much higher than that of the ceramic, will it have significant effect on the quality factor of a piezocomposite, as shown in Fig. 7(b).

The acoustic coupling between the ceramic and polymer in a composite changes the phase relationship between the stress and strain in both phases. Shown in Figs. 8 and 9 are the phase angle  $\delta$  between the stress ( $T_{zz}$ ) and strain ( $S_{zz}$ ) along the  $z$  direction at the polymer center ( $r=r_2$ ) and ceramic rod center ( $r=0$ ) as a function of  $Q^P/Q^C$ , the ratio of the mechanical  $Q$  in the two phases. Two compositions are

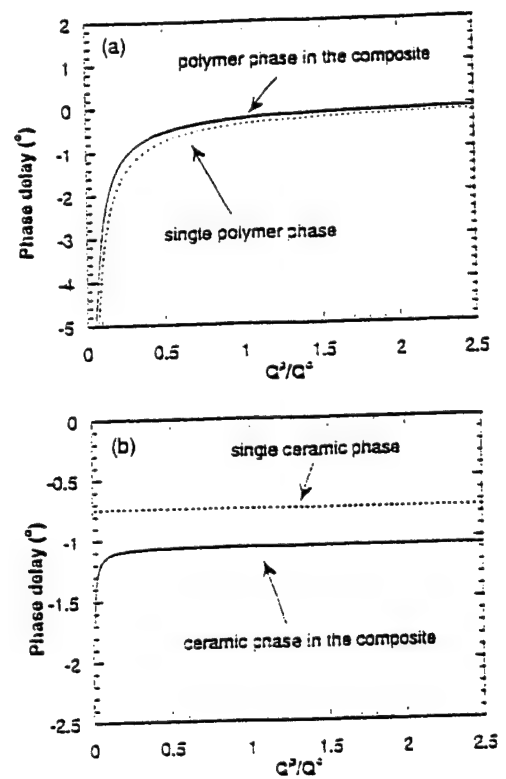


FIG. 9. (a) Comparison of the phase delay between the strain and stress in polymer as a single phase material (dashed line) and in composite (solid line). (b) Comparison of the phase delay between the strain and stress in ceramic as a single phase material (dashed line) and in composite (solid line). The ceramic volume content is 40%.

examined, one with the ceramic content at 10% (Fig. 8) and the other at 40% (Fig. 9). In the figures, the dashed lines are the  $\delta$  in the single phase material and the solid lines are the  $\delta$  in the composites. Apparently, for the polymer phase, the  $\delta$  is reduced when the polymer is in the composite while for the ceramic, it is increased in the composite. Further more, the reduction in  $\delta$  in the polymer increases with ceramic volume content of the composite, and as shown in Fig. 10, for composites with ceramic volume fraction higher than

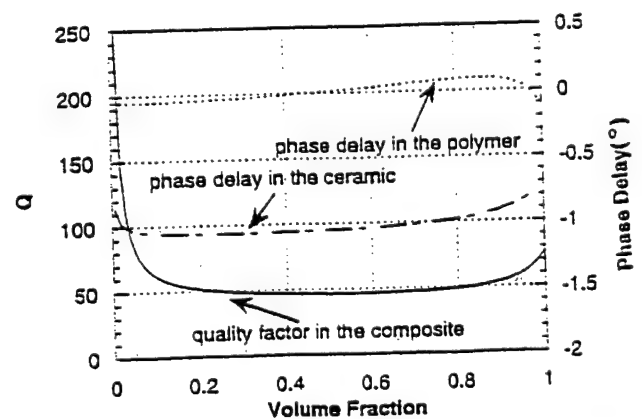


FIG. 10. Change of the phase delay  $\delta$  in the center of the polymer region and the center of the ceramic region of a composite as a function of the ceramic volume content. The polymer has a  $Q=2220$  and the calculation is carried out at  $d/t=0.063$ . The corresponding quality factor of the composite is also included in the figure.



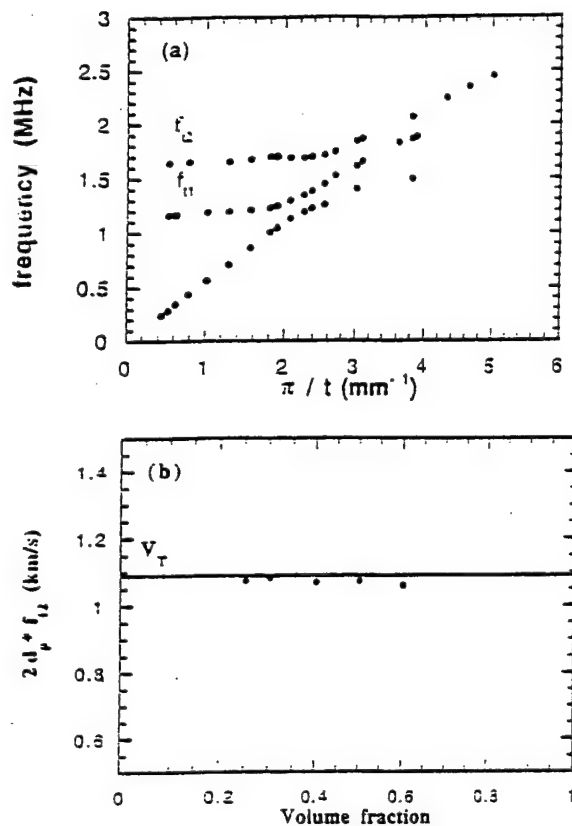


FIG. 11. (a) Experimental dispersion curves of a 40% 1-3 composite with a square unit cell. (b) Comparison between  $2d_p f_{12}$  (open circles, experimental data) and the shear wave velocity  $V_t$  of the polymer (solid line) for 1-3 composites with square unit cell with different ceramic volume fraction.

45%, the phase delay in the polymer even becomes positive. Hence, the large increase in the  $\delta$  in the ceramic phase of the composite is the main reason causing the drop in the quality factor of composites since, as pointed out, the high elastic constants in the ceramic phase implies that in most cases, the loss in the ceramic region plays a dominant role in controlling the mechanical  $Q$  of the thickness mode of a composite.

## VI. DISPERSION CURVES AND THE LATERAL MODES IN 1-3 COMPOSITES

In designing 1-3 composites, the frequency of lateral modes with respect to the thickness mode is often a concern. In this section, the experimental results on the lateral modes from piezocomposites as schematically shown in Fig. 1(a) will be presented which reveal several relations between the frequency of these modes and the gap width and shear velocity of the polymer matrix.

Presented in Fig. 11(a) are the first three branches of the dispersion curves for a 1-3 composite with 40% ceramic volume fraction: thickness  $t$  from 0.6 to 8 mm and the polymer gap width  $d_p = 0.36$  mm. At small  $\pi/t$  limit, the first branch corresponds to the thickness resonance and the second and third branches are the two lateral modes  $f_{11}$  and  $f_{12}$ , respectively. It was found that at small  $\pi/t$ , the frequency of the second lateral mode  $f_{12}$  can be related to the polymer gap width  $d_p$  through

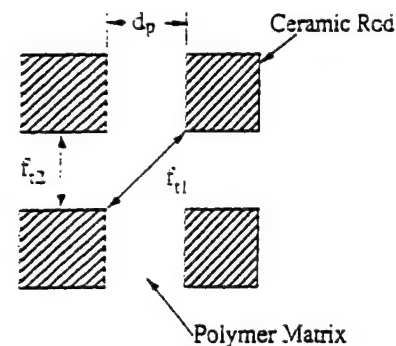


FIG. 12. Schematic of the lateral resonance modes in a 1-3 composite with square unit cell.  $f_{12} = V_t/2d_p$  and  $f_{11} = V_t/(2\sqrt{2}d_p)$ .

$$f_{12} = \frac{V_t}{2d_p} \quad (14)$$

where  $V_t$  is the shear velocity of the polymer phase. The result indicates that the second lateral mode can be viewed as a half-wave resonance in the polymer gap as depicted in Fig. 12. In addition, the frequency  $f_{11}$  (the first lateral mode) can be related to  $f_{12}$ .

$$f_{11} = f_{12}/\sqrt{2}$$

a relation which has been known previously.<sup>11</sup> This result suggests that the first lateral mode may correspond to a half-wave resonance across the diagonal direction as shown in Fig. 12. The interpretation here provides a much simpler and reasonable understanding on the nature of the lateral modes in a 1-3 composite and is consistent with the surface vibration profiles obtained from a laser probe reported in Refs. 17 and 23. As shown in Fig. 11(b), Eq. (14) is valid for 1-3 piezocomposites over a broad composition range as examined.

The results suggest that the lateral mode frequencies for 1-3 composites investigated here are determined mainly by the parameters of the polymer matrix: the shear wave velocity and the gap width. This is analogous to the behavior observed in 2-2 composites.<sup>11</sup> In addition, experiment was also conducted and result shows that  $f_{12}$  in Fig. 11(a) is nearly the same as the frequency of the first lateral mode in a 2-2 composite made with the same polymer and gap width (2-2 composite with 63% ceramic volume fraction). Hence, in analogy to 2-2 composites, because the elastic stiffness of the piezoceramic is much higher than that of the polymer, the ceramic can be viewed approximately as having stress free boundary condition and the polymer having fixed boundary condition (both  $u_3$  and  $u_1$  are zero at the interface). As has been demonstrated in our earlier paper,<sup>11</sup> this leads to the result that there are lateral resonance modes in a composite whose frequencies are determined mainly by the polymer gap properties.

## VII. SUMMARY

A dynamic model is derived for the analysis of the ultrasonic performance of 1-3 piezocomposites. To simplify the mathematics, 1-3 composites with the concentric unit cell was treated in the model which should closely resemble the

unit cell of a 1-3 composite with ceramic rods arranged in a hexagonal lattice. It is shown that the model can describe the thickness resonance of 1-3 composites quite well in the frequency range away from the mode coupling region. In addition, the lateral mode frequencies are examined experimentally and the data reveal that for 1-3 piezocomposites investigated (the elastic stiffness of the ceramic is much higher than that of polymer), the lateral mode frequencies are determined mainly by the polymer gap width and shear velocity. The result provides a useful guideline for the design of 1-3 composite transducers and is also important for the future development of theoretical models regarding the behavior of lateral modes in a 1-3 composite.

In the article, special attention is also paid to the losses in a 1-3 composite and it is found that the quality factor of the thickness mode for a composite is largely determined by the mechanical  $Q$  of the ceramic and its coupling to the polymer phase, which seem to be in contrary to the common belief that the low  $Q$  in a composite is due to the loss in the polymer. Even for a composite with the mechanical  $Q$  of the polymer larger than that of the ceramic, the quality factor (or mechanical  $Q$ ) of the composite is lower than both constituents. It is found that the phase delay between the strain  $S_{xx}$  and stress  $T_{xx}$  in the ceramic increases significantly in the composite compared with the single ceramic material, which is the main reason for the reduction of the quality factor  $Q$  in a composite. On the other hand, the coupling with the ceramic phase reduces the phase delay between the strain  $S_{xx}$  and stress  $T_{xx}$  in the polymer when compared with that in the single phase polymer. Due to the piezoelectric coupling, both the dielectric and piezoelectric losses affect the quality factor of a piezocomposite.

- <sup>1</sup> R. Newnham, *Annu. Rev. Mater. Sci.* **16**, 47 (1986).
- <sup>2</sup> W. A. Smith, *Proceeding of 1990 IEEE ISAF7*, Urbana, Illinois, 1990, p. 145.
- <sup>3</sup> W. A. Smith and B. A. Auld, *IEEE Trans. Ultrason. Ferroelectr. Freq. Control* **38**, 40 (1988).
- <sup>4</sup> K. Y. Hashimoto and M. Yamaguchi, *Proceedings 1986 IEEE Ultrasonics Symposium*, Williamsburg, VA, 1986, p. 697.
- <sup>5</sup> B. A. Auld, H. Kunkel, Y. A. Shui, and Y. Wang, *Proceedings of 1983 IEEE Ultrasonics Symposium*, Atlanta, GA, 1983, p. 554.
- <sup>6</sup> B. A. Auld, Y. A. Shui, and Y. Wang, *J. Phys. (Paris)* **45**, 159 (1984).
- <sup>7</sup> M. Yamaguchi, K. Y. Hashimoto, and H. Makita, *Proceedings of the 1987 IEEE Ultrasonics Symposium*, Denver, CO, 1987, p. 657.
- <sup>8</sup> J. A. Hossack and G. Hayward, *IEEE Trans. Ultrason. Ferroelectr. Freq. Control* **38**, 618 (1991).
- <sup>9</sup> A. Christine, H. Hennen, and J. N. Decarpigny, *J. Acoust. Soc. Am.* **94**, 621 (1993).
- <sup>10</sup> X. Geng and Q. M. Zhang, *Appl. Phys. Lett.* **67**, 3093 (1995).
- <sup>11</sup> X. Geng and Q. M. Zhang, *IEEE Trans. Ultrason. Ferroelectr. Freq. Control* **44**, 857 (1997).
- <sup>12</sup> PZT-5H is the trademark of Morgan Marroc, Inc. OH for one of its piezoceramics. Spurr epoxy is the trademark of Polysciences Inc., PA for one of its epoxy.
- <sup>13</sup> K. Nagaya, *J. Acoust. Soc. Am.* **67**, 2029 (1980).
- <sup>14</sup> H. S. Paul and M. Venkatesan, *J. Acoust. Soc. Am.* **85**, 163 (1989).
- <sup>15</sup> B. A. Auld, *Acoustic Fields and Waves in Solids* (Wiley, New York, 1973).
- <sup>16</sup> Q. M. Zhang and X. Geng, *J. Appl. Phys.* **76**, 6014 (1994).
- <sup>17</sup> T. R. Gururaja, W. A. Schuiza, L. E. Cross, R. E. Newnham, B. A. Auld, and J. Wang, *IEEE Trans. Sonics Ultrason.* **SU-32**, 481 (1985).
- <sup>18</sup> *IEEE Standard on Piezoelectricity*, ANSI/IEEE Std 176, 1987.
- <sup>19</sup> R. Holland, *IEEE Trans. Sonics Ultrason.* **SU-14**, 18 (1967).
- <sup>20</sup> A. G. Evans, B. R. Tittman, L. Ahlberg, B. T. Khuri-Yakub, and G. S. Kino, *J. Appl. Phys.* **49**, 1669 (1973).
- <sup>21</sup> R. Holland, *Design of Resonant Piezoelectric Devices* (MIT, Cambridge, MA, 1969).
- <sup>22</sup> H. Wang, Q. M. Zhang, and L. E. Cross, *Jpn. J. Appl. Phys., Part 2* **32**, L1281 (1993).
- <sup>23</sup> Dominique Certon, O. Casula, F. Patat, and D. Royer, *IEEE Trans. Ultrason. Ferroelectr. Freq. Control* **44**, 543 (1997).

# **APPENDIX 37**

## 5.25

# Piezoelectric Composite Sensors

JAMES F. TRESSLER

*Consortium for Oceanographic Research and Education,  
Washington, DC, USA*

and

KENJI UCHINO

*The Pennsylvania State University, University Park, PA, USA*

5.25.1 INTRODUCTION	1
5.25.2 PIEZOELECTRICITY	1
5.25.3 PIEZOELECTRIC MATERIALS	2
5.25.4 SENSOR CHARACTERIZATION	3
5.25.5 COMPOSITES	4
5.25.5.1 Piezoelectric-Polymer Composites	4
5.25.5.2 Piezoelectric-Metal Composites	8
5.25.6 SUMMARY	8
5.25.7 REFERENCES	9

### 5.25.1 INTRODUCTION

Piezoelectric composite sensors consist of an electrically active piezoelectric phase combined with an electrically inert second phase. Typically, this second phase is a polymer, although in some cases it is a metal. This chapter will discuss the rationale behind this approach to sensor design. It will begin with a brief review of piezoelectricity, followed by the important commercial piezoelectric sensor materials and their relevant properties, and subsequently the need for incorporating them into composite form. The chapter will conclude by discussing the principle two-phase composite sensor configurations and their properties, the main commercial manufacturing techniques, and some practical applications.

### 5.25.2 PIEZOELECTRICITY

Piezoelectric materials develop an electrical charge on their electroded faces when subjected to stress. They also exhibit a shape change that is linearly proportional to an applied electric field. The latter, known as the converse piezoelectric effect, is used in actuation and acoustic source generation. The former, called the direct piezoelectric effect, is utilized in sensing changes in force, displacement, or velocity.

Physically, piezoelectricity describes the coupling between the elastic variables (stress and strain) of a material and its electrical parameters (electric field and dielectric displacement). There are four piezoelectric coefficients that are designated as  $d$ ,  $e$ ,  $g$ , and  $h$  by convention. These coefficients are not independent but rather are inter-related through the material

dielectric and elastic constants. The charge coefficient,  $d$ , relates (i) the applied electric field to induced strain and (ii) stress to dielectric displacement. The stress coefficient,  $e$ , relates (i) applied electric field to stress and (ii) strain to dielectric displacement. The voltage coefficient,  $g$ , relates (i) the applied stress to generated electric field and (ii) the dielectric displacement to strain. The strain coefficient,  $h$ , relates (i) strain to electric field and (ii) dielectric displacement to stress. The constitutive equations and the relationships between the piezoelectric constants can be found in any quality text which covers piezoelectricity such as Moulson and Herbert (1992), Rosen *et al.* (1992), Ikeda (1990), Jaffe *et al.* (1971), and Berlincourt *et al.* in Mason's series on Physical Acoustics (1964).

The constitutive equations show that piezoelectric materials exhibit a linear relationship between their elastic and electrical variables. This is only true, however, at low levels of stress and small electric fields. The effects of high mechanical stress on nonlinearity depend primarily on the orientation and frequency of the applied stress with respect to the polar axis, as well as the electrical load conditions (Berlincourt *et al.*, 1964).

### 5.25.3 PIEZOELECTRIC MATERIALS

Piezoelectricity only occurs in materials whose crystal structure is noncentric. As such, it is exhibited in certain classes of crystals, ceramics, and polymers. In sensor applications where a variable has to be monitored over a long period of time, piezoelectric crystals are typically preferred over their piezoelectric ceramic counterparts (Maines, 1989). This is because crystals have much more stable piezoelectric properties compared to poled ceramics. Even though some piezoelectric crystals used in sensor applications occur abundantly in nature, they are more commonly grown synthetically. To be of practical use, however, they must be oriented and cut along specific crystallographic directions to obtain the best piezoelectric response. A number of important piezoelectric crystals and their properties are described in Ikeda (1990) and by Bhalla *et al.* (1993) in the Landolt-Börnstein tables. The most common ones used in sensor applications will be discussed here briefly.

Piezoelectric crystals are used most often in accelerometers and specialty hydrophones (underwater microphones). Quartz is the predominant material used for accelerometers (Maines, 1989). Lithium sulfate (because of its large  $g_h$

coefficient) and tourmaline are two piezoelectric crystals still used in commercial hydrophones. Tourmaline, along with Rochelle salt, are used in hydrophones designed for shock and blast measurements (Wilson, 1988). Lithium niobate and lithium tantalate are used as high-temperature acoustic sensors because they both maintain high sensitivity up to 400 °C (Turner *et al.*, 1994).

The piezoelectric materials found in many force and displacement sensors, however, are poled polycrystalline ferroelectric ceramics. Ceramic materials in general are characterized as having high mechanical strength and reproducible properties, possess a high resistance to severe ambient conditions such as temperature, pressure, and humidity, and perhaps most importantly can usually be made into complex shapes and large area pieces with little difficulty.

Bulk polycrystalline ceramics are typically synthesized via a high-temperature solid-state reaction of mixed oxides. In ferroelectric ceramics, like-polarized regions within each ceramic grain are formed as the ceramic cools through a specific temperature. This temperature, known as the Curie temperature, depends primarily on the chemical composition of the ceramic. On a macroscopic scale, these like-polarized regions (domains) are randomly oriented throughout the ceramic, resulting in no preferred polarization direction. The ferroelectric is therefore nonpiezoelectric.

Piezoelectricity is induced, however, by a process known as poling. During poling, a large static electric field is applied to the ceramic in a certain direction to switch the polarization axes of the domains to those directions (allowed by symmetry) which are nearest to that of the applied field (Gallego-Jurez, 1989). When the electric field is removed, some of the more highly strained domains revert to their original positions (depolarization), but a large majority remain aligned (remnant polarization).

When poled, polycrystalline ferroelectrics are often referred to as piezoelectric ceramics, or simply piezoceramics (Berlincourt *et al.*, 1964). The piezoceramic will remain in a poled state until it is either subjected to a mechanical stress or electric field (the coercive field) sufficiently large to reorient the domains or until it is heated above its Curie temperature, at which time its crystal structure will again become centric and piezoelectricity will be lost. Depolarization over a long period of time (i.e., months to years) due to internal stress relaxation is known as aging.

The lead zirconate titanate family of compositions, which are better known as PZTs (a

59 Wilson O. B.

54 Turner R. C.

sx0050

sx0055

sx0060

19 Gallego-Jur-

sx0065

6 Berlincourt D.

sx0070

sx0025

34 Moulson A. J.  
42 Rosen C. Z.  
26 Ikeda T.  
28 Jaffe B.

6 Berlincourt D.

sx0030

6 Berlincourt D.

sx0035

31 Maines R.

sx0040

26 Ikeda T.

7 Bhalla A. S.

sx0045

31 Maines R.

27 JaffeH.  
sx0075  
27 JaffeH.  
5 BerlincourtD.  
sx0080  
26 IkedaT.  
5 BerlincourtD.  
sx0085  
T001  
6 BerlincourtD.  
sx0090  
26 IkedaT.  
19 Gallego-Jur.  
54 TurnerR. C.  
sx0095  
59 WilsonO. B.

registered trademark of Clevite Corporation (Jaffe and Berlincourt, 1965)), are the piezoelectric ceramics of choice for many sensor applications. This is because of their easily tailorable, high piezoelectric properties as well as their high electromechanical coupling and relative ease of fabrication. In general, lead zirconate titanate compositions are modified by the addition of very small amounts (typically less than 2 mol.%) of either donor or acceptor dopants. The addition of dopants has a profound impact on both the physical and electrical properties of PZT. Donor dopants cause cation (metal) vacancies in the crystal structure which enhance domain reorientation and hence the extrinsic contribution to piezoelectric properties. These piezoelectrically "soft" PZTs are characterized by large piezoelectric coefficients, large dielectric constants, high dielectric losses, large electromechanical coupling factors, very high electrical resistance, low mechanical quality factors, a low coercive field and poor linearity (Jaffe and Berlincourt, 1965; Berlincourt, 1981).

Acceptor dopants cause anion (oxygen) vacancies in the crystal structure. This leads to piezoelectrically "hard" PZTs. Compared to soft PZTs, hard PZTs have lower piezoelectric coefficients, lower permittivity, lower dielectric losses, lower electrical resistivity, a higher mechanical quality factor, higher coercive field, are more difficult to pole and depole, and have better linearity (Ikeda, 1990; Berlincourt, 1981). Commercial PZT manufacturers have developed a general nomenclature based on US military specifications (1995) to differentiate the different PZT types, the physical and piezoelectric properties of which are listed in Table 1. Piezoelectric properties can show statistical and systematic fluctuations (up to 20%) from batch to batch or even within a batch due to slight chemical differences, variations in density, inhomogeneous chemical compositions, variations in grain size, and varying response to the poling treatment, etc. (Berlincourt *et al.*, 1964).

Other poled piezoceramic materials are used for specialty sensor applications. For instance, lead titanate is sometimes used as a hydrophone material or as a transceiver for use in medical diagnosis when it is doped with either calcium or strontium (Ikeda, 1990; Gallego-Jurez, 1989). This is due to its strong piezoelectric anisotropy. When doped with other elements, lead titanate is used as a knock sensor in automobiles. Its higher operating temperature range allows it to be mounted closer to the combustion chamber, giving it a faster response time than PZT (Turner *et al.*, 1994). Because of the difficulty in making and poling lead titanate, it

is not used in more applications. Bismuth titanate, when doped with sodium, can be used for accelerometers at temperatures up to 400 °C (Turner *et al.*, 1994). Lead metaniobate, a member of the tungsten bronze family, is often used in nondestructive testing, medical diagnostic imaging, and for deep submergence hydrophones (Wilson, 1988). However, problems such as a high level of porosity and relatively low mechanical strength are often encountered in its use. Antimony sulfur iodide has a very high  $g_h$  coefficient, especially when it is modified with 4–8% oxygen, making it attractive for some hydrophone applications. It can only be used at temperatures below 34 °C though (Wilson, 1988).

#### 5.25.4 SENSOR CHARACTERIZATION

For a poled ferroelectric ceramic, there are five nonzero piezoelectric coefficients. They are  $C_{31}$ ,  $C_{32}$ ,  $C_{33}$ ,  $C_{24}$ , and  $C_{15}$ , where  $C$  can represent either  $d$ ,  $e$ ,  $g$ , or  $h$ . Because of crystal symmetry,  $C_{31} = C_{32}$  and  $C_{24} = C_{15}$ . In the case of the  $g_{ij}$  coefficient, the first digit in the subscript,  $i$ , refers to the direction in which the voltage is measured and the second digit,  $j$ , refers to the direction of the applied stress. For a piezoceramic poled in the 3- (or thickness) direction, a voltage ( $V_3$ ) will be generated across the electrodes which is proportional to the voltage coefficient ( $g_{33}$ ), thickness of the element ( $t$ ), and magnitude of the applied stress ( $\sigma_3$ ) as:

$$V_3 = g_{33} \cdot t \sigma_3 \quad (1)$$

The receiving sensitivity ( $M$ ) of a piezoelectric is equal to the open circuit voltage ( $V_i$ ) that it generates due to an applied stress ( $\sigma_j$ ), or

$$M = V_i / \sigma_j = g_{ij} \cdot t \quad (2a)$$

Often, the sensitivity is reported in terms of decibels (dB) referenced to 1 volt per  $10^{-6}$  Pascal ( $\mu\text{Pa}$ ) of pressure as

$$M(\text{dB}) = 20 \cdot \log \left( \frac{g_{ij} \cdot t}{10^6} \right) \quad (0 \text{ dB re } 1 \text{ V}/\mu\text{Pa}) \quad (2b)$$

The sensitivity needs to be sufficiently high so that the generated signal can be detected above the background noise. In practice, the generated signal is small and has to be enhanced by an appropriate charge or voltage amplifier. The sensitivity is maximized when the  $g$  coefficient is maximized. The  $g$  coefficient is related to the  $d$  coefficient through the material's dielectric constant,  $K_{ij}^T$ , as:



$$g = d/K_{ij}^T \epsilon_0 \quad (3)$$

where  $\epsilon_0$  is the permittivity of free space. Typically a large capacitance, which is directly proportional to dielectric constant, is also desirable for sensors in order to overcome the electrical losses associated with the cables. Unfortunately, an increase in dielectric constant results in a lower voltage coefficient, as seen in the aforementioned equation. A flat sensitivity response over the frequency band of interest is another desirable characteristic for a sensor.

For in-air applications, either the  $g_{33}$  (longitudinal mode) or the  $g_{15}$  (shear mode) coefficient of the piezoceramic is typically utilized. When operating in the hydrostatic mode (i.e., when the incident stress is equal on all sides), the tensor coefficients are represented as  $d_h = d_{33} + 2d_{31}$  and  $g_h = g_{33} + 2g_{31}$ . Unfortunately, for poled piezoceramics (namely PZT), the  $d_{33}$  coefficient is approximately twice the magnitude and opposite in sign to the  $d_{31}$  coefficient (see Table 1). Since  $K_{ij}^T$  for most ferroelectric ceramics is very large ( $> 1000$ ), the  $g_h$  coefficient is also small (Equation (3)). As a consequence, the voltage generated by an incoming pressure wave is very low. In order to improve the sensitivity of the piezoceramic, it must be configured in such a way that the effect of the hydrostatic pressure is minimized. This usually takes the form of air backing one side of the ceramic element, encapsulating part of the ceramic in a soft polymer to absorb a portion of the hydrostatic stress, or incorporating air spaces into the sensor itself.

A figure-of-merit, the  $d_h \cdot g_h$  product, is often reported as a measure of the quality of the sensing capability of the piezoelectric element or to compare different hydrophone materials (Bhalla and Ting, 1988). Quantitatively, it is used to ascertain the type of amplifier required in the electronic circuitry to overcome the self-noise of the system. In the case of piezocomposites, the  $d_h \cdot g_h$  product should be normalized by the volume of the device in order to make accurate comparisons between the different configurations (Gabrielson, 1997).

### 5.25.5 COMPOSITES

The basic idea behind a composite structure is to maximize the desirable traits of each component in the composite while minimizing the effects of the less desirable features. In a two-phase composite, each individual phase can be connected to itself throughout the volume of the composite in either 0, 1, 2, or 3 directions. The connectivity of the individual phases is of utmost importance because it controls the elec-

tric flux pattern as well as the mechanical properties of the composite. Both, in turn, can be changed by orders of magnitude depending on how the individual phases are connected (Pilgrim *et al.*, 1987).

The notation used to denote the different connectivity patterns is known as the Newnham connectivity (or classification) system (Pilgrim *et al.*, 1987; Newnham *et al.*, 1978). The convention is for the connectivity of the active phase to appear first, followed by the connectivity of the passive phase (Pilgrim *et al.*, 1987). There are 16 possible two-phase piezocomposite structures. The configurations for which sensitivity measurements have been reported are shown schematically in Figure 1.

#### 5.25.5.1 Piezoelectric-Polymer Composites

The two most common composite types used for sensor applications are those with 0-3 and 1-3 connectivity. The remainder of this chapter will focus on describing in more detail the manufacturing techniques, properties, and some practical applications for these two types of piezocomposite. Other configurations for which sensitivity results have been reported will also be briefly discussed for the sake of completeness.

Piezocomposites with 0-3 connectivity consist of tiny nontouching piezoelectric particulates randomly dispersed within a chloroprene rubber host matrix. These composites are characterized by their mechanical robustness, flexibility, and by their good acoustical impedance match to air and especially water. Currently, the primary commercial manufacturer of 0-3 type piezocomposites is the NTK Technical Ceramics Division of the NGK Spark Plugs Corporation in Japan. NTK markets their products under the tradename *Piezo Rubber* (usually abbreviated as PR or PZR). Although the PZT family predominates as the active phase in most other piezocomposite designs, lead titanates (PTs) are preferred in the 0-3s (Newnham *et al.*, 1984; Banno, 1983). The reason for this is the large piezoelectric anisotropy inherent in lead titanate and modified lead titanates, which ultimately results in a higher piezoelectric activity in the poled composite.

*Piezo Rubbers* are fabricated by rolling a well-dispersed ceramic-rubber mixture into thin ( $\approx 5$  mm) large surface area sheets using a hot roller, followed by an additional heat and pressure treatment (Banno, 1990). Finally, both the upper and lower surfaces are electroded using an elastomer-based silver coating. Be-

39 PilgrimS. M.  
sx0135

39 PilgrimS. M.  
36 NewnhamR.

39 PilgrimS. M.

F001

sx0140

sx0145

sx0150

35 NewnhamR.  
2 BannoH.

sx0155

3 BannoH.

sx0115

sx0120

sx0125

8 BhallaA. S.

18 T.B. Gabriel-

sx0130

cause the individual ceramic particulates in the composite are all surrounded by a low permittivity dielectric polymer, poling requires a very large static electric field. Fields of the order of  $100 \text{ kV cm}^{-1}$  applied for 1 h are not unreasonable. Adequate poling can be accomplished at much lower fields ( $35\text{--}40 \text{ kV cm}^{-1}$ ) and for shorter poling times (a few minutes) if a small amount (about 1.5%) of carbon is added to the polymer matrix during the mixing stage (Newnham *et al.*, 1984). Unfortunately, the addition of carbon contributes to an increase in the dielectric dissipation loss (and subsequently Johnson noise) in the composite. As a consequence, the sensor signal-to-noise ratio is reduced. An alternative approach to reduce the poling field without introducing an electrically conducting material into the system is to deliberately select a polymer host matrix with a relatively high temperature coefficient of resistivity. By poling the composite at an elevated temperature, it becomes possible to use the improved ceramic/polymer resistivity balance to give saturation poling, while at the same time retaining the low resistivity and low loss at the temperatures of operation (Twiney, 1992).

In addition to sheet form, NTK also manufactures 0-3s in the form of long thin wires under the tradename *Piezo Wire*. NTK *Piezo Wire* is marketed primarily as a flexible acceleration sensor, although it can also be used as a pick up for an electric piano or electric guitar, stretched across a street to monitor traffic flow, or wrapped around the body to detect heart sound and blood pressure. Research has also included using 0-3s in smart systems to actively control acoustic noise (Salloway, 1996). In addition, it has been investigated as a potential thin-layer vibration detector which can be coated directly onto a structure due to its paint-like texture in the initial stage of manufacture (Egusa and Iwasawa, 1994).

Table 2 shows the relevant low-frequency properties of various *Piezo Rubber* compositions. The various numerical designations are based on different ceramic powder volume fractions and/or different particle size distributions. The dielectric constant of each of the composites is much less than that of the lead titanate active phase (see Table 1) due to the presence of the polymer matrix. Nevertheless, the acoustic impedance, dielectric constant, and dielectric loss are approximately constant for all the PR types shown. The low characteristic impedance implies that the *Piezo Rubbers* have a better acoustic impedance match to either an air or water medium than does the ceramic alone. The reduction (compared to the monolithic ceramic) and the variation in the  $d_h$  coefficients

are a result of the change in the volume fraction of ceramic present from one PR type to another. The large increase in the  $g_h$  coefficient is due to the associated decrease in dielectric constant.

Figure 2 shows the frequency dependence of the receiving sensitivity (as defined by Equation 2(b)) for four different types of *Piezo Rubbers* when used as a hydrophone. The nearly flat sensitivity response between 10 Hz and 10 kHz indicates that they can be used effectively over this entire frequency band. The pressure dependencies of the receiving sensitivity (measured at 160 Hz) for these same PR types (plus 06) are compared in Figure 3. As a rule of thumb, the pressure in MPa is equivalent to 100 m of water depth. The sensitivity of PR-305 is the most pressure dependent. This was attributed to the presence of porosity in the epoxy matrix (Banno *et al.*, 1987). The other compositions are approximately pressure independent up through 15 MPa. Taking into account the thickness of the various *Piezo Rubbers* in the figure, their receiving sensitivities are 20–40 dB better than bulk PZT and up to 10 dB better than pure lead titanate (see Table 1). The dielectric, piezoelectric, and elastic properties of 0-3 composites also vary as a function of temperature. These property variations are attributed to the transition of the polymer matrix from stiff glass-like to soft rubber-like behavior as the temperature is increased (Rittenmyer and Dubbelday, 1992).

Piezoelectric-polymer composites with 1-3 connectivity consist of parallel aligned piezoceramic (generally PZT) rods or fibers imbedded within a three-dimensional polymer host matrix (Figure 1). This composite design is intended to operate in its pure thickness mode. The 1-3 type composites have been used effectively as sensors at frequencies spanning from Hz to MHz. When used solely as a sensor, the volume fraction of PZT in the composite is generally between 5 and 25%. When used for both transmit as well as receive, the optimum PZT volume fraction is between 30 and 50%. As such, 1-3 type piezocomposite sensors are generally much lighter in weight than their 0-3 counterparts.

The polymer phase in a 1-3 composite serves a dual purpose. First, it improves the mechanical compliance as well as the acoustic impedance match to either air or water compared to the monolithic ceramic. Second and most importantly, the polymer acts as a stress transfer mechanism to decouple the longitudinal and transverse contributions of the piezoceramic to a hydrostatic stress. When subject to a hydrostatic stress, there are three contributions to the hydrostatic piezoelectric voltage coefficient,

35 Newnham R.  
sx0160

55 Twiney R. C.  
sx0165

44 Salloway A. J.

14 Egusa S.  
sx0170  
T002

xx0175  
F002

F003

4 Banno H.  
sx0180

40 Rittenmyer K.  
sx0185

xx0190



- 49 Smith W. A.  $g_h$  of the composite (Smith, 1993). The first comes from the composite  $g_{33}$ , in which the longitudinal, or axial, stress is transferred directly to the piezoceramic rods. The second contribution comes from the composite  $g_{31}$ . In this case, the transverse stresses are transmitted to the sides of the piezoceramic elements via the polymer. The third contribution also arises from the composite  $g_{31}$ . When squeezed from all sides, the polymer bulges due to the Poisson ratio effect, pulling on the ceramic rods and lengthening them. This  $g_{31}$  contribution from the composite effectively counteracts the  $g_{33}$  contribution and consequently lowers the  $g_h$  of the structure. The effectiveness of the stress transfer is characterized by a stress amplification factor which depends on the individual rod diameters, the rod-to-rod spacing, the volume percent and arrangement of the rods, as well as the stiffness of the polymer. Under a hydrostatic pressure, the stress amplification factor is practically reduced by a factor of  $(1-2\nu)$ , where  $\nu$  is the Poisson ratio of the polymer phase (Cao *et al.*, 1992). Since the applied stress incident on a 1-3 piezocomposite is designed to be carried mainly by the piezoceramic rods, a pressure-induced depolarization effect also occurs in the rods. This effect can become quite pronounced under large loads as well as for a low volume fraction of rods, which is often the preferred design choice for sensor applications. When used under these conditions, the performance of a 1-3 piezocomposite degrades, causing reliability problems in the device.

11 Cao W.  $g_{33}$  mode (Zhang *et al.*, 1993; Wang *et al.*, 1995). This latter design also has the advantage of not depoling under high pressures. Incorporating a softer polymer phase between the ceramic rods and the stiffer polymer matrix has also been tried (Kim *et al.*, 1994), as well as a glass fiber reinforcement phase in the lateral direction to support the transverse direction stress (Haun *et al.*, 1986). All these solutions, however, add complexity and manufacturing cost to the composite.

24 Haun M. J. The two primary commercial methods used to manufacture 1-3 piezocomposites are the dice-and-fill technique and injection molding. The technology used typically depends on the desired properties of the end product. For the dice-and-fill technique (Savakus *et al.*, 1981), a diamond saw is used to cut perpendicular grooves nearly through a piezoceramic plate to form rows and columns of pillars. A suitable polymer is then vacuum cast into the grooves. After the polymer has cured, the ungrooved backplate is ground away and the composite is polished to the desired thickness. The composite assembly is completed by electroding both the upper and lower surfaces and poling. The dice-and-fill technique limits the shape of the pillars to be square or rectangular. Pillars 100  $\mu\text{m}$  on edge and groove sizes down to 25  $\mu\text{m}$  can be achieved (Janas and Safari, 1995; Smith, 1992). Both are limited by the machinability of the ceramic as well as the width of saw blade. The dice-and-fill technique is adequate for the production of small area samples, such as required in medical transducers. However, it is not cost effective and is too time consuming for applications requiring large area coverage.

48 Smith W. A. Manufacturing 1-3 composites for large area coverage is better suited to injection molding. In order to perform the injection molding technique, the piezoceramic powder first has to be thoroughly mixed with a suitable organic binder which acts as a carrier during molding, allowing its transfer as a viscous fluid under heat and pressure (Bowen *et al.*, 1993). This hot thermoplastic mixture is then rammed, or injected, into a cold metal mold which is the negative of the desired end product. This gives a green (i.e., unfired) ceramic preform. When the preform has been ejected from the mold, it is slowly heated to burn out the organic binder before being sintered. The sintered preform is electroded, poled, encapsulated in a polymer, and has the backing plate ground off (in that order). Injection molding is a fast and simple net-shape process which can provide dense, large area pieces with different rod shapes, arrangements, and diameters. The most expensive feature of this technique is the production of the mold. The primary commercial manufacturer of injection molded 1-3 piezocomposites at the present time is Material Systems Incorporated (MSI) in the USA. Their composites, sold under the tradename SonoPanels, can have rod diameters between 70  $\mu\text{m}$  and 5 mm with thicknesses upwards of 25 mm. In addition, ceramic volume fractions have ranged from 15 to 40% (Bowen *et al.*, 1993, 1996).

10 Bowen L. J. There has been a long-term interest by the US Navy in developing piezocomposites for underwater sensor applications because of their high hydrostatic sensitivity response.

Over the years, this research effort has resulted in the development of the piezo-polymer PVDF as well as 0-3 piezocomposites. Advancement of the 1-3 type piezocomposites, however, was hindered due to the lack of manufacturing technology. With the advent of advanced processing methods, including the highly successful injection molding technique previously described, the advantages of the 1-3 piezocomposites are now being realized. For example, one application is a hull-mounted conformal array for acoustical detection. Other recent applications based on the advanced material processing capabilities include in-air and in-water active control applications which use 1-3s consisting of integrated pressure sensors, accelerometers, and actuators (Gentilman *et al.*, 1996; Fiore *et al.*, 1997a, 1997b; Corsaro *et al.*, 1997). A photograph of the cutaway of a panel used for vibration control applications is shown in Figure 4.

Additional interest in 1-3 piezocomposites include their use in medical pulse-echo ultrasonic transducers for acoustic imaging. The primary manufacturers of ultrasonic probes that feature 1-3 piezocomposite materials as the active component have been Phillips Medical Systems, Echo Ultrasound, Acuson, Acoustic Imaging, Precision Acoustic Devices, Hitachi, and Siemens AG (Smith, 1992; Oakley, 1991; Wersing, 1986; Takeuchi *et al.*, 1984). Medical ultrasonic transducers use the 1-3 design because of their lower acoustic impedance matching to the medium, higher bandwidth, and clean, mode-free operations.

The receiving sensitivity as a function of frequency for a 6.3 mm thick 1-3 piezocomposite (SonoPanel™) containing 15 vol.% PZT-5H rods each 1.15 mm in diameter is shown in Figure 5. The receive sensitivity is quite high at about  $-186$  dB, re:  $1 \text{ V } \mu\text{Pa}^{-1}$ , and is nearly constant from 1 kHz to almost 100 kHz. The sensitivity of the composite is over 30 dB higher than monolithic PZT-5H of the same thickness and also compares well to a 0-3 *Piezo Rubber*.

The pressure dependence of the receive sensitivity (measured at both 4°C and 29°C at 1 kHz) of a 1-3 type piezocomposite is shown in Figure 6. The composite contains 30 vol.% PZT-4 rods each 1 mm on edge and 3 mm thick and is encapsulated in an epoxy resin. The response is flat up to at least 15 MPa of pressure. Compared to the 1-3 piezocomposite in Figure 5, the lower sensitivity response in this case is likely due to a combination of effects from different PZT type, different epoxy matrix, and thinner sample.

The low frequency properties of 1-3 piezocomposites are shown in Table 3. In comparison with 0-3 piezocomposites, the 1-3s exhibit

higher  $d_{33}$  and  $d_h$  coefficients, indicating that they make better electromechanical actuators and acoustic transmitters. Conversely, the 1-3s have comparable or slightly lower  $g_h$  constants (due to their higher dielectric constants). This indicates that 1-3s and 0-3s are roughly equivalent in terms of receive, or sensor, capability. However, because of the lower dielectric dissipation of 1-3 piezocomposites compared to the 0-3s, the self-noise level is 3–6 dB less for 1-3 devices (Geil and Matteson, 1992; Geil *et al.*, 1996). Another advantage that the 1-3 configuration has over the 0-3 design is in design tailorability. The 1-3 design can be easily modified to change the mechanical resonance frequency and the mechanical  $Q$ , as well as other aspects.

Other piezocomposite connectivities schemes are either in the developmental stage, such as the 3-3s, or essentially have been abandoned because they are too difficult/costly to manufacture or show no significant advantage over the 0-3 or 1-3 type piezocomposites (i.e., the 2-2s). Composites with 3-3 connectivity were initially fabricated by a technique known as the replamine process (Skinner *et al.*, 1978) which is the lost wax replication of a coral skeleton. Since then, additional technologies have been developed such as the fugitive phase, or BURPS (BURNed out Polymer Spheres), process (Shrout *et al.*, 1979; Rittenmyer *et al.*, 1982) which produces a porous three-dimensionally interconnected ceramic structure by sintering a compacted mixture of volatilizable plastic spheres and PZT powder. A reticulated ceramic technology (Creeden and Schulze, 1996) and solid freeform fabrication (Bandyopadhyay *et al.*, 1997) are two recently developed potential manufacturing methods. In the latter technique, a honeycomb-like piezoceramic structure is built up layer by layer by computer-aided fused deposition technology. The ceramic lattice is then backfilled with polymer and electroded to complete the composite.

In some 3-3 composites, the passive phase is air rather than polymer. This kind of composite is called a porous piezoceramic composite. Mitsubishi Mining and Cement (now Mitsubishi Materials) has developed several techniques for introducing connected porosity into PZT ceramics: reactive sintering, foaming agents, organic additives, and careful control of particle size and firing conditions (Gururaja *et al.*, 1988). The receiving sensitivity of such a composite is shown in Figure 7. This composite exhibits a nearly constant receive sensitivity of  $-207$  dB, re:  $1 \text{ V } \mu\text{Pa}^{-1}$ , from 1 kHz through 40 kHz. When the  $g_h$  constant of this composite was measured as a function of hydrostatic pressure, a nearly flat response was observed up

22 Gentilman R.  
16 Fiore D.  
17 Fiore D.  
12 Corsaro R. D.

F004  
sx0240

48 Smith W. A.  
38 C.G. Oakley.  
58 Wersing W.  
50 Takeuchi H.

sx0245

F005

sx0250

F006

sx0255

T003

20 Geil F.

21 Geil F. G.

sx0260

47 Skinner D. P.

46 Shrout T. R.

41 Rittenmyer K.

sx0265

13 Creeden M. J.

1 Bandyopad-

sx0270

23 Gururaja T. R.  
sx0275  
F007

through 60 MPa. At this pressure, the response had decreased by only 1 dB from its initial value (Ting, 1990).

Conventional composites exhibiting 3-1 and 3-2 connectivity consist of a PZT block with holes drilled through either one side (3-1) or both sides (3-2) in a direction perpendicular to the poled direction of the PZT. The holes are subsequently back-filled with polymer. In 3-1 and 3-2 composites manufactured in this way, the dielectric constant, as well as the  $d_h$  and  $g_h$  coefficients, are all functions of hole size, PZT thickness, poling technique, and center-to-center distance between adjacent holes (Safari *et al.*, 1982). The receiving sensitivity for a typical 3-1 piezocomposite at three different frequencies is shown in Figure 8. The response is relatively independent of frequency and pressure up through 6 MPa. A higher response is generated in the 3-2 composite because of its greater mechanical compliance. The primary drawbacks of these latter two configurations are in manufacturing, durability, and mechanical flexibility.

#### 5.2.5.2 Piezoelectric-Metal Composites

In ceramic-metal composites, metal faceplates, shells, or caps are mechanically coupled to both the active ceramic as well as the surrounding medium and are the means by which the incident stress is transferred to the piezoceramic. The best ceramic-metal composite sensors are the flextensional-type transducers. In a flextensional sensor, the flexural vibration of the metal shell causes an extensional (or contractional) vibration in the piezoelectric element. Flextensional transducers are typically quite massive, in terms of both size and weight. The "moonie" and "cymbal" type transducers are miniaturized versions of flextensionals.

The moonie and cymbal transducers possess 2-(0)-2 connectivity. These transducers consist of a piezoceramic disk sandwiched between two metal caps, each of which contains a shallow air-filled cavity on its inner surface. In the case of the moonie, the cavities are in the shape of a half-moon, whereas the cymbal has a truncated cone-shaped cavity (Figure 9). The presence of these cavities allows the metal caps to serve as mechanical transformers for converting and amplifying a portion of the incident axial-direction stress into tangential and radial stresses of opposite sign. Thus, the  $g_{31}$  and  $g_{33}$  contributions of the PZT now add together (rather than subtracting) in the effective  $g_h$  of the device (Tressler *et al.*, 1995). For a moonie transducer, an effective  $d_h \cdot g_h$  product exceeding

$50\,000 \times 10^{-15} \text{ m}^2 \text{ N}^{-1}$  is achievable (Xu *et al.*, 1991). A cymbal transducer, on the other hand, can exhibit an effective  $d_h \cdot g_h$  product exceeding  $100\,000 \times 10^{-15} \text{ m}^2 \text{ N}^{-1}$  because of its more efficient stress-transfer mechanism (Tressler *et al.*, 1995). The higher sensitivity in the case of the cymbal compared to the moonie is at the expense of an increase in pressure dependence in its performance. Flextensional moonie-type transducers have seen extensive use as the sensor component in towed arrays used for underwater oil exploration.

#### 5.2.5.6 SUMMARY

The sensitivity ( $M$ ) of a piezoelectric is a function of its voltage coefficient ( $g_{ij}$ ) and its thickness ( $t$ ) as  $M = g_{ij} \cdot t$ . A poled piezoelectric ceramic such as PZT has five nonzero coefficients:  $g_{31} = g_{32}$ ,  $g_{33}$ , and  $g_{15} = g_{24}$ . For in-air applications, either the  $g_{33}$  (longitudinal mode) or  $g_{15}$  (shear mode) coefficients are typically used. When used in a hydrostatic mode, such as when fully immersed in water, the sensitivity is proportional to the hydrostatic  $g$ -coefficient ( $g_h$ ) which is equal to  $g_{33} + 2g_{31}$ . For a poled piezoelectric ceramic,  $g_{33} \approx -2g_{31}$  due to crystallographic symmetry arguments. Thus, the sensitivity of a monolithic piezoelectric ceramic under hydrostatic conditions is rather low. This is the main reason why piezoelectric ceramics are incorporated into composite configurations.

Piezoceramic-polymer composites are designed to eliminate either the  $g_{31}$  or  $g_{33}$  contribution to  $g_h$ . The manner in which the ceramic and polymer are self-connected throughout the composite volume has a marked effect on its properties. Composites with 0-3 connectivity are typically in the form of flexible rubber sheets. They are characterized by high sensitivity, high pressure tolerance, a broad operating bandwidth, as well as a good acoustical impedance match to air or water. Piezocomposites with 1-3 connectivity have roughly the same performance characteristics as 0-3s. Physically, though, they are more rigid, lighter in weight, and can be more easily tailored to application-specific needs. As seen in Table 3, other piezocomposite designs have not shown any marked advantage over the 0-3 or 1-3 composite designs. Piezoceramic-metal composites (flextensional devices) exhibit very high sensitivity because they are engineered such that the  $g_{33}$  and  $g_{31}$  coefficients of the piezoceramic constructively contribute to the  $g_h$  of the device (i.e., they effectively add together rather than

51 Ting R. Y.  
sx0280

60 Xu Q. C.

53 Tressler J. F.

43 Safari A.  
sx0285

F008

xx0305

xx0290

xx0310

xx0295

F009

xx0315

53 Tressler J. F.  
sx0300

subtract). Compared to the aforementioned piezoceramic-polymer composites, metal ceramic composites have a much narrower operating bandwidth and show more highly pressure-dependent performance characteristics.

## 5.25.7 REFERENCES

sx0320

- 1 A. Bandyopadhyay, R. K. Panda, V. F. Janas, M. K. Agarwala, S. C. Danforth and A. Safari, *J. Am. Ceram. Soc.*, 1997, **80**, 1366-1372.
- 2 H. Banno, *Ferroelectrics*, 1983, **50**, 3-12.
- 3 H. Banno, in 'Proceedings of the 7th IEEE International Symposium on Applications of Ferroelectrics', University of Illinois at Urbana-Champaign, eds. S. B. Krupanidhi and S. K. Kurtz, IEEE, Piscataway, NJ, 1990, pp. 67-72.
- 4 H. Banno, K. Ogura, H. Sobue and K. Ohya, *Jpn. J. Appl. Phys.*, 1987, **26 Suppl.** 26-1, 153-155.
- 5 D. Berlincourt, *J. Acoust. Soc. Am.*, 1981, **70**, 1586-1595.
- 6 D. A. Berlincourt, D. R. Curran and H. Jaffe, in 'xPhysical Acoustics', ed. W. P. Mason, Academic Press, New York, 1964, vol. 1, Part A, pp. 169-270.
- 7 A. S. Bhalla, W. R. Cook, Jr., S. T. Liu, in 'Landolt-Börnstein Numerical Data and Functional Relationships in Science and Technology New Series: Low Frequency Properties of Dielectric Crystals—Piezoelectric, Pyroelectric, and Related Constants', ed. D. F. Nelson, vol. III/29b Springer, New York, Berlin, Heidelberg, 1993.
- 8 A. S. Bhalla and R. Y. Ting, *Sensors and Materials*, 1988, **4**, 181-185.
- 9 L. Bowen, R. Gentilman, D. Fiore, H. Pham, W. Serwatka, C. Near and B. Pazol, *Ferroelectrics*, 1996, **187**, 109-120.
- 10 L. J. Bowen, R. L. Gentilman, H. T. Pham, D. F. Fiore and K. W. French, in 'Ultrasonics Symposium Proceedings, Baltimore', eds. M. Levy and B. R. McAvoy, IEEE, Piscataway, NJ, 1993, vol. 1, pp. 499-503.
- 11 W. Cao, Q. M. Zhang and L. E. Cross, *J. Appl. Phys.*, 1992, **72**, 5814-5821.
- 12 R. D. Corsaro, B. Houston and J. A. Bucaro, *J. Acoust. Soc. Am.*, 1997, **102**, 1573-1581.
- 13 M. J. Creeden and W. A. Schulze, in 'Proceedings of the 10th IEEE International Symposium on Applications of Ferroelectrics', New Brunswick, NJ, 1996, eds. B. M. Kulwicki, A. Amin, and A. Safari, IEEE, Piscataway, NJ, 1996, vol. 1, pp. 527-530.
- 14 S. Egusa and N. Iwasawa, *J. Intell. Mater. Sys. Struct.*, 1994, **5**, 140-144.
- 15 L. Eyraud, C. Richard and D. Guyomar, in 'Ultrasonics Symposium Proceedings', Cannes, 1994, eds. M. Levy, S. C. Schneider and B. R. McAvoy, IEEE, Piscataway, NJ, 1994, vol. 2, pp. 929-934.
- 16 D. Fiore, R. Gentilman, H. Pham, W. Serwatka, P. McGuire, C. Near and L. Bowen, in 'Proceedings of the SPIE: Smart Structures and Materials 1997—Industrial and Commercial Applications of Smart Structures Technologies', San Diego, ed. J. M. Sater, SPIE, Bellingham, WA, 1997, pp. 391-396.
- 17 D. Fiore, R. Torri and R. Gentilman, in 'Proceedings of the 8th US-Japan Seminar on Dielectric and Piezoelectric Ceramics', Plymouth, MA, 1997, eds. R. Gururaja and T. R. Shrout, Internal Publication, 1997b, pp. 344-347.
- 18 T. B. Gabrielson, Presented at the 1997 ONR Transducer Materials and Transducers Workshop, The Pennsylvania State University, University Park, PA, April 1997.
- J. A. Gallego-Jurez, *J. Phys. E. Sci. Instrum.*, 1989, **22**, 804-816.
- F. Geil and L. Matteson, in 'Proceedings of the ADPA/AIAA/ASME/SPIE Conference on Active Materials and Adaptive Structures', Alexandria, VA, 1992, ed. G. J. Knowles, Institute of Physics Publishing, Philadelphia, PA, 1992, pp. 135-138.
- F. G. Geil, R. Gentilman, W. Serwatka and K. Webman, *J. Acoust. Soc. Am.*, 1996, **100**, 2583.
- R. Gentilman, D. Fiore, H. Pham-Nguyen, W. Serwatka, B. Pazol, C. Near, P. McGuire and L. Bowen, in 'Proceedings of the SPIE: Smart Structures and Materials 1996—Industrial and Commercial Applications of Smart Structures Technologies', San Diego, ed. C. R. Crowe, SPIE, Bellingham, WA, 1996, pp. 234-239.
- T. R. Gururaja, A. Safari, R. E. Newnham and L. E. Cross, in 'Electronic Ceramics: Properties, Devices, and Applications', ed. L. M. Levinson, Marcel Dekker, New York, 1988, pp. 92-145.
- M. J. Haun, R. E. Newnham and W. A. Schulze, *Adv. Ceram. Mater.*, 1986, **1**, 361-365.
- J. A. Hossack and R. L. Bedi, *Key Engr. Mater.*, 1994, **92-93**, 92-93.
- T. Ikeda, 'Fundamentals of Piezoelectricity', Oxford University Press, New York, 1990, p. 16, 210-226.
- H. Jaffe and D. A. Berlincourt, *Proc. IEEE*, 1965, **53**, 1372-1386.
- B. Jaffe, W. R. Cook and H. Jaffe, 'Piezoelectric Ceramics', Academic Press, New York, 1971.
- V. F. Janas and A. Safari, *J. Am. Ceram. Soc.*, 1995, **78**, 2945-2955.
- C. Kim, K. M. Rittenmyer, and M. Kahn, *Ferroelectrics*, 1994, **156**, 19-24.
- R. Maines, *Sensors*, 1989, **6**, 26-27.
- Military Standard, *Piezoelectric Ceramic Material and Measurements Guidelines for Sonar Transducers*, MIL-STD-1376B (SH), 24 February 1995.
- Morgan Matroc, Product literature.
- A. J. Moulson and J. M. Herbert, 'Electroceramics', Chapman & Hall, New York, 1992, pp. 265-317.
- R. E. Newnham, A. Safari, G. Sa-gong and J. Giniewicz, in 'Ultrasonics Symposium Proceedings', Dallas, ed. B. McAvoy, IEEE, Piscataway, NJ, 1984, 1984, pp. 501-506.
- R. E. Newnham, D. P. Skinner and L. E. Cross, *Mat. Res. Bull.*, 1978, **13**, 525-536.
- NTK Technical Ceramics, NTK *Piezo Rubber* product information.
- C. G. Oakley, Ph.D. Thesis, The Pennsylvania State University, 1991, pp. 3-4.
- S. M. Pilgrim, R. E. Newnham and L. L. Rohlfling, *Mat. Res. Bull.*, 1987, **22**, 677-684.
- K. M. Rittenmyer and P. S. Dubbelday, *J. Acoust. Soc. Am.*, 1992, **91**, 2254-2260.
- K. Rittenmyer, T. Shrout, W. A. Schulze and R. E. Newnham, *Ferroelectrics*, 1982, **41**, 189-195.
- C. Z. Rosen, B. V. Hiremath and R. E. Newnham (eds.), 'Piezoelectricity', American Institute of Physics, New York, 1992.
- A. Safari, R. E. Newnham, L. E. Cross and W. A. Schulze, *Ferroelectrics*, 1982, **41**, 197-205.
- A. J. Salloway, *Ferroelectrics*, 1996, **187**, 219-226.
- H. P. Savakus, K. A. Klicker and R. E. Newnham, *Mat. Res. Bull.*, 1981, **16**, 677-680.
- T. R. Shrout, W. A. Schulze and J. V. Biggers, *Mat. Res. Bull.*, 1979, **14**, 1553-1559.
- D. P. Skinner, R. E. Newnham and L. E. Cross, *Mat. Res. Bull.*, 1978, **13**, 599-607.
- W. A. Smith, in 'Proceedings of the SPIE: New Developments in Ultrasonic Transducers and Transducer Systems', San Diego, ed. F. L. Lizzi, SPIE, Bellingham, WA, 1992, pp. 3-26.
- W. A. Smith, *IEEE Trans. Ultrason., Ferroelect., Freq.*

*Contr.*, 1993, 40, 41-49.

50 H. Takeuchi, C. Nakaya and K. Kutakura, in 'Ultrasonics Symposium Proceedings', Dallas, 1984, ed. B. R. McAvoy, IEEE, Piscataway, NJ, 1984, pp. 507-510.

51 R. Y. Ting, *Ferroelectrics*, 1990, 102, 215-224.

QA152 R. Y. Ting, *Applied Acoustics*, 1994, 41, 325-335.

53 J. F. Tressler, A. Dogan, J. F. Fernandez, J. T. Fielding, Jr., K. Uchino, R. E. Newnham, in 'Ultrasonics Symposium Proceedings', Seattle, 1995, eds. M. Levy, S. C. Schneider and B. R. McAvoy, IEEE, Piscataway, NJ, 1995, pp. 897-900.

54 R. C. Turner, P. A. Fuierer, R. E. Newnham and T. R. Shrout, *Applied Acoustics*, 1994, 41, 299-324.

55 R. C. Twiney, *Adv. Mater.*, 1992, 4, 819-822.

56 Vernitron Piezoelectric Division, *Piezoelectric Tech-*

*nology—Data for Designers.*

H. Wang, Q. M. Zhang, L. E. Cross and C. M. Trottier, *Ferroelectrics*, 1995, 173, 181-189.

W. Wersing, in 'Proceedings of the 6th IEEE International Symposium on the Application of Ferroelectrics', Lehigh University, Bethlehem, PA, 1986, ed. W. A. Smith, IEEE, Piscataway, NJ, 1986, pp. 212-223.

O. B. Wilson, 'Introduction to Theory and Design of Sonar Transducers', Peninsula Publishing, Los Altos, CA, 1988.

Q. C. Xu, S. Yoshikawa, J. R. Belsick and R. E. Newnham, *IEEE Trans. Ultrason., Ferroelect., Freq. Contr.*, 1991, 38, 634-639.

Q. M. Zhang, H. Wang and L. E. Cross, *J. Mater. Sci.*, 1993, 28, 3962-3968.

57

58

59

60

61

## References

11

**Table 1** Room temperature piezoelectric properties of common piezoceramic materials.

<i>Military specification</i>	<i>Commercial specification</i>	$T_c$	$d_{33}$	$d_{31}$	$d_{15}$	$K_{33}^T$	$M^*$
Type I	PZT-4	328	289	-123	96	1300	-229
Type II	PZT-5A	365	374	-171	584	1700	-234
Type III	PZT-8	300	218	-93	330	1000	-229
Type V	PZT-5J	250	500	-220	670	2600	-232
Type VI	PZT-5H	193	593	-274	741	3400	-236
	(Pb,Ca)TiO <sub>3</sub>	255	68	-3	71	209	-209

Source: Gallego-Juárez, &lt;19&gt; 1989; Jaffe and Berlincourt, &lt;27&gt; 1965; Morgan Matroc; &lt;33&gt; Vernitron Piezoelectric Division, &lt;56&gt;

Table 2 Properties of 0-3 Piezo Rubber composites.

NTK designation	$\rho$	$\rho_c$	$K_{33}^T$	$\tan \delta$	$d_{33}$	$d_{31}$	$d_h$	$g_h$	$M^*$
PR-303	5300	7.0	43	0.06	48	-15.5	17	45	-207
PR-304	5300	8.3	40	0.03	56	-18.5	19	55	-205
PR-305	5500	6.7	37	0.03	46	-2.5	41	124	-198
PR-306	5300	8.5	38	0.02	34	-7.0	20	58	-205
PR-307	5900	8.4	45	0.05	52	-4.0	44	111	-199
PR-308	6200	9.1	57	0.05	58	-5.0	48	95	-200

Source: NTK Technical Ceramics. &lt;37&gt;

**Table 3** Comparison of typical low-frequency piezoelectric properties of various piezocomposite structures.

Type	$\rho$	$K_{33}^T$	$d_{33}$	$d_h$	$g_h$	$d_h g_h$	$M^*$
0-3	5900	45	52	44	111	4884	-199
1-3	1800	460	550	268	66	17688	-204
3-1		760	350	230	34	7800	-209
3-2		320	300	322	113	36300	-199
3-3	3840	200	190	90	50	4500	-206

Source: NTK Technical Ceramics; <37> Bowen *et al.*, <9> 1996; Safari *et al.*, <43> 1982; Gururaja *et al.*, <23> 1988.



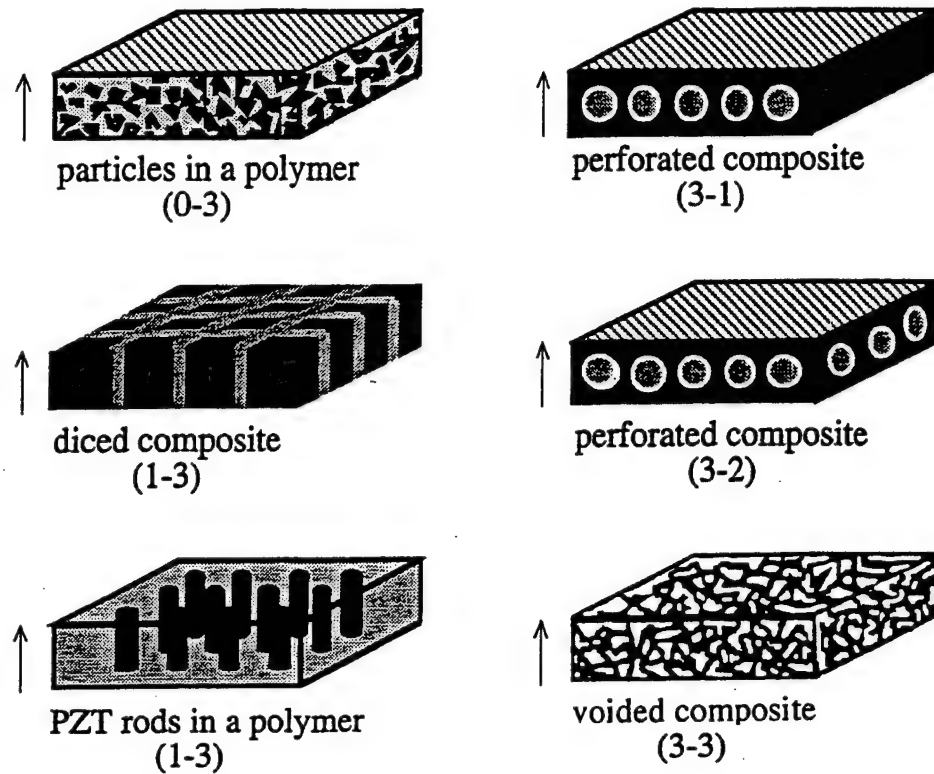


Figure 1 Diagram of the various composite connectivity schemes described in this chapter. The poling direction is noted by the arrows.

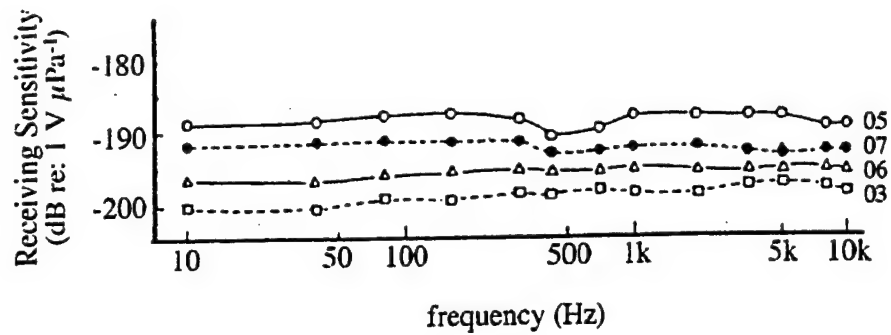


Figure 2. Frequency dependence of the receiving sensitivity for *Piezo Rubber* composites PR-303, PR-305, PR-306, and PR-307, which are designated by 03, 05, 06, and 07 in the figure. PR-303, PR-305, and PR-306 were each 3 mm thick, whereas PR-307 was 2 mm thick (reproduced by permission of the American Institute of Physics from *Jpn. J. Appl. Phys.*, 1987, 26 Suppl. 26-1, 153-155).

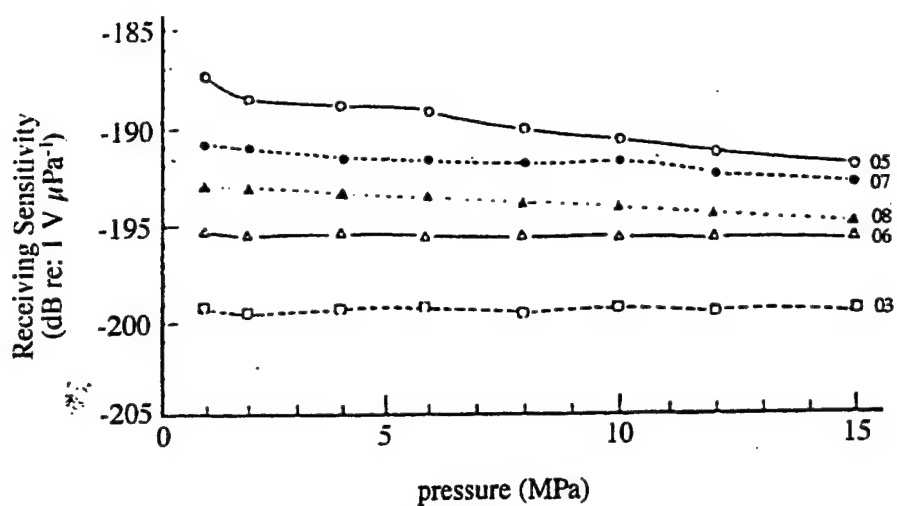
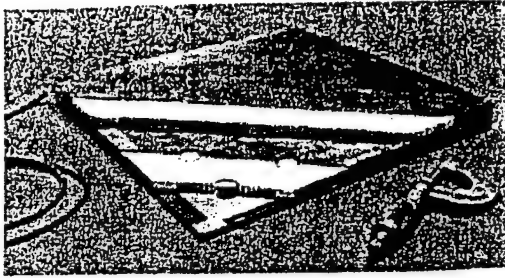


Figure 3 Pressure dependence of the receiving sensitivity (measured at 160 Hz) for *Piezo Rubbers* PR-303, PR-305, PR-306, PR-307, and PR-308 which are designated by 03, 05, 06, 07, and 08 in the figure. PR-303, PR-305, and PR-306 were each 3 mm thick, whereas PR-307 and PR-308 were both 2 mm thick (reproduced by permission of the American Institute of Physics from *Jpn. J. Appl. Phys.*, 1987, 26 Suppl. 26-1, 153-155).



**Figure 4** Piezocomposite SmartPanel™ from MSI used for active control of underwater vibration and noise (reproduced by permission of the SPIE from 'Proceedings of the SPIE: Smart Structures and Materials 1997—Industrial and Commercial Applications of Smart Structures Technologies', 1997, vol. 3044, pp. 391–396).

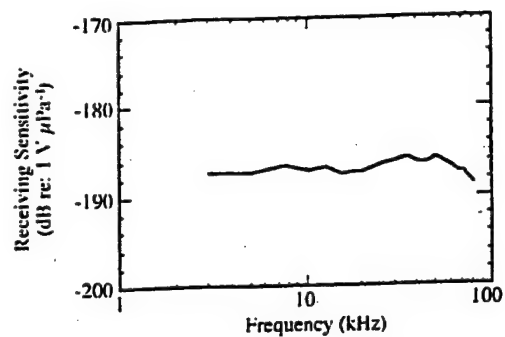
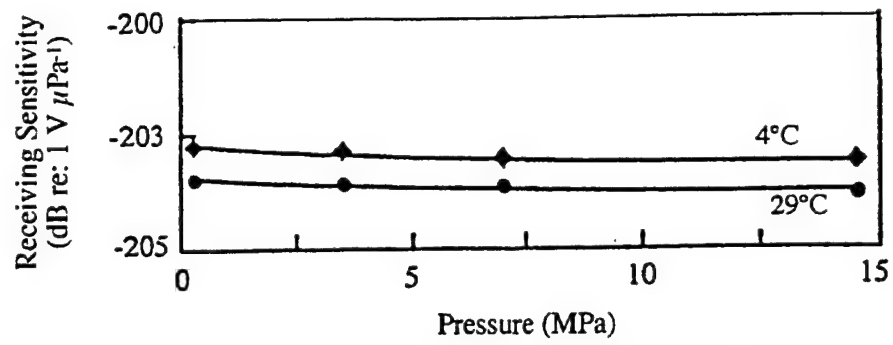
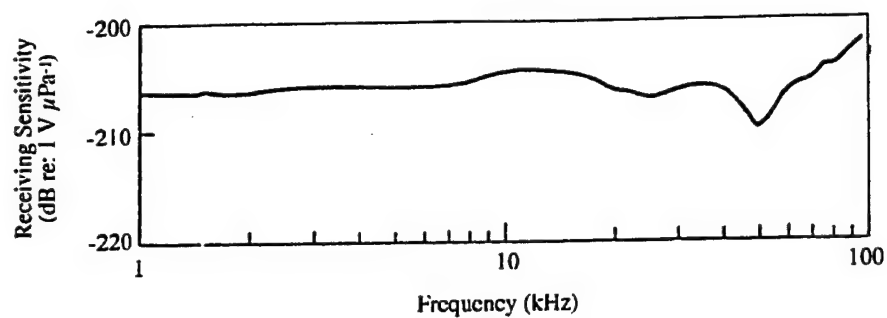


Figure 5 Frequency dependence of the receiving sensitivity of a 6.4 mm thick MSI injection molded 1-3 composite utilizing PZT-5H (reproduced by permission of the IEEE from 'Ultrasonics Symposium Proceedings', 1993, vol. 1, pp. 499-503).



**Figure 6** Pressure and temperature dependence of the low-frequency receiving sensitivity of a 1-3 composite utilizing PZT-4 (reproduced by permission of Gordon and Breach Publishers from *Ferroelectrics*, 1990, 102, 215-224).



**Figure 7** Frequency dependence of the receiving sensitivity of a porous (3-3) composite PZT-5 hydrophone (reproduced by permission of Gordon and Breach Publishers from *Ferroelectrics*, 1990, 102, 215-224).

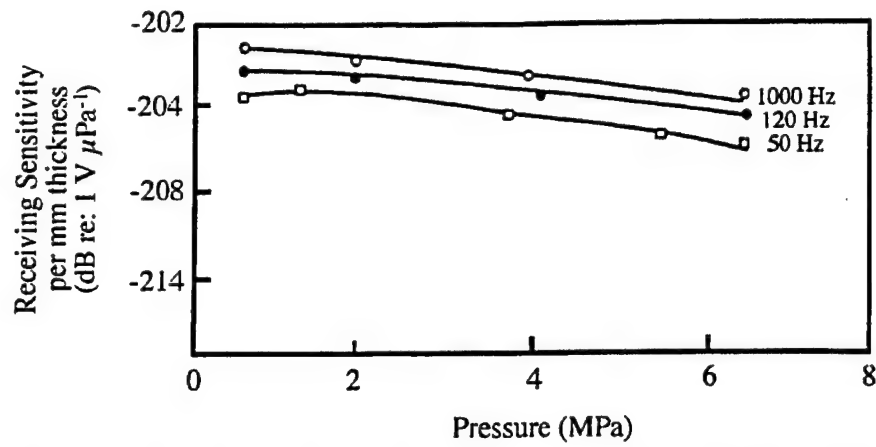
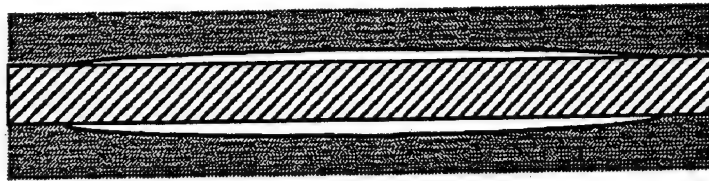


**Figure 8** Pressure and frequency dependence of the receiving sensitivity of a 3-1 composite utilizing PZT-5 (reproduced by permission of Elsevier Applied Science Publishers Ltd. from *Applied Acoustics*, 1994, **41**, 325–335).



(a)



(b)

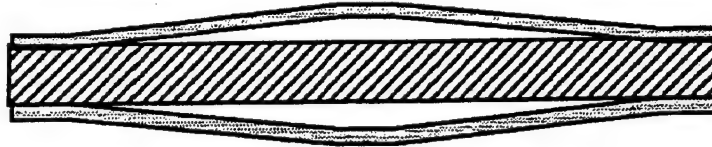


**Figure 9** Cross-sectional views of the (a) moonie-type and (b) cymbal-type flextensional metal-ceramic composite sensors. The cross-hatched areas represent the piezoceramic disk and the gray areas designate the metal caps.

# **APPENDIX 38**

## Functional composites for sensors, actuators and transducers

J.F. Tressler<sup>a</sup>, S. Alkoy<sup>a</sup>, A. Dogan<sup>b</sup>, R.E. Newnham<sup>a,\*</sup>

<sup>a</sup>Materials Research Laboratory, Pennsylvania State University, University Park, PA 16802, USA

<sup>b</sup>Department of Ceramic Science, Eskişehir Anadolu University, Eskişehir, Turkey

Received 20 November 1997

---

### Abstract

Following the trend in structural applications, composite structures are being used more commonly in transducer applications to improve acoustic, mechanical and electrical performance of piezoelectric devices. Functional composite transducers for actuators and sensors generally consist of an active ceramic phase incorporated with a passive polymer phase, each of which has a phase transition associated with it. In this paper, several polymer–piezoelectric ceramic composite transducers, mostly designed for sensing hydrostatic waves, are discussed based on the connectivity of the constituent phases. Also discussed are some recent examples of metal–ceramic composites, and single element ceramic transducers with modified shapes for improved performance. A comparison of these designs is given based on their hydrophone figure of merit ( $d_h \cdot g_h$ ). © 1999 Elsevier Science Ltd. All rights reserved.

**Keywords:** Composites; Transducers; Piezoelectrics

---

### 1. Introduction

Composite materials have found use in a number of structural applications, but their use in the electronics industry has been relatively limited. As the advantages of composites, sensors, and actuators become more clear, this picture is expected to change.

Functional composites make use of a number of underlying ideas, including the following: connectivity patterns leading to field and force concentration; the use of periodicity and scale in resonant structures; the symmetry of a composite structure and its influence on physical properties; polychromatic percolation and coupled conduction paths; varistor action and other interfacial effects; sum, combination, and other product properties; coupled phase-transformation phenomena; and the important roles that porosity and inner surface play in many functional composite materials. These ideas provide a basic understanding of functional composite sensors and actuators.

An important approach to making functional composites is to bring together two or more different materials, each of which has a phase transition associated with it. As an example, polymeric materials having phase transitions in which the elastic properties undergo large changes are combined

with ferroelectric materials in which the dielectric properties have an associated instability. The two materials have different types of instability, allowing for the building up of structures especially good for sensing and actuating.

When constructing functional composites, one is generally not trying to optimize all of the tensor coefficients but only those appearing in the figure of merit. Combining a mechanically soft but electrically hard (with a low dielectric constant) polymer with a mechanically stiff but electrically soft ferroelectric ceramic in various connectivity schemes allows for the build-up of parallel and series connections that optimize particular combinations of tensor coefficients.

In addition to the ceramic polymer composites, other novel approaches in sensor and actuator design for improved performance and amplified sensing and/or actuation response include incorporating metals and ceramics into a composite structure, as well as modifying the geometry of the ceramic. One example of a metal–ceramic composite sensor configuration is the flextensional-type transducer, in which metal endcaps are used to transfer stress to the piezoelectric ceramic. Recent examples of flextensional transducers, namely the ‘moonie’ and the ‘cymbal’ type miniaturized versions, will be discussed in the following sections. Improving transducer performance through modified geometry will also be discussed using the shell shape monomorph ‘rainbow’ and the hollow spherical ‘BB’ transducers as examples.

---

\* Corresponding author. Tel.: + 1-814-865-1612; fax: + 1-814-865-7593.

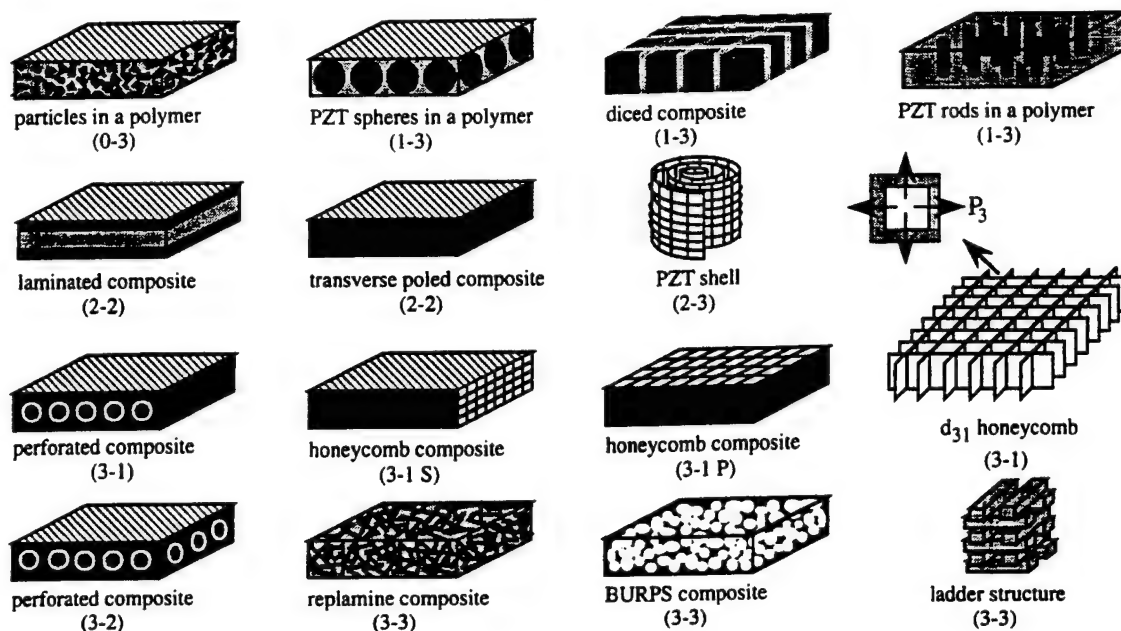


Fig. 1. Connectivity of constituent phases in piezoelectric ceramic-polymer composites.

## 2. Ceramic-polymer composites

Newnham et al. [1] established the notation for describing the number of dimensions that each phase is physically in contact with itself. To date, eight different types of two-phase piezoelectric composites (piezocomposites) have been studied: 0-3, 1-3, 2-2, 2-3, 3-0, 3-1, 3-2, and 3-3. In the case of piezocomposites, the first number in the notation denotes the physical connectivity of the active phase and the second number refers to the physical connectivity of the passive phase. A schematic of these different connectivities is shown in Fig. 1.

Most ceramic-polymer composites have been used as hydrophones and as biomedical transducers. The purpose of the polymer is to detect a portion the hydrostatic stress in either the transverse or longitudinal direction, to effectively eliminate either the  $g_{33}$  or  $g_{31}$  contribution to the  $g_h$  of the poled ceramic. Extensive investigations have been performed to determine which ceramic-polymer connectivity configuration will provide the optimum hydrophone performance. The optimum performance is associated with maximizing the figure of merit, which in this case is the  $d_h \cdot g_h$  product. The  $d_h$  coefficient is the hydrostatic piezoelectric charge coefficient and is reported in terms of  $10^{-12}$  Coulombs per Newton (pC/N). The  $g_h$  coefficient is the hydrostatic piezoelectric voltage coefficient and is reported in terms of  $10^{-3}$  Volt-meters per Newton (mV·m/N). Thus, the figure of merit has units of  $10^{-15}$  meters squared per Newton, or  $\text{fm}^2/\text{N}$ . In the following sections examples of ceramic polymer composites with various connectivities are discussed.

### 2.1. Composites with 3-3 connectivity

Composites with 3-3 connectivity were the first of the two-phase composites to be investigated. Composites with this connectivity have unpoled reinforcement in the lateral directions which serves to further decouple negative contributions from lateral stresses [2]. They were initially fabricated by a technique known as the replamine process [3] which involves the lost wax replication of a coral skeleton. Since then, additional technologies have been developed such as the fugitive phase, or BURPS, process [4] which produces a porous three-dimensionally interconnected ceramic structure by sintering a compacted mixture of volatilizable plastic spheres and PZT powder. Mitsubishi Mining and Cement has developed several techniques for introducing connected porosity into PZT ceramics: reactive sintering, foaming agents, organic additives, and careful control of particle size and firing conditions [5]. A reticulated ceramic technology has recently been used to produce 3-3 composites [2]. Reticulated ceramics are created by coating an organic foam substrate (i.e. polyurethane) with a ceramic slurry, pyrolyzing the foam, and then sintering the ceramic.

### 2.2. Composites with 0-3 and 3-0 connectivity

Composites with 0-3 connectivity consist of a random array of piezoelectric particles dispersed in a 3D polymer matrix [6]. The primary advantage of these composites is their ability to be formed into shapes while remaining piezoelectrically active. These composites are manufactured commercially by NTK Technical Ceramic Division of the NGK Spark Plugs Corporation in Japan under the name

*PiezoRubber* (NTK-306). *PiezoRubber* was developed by Banno and Saito and utilizes PT (lead titanate) rather than PZT in order to take advantage of the large piezoelectric anisotropy in PT [7]. The  $g_h$  value reported by NTK for their *PiezoRubber* depends on the volume fraction of ceramic present and can be pressure insensitive up to 35 MPa [8–11].

The first 3–0 composites were fabricated by a tape casting technique. Fugitive ink was screen printed onto green PZT sheets which were subsequently stacked. When the ink and binder were burned out and the ceramic sintered, the resultant PZT block contained pores where the ink was originally located. A second method for fabricating 3–0 composites consisted of hot pressing a mixture of large polymer spheres and PZT powder [5].

### 2.3. Composites with 3–1, 3–2 and 2–3 connectivity

Conventional composites exhibiting 3–1 and 3–2 connectivity consist of a PZT block with holes drilled through either one side (3–1) or both sides (3–2) in a direction perpendicular to the poled direction of the PZT. The holes are subsequently backfilled with polymer. The one-dimensional or two-dimensional interconnected polymeric phases in the transverse direction reduce the  $g_{31}$  and  $g_{32}$  contributions to the hydrostatic voltage response by decreasing the stress coupling in the plane normal to the poled direction [12]. A negligible change in properties occurs up to 7 MPa. In 3–1 and 3–2 composites manufactured in this way, the dielectric constant, as well as the  $d_h$  and  $g_h$  coefficients are all functions of hole size, PZT thickness, poling technique, and center-to-center distance between adjacent holes [5].

The relic process [13], in combination with a weaving technique, has been developed at Rutgers University to easily manufacture large area composites consisting of fine PZT fibers interconnected in two dimensions and embedded in a 3D interconnected polymer matrix (2–3 connectivity). In this process, carbon fabric fibers of 10 to 20  $\mu\text{m}$  in diameter are soaked in PZT slurry and then woven into yarns with the desired structure. The carbon is then burned out and the resulting PZT relic is sintered to leave a structure similar to the original carbon template. A piezoelectric/polymer composite is subsequently formed by infiltrating with epoxy.

Another type of 3–1 composite configuration utilizes a thin-walled 3D interconnected piezoceramic frame (also known as a honeycomb). The first honeycombs were poled in directions either parallel or perpendicular (transverse) to the extrusion direction with the epoxy phase and PZT connected mechanically in parallel and series, respectively [5]. Recently, a configuration has been devised where the poling direction of the piezoceramic is parallel to the frame direction [14]. Thus, it operates in the  $d_{31}$  mode. The high hydrostatic response comes from the sum of the individual responses of the three orthogonal directions of the

frame. That makes this composite better than a capped cylinder, in which only the axial direction contributes to the hydrostatic response.

### 2.4. Composites with 1–3 connectivity

Unquestionably, the composites with 1–3 connectivity are the most studied, understood, and utilized of all the two-phase connectivity types. This composite consists of individual PZT rods or fibers aligned in a direction parallel to the poling direction and surrounded by a polymer matrix. A decoupling of the  $d_{33}$  and  $d_{31}$  coefficients of the composite enhances the  $d_h$ . The rod diameter, rod spacing, composite thickness, volume percent of rods, and polymer compliance all influence the composite performance.

The first 1–3s were made from extruded PZT rods, ranging in diameter from 254 to 840  $\mu\text{m}$ , which were aligned in a specially designed fixture which allowed for the epoxy to be poured around the rods [15]. Because of the labor-intensive procedure, this technique does not lend itself well to mass production. The dice and fill technique [16] is more easily adapted to the mass production of smaller samples, but is too costly to meet the needs of large area coverage [8]. This technology involves the cutting of deep grooves into a solid block of PZT using a diamond saw. Square rods with sides of length down to 50  $\mu\text{m}$  are achievable with aspect ratios approaching 20 [17]. Square rods can give rise to undesirable inter-post resonant activity. This problem can be alleviated if circular or irregularly shaped rods are used instead [18]. By dicing a honeycomb configuration, ‘+’, ‘L’, and ‘T’ shapes were easily fabricated [13]. Materials Systems has developed a new technology for the mass production of large area 1–3 composites using an injection molding process [19]. This process is capable of producing arrays with rod diameters < 100  $\mu\text{m}$ . It is also possible to easily vary the PZT element type, layout, and shape.

Cao et al. [20] have shown that the stress transfer in 1–3 composites is accomplished through shear coupling at the interface between the ceramic and the polymer. The effectiveness of the stress transfer can be characterized by a stress amplification factor which depends upon the elastic properties of both phases, the ceramic content, and, most importantly, the aspect ratio (radius/length) of the ceramic rods. These same parameters also affect the displacement uniformity over the surface of the composite [21]. When subject to a hydrostatic pressure, the stress applied in the transverse direction reduces the stress enhancement effect in the axial direction. This is due to the Poisson ratio effect. When squeezed from both sides, the polymer bulges, pulling on the ceramic rods and trying to lengthen them. Hence, under hydrostatic pressure, the stress amplification factor is practically reduced by a factor of  $(1 - 2\nu)$ , where  $\nu$  is the Poisson ratio. Essentially, this produces a contribution to the  $d_{31}$  of the composite from the  $d_{33}$  of the ceramic [22], which in turn lowers the  $d_h$  of the structure.

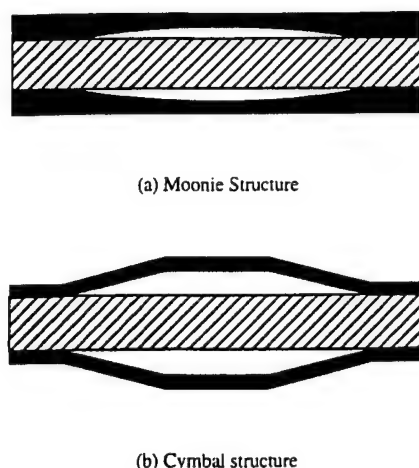


Fig. 2. Cross-sectional views of the (a) moonie and (b) cymbal transducers. The dark areas represent the caps, and the hatched areas the PZT disk.

Preparing a 1–3 composite using thin-wall piezoelectric hollow spheres as the active ceramic phase is also feasible. The resultant structure has a good acoustic matching with water due to the low acoustic impedance of polymer and the air-filled space in the ceramic part. Hollow spheres are discussed in more detail in Section 4.

#### 2.5. Composites with 2–2 connectivity

For large area acoustic projectors, it is necessary to generate large surface displacements while operating at a moderate driving voltage to get high radiative power over a wide frequency range. The 1–3 type composites often cannot meet these requirements. In addition, the  $d_h$  coefficient is limited by the longitudinal piezoelectric strain coefficient  $d_{33}$ . The 2–2 piezocomposites might be an answer to these problems. In a 2–2 composite the stress transfer between the two phases depends on the volume percent of active component as well as the aspect ratio of the two components [23]. There are two different configurations for 2–2 composites: laminated 2–2 which consists of layers of PZT sandwiched between layers of polymer and poled through the layers, and 2–2 piezocomposites poled over the side faces, parallel to the layers. The latter operates in the transverse  $d_{31}$  mode and possesses the advantages of the PZT 1–3 tubular composite but with lower manufacturing costs and a simpler fabrication process [24]. This transverse operating mode 2–2 composite also exhibits much better performance than the conventional longitudinal mode 2–2 laminated [13,24].

### 3. Ceramic–metal composites

Ceramic–metal composites generally have a simple design with a metal faceplate, shell, or cap that couples to both the ceramic as well as the surrounding medium. The metal component transfers the incident stress to the ceramic or the displacement to the medium. Flexensional

transducers are good examples of ceramic–metal composites. In flexensional transducers, the flexural vibration of the metal shell causes an extensional (or contractional) vibration of the piezoelectric element [25]. The miniaturized versions of flexensionals, the moonie and cymbal transducers possess 2–(0)–2 connectivity. These transducers, shown in Fig. 2, consist of a poled piezoelectric disk (fully electroded on both faces) which is sandwiched between two metal endcaps, each containing a shallow air-filled cavity on their inner surface.

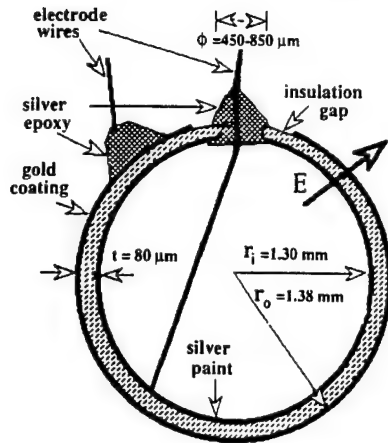
In the case of the moonie, the cavities are in the shape of a half moon, whereas the cymbal has a truncated cone-shaped cavity. The presence of these cavities allows the metal caps to serve as mechanical transformers for transforming and amplifying a portion of the incident axial-direction stress into tangential and radial stresses of opposite sign. Thus, the  $d_{33}$  and  $d_{31}$  contributions of the PZT now add together (rather than subtracting) in the effective  $d_h$  of the device [26].

### 4. Single element transducers

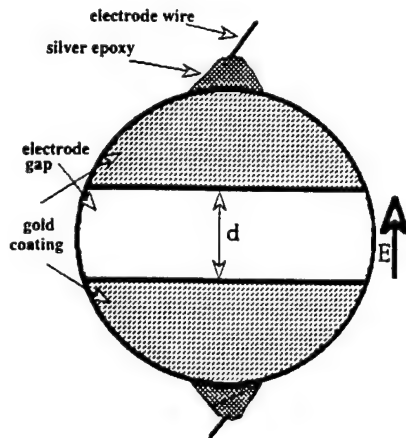
A single piezoelectric ceramic element with electroded surfaces is the most basic and simple transducer, but this type of transducer has severe limitations, such as low  $d_h$  and high acoustic impedance. As a result, composite structures which have good acoustic matching to water, and with their designs to amplify externally applied stress, became the main transducer configuration. However, composite structures are not the only avenue to an improved transducer performance. In recent years, several single element ceramic transducers with specially designed geometries were shown to display a performance comparable to composite transducers. Two of these, miniature hollow sphere transducers (BBs) and monomorph ‘rainbow’, transducers will be discussed in this section.

Directional characteristics are important in designing a transducer for underwater applications, and when omnidirectional reception is required a spherical design is most often used. Miniature piezoelectric hollow spheres, also known as BBs due to their similarity in size to the pellets used in buckshot, are made using a coaxial nozzle slurry technique with a diameter of 1–6 mm and a wall thickness of 40 to 150  $\mu\text{m}$  [27]. Spheres with both tangential and radial poling configurations, shown in Fig. 3, exhibit a very large hydrophone figure of merit ( $d_h g_h$ ). The amplification of  $d_h$  and figure of merit in BBs results purely from the spherical geometry. An applied hydrostatic pressure is transformed into radial and tangential stress components, which are amplified with a factor which can be defined as the ratio of radius to wall thickness ( $r/t$ ). Properties of the BBs are reported to remain stable up to 7 MPa.

Another novel design exploiting the geometry of a single ceramic element is the monomorph flexural disk transducer ‘rainbow’. The rainbow transducer shows excellent promise



(a) Radial poling configuration



(b) Tangential poling configuration

Fig. 3. Radial (a) and tangential (b) poling configurations of BB transducers.

as a low pressure ( $< 100$  kPa) sensor and/or acoustic transmitter. It consists of an electromechanically active layer, such as PZT, in direct contact with a lead-rich constraining layer [28]. This constraining layer is formed by exposing one side of the ceramic to a reducing atmosphere at high temperature by placing the ceramic in contact with a carbon block. Due to the thermal expansion mismatch between the reduced non-piezoelectric layer and the oxide piezoelectric layer, a curvature develops in the structure, giving it a dome shape, with the oxide layer in compression throughout its volume. The dome needs to be fixed on a base plate when it is used as a pressure sensor; otherwise, the voltage response will only be equal to that of the bulk ceramic. Rainbows exhibit highly pressure-dependent properties but are extremely robust. As pressure increases, the dome gradually flattens, decreasing the bending contribution to  $g_h$  until it reaches the bulk value. Hydrophone figures of merit

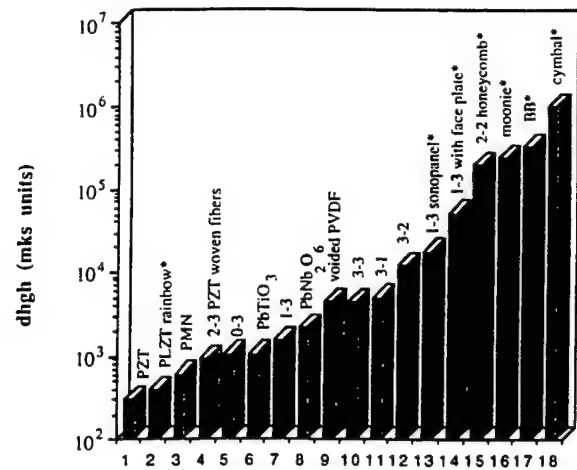


Fig. 4. Comparison of hydrophone figure of merit of several piezoelectric ceramics and transducer designs.

( $d_h g_h$ ) of all the composite and single element transducers discussed so far are compared in the plot in Fig. 4. In this figure, the figure of merit of the transducers marked with an asterisk is size dependent. Therefore, the figure of merit is calculated for a  $1 \text{ cm}^2$  transducer for a valid comparison.

## 5. Conclusions

Some important goals in composite transducer research include: improved acoustic impedance—better coupling to air, fluids, and metals; lower drive voltage through the use of internal electrodes; improved sensitivity to hydrostatic waves; strain amplification to produce enlarged displacements; acoustic isolation of adjacent sound sources; passive and active vibration suppression; enhanced high-frequency performance through mode control; mechanical strength and flexibility; backing layers to absorb unwanted vibrations; reduced hysteresis; internal stress and field rearrangement; improved breakdown strength; tuned coupling coefficients, including permittivity, and elasticity; beam-forming capability; and rapid shutdown.

Integration and miniaturization of electroceramic components is an ongoing process in the automotive and consumer electronics areas. Multilayer packages containing signal processing layers made up of low permittivity dielectrics and printed metal interconnections are in widespread production. Further integration with embedded resistors and capacitors is under development and it seems likely that sensor and actuator systems will make use of the same processing technology. Tape casting and screen printing are processes used most often, and varistors, chemical sensors, thermistors, and piezoelectric transducers can all be fabricated this way, opening up the possibility of multicomponent multifunction integrated ceramics.



## Acknowledgements

The authors wish to thank the Office of Naval Research (ONR) for its financial support.

## References

- [1] Newnham RE, Skinner DP, Cross LE. Connectivity and piezoelectric-pyroelectric composites. *Mater Res Bull* 1978;13:525.
- [2] Creedon MJ, Gopalakrishnan S, Schulze WA. 3-3 Composite hydrophones from distorted reticulated ceramics. In: Pandey RK, Liu M, Safari A, editors. *Proceedings of 9th IEEE International Symposium on the Applications of Ferroelectrics*. New York: IEEE, 1995:299-302.
- [3] Skinner DP, Newnham RE, Cross LE. Flexible composite transducers. *Mater Res Bull* 1978;13:599.
- [4] Safari A, Newnham RE, Cross LE, Schulze WA. Perforated PZT-polymer composites for piezoelectric transducer applications. *Ferroelectrics* 1982;41:197.
- [5] Gururaja TR, Safari A, Newnham RE, Cross LE. Piezoelectric ceramic-polymer composites for transducer applications. In: Levinson LM, editor. *Electronic ceramics: properties, devices, and applications*. New York: Marcel Dekker, 1988:92.
- [6] Twine RC. Novel piezoelectric materials. *Adv Mater* 1992;4:819.
- [7] Banno H. Recent developments of piezoelectric ceramic products and composites of synthetic rubber and piezoelectric ceramic particles. *Ferroelectrics* 1983;50:3.
- [8] Ting RY. The hydroacoustic behavior of piezoelectric composite materials. *Ferroelectrics* 1990;102:215.
- [9] Ting RY. Composite piezoelectric materials for transduction. *Appl Acoustics* 1994;41:325.
- [10] Ting RY, Geil FG. Recent development in the application of 0-3 piezoelectric composites for hydrophone arrays. In: 1990 IEEE 7th International Symposium on the Applications of Ferroelectrics. New York: IEEE, 1991:14-17.
- [11] Ting RY. A review on the development of piezoelectric composites for underwater acoustic applications. *IEEE Trans Instrum Meas* 1992;41:64.
- [12] Newnham RE, Fernandez JF, Markowski KA, Fielding JT, Dogan A, Wallis J. Composite piezoelectric sensors and actuators. *Mater Res Soc Proc* 1995;360:33.
- [13] Janas VF, Ting SM, Livneh SS, Walker FR, Schaeffer R, McNulty TF, Safari A. Fine-scale, large area piezoelectric fiber/polymer composites for transducer applications. In: Pandey RK, Liu M, Safari A, editors. *Proceedings of 9th IEEE International Symposium on the Applications of Ferroelectrics*. New York: IEEE, 1995:295-298.
- [14] Zhang QM, Wang H, Zhao J, Fielding JT, Newnham RE, Cross LE. A high sensitivity hydrostatic piezoelectric transducer based on transverse piezoelectric mode honeycomb ceramic composites. *IEEE Trans UFFC* 1996;43:36.
- [15] Klicker KA, Biggers JV, Newnham RE. Composites of PZT and epoxy for hydrostatic transducer applications. *J Am Ceram Soc* 1981;64:5.
- [16] Smith WA. New opportunities in ultrasonic transducers emerging from innovations in piezoelectric materials. *SPIE* 1992;1733:3.
- [17] Smith WA, Shaulov AA. Composite piezoelectrics: basic research to a practical device. *Ferroelectrics* 1992;87:309.
- [18] Hossack JA, Bedi RL. Design of composite piezoelectric transducers. *Key Engng Mater* 1994;92-93:301.
- [19] Bowen L, Gentilman R, Fiore D, Pham H, Serwatka W, Near C, Pazol B. Design, fabrication, and properties of sonopanel™ 1-3 piezocomposite transducers. *Ferroelectrics* 1996;187:109.
- [20] Cao W, Zhang QM, Cross LE. Theoretical study on the static performance of piezoelectric ceramic-polymer composites with 1-3 connectivity. *J Appl Phys* 1992;72:5814.
- [21] Cao W. Simulation of the dynamical behavior of 1-3 piezocomposite using finite element method. *Ceramic Engineering and Science Proc* 1996;17:83.
- [22] Smith WA. The application of 1-3 piezocomposites in acoustic transducers. In: 1990 IEEE 7th International Symposium on the Applications of Ferroelectrics. New York: IEEE, 1991:145-152.
- [23] Cao W, Zhang QM, Cross LE. Theoretical study on the static performance of piezoelectric ceramic-polymer composites with 2-2 connectivity. *IEEE Trans UFFC* 1993;40:103.
- [24] Zhang QM, Chen J, Wang H, Zhao J, Cross LE, Trottier MC. A new transverse piezoelectric mode 2-2 piezocomposite for underwater transducer applications. *IEEE Trans UFFC* 1995;42:774.
- [25] Rolt KD. *J Acoust Soc Am* 1990;87:1340.
- [26] Tressler JF, Dogan A, Fernandez JF, Fielding JT Jr., Uchino K, Newnham RE. Capped ceramic hydrophones. In: Levy M, Schneider SC, McAvoy BR, editors. *IEEE Ultrasonics Symposium Proceedings*. Piscataway, NJ: IEEE, 1995:987.
- [27] Alkoy S, Dogan A, Hladky A-C, Langlet P, Cochran JK, Newnham RE. Miniature piezoelectric hollow sphere transducers (BBs). *IEEE Trans UFFC* 1997;44:1067.
- [28] Haertling GH. *Am Ceram Soc Bull* 1994;73:93.



# **APPENDIX 39**

# Capped ceramic underwater sound projector: The "cymbal" transducer<sup>a),b)</sup>

James F. Tressler<sup>c)</sup> and Robert E. Newnham

Materials Research Laboratory, The Pennsylvania State University, University Park, Pennsylvania 16802

W. Jack Hughes

Applied Research Laboratory, The Pennsylvania State University, University Park, Pennsylvania 16802

(Received 11 February 1998; accepted for publication 26 September 1998)

A new type of transducer has been developed for use as a shallow-water sound projector at frequencies below 50 kHz. Dubbed the "cymbal," it is similar to the more commonly known "moonie" and class V ring/shell flextensional designs. Prototype cymbal arrays 2 mm thick with a radiating area of 11.4 cm<sup>2</sup> have been developed and calibrated. Two mounting schemes have been examined: unpotted (oil-filled) and potted in a 5-mm thick layer of stiff polyurethane. In both cases, a transmitting response comparable to the more widely used Tonpilz transducer (with an equivalent radiating area) is attainable. When tested under hydrostatic pressures, a standard cymbal configuration has been shown to withstand exposures of 2.5 MPa (which corresponds to 250 m of water depth) before failure. © 1999 Acoustical Society of America. [S0001-4966(99)02801-5]

PACS numbers: 43.10.Ln, 43.38.Fx, 43.30.Yj [SLE]

## INTRODUCTION

Sound transmission is the single most effective means of directing energy transfer over large distances underwater.<sup>1</sup> The acoustic frequency range for various types of underwater transducer applications spans seven decades, from 10 Hz to 100 MHz.<sup>2</sup> There is currently a great interest in the development of shallow-water (<250 m) acoustic projectors that operate in the frequency range from 1 kHz to 100 kHz.<sup>3</sup> Potential applications include seabed penetration for buried mines as well as underwater surveillance, navigation, target detection and classification. Ideally, these transducers should be thin, lightweight, exhibit medium to high acoustic-output power, be able to conform to a curved surface, and be of simple design such that they are easy and inexpensive to mass produce.

Currently, the predominant underwater projector systems that operate in the 1 kHz to 100-kHz frequency band are Tonpilz transducers and 1-3 type piezoelectric composites. The Tonpilz transducer consists of a stack of piezoelectric ceramic (typically lead zirconate titanate-PZT) rings connected mechanically in series and electrically in parallel. The ring stack is sandwiched between two metal masses: a heavy tailmass and a light, flared headmass which serves to transmit the generated acoustic energy into the surrounding medium. Tonpilz transducers are characterized by their very large acoustic-output power, are typically tens of centimeters in thickness, weigh up to several kilograms, and are designed to operate at frequencies up to 100 kHz.

The 1-3 type piezoelectric composites consist of a number of piezoelectric ceramic rods separated by a 3-D interconnected polymer matrix. These composites have been manufactured in a number of ways.<sup>4</sup> The current state-of-the-art fabrication technique is injection molding.<sup>5</sup> The performance of 1-3 piezoelectric composites is strongly affected by the elastic properties of both the ceramic and polymer phases as well as the aspect ratio, the volume fraction, and the arrangement of the piezoelectric ceramic rods.<sup>6</sup> These types of composites can be conformed to a curved surface and acoustically matched with water. The 1-3 piezoelectric composites designed for use below 100 kHz are at least 10 mm thick.

Polyvinylidene fluoride (PVDF) and its chemically related copolymers are piezoelectric polymers that are readily available from a number of commercial manufacturers in material thicknesses ranging from 5 to at least 600  $\mu\text{m}$ .<sup>7</sup> The high compliance and low density of these piezoelectric polymers allow them to be easily shaped to conform to curved surfaces and to acoustically match to water. The large piezoelectric voltage coefficient,  $g_h$ , of PVDF renders it an excellent acoustic receiver material. However, its low piezoelectric strain coefficient,  $d_h$ , makes it a rather poor sound projector. A low permittivity also requires the use of expensive built-in electronics packaging because of the large electrical impedance mismatch between the piezoelectric polymer and the circuitry.<sup>8</sup>

A third type of underwater projector that is seeing a resurgence in interest is the flextensional transducer. Flextensionals have been in existence since the 1920s and have seen use as underwater projectors since the late 1950s.<sup>9</sup> Flextensionals consist of a piezoelectric ceramic drive element or assembly encapsulated by a metal shell. The metal shell acts as a mechanical transformer to convert the large generative force of the piezoelectric ceramic into increased displacement. The shape of the shell has become quite diverse over the years, and so a classification system has been established to group the common designs together.<sup>10</sup> Flextensional trans-

<sup>a)</sup>"Selected research articles" are ones chosen occasionally by the Editor-in-Chief that are judged (a) to have a subject of wide acoustical interest, and (b) to be written for understanding by broad acoustical readership.

<sup>b)</sup>Presented at the 133rd meeting of the Acoustical Society of America held at The Pennsylvania State University, June 1997 [J. Acoust. Soc. Am. **101**, 3094(A) (1997)].

<sup>c)</sup>Present address: Naval Research Laboratory, 4555 Overlook Avenue, Washington, DC 20375-5350.

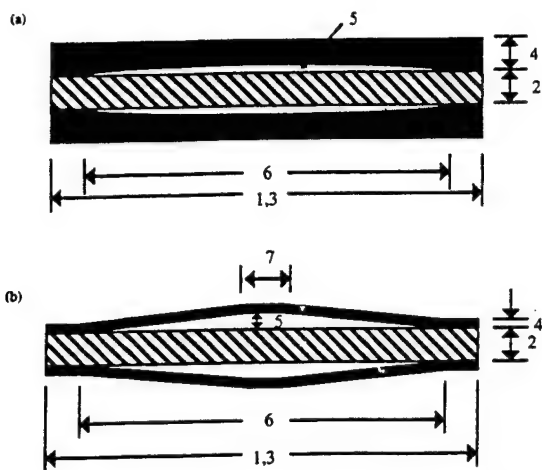


FIG. 1. Cross-sectional views of the (a) moonie-type, and (b) cymbal-type transducers. The dark areas represent the caps and the cross-hatched areas the PZT disks. The dimensions designated by the numerals shown are listed in Table I.

ducers typically range in size from several centimeters to several meters in length and can weigh up to several hundreds of kilograms.

A miniaturized version of the class V flextensional transducer was developed in the late 1980s at the Materials Research Laboratory at The Pennsylvania State University for use as a hydrophone.<sup>11,12</sup> This transducer is named the moonie due to the crescent moon-shaped cavity on the inner surface of the caps. A second generation moonie-type transducer, which consists of a thinner cap with a slightly different shape, has recently been developed for use as a micropositioning actuator.<sup>13,14</sup> This transducer has been dubbed the cymbal due to the similarity in the shape of its caps to that of the musical instrument of the same name. The cymbal cap shape is also more conducive to mass production than the moonie. A comparison of the moonie and cymbal designs is shown in Fig. 1.

The moonie and cymbal transducers consist of a piezoelectric ceramic (usually PZT) disk poled in the thickness direction which is sandwiched between and mechanically coupled to two metal caps, each of which contains a shallow, air-filled cavity on its inner surface. When used as a sound projector, the caps convert and amplify the small radial displacement and vibration velocity of the piezoelectric ceramic disk into a much larger axial displacement and vibration velocity normal to the surface of the caps. This enhanced displacement and vibration velocity from the caps contribute to a much larger acoustic-pressure output than would occur in the uncapped ceramic. The principle of using the cymbal as a hydrophone has been explained previously.<sup>15</sup> The dimensions of the standard-size moonie and cymbal transducers are presented in Table I.

The cymbal cap design was an outgrowth of results obtained via finite element analysis (using SAP90, MARK, and ANSYS<sup>®</sup>) on transducers with the moonie-style cap. Large stress concentrations were calculated in the moonie cap in the region above the bonding area.<sup>14,16</sup> In order to reduce this stress concentration, ring-shaped grooves of varying size were introduced into the moonie-type caps. This design

TABLE I. Dimensions of the standard moonie and cymbal transducers.

Moonie parameter	Dimension (mm)
1—PZT diameter	12.7
2—PZT thickness	1.0
3—cap diameter	12.7
4—cap thickness	1.0
5—cavity depth	0.25
6—cavity diameter	9.0
Cymbal parameter	Dimension (mm)
1—PZT diameter	12.7
2—PZT thickness	1.0
3—cap diameter	12.7
4—cap thickness	0.25
5—cavity depth	0.32
6—base cavity diameter	9.0
7—dimple diameter	3.0

modification was found to not only reduce the stress concentration in the metal, but also enhanced the axial displacement at the center of the caps.<sup>17,18</sup> Onitsuka's results showed that the optimum groove size extended from the edge of the inner air cavity to the outer edge of the cap.<sup>18</sup> Dogan extended this concept and devised the cymbal cap design along with a fabrication technique applicable to mass produce the caps.<sup>19</sup> The effects of materials properties and cap geometry on the actuator performance of the cymbals have been modeled both analytically<sup>20</sup> and using finite element analysis.<sup>21</sup> Finite element modeling to ascertain underwater acoustic performance is ongoing.

## I. PARAMETERS TO MEASURE

Among the relevant parameters required to fully characterize an underwater projector, the most important are resonance frequency, mechanical  $Q(Q_m)$ , electroacoustic efficiency, electromechanical coupling coefficient ( $k_{eff}$ ), transmitting voltage response (TVR), source level (SL), and acoustic directivity (beam) patterns. Transmitting voltage response is equal to the ratio of the sound pressure produced by the projector, referenced ( $re$ ) to a distance of one meter from its acoustic center, to unit voltage applied across the electrical terminals of the transducer.<sup>22</sup> It is reported in terms of dB  $re$ : 1  $\mu Pa/V$  @ 1 m, or as 1  $\mu Pa \cdot m/V$ . Source level is the intensity of the radiated sound field relative to the intensity of a plane wave of rms pressure 1  $\mu Pa$  referred to a point one meter from the acoustic center of the projector.<sup>23</sup> Source level is related to the transmitting voltage response through the applied input rms voltage as:

$$SL = TVR + 20 \cdot \log V_{in,rms} \quad (1)$$

In general, a source level of greater than 200 dB  $re$ : 1  $\mu Pa$  @ 1 m is desirable. The beam pattern describes the response of the transducer relative to its main acoustic axis.

## II. EXPERIMENTAL PROCEDURE

Single-element cymbal transducers were fabricated by first punching 12.7-mm-diam blanks from a sheet of metal foil. These blanks were then molded into caps of the desired

TABLE II. Relevant materials properties of the caps<sup>a</sup> and PZT.<sup>b</sup>

Cap material	Young's modulus	Density	Poisson's ratio
brass	100.6 GPa	8550 kg/m <sup>3</sup>	0.35
titanium	120.2 GPa	4500 kg/m <sup>3</sup>	0.361
molybdenum	324.8 GPa	10 200 kg/m <sup>3</sup>	0.28

PZT type	$d_{31}$	$d_{33}$	Dielectric constant ( $\epsilon_{33}^T/\epsilon_0$ )
552 (5H)	-274 pC/N	593 pC/N	3400
5A	-171 pC/N	374 pC/N	1700
4	-123 pC/N	289 pC/N	1300
8	-93 pC/N	218 pC/N	1000

<sup>a</sup>Smithell's Metals Reference Book, edited by E. A. Brandes (Butterworth, New York, 1983), 6th ed., Table 15.1.

<sup>b</sup>H. Jaffe and D. A. Berlincourt, "Piezoelectric Transducer Materials," Proc. IEEE 53(10), 1372-1386 (1965).

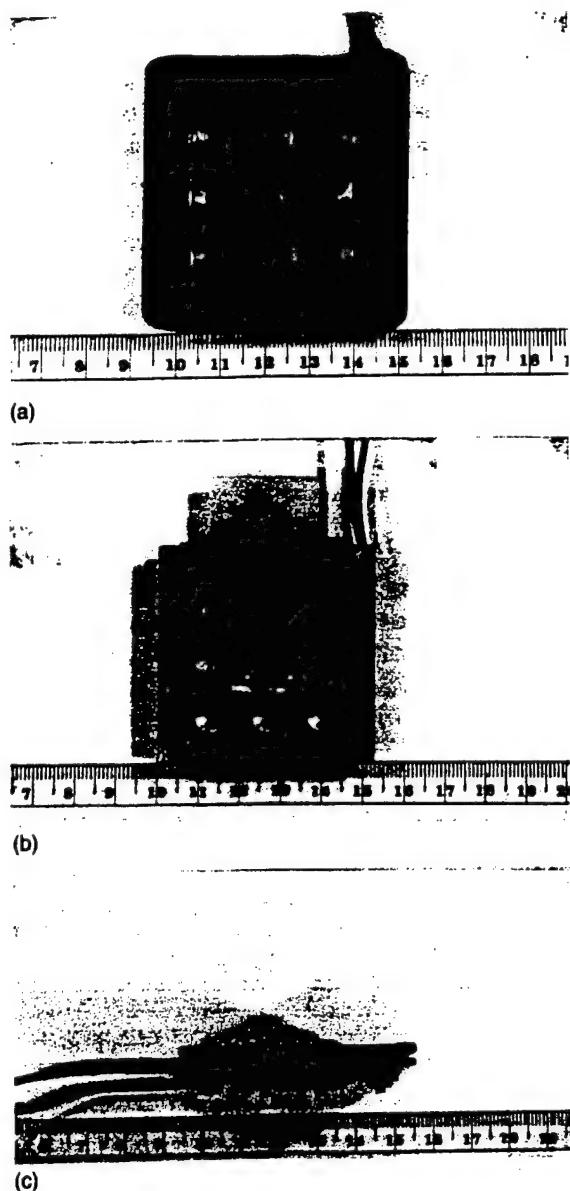


FIG. 2. Top views of the 9-element cymbal arrays (a) potted in polyurethane and (b) unpotted; (c) unpotted cymbal array viewed from the side. The scale is ruled in centimeters.

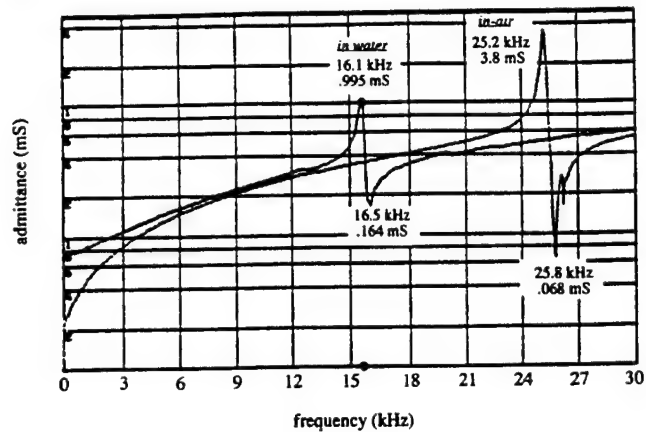


FIG. 3. Measured admittance spectra of a standard-size brass-capped cymbal both in air and in water. Resonance is associated with the fundamental flexural vibration mode of the caps.<sup>21</sup>

shape using a die press. Since there is no machining involved, this process is relatively inexpensive and hospitable to mass production. The flanges of the caps were bonded to a poled PZT-552 disk (Piezo Kinetics, Inc., Bellefonte, PA) using a very thin ( $\approx 20 \mu\text{m}$ ) layer of insulating epoxy (Eccobond<sup>®</sup> 45LV/Catalyst 15LV; Emerson and Cuming, Inc., Woburn, MA). The entire assembly was allowed to cure at room temperature for at least 24 h while under moderate pressure. The relevant properties of the cap materials and piezoelectric ceramics used are given in Table II.

The quality of the bonding layer after curing was characterized by measuring the in-air admittance spectra of the transducer using an HP 4194A impedance/gain phase analyzer. Spurious vibration modes are indicative of a poorly bonded transducer.<sup>24</sup> Admittance characteristics, both in air and in water, were also used to determine resonance frequency,  $k_{\text{eff}}$ ,  $Q_m$ , and electroacoustic efficiency. Charge amplification on the PZT electrodes (due to the presence of the caps) was measured using a modified Berlincourt  $d_{33}$  meter. The water depths to which the cymbal transducers can be taken before failure was ascertained by measuring their effective hydrostatic piezoelectric charge coefficient ( $d_h^{\text{eff}}$ ) as a function of hydrostatic pressure. A thorough explanation of this procedure has been previously provided.<sup>15</sup>

Single-element transducers utilizing the PZT-552 composition as the active component were incorporated into 9-element square arrays. Two mounting schemes were investigated: unpotted (i.e., oil-filled boot) and potted in approximately 5 mm of water-impedance-matching polyurethane

TABLE III. Typical air- and water-loaded characteristics of the standard-size brass-capped cymbal transducer.

	Air-loading	Water-loading
Resonance frequency	25.2 kHz	16.1 kHz
$k_{\text{eff}}$	0.214	0.219
$Q_m$	200	20
electroacoustic efficiency		90%
$d_{33}^{\text{eff}}$ (PZT-552)	12 000 pC/N	
$d_{33}^{\text{eff}}$ (PZT-5A)	8 000 pC/N	
$d_{33}^{\text{eff}}$ (PZT-4)	6 000 pC/N	
$d_{33}^{\text{eff}}$ (PZT-8)	5 000 pC/N	

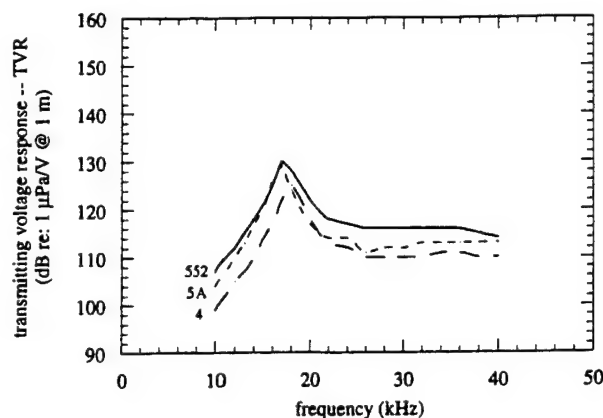


FIG. 4. Transmitting voltage response in the neighborhood of the fundamental resonance frequency of single-element, standard-size brass-capped cymbals utilizing PZT-552, 5A, or 4.

with hardness Shore-A90. In both cases, the center-to-center spacing between the elements was about 13.4 mm. For the potted array, electrical leads were attached to the caps on the positive side on each of the nine cymbals in the array using silver epoxy, and the assembly was wired together in parallel. The other surface of the array was attached to a kapton backing with conductive transfer tape, which served as the ground electrode.

The single elements in the unpotted array were sandwiched between two copper-clad printed circuit boards, each 1.5 mm thick. Holes 11.2 mm in diameter were drilled equidistant from one another through the boards which then housed the elements, thus allowing the dome of the cymbal caps to flex freely. Plastic spacers 1.5 mm thick were used to maintain a uniform distance between the upper and lower panels, which were screwed together tightly, as well as to keep the cymbal elements in place. Pictures of the two mounting configurations are shown in Fig. 2.

Underwater calibration tests were performed in the anechoic water tank at the Applied Research Laboratory at Penn State. The tank measured 7.9 m in length, 5.3 m in width, and 5.5 m in depth. A pure-tone sinusoidal pulse signal of 2 ms duration was applied to the test transducer, and its acoustic output was subsequently measured by a standard F33 recalibrated as a hydrophone. The test transducer and

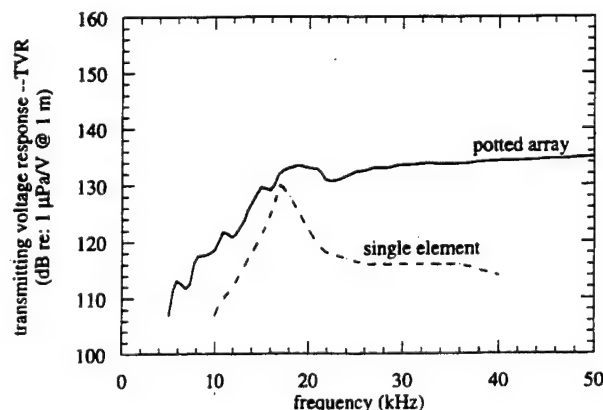


FIG. 5. Comparison of the transmitting voltage response of a single-element brass-capped cymbal with that of the potted 9-element array.

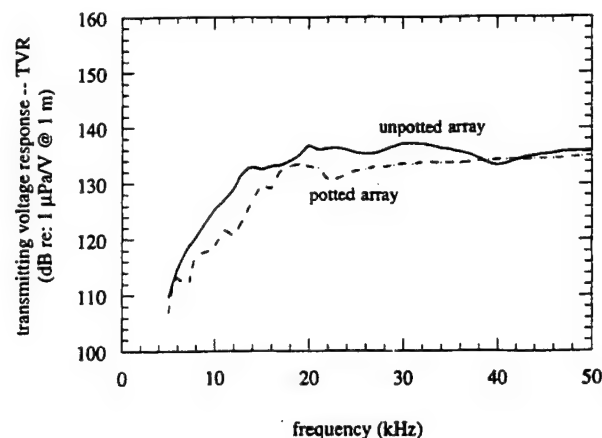


FIG. 6. Comparison of the transmitting voltage response of the potted and unpotted (oil-filled) 9-element cymbal arrays.

the standard were positioned so that they were at a depth of 2.74 m and separated by a distance of 3.16 m.

### III. RESULTS AND DISCUSSION

Figure 3 shows the measured admittance spectra of a well-bonded, standard-size brass-capped cymbal transducer in the neighborhood of its fundamental resonance frequency both in air and in water. The downward shift in the resonance frequency is due to the acoustic mass-loading effect of the water. The resonance frequency of the cymbal transducer is controlled by the elastic properties of the cap material, the cap shape, and the overall diameter of the device.<sup>21</sup> Table III provides typical measured data for the parameters described in Sec. I. These are all values for standard-size, single-element brass-capped cymbals. The reported  $d_{33}$  coefficient is actually an effective  $d_{33}$  coefficient (since it is reported for a device) and will hereafter be designated as  $d_{33}^{eff}$ . The PZT type in parentheses is the type used as the active element in the transducer.

The transmitting voltage response in the neighborhood of the first resonance frequency for same-size, single-element brass-capped cymbal transducers utilizing different PZT types is shown in Fig. 4. The peak value of the transmitting response correlates with the  $d_{33}^{eff}$  coefficient of the device, as seen from Table III. The higher  $d_{33}$  (and thus  $d_{31}$ ) coefficient of the piezoelectric ceramic results in a larger axial displacement in the caps; hence, a larger volume velocity which

TABLE IV. The calculated increase in TVR (in the neighborhood of the fundamental resonance of the single element) for unpotted oil-filled brass-capped cymbal arrays of different radiating area. The measured TVR at this frequency is shown for comparison. Active element is PZT-552.

Radiating area	Number of cymbals in the array	Expected increase in TVR at 18 kHz <sup>a</sup>	Measured TVR at 18 kHz
1.27 cm <sup>2</sup>	1	0 dB	130 dB
11.4 cm <sup>2</sup>	9	4 dB	134 dB
127 cm <sup>2</sup>	100	23 dB	153 dB <sup>b</sup>
507 cm <sup>2</sup>	400	35 dB	...

<sup>a</sup>As compared to the single element, includes mutual acoustic interactions between elements.

<sup>b</sup>J. Zhang and W. J. Hughes, The Pennsylvania State University, unpublished data, 1998.



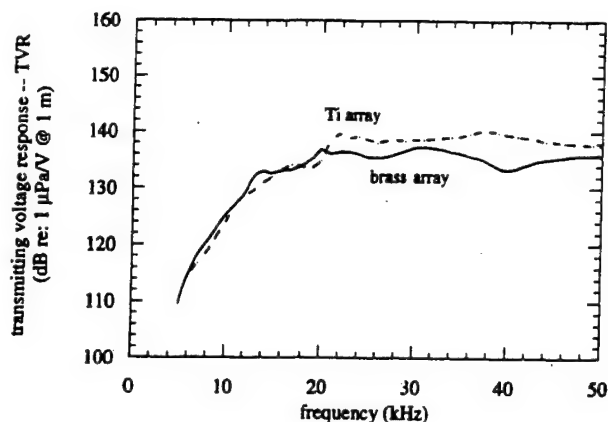


FIG. 7. Comparison of the transmitting voltage response of unpotted 9-element cymbal arrays with either brass caps or titanium caps.

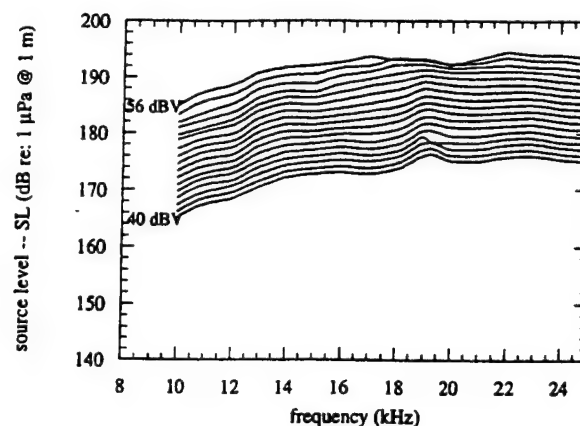


FIG. 8. Source level curves for the 9-element unpotted brass-capped array for drive levels starting at 40 dB re: 1 V and ending at 56 dB re: 1 V in increments of 1 dB re: 1 V.

leads to a higher acoustic-output pressure and subsequently, a higher TVR at resonance. Single-element cymbals are characterized by a relatively high  $Q_m$  ( $\approx 20$ ), low  $k_{eff}$  ( $\approx 0.22$ ) and consequently, a narrow bandwidth.

If the acoustic impedance loading of a single cymbal were purely real (i.e., no mass loading), then incorporating the single-cymbal elements into a 9-element square array should theoretically enhance the transmitting voltage response by a factor of about 19 dB ( $= 20 \cdot \log 9$ ). A single cymbal, however, is mass loaded. Increasing the radiating area of the projector should serve to increase its radiation resistance and hence boost its acoustic-output power. Figure 5 compares the TVR of the single-element cymbal transducer to that of the 9-element potted array. When the single elements were potted in an array, the fundamental resonance was strongly damped, and there was only about a 4-dB enhancement in the TVR. The damping of the resonance was attributed to two detrimental effects: the shear components of the polyurethane potting layer acting to damp the resonance, and array element interactions. Interestingly, though, a more broadband transmitting response was observed. The larger radiating area also means that the array begins to approach " $\rho c$ " loading conditions as compared to the "mass" radiation loaded single element. The array resonance, therefore, does not shift down in frequency from the in-air measurement as much as does the single element. No significant difference in projector performance was observed when comparing results with the polyurethane layer (front) or the kapton layer (back) facing the standard receiver. The phasing of the displacements of the single-element cymbals relative to one another in the array was measured using a fiber-optic interferometer. When the array was driven at 100 V (peak) at 10 kHz, all the transducers were found to vibrate in phase within one deg.

In order to further examine the effect the potting layer had on the performance of the cymbal array, a second array was built and tested. This array was unpotted (i.e., oil filled). The TVR curves for the potted and unpotted arrays are compared in Fig. 6. Even in the case of the oil-filled array, the resonance frequency is again strongly damped. The mutual acoustic impedance between the individual radiators in the array was then estimated using a technique described by

Pritchard.<sup>25</sup> In his analysis of same-size circular disks vibrating (all with the same velocity) in an infinite rigid plane, the mutual radiation impedance ( $Z_{12}$ ) can be expressed as:

$$Z_{12} = (R_{12} + jX_{12}) \cong \left\{ \rho c \pi a^2 \cdot \frac{(ka)^2}{2} \right\} \cdot \left[ \frac{\sin(kd_i)}{kd_i} + j \frac{\cos(kd_i)}{kd_i} \right], \quad (2)$$

when  $(ka)^2 \ll 1$  and  $(a/d) \ll 1$  and where  $R_{12}$  is the mutual radiation resistance,  $X_{12}$  is the mutual radiation reactance,  $\rho c$  is the characteristic impedance of the medium,  $a$  is the radius of the disk,  $d_i$  is the respective center-to-center spacing between the disks, and  $k$  is the wave number. Since the  $ka$  for the nine element array ( $\approx 2$  at 18 kHz) is sufficiently large such that  $R \gg X$ , the mutual radiation impedance can be taken as simply the real part of  $Z_{12}$  at this frequency. The term in braces  $\{ \}$  in Eq. (2) is equal to the self-radiation resistance ( $R_s$ ) of a single radiator in the array. Ultimately, the mutual radiation resistance ( $R_m$ ) seen by the array is equal to nine times the self-radiation resistance (due to the ninefold increase in area) multiplied by a factor representing the inter-element interactions,  $R_i$  [i.e., the bracketed term  $[ \ ]$  in Eq. (2)]. Taking the radiating frequency as 18 kHz and the closest center-to-center spacing between two adjacent elements in the array as 13.4 mm, the real part of the bracketed term,  $R_i$ , is equal to 5.714. The expected increase in TVR in an array as compared to a single element at a given frequency is therefore actually equal to  $(20 \cdot \log N - 20 \cdot \log R_i)$ , where  $N$  is the increase in radiating area (or number of elements in the array). In the case of the nine-element arrays used in this analysis, the calculated increase in TVR (taking into account the mutual radiation impedance) at 18 kHz as compared to the single element should be 4 dB, which is what was experimentally observed in the case of the unpotted array (see Table IV). The slightly lower TVR seen in the case of the potted array can then be attributed to additional damping effects due to the stiff polymer. At frequencies beyond the resonance, mutual radiation impedance becomes less significant, and the approximate 19-dB increase in TVR as expected in the case of the unloaded array is observed.

Figure 7 compares the TVR curves for unpotted

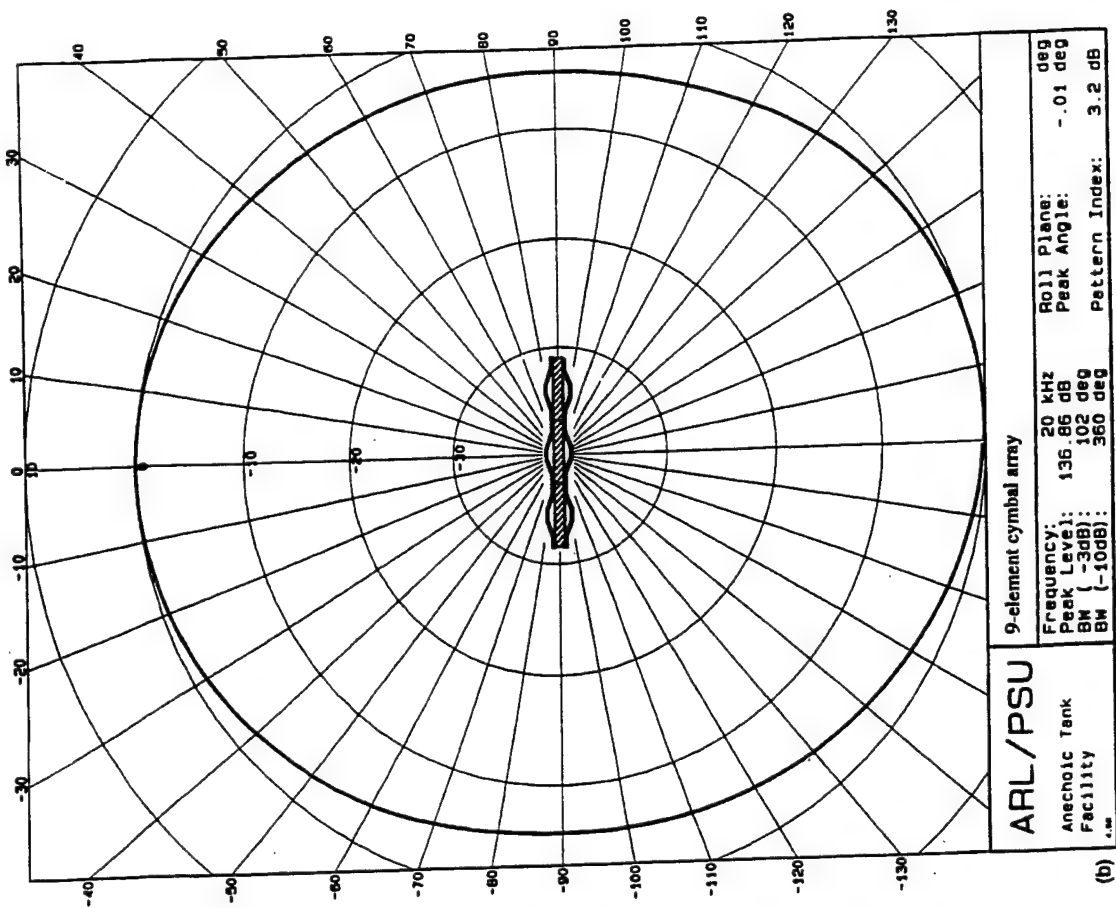
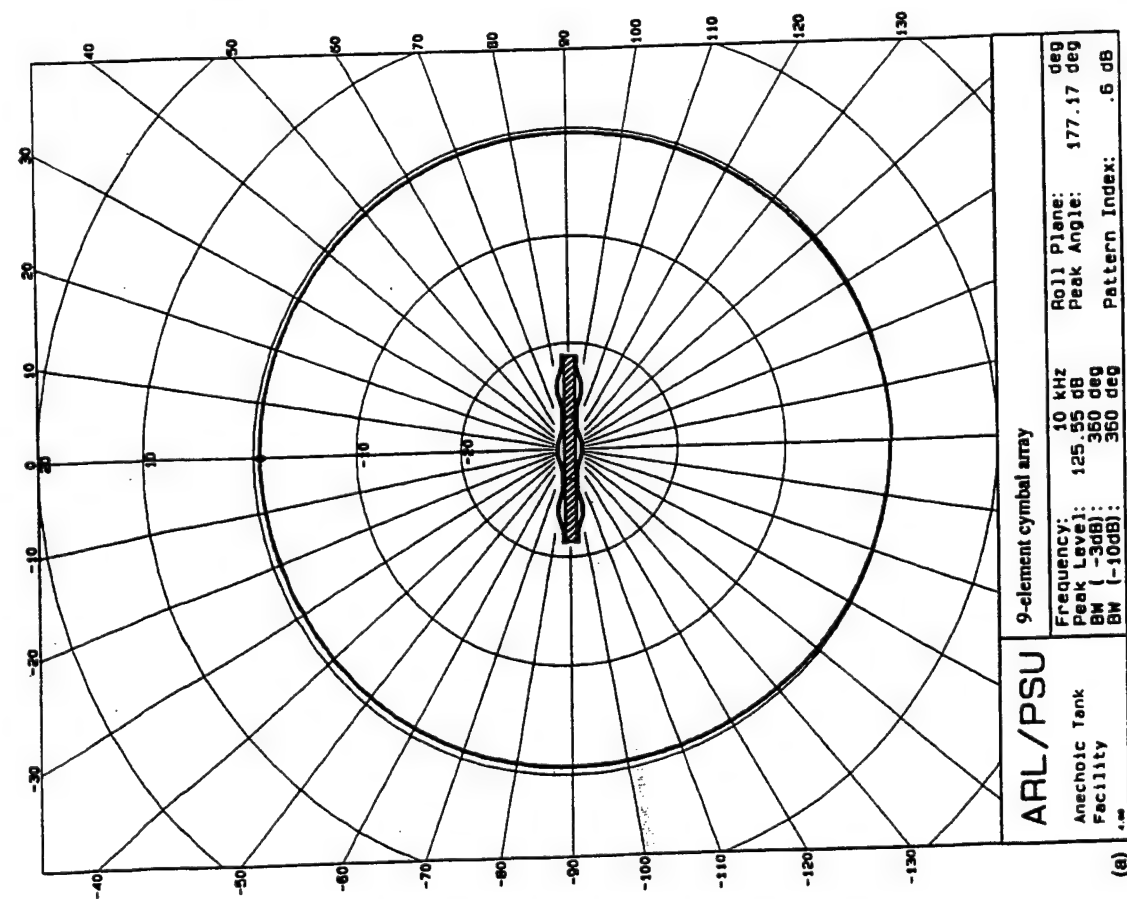
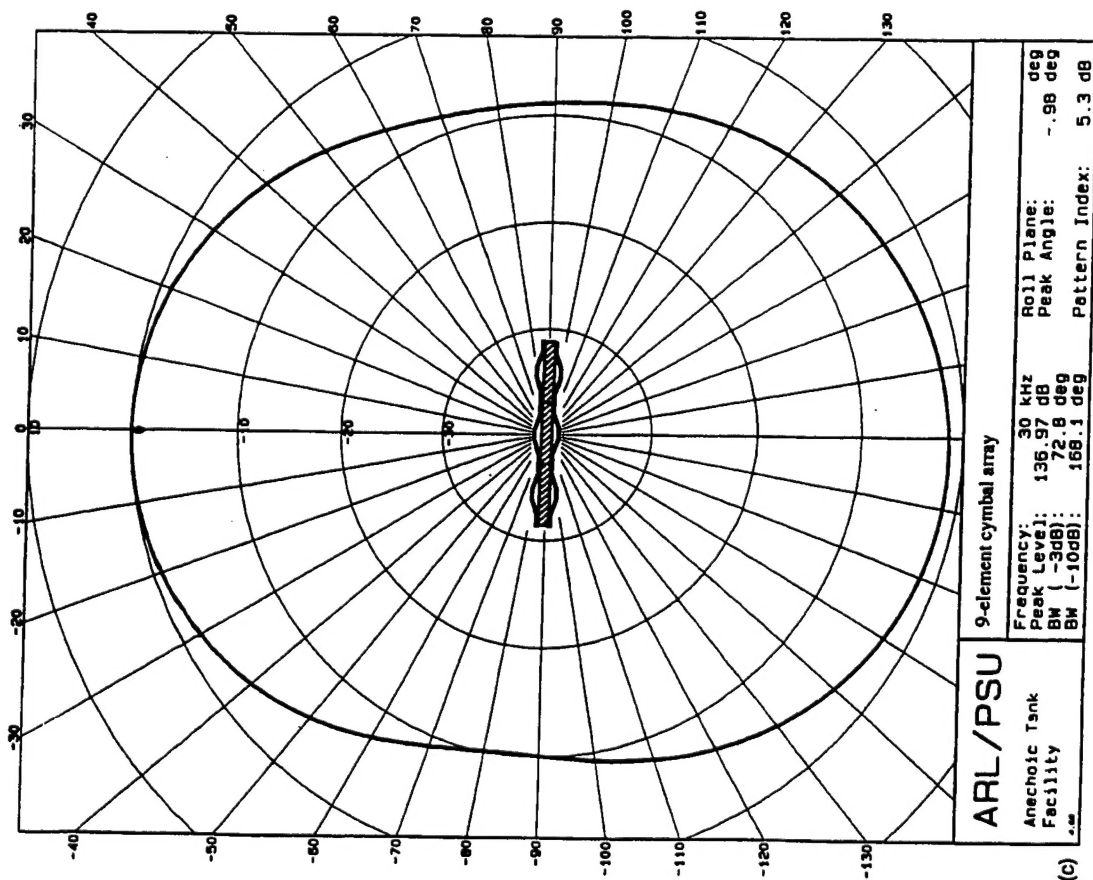
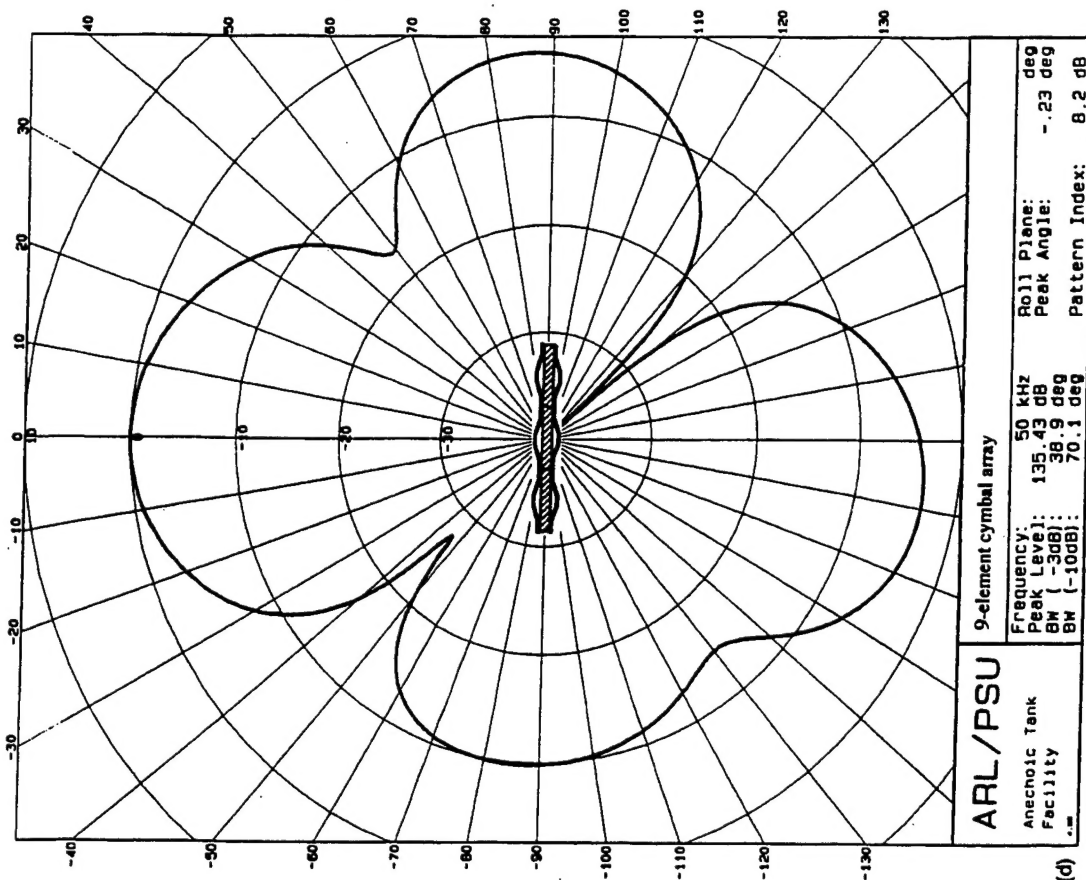


FIG. 9. Transmit-beam patterns for the cymbal arrays at (a) 10 kHz, (b) 20 kHz, (c) 30 kHz, (d) 50 kHz, and (e) 130 kHz.



(c)



(d)

FIG. 9. (Continued.)



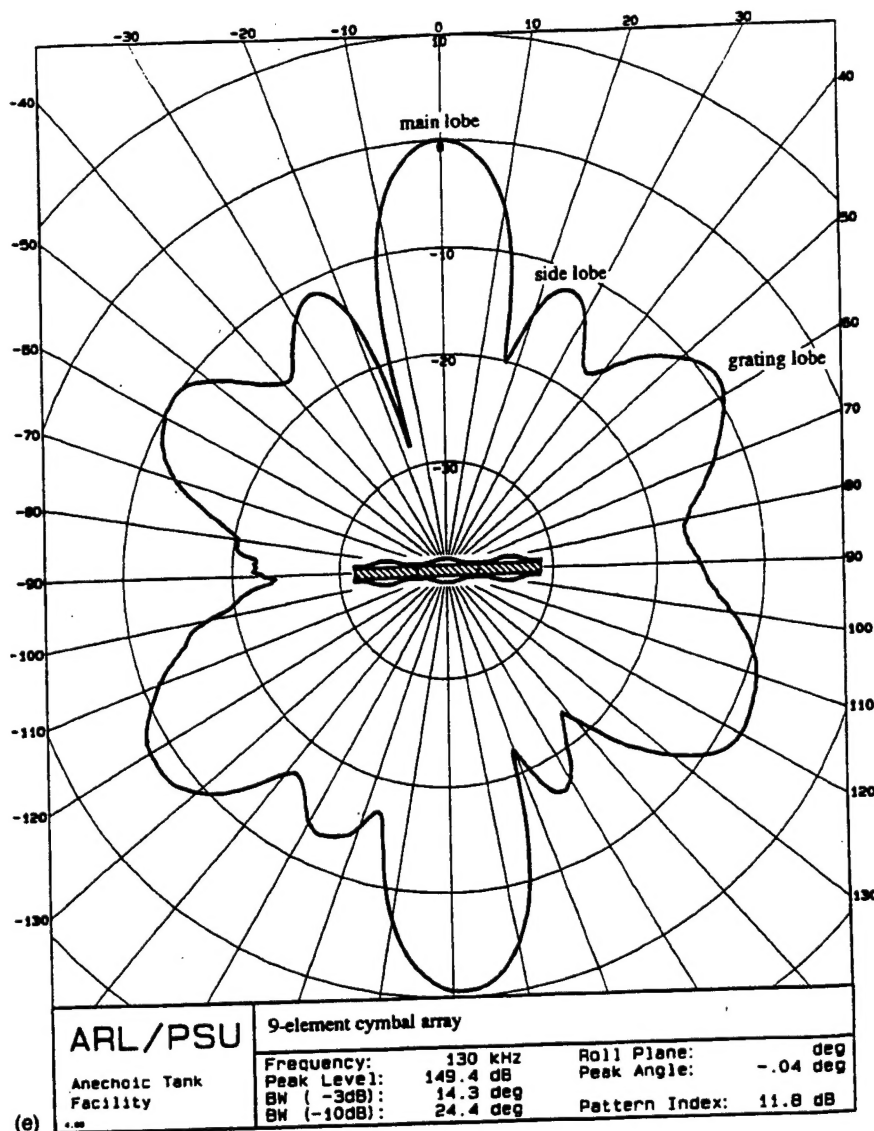


FIG. 9. (Continued.)

9-element cymbal arrays consisting of either brass or titanium caps. Below 20 kHz, the curves are practically identical. At higher frequencies, however, the titanium-capped cymbal array exhibits about a 3-dB higher TVR than the brass-capped cymbal array. The specific acoustic impedance ( $z = \rho c$ ) of brass, titanium, and water are 40.4, 27.3, and 1.5 MPa·s/m, respectively.<sup>26</sup> Since the ratio of the characteristic impedance of brass to water is approximately  $\sqrt{2}$  times the ratio of the characteristic impedance of titanium to water, and  $20 \cdot \log \sqrt{2}$  is 3 dB, the increase in TVR may be due to the better acoustic match of titanium to the water environment.

Figure 8 shows the measured source-level curves for the unpotted brass-capped array. The curves correspond to drive levels ranging from 40 dB re: 1 V to 56 dB re: 1 V in increments of 1 dB re: 1 V. At a drive level of 57 dB re: 1 V, the array failed and hence no measurement was recorded. The cause of failure was cracking in the caps due to work hardening.<sup>27</sup> The primary resonance is evident at 18.5 kHz, when the drive level is 40 dB re: 1 V and is present up to a drive level of 54 dB re: 1 V, above which it is suppressed

and nonlinear behavior becomes apparent. When driven slightly below its failure level (e.g., 52 dB re: 1 V), a source level of 180 dB re: 1  $\mu$ Pa·m or greater is generated between 10 and at least 25 kHz. However, this is for a radiating area of only 11.4 cm<sup>2</sup>. A simple way to enhance the source level is by increasing the number of elements in the array and hence increase the radiating area.

The beam patterns at various frequencies for the cymbal array are shown in Fig. 9. At low frequency (half-wavelength aperture or less), the array exhibits near-omnidirectionality. Interference between the signals generated by the individual elements in the array leads to more complex beam patterns seen at higher frequencies. Nonsymmetry in the patterns is a result of individual elements in the array not being matched in phase. It is important to be able to determine the theoretical patterns to know what to expect from the measured array. In order to calculate the patterns in this 3×3 array, simple line theory was used. The patterns in the horizontal plane can be calculated by using a line array consisting of  $N$  ( $=3$  in this case) equally spaced, equally phased, equal strength sources. The relative strength,  $P$ , at any incident

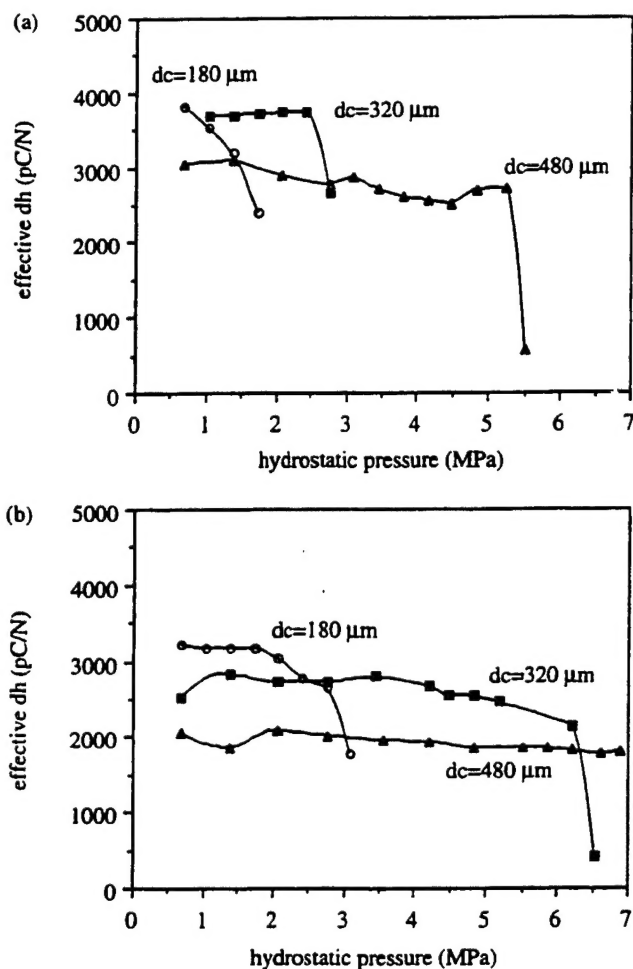


FIG. 10. Pressure dependence of the effective  $d_h$  coefficient for standard-size single-element cymbal transducers with (a) brass caps and (b) molybdenum caps of varying cavity depth.

angle,  $\varnothing$ , normal to the face of the projector can be calculated from the expression:<sup>28</sup>

$$P = \frac{\sin\left(\frac{Nkd \cdot \sin \varnothing}{2}\right)}{N \cdot \sin\left(\frac{kd \cdot \sin \varnothing}{2}\right)}, \quad (3)$$

where  $d$  is the center-to-center spacing between the elements and  $k$  is the wave number. The nulls are found by calculating the angles which make  $P=0$ . From Eq. (3), the appearance of the first null is predicted to occur at 37 kHz when  $\varnothing$  is 90 deg. Nulls in the pattern occur at angles where the radiated waves from each cymbal are separated by a distance of one half-wavelength. Grating lobes, which are secondary major lobes, will appear at higher frequencies. The number of side lobes present between the main and grating lobes is equal to the number of cymbal elements along a side in the array less two. As seen at 130 kHz [Fig. 9(e)], there is one side lobe between the main lobe and the grating lobe. In Fig. 9(d), 50 kHz, the side lobes becomes significant. The only null in the first quadrant at 50 kHz was calculated to be about 48 deg, which compares well to the null seen in the pattern in Fig. 9(d). The first quadrant nulls at 130 kHz were calculated to be at about 17, 35, and 59 deg. The first two correlate well

with those seen in the pattern [Fig. 9(e)]. However, the null at 59 deg is masked by the grating lobe.

Figure 10 shows the measured pressure dependence of the  $d_h^{\text{eff}}$  coefficients of single-element brass-capped and molybdenum-capped cymbal transducers with different cavity depths ( $dc$ ). The standard brass-capped cymbal can withstand hydrostatic pressures of up to 2.5 MPa (250 m water depth) before failing. Failure was found to be due to the caps being deformed beyond their elastic limits, hence eliminating the effective stress-transfer mechanism between the piezoelectric ceramic and the caps.<sup>27</sup> As can be seen, the pressure tolerance of the transducer is dependent upon the stiffness of the cap material as well as the cap shape. With the stiff molybdenum caps, cymbals with deep cavities can withstand at least 7 MPa of pressure. Unfortunately, the stiff molybdenum caps cannot flex as readily as the softer brass caps, hence their displacement (and ultimately the TVR) is expected to be lower than that of the brass-capped cymbals.

#### IV. CONCLUSIONS

The cymbal transducer array appears to be a viable candidate for medium- to high-power shallow-water acoustic projector applications at frequencies below 50 kHz. Preliminary results indicate that it compares quite favorably with both the Tonpitz and 1-3 composites, at least in terms of output power. Its thin profile when incorporated into arrays makes it ideal for conforming to a curved surface. In addition, its simple design and uncomplicated construction method should render it easy and hence inexpensive to mass produce.

#### ACKNOWLEDGMENTS

The authors would like to thank Robert Dashem and Greg Granville of the Applied Research Laboratory, the Center for Acoustics and Vibration at Penn State, as well as Ender Kuntsal of International Transducer Corporation in Santa Barbara, CA, for their contributions. The authors would also like to acknowledge the Office of Naval Research and the Defense Advanced Research Projects Agency (DARPA) for their financial support.

<sup>1</sup>R. F. W. Coates, *Underwater Acoustic Systems* (Macmillan, Hong Kong, 1990), p. 2.

<sup>2</sup>W. J. Hughes, "Transducers, Underwater Acoustic," in *Encyclopedia of Applied Physics*, Vol. 22, edited by G. L. Trigg, W. Greulich, and E. S. Vera (Wiley-VCH GmbH, Weinheim, Germany, 1998), pp. 67–84.

<sup>3</sup>T. R. Howarth, "A Multilayer 1-3 Piezoelectric Composite Underwater Projector," presented at the 133rd meeting of the Acoustical Society of America, The Pennsylvania State University, June 1997 [J. Acoust. Soc. Am. **101**, 3095(A) (1997)].

<sup>4</sup>V. F. Janas and A. Safari, "Overview of Fine-Scale Piezoelectric Ceramic/Polymer Composite Processing," J. Am. Ceram. Soc. **78**(11), 2945–2955 (1995).

<sup>5</sup>L. Bowen, R. Gentilman, D. Fiore, H. Pham, W. Serwatka, C. Near, and B. Pazol, "Design, Fabrication, and Properties of Sonopanel™ 1-3 Piezocomposite Transducers," Ferroelectrics **187**, 109–120 (1996).

<sup>6</sup>W. Cao, Q. M. Zhang, and L. E. Cross, "Theoretical Study on the Static Performance of Piezoelectric Ceramic-Polymer Composites with 1-3 Connectivity," J. Appl. Phys. **72**, 5814–5821 (1992).

<sup>7</sup>Q. X. Chen and P. A. Payne, "Industrial Applications of Piezoelectric

- Polymer Transducers," *Meas. Sci. Technol.* 6(3), 249-267 (1995).
- <sup>8</sup> R. Y. Ting, "Composite Piezoelectric Materials for Transduction," *Appl. Acoust.* 41, 325-335 (1994).
  - <sup>9</sup> K. D. Rolt, "History of the Flexensional Electroacoustic Transducer," *J. Acoust. Soc. Am.* 87, 1340-1349 (1990).
  - <sup>10</sup> E. F. Rynne, "Innovative Approaches for Generating High Power, Low Frequency Sound," in *Transducers for Sonics and Ultrasonics*, edited by M. D. McCollum, B. F. Hamonic, and O. B. Wilson (Technomic, Lancaster, PA, 1993), Chap. 3, pp. 38-49.
  - <sup>11</sup> Q. C. Xu, S. Yoshikawa, J. R. Belsick, and R. E. Newnham, "Piezoelectric Composites with High Sensitivity and High Capacitance for Use at High Pressures," *IEEE Trans. Ultrason. Ferroelectr. Freq. Control* 38, 634-639 (1991).
  - <sup>12</sup> R. E. Newnham, Q. C. Xu, and S. Yoshikawa, "Transformed Stress Direction Acoustic Transducer," U.S. Patent 4,999,819 (1991).
  - <sup>13</sup> R. E. Newnham and A. Dogan, "Metal-Electroactive Ceramic Composite Transducer," U.S. Patent 5,729,077 (1998).
  - <sup>14</sup> A. Dogan, K. Uchino, and R. E. Newnham, "Composite Piezoelectric Transducer with Truncated Conical Endcaps 'Cymbal'," *IEEE Trans. Ultrason. Ferroelectr. Freq. Control* 44, 597-605 (1997).
  - <sup>15</sup> J. F. Tressler, A. Dogan, J. F. Fernandez, J. T. Fielding Jr., K. Uchino, and R. E. Newnham, "Capped Ceramic Hydrophones," in *1995 IEEE Ultrasonics Symposium Proceedings*, edited by M. Levy, S. C. Schneider, and B. R. McAvoy (IEEE, Piscataway, NJ, 1995), pp. 897-900.
  - <sup>16</sup> K. Onitsuka, A. Dogan, J. F. Tressler, Q. Xu, S. Yoshikawa, and R. E. Newnham, "Metal-Ceramic Composite Transducer, the 'Moonie'," *J. Intell. Mater. Syst. Struct.* 6, 447-455 (1995).
  - <sup>17</sup> K. Onitsuka, A. Dogan, Q. Xu, S. Yoshikawa, and R. E. Newnham, "Design Optimization for Metal-Ceramic Composite Actuator, 'Moonie'," *Ferroelectrics* 156, 37-42 (1994).
  - <sup>18</sup> K. Onitsuka, "Effects of Bonding and Geometry on the Flexensional Transducer, 'Moonie'," Ph.D. thesis, The Pennsylvania State University, 1993, Chap. 3, pp. 30-139.
  - <sup>19</sup> A. Dogan, "Flexensional 'Moonie and Cymbal' Actuators," Ph.D. thesis, The Pennsylvania State University, 1994, Chap. 3, p. 42.
  - <sup>20</sup> J. F. Fernandez, A. Dogan, J. T. Fielding, K. Uchino, and R. E. Newnham, "Tailoring the Performance of Ceramic-Metal Piezocomposite Actuators, 'Cymbals'," *Sens. Actuators A* 65, 228-237 (1998).
  - <sup>21</sup> J. F. Tressler, W. Cao, K. Uchino, and R. E. Newnham, "Finite Element Analysis of the Cymbal-Type Flexensional Transducer," *IEEE Trans. Ultrason. Ferroelectr. Freq. Control* 45, 1363-1369 (1998).
  - <sup>22</sup> R. J. Bobber, *Underwater Electroacoustic Measurements* (Naval Research Laboratory, Washington, DC, 1970), p. 6.
  - <sup>23</sup> R. J. Urlick, *Principles of Underwater Sound* (McGraw-Hill, New York, 1983), 3rd ed., p. 71.
  - <sup>24</sup> A. Dogan, "Flexensional 'Moonie and Cymbal' Actuators," Ph.D. thesis, The Pennsylvania State University, 1994, Chap. 8, pp. 144-171.
  - <sup>25</sup> R. L. Pritchard, "Mutual Acoustic Impedance between Radiators in an Infinite Rigid Plane," *J. Acoust. Soc. Am.* 32, 730-737 (1960).
  - <sup>26</sup> C. T. Lynch, editor, *CRC Handbook of Materials Science, Vol. 1: General Properties* (CRC Press, Cleveland, OH, 1974), Table 3-47, pp. 405-407.
  - <sup>27</sup> J. F. Tressler, "Capped Ceramic Underwater Sound Projector, the 'Cymbal'," Ph.D. thesis, The Pennsylvania State University, 1997, Chap. 8, pp. 209-228.
  - <sup>28</sup> O. B. Wilson, *Introduction to Theory and Design of Sonar Transducers* (Peninsula, Los Altos, CA, 1988), p. 169.